UNIVERSIDADE ESTADUAL DE CAMPINAS

Faculdade de Engenharia Civil, Arquitetura e Urbanismo

Ingrid Rocio Irreño Palomo

Analytical and numerical study of reinforced concrete beam-column joints (BCJs) retrofitted with UHPFRC under cyclic loading

Estudo analítico e numérico de ligações viga-pilar (LVP) reforçadas com UHPFRC sujeitas a carregamento cíclico

CAMPINAS

2025

Ingrid Rocio Irreño Palomo

Analytical and numerical study of reinforced concrete beam-column joints (BCJs) retrofitted with UHPFRC under cyclic loading

Estudo analítico e numérico de ligações viga-pilar (LVP) reforçadas com UHPFRC sujeitas a carregamento cíclico

Tese apresentada à Faculdade de Engenharia Civil, Arquitetura e Urbanismo da Universidade Estadual de Campinas como parte dos requisitos exigidos para obtenção do título de Doutora em Engenharia Civil, na área de Estruturas e Geotécnica

Thesis presented to the Faculty of Civil Engineering, Architecture and Urbanism of the University of Campinas in partial fulfillment of the requirements for the degree of Doctor, in Civil Engineering in the area of Structures and Geotechnics

Orientador Prof. Dr. Luiz Carlos de Almeida

ESTE TRABALHO CORRESPONDE À VERSÃO FINAL DA TESE DEFENDIDA PELA ALUNA INGRID ROCIO IRREÑO PALOMO E ORIENTADA PELO PROF. DR. LUIZ CARLOS DE ALMEIDA

CAMPINAS
2025

Ficha catalográfica
Universidade Estadual de Campinas (UNICAMP)
Biblioteca da Área de Engenharia e Arquitetura
Vanessa Evelyn Costa - CRB 8/8295

Irreño Palomo, Ingrid Rocio, 1993-
Ir7a Analytical and numerical study of reinforced concrete beam-column joints (BCJs) retrofitted with UHPFRC under cyclic loading / Ingrid Rocio Irreño Palomo. – Campinas, SP : [s.n.], 2025.

Orientador: Luiz Carlos de Almeida.
Tese (doutorado) – Universidade Estadual de Campinas (UNICAMP), Faculdade de Engenharia Civil, Arquitetura e Urbanismo.

1. Concreto armado. 2. Análise não-linear. 3. Método dos elementos finitos. 4. Concreto de ultra desempenho reforçado com fibras. 5. Método analitico. I. Almeida, Luiz Carlos de, 1955-. II. Universidade Estadual de Campinas (UNICAMP). Faculdade de Engenharia Civil, Arquitetura e Urbanismo. III. Título.

Informações complementares

Título em outro idioma: Estudo analítico e numérico de ligações viga-pilar (LVP) reforçadas com UHPFRC sujeitas a carregamento cíclico
Palavras-chave em inglês:
Reinforced concrete
Non-linear analysis
Finite element method
Ultra-high performance concrete
Analytical method
Área de concentração: Estruturas e Geotécnica
Titulação: Doutora em Engenharia Civil
Banca examinadora:
Luiz Carlos de Almeida [Orientador]
António Manuel Pinho Ramos
Pablo Augusto Krahl
Thomaz Eduardo Teixeira Buttignol
Leandro Mouta Trautwein
Data de defesa: 21-03-2025
Programa de Pós-Graduação: Engenharia Civil

Objetivos de Desenvolvimento Sustentável (ODS)
ODS: 11. Cidades e comunidades sustentáveis

Identificação e informações acadêmicas do(a) aluno(a)
- ORCID do autor: https://orcid.org/0000-0002-4517-0076
- Currículo Lattes do autor: http://lattes.cnpq.br/9909527948849683

Prof. Dr. Luiz Carlos de Almeida
Presidente e Orientador(a)/ Universidade Estadual de Campinas

Prof. Dr. António Manuel Pinho Ramos
Universidade NOVA de Lisboa

Prof. Dr. Pablo Augusto Krahl
Universidade Presbiteriana Mackenzie

Prof. Dr. Thomaz Eduardo Teixeira Buttignol
Universidade Estadual de Campinas

Prof. Dr. Leandro Mouta Trautwein
Universidade Estadual de Campinas

A Ata da defesa com as respectivas assinaturas dos membros encontra-se no SIGA/Sistema de Fluxo de Dissertação/Tese e na Secretaria do Programa da Unidade.

"I dedicate this work to my beloved husband Cristhian, my parents Gloria and Libardo, my siblings Jessica and Fabian, and my nephew Matias."

Acknowledgments

First and foremost, I would like to express my heartfelt gratitude to God for the opportunities He has granted me to complete my doctoral studies, for without His assistance and guidance, none of this would have been possible. I also wish to extend my sincere thanks to my parents, Glória Palomo and Libardo Irreño, who have been pillars of support and motivation, encouraging me not to give up, offering prayers, long conversations, and numerous pieces of advice during the most challenging moments of this journey. I am deeply grateful to my siblings, Jessica and Fabian Irreño, and my nephew, Matias Salas, who have been there for me throughout, even from a distance, always offering their support and assistance whenever needed. To my beloved husband, Cristhian Lopes, who has been my unwavering support here in Brazil, emotionally, spiritually, and academically, motivating me and providing constant help.

I would like to express my profound appreciation to my advisor, Professor Luiz Carlos de Almeida, for the opportunity to accept the challenge of guiding me throughout my doctoral studies, and to Professor Leandro Mouta for his valuable assistance and guidance during the entire research process.

I am also deeply grateful to my professor, Margueritha Pauletta, and postdoctoral researcher Giada, who welcomed and mentored me during my doctoral exchange in Italy, making me feel warmly received throughout the entire internship. Additionally, I would like to extend my thanks to all my friends and colleagues at the LABMEM and RELAB laboratories for their partnership and companionship over the years, particularly to my friends Carlos Benedetti and Fabio Leitão, who have been my steadfast friends since the beginning of my master's program, and whose academic contributions have greatly enriched my research. I also express my gratitude to Professor and friend Pablo Krahl, who has been a tremendous help throughout my research, always providing guidance on various aspects of the work I developed.

Finally, I would like to convey my deepest thanks to all my friends and brothers and sisters in faith at the Christian Church Assemblies of God of Barão Geraldo, who have always been a great source of companionship and support throughout my doctoral journey.

I am truly grateful to all those mentioned, and I pray that God blesses you abundantly, bringing forth great projects for all of us, as I am certain that each of you has planted a very special seed in my heart. Thank you!

"Our hope is in the Lord; He is our help and our protection. In Him our hearts rejoice, for we trust in His holy name. May your love be upon us, Lord, as our hope is in You."

Psalm 33:20-22

Abstract

By the late 1970s, beam-column joints (BCJs) were typically designed to withstand only gravity loads, with little consideration for seismic forces. This oversight was a major contributor to both local and global structural collapses worldwide. Extensive research has since highlighted the critical importance of accounting for seismic forces in the design of new reinforced concrete (RC) structures. However, older structures designed without these considerations remain vulnerable to collapse. Today, various retrofit techniques can be applied to BCJs to enhance their shear strength and restore their integrity after seismic damage. However, the use of materials such as HPFRC/UHPFRC to improve the shear behavior of BCJs needs to be deeply explored. This study investigates the behavior of exterior BCJs, both with and without HPFRC/UHPFRC retrofitting, under cyclic loading representative of seismic action. To achieve this, a comprehensive review of analytical models for predicting the shear strength of RC BCJs was conducted. Additionally, a new analytical methodology was developed to estimate the ultimate bending moment in the beam and the shear capacity of retrofitted exterior BCJs. Furthermore, numerical simulations of exterior joints with and without retrofit were performed using the computational software ATENA, incorporating interface models. The analytical and numerical results demonstrated good accuracy with experimental data in terms of peak column load (V_c), hysteresis curve, and crack patterns, showing the retrofit efficiency in the joints with HPFRC/UHPFRC to prevent the diagonal shear failure. Finally, a parametric study was conducted to evaluate the influence of key factors, including beam reinforcement ratio, thickness and the compressive strength of HPFRC/UHPFRC. The results indicated that increasing any of these parameters enhanced joint shear strength. However, the greatest improvement in column force (V_c) was observed when increasing the beam reinforcement ratio, compared to increasing the compressive strength of HPFRC. Additionally, joints with beam reinforcement ratios of 0.4% and 0.7% exhibited V_c values similar to those obtained with compressive strengths of 110.5 MPa and 165.8 MPa, respectively. However, a reinforcement ratio of 1.2% resulted in higher V_c values compared to those achieved with a compressive strength of 221.0 MPa.

Keywords: reinforced concrete; non-linear analysis; finite element method; ultra-high performance concrete, analytical method.

Resumo

Até o final da década de 1970, as ligações viga-pilar (LVPs) eram geralmente projetadas para resistir apenas às cargas gravitacionais, com pouca consideração para as forças sísmicas. Essa negligência foi um dos principais fatores que contribuíram para colapsos estruturais locais e globais em todo o mundo. Diversas pesquisas têm destacado a importância fundamental de considerar as forças sísmicas no projeto de novas estruturas de concreto armado (CA). No entanto, estruturas mais antigas, projetadas sem essas considerações, continuam vulneráveis ao colapso. Atualmente, diversas técnicas de reforço estrutural (retrofit) podem ser aplicadas às LVPs para aumentar sua resistência ao cisalhamento e restaurar sua integridade após danos sísmicos. No entanto, o uso de materiais como HPFRC/UHPFRC para melhorar o comportamento ao cisalhamento das LVPs ainda precisa ser mais explorado. Este estudo investiga o comportamento de LVPs externas, com e sem reforço de HPFRC/UHPFRC, sob carregamento cíclico representativo da ação sísmica. Para isso, foi realizada uma revisão bibliográfica de modelos analíticos para prever a resistência ao cisalhamento das LVPs de concreto armado. Além disso, foi desenvolvida uma nova metodologia analítica para estimar o momento fletor último na viga e a capacidade ao cisalhamento de LVPs externas reforçadas. Foram também realizadas simulações numéricas de ligações externas, com e sem reforço, utilizando o programa computacional ATENA, incorporando modelos de interface. Os resultados analíticos e numéricos apresentaram boa semelhança com os dados experimentais em termos de carga máxima no pilar (V_c), curva de histerese e padrão de fissuração, mostrando a eficiência do reforço com HPFRC/UHPFRC na prevenção da falha diagonal por cisalhamento. Por fim, foi conduzido um estudo paramétrico para avaliar a influência de importantes fatores, incluindo a taxa de armadura da viga, a espessura do reforço e a resistência à compressão do HPFRC/UHPFRC. Os resultados indicaram que o aumento de qualquer um desses parâmetros melhorou a resistência ao cisalhamento da ligação. No entanto, a maior melhoria na força do pilar (V_c) foi observada com o aumento da taxa de armadura da viga, em comparação com o incremento da resistência à compressão do HPFRC. Além disso, ligações com taxas de armadura na viga de 0,4% e 0,7% apresentaram valores de V_c semelhantes aos obtidos com resistências à compressão de 110,5 MPa e 165,8 MPa, respectivamente. Entretanto, uma taxa de armadura de 1,2% resultou em valores de V_c superiores aos alcançados com uma resistência à compressão de 221,0 MPa.

Palavras-chave: concreto armado; análise não-linear; método dos elementos finitos; concreto de ultra-alto desempenho reforçado com fibras; método analítico.

List of Figures

List of Tables

List of symbols

Below are the definitions of the parameters that have been used in this thesis.

Latin upper-case letters

A_b	Gross area of beam section
A_c	Joint core horizontal area
A_g	Gross area of column section
A_j	Effective area of joint
A_R	UHPFRC jacket horizontal area at mid-height of the joint
A_{str}	Effective area of the diagonal strut
A_{sb}	Area of the beam longitudinal reinforcement
A_{sco}	Area of the column longitudinal reinforcement
A_{sjh}	Area of horizontal joint reinforcement
A_{sjv}	Area of vertical joint reinforcement (intermediate column bars)
A_{sc}	Area of the bottom longitudinal steel reinforcements
A_{sc}	Area of the top longitudinal steel reinforcements
A_s	Area of the top steel reinforcement
BI	Beam reinforcement index
B	Width of the beam section with jacket
C_c	Compressive force in the normal concrete
C_{R1}	Compressive force in the UHPFRC
C_{R2}	Compressive force in the UHPFRC
C_{R1}	Compressive force on the UHPFRC layer
C_s	Resultant force of the compressive reinforcement in the beam
C_s	Resultant force of the compressive reinforcement in the column
C_s	Resultant force of the compressive reinforcement in the column
C_{sc}	Force of the bottom longitudinal steel reinforcements
C_{sc}	Force of the top longitudinal steel reinforcements
E_c	Young's modulus of normal concrete
E_R	Young's modulus of UHPFRC
E_s	Young's modulus of steel bars
E_{sh}	Hardening modulus
F_{yh}	Yield force of the horizontal tie of the joint
F_{yv}	Yield force of the vertical tie of the joint
G_c	Shear modulus of the normal concrete
G_R	Shear modulus of the UHPFRC jacket
H	Depth of the beam section with jacket

JI	Joint transverse reinforcement index
K	Factor that considers the favorable effect of vertical and horizontal reinforcement in the joint
$\overline{K_h}$	Index of the horizontal ties of the joint
$\overline{K_v}$	Index of the vertical ties of the joint
L_b	Beam length
L_c	Column length
N_c	Axial force of the column
SI_J	Shear index of the joint
T	Tensile steel force in the beam
T	Tensile steel force in the column
T	Tensile steel force in the column
T_{R1} - T_{R7}	Components of the tensile resultant force of UHPFRC jacket
T_R	Tensile force on the retrofit material
T_s	Tensile force on the top reinforcement
V_{sh}	Shear strength provided by stirrups
V_b	Shear force acting on the beam
V_c	Shear force acting on the column
V_{ch}	Shear strength provided by concrete
V_{jh}	Shear strength of the retrofitted joint
V_{jhc}	Concrete contribution to the joint shear strength
V_{jhc}	UHPFRC contribution to the joint shear strength
V_{jh}^A	Acting shear force in the retrofitted joint
V_{jhc}^A	Acting shear force in the retrofitted joint given by the joint core
V_{jhR}^A	Acting shear force in the retrofitted joint given by the UHPFRC jacket

Latin lower-case letters

a_b	Depth of the compression zone in the beam
a_c	Depth of the compression zone in the column
a_s	Depth of the diagonal strut
b	Beam width (without jacket)
b_c	Core dimension of tied column, outside to outside edge of transverse reinforcement bars, perpendicular to the transverse reinforcement area
b_c	Column width (without jacket)
b_j	Width of the joint core
d	Distance between the centroid of the top longitudinal reinforcement and the extreme compressed concrete fiber of the beam section without jacket
d_b	Distance from the extreme compressed concrete fiber to the centroid of the compressed longitudinal reinforcement
d_{sb}	Average diameter of beam tensile reinforcement

f_a	corresponds to the average compressive stress in the column
f_b	Stress of beam bars in tension
f_c	Cylindrical compressive concrete strength
f_{cc}	Confined concrete strength
f_{cd}	Design compressive concrete strength
f_{ck}	Characteristic value of the compressive strength of concrete
f_{ct}	Contribution of concrete to nominal tensile strength
f_{cR}	Cylindrical compressive UHPFRC strength
f_{cu}	Effective strength of the compressed strut
f_{cuR}	Cubical compressive UHPFRC strength
f_{sy}	Yield strength of steel bars
f_{tn}	Nominal tensile strength with contributions from steel share reinforcement
$f_{ut}1$	Ultimate tensile stress of UHPFRC
f_{ut}	Tensile stress in the jacket at the interface with the joint core
f_{yb}	Yield strength of beam tensile reinforcement
f_{yc}	Yield strength of column reinforcement
f_{yjh}	Yield strength of horizontal joint reinforcement
f_{yjv}	Yield strength of vertical joint reinforcement
h	Beam depth (without jacket)
h_c	Column height (without jacket)
h_j	Depth of the joint core
h_{jc}	Distance between the faces of the longitudinal bars of the column
j_{bd}	Internal moment arm of the beam cross-section
k	Beneficial effect factor of the force on the shear strength
k	Resistance factor (Park and Mosalam (2012a) model)
k	Factor that considers the influence of the axial force in the column (Hassan and Moehle (2018) model)
l_h	Horizontal projection of the diagonal concrete strut
n_b	Maximum number of the top and the bottom beam bars
p_t	Principal tension stress
s_h	Spacing between hoops
x_c	Neutral axis depth
x	Orthogonal length from the longitudinal axis of the beam to the exterior face of the column (ASCE SEI/41 (2007) and ACI 318 (2014) models)
y	Distance from the neutral axis to the strain

Greek letters

	Factor that depends on the tensile stress f_b
$_c$	Factor used to calculate the tensile resultant force of concrete
$_R$	Factor used to calculate the tensile resultant force of UHPFRC (equivalent rectangular compressive stress block)
$_t$	Factor describing in-plane geometry
	Ratio between the bottom and top reinforcement of beam
$_s$	Concrete softening factor (Hassan and Moehle (2018) model)
$_t$	Factor describing out-of-plane geometry
$_c$	Factor used to calculate the tensile resultant force of concrete
$_R$	Factor used to calculate the tensile resultant force of UHPFRC (equivalent rectangular compressive stress block)
$_{sb}$	Distance from the extreme compressed concrete fiber to the centroid of the compressed longitudinal reinforcement
Δ	Horizontal displacement applied in the beam/column
$_{cuR}$	Maximum compressive strain in the UHPFRC layer
$_{ut,crack}$	strain corresponding to the tensile cracking strength f_{ut} of UHPFRC
$_{ut}$; $_{ut}$	Strains corresponding to the stresses f_{ut} and f_{ut} localized in the horizontal edges of the beam original cross-section
$_{ut}1$	ultimate tensile strain of UHPFRC
$_{sc}$	Strain in the bottom longitudinal reinforcement
$_{sc}$	Strain in the top longitudinal reinforcement
$_{sc}$	Strain of the bottom longitudinal steel reinforcements
$_{sc}$	Strain of the top longitudinal steel reinforcements
	Ratio between the elasticity modulus of the materials
$_t$	Parameter to account for the influence of beam eccentricity
$_o$	Overstrength factor of the steel
$_b$	Reinforcement ratio of beam
$_c$	Reinforcement ratio of column
$_s$	Horizontal reinforcement ratio of the joint
$_{sv}$	Vertical reinforcement ratio of the joint
$_{sjh}$	Volume ratio of horizontal reinforcement
$_{sjv}$	Volume ratio of vertical reinforcement
	Steel ratio for compression reinforcement beam
	Steel ratio for tensile reinforcement beam
$_b$	Beam bar index
$_{jh}$	Shear stress of joint
	Shear strength factor representing confinement of joint by lateral members
$_h$	Fraction of diagonal compression transferred by the horizontal tie in the absence of a vertical tie

v	Fraction of diagonal compression taken by the vertical tie in the absence of a horizontal tie
ext	Upper limit of shear strength normalized
	Non-dimensional function
R	Thickness of UHPFRC jacket
h	Angle of inclination of the concrete strut
b	Mean diameter of beam longitudinal bars in tension
$c2,c$	Compressive strain in the confined concrete at the peak stress
y	Axial stress of the column
2	Effective mean lateral confining pressure produced by the jacket
th	Normal strain of the confined concrete strut in the horizontal plane
$c2,c$	Initial value of the confined concrete strain used in the iterative process
$c2$	Unconfined ultimate compressive strain of normal concrete at peak stress
s	Tensile strain in the top steel reinforcement
t	Transverse strain of the confined concrete strut in the presence of the UHPFRC jacket
c	Poisson's coefficient of concrete
R	Poisson's coefficient of UHPFRC
0	Poisson's coefficient utilized to calculate the transverse strain of the confined concrete strut
l,x	Lateral pressure exerted by the UHPFRC jacket on the joint core acting in x horizontal direction
l,y	Lateral pressure exerted by the UHPFRC jacket on the joint core acting in y horizontal direction
l	Mean lateral confinement pressure
2	confining pressure orthogonal to the direction of the concrete diagonal strut
2	Compressive stress acting along the axis of the diagonal concrete strut
$c2,c$	Compressive strain in the confined concrete strut at the peak stress
	Non-dimensional interpolating function accounting for concrete softening softening factor

Contents

1 Introduction

Reinforced concrete (RC) structures can present several damages under seismic events (*e.g.*, earthquakes), risking human lives. Due to this, a high interest in studying structural elements subjected to cyclic loads has increased in the last decades, particularly for beam-column joints (BCJs), which are considered critical structural regions and are subjected to brittle failure if not adequately designed.

BCJs can cause failures during seismic events, mainly in the case of systems designed only with gravitational loads or with designed failures, such as inadequate anchorage in the joints, low ductility, low strength in the concrete, insufficient longitudinal reinforcement, and loss of bonding between the materials (PAMPANIN et al., 2002). Braga et al. (2009) and Vaghani et al. (2015), observed that those structural characteristics cause failures in the joints, slipping in the beam longitudinal bars, and loss of capacity and flexibility. Frequently, those aspects are more evident in exterior than interior joints. Figure 1.1 shows examples of failures in exterior BCJs caused by seismic events. Thus, the analysis of BCJs is fundamental in the design of new structures (including seismic action) and the verification of old structures, which did not consider seismic action, as in the case of Italian constructions built before the 1970s (PAMPANIN et al., 2002).

(a) (b)

Figure 1.1 – Failure in corner BCJ caused by earthquakes: a) Earthquake Izmir in Turkey 1999, b) Earthquake Abruzzo in Italy 2009.
Font: Adapted from Park and Mosalam (2013)

ACI 352R (2002) defines beam-column joint as the portion of the column localized within the depth of the deepest beam. The connections between beams and columns are essential to provide ductility in the structural frames and to transfer loads between the elements. The joints can be classified as interior, exterior, and corner according to their geometry.

Several experimental tests of BCJs subjected to cyclical load were developed to evaluate

this behavior, and diverse analytical models were proposed to determine the shear strength of RC beam-column joints, considering mechanical and geometrical parameters of the elements. In addition, some guidelines and codes present requirements to determine the shear strength, which depends on the confinement effect given by the adjacent members of the joint, (NZS 3101, 1995; FEMA 273, 1997; ACI 352R, 2002; Eurocodigo 8-Part I 1998, 2004; ASCE SEI/41, 2007; ACI 318, 2014).

Given the unpredictability of natural phenomena such as earthquakes, diverse retrofit techniques have been developed, both for strengthening and structural repair of existing structures, enhancing their shear capacity during seismic events. Some examples of retrofit material are steel jacketing (NOYAN, 2014), RC jacketing (KARAYANNIS et al., 2008), epoxy resin injections (KARAYANNIS et al., 1998), application of steel plates (LI et al., 2017; EBANESAR et al., 2022), Fiber Reinforcement Polymers of carbon or steel (FRP) (MUKHERJEE; JOSHI, 2005; PAMPANIN et al., 2007; BEYDOKHTY; SHARIATMADAR, 2016), and High-Performance Fiber Reinforced Concrete/Ultra High-Performance Fiber Reinforced (HPFRC/UHPFRC) (SHANNAG; ALHASSAN, 2005; BESCHI et al., 2015; KHAN et al., 2018; SAHARAN et al., 2023),

The Ultra-High Performance Concrete (UHPC) is characterized by its exceptional compressive and tensile strength, as well as its high stiffness. However, due to its brittle nature, fibers are often added to improve its ductility, resulting in what is known as Ultra-High Performance Fiber-Reinforced Concrete (UHPFRC) (FEHLING; SCHMIDT, 2014). UHPFRC combines the superior mechanical properties of UHPC with enhanced ductility and crack resistance provided by the fibers. It is also highly flowable, comparable to or even exceeding the workability of Self-Compacting Concrete (SCC), and typically achieves compressive strengths of no less than 150 MPa (AFGC, 2002; NF P 18-710, 2016; WILLE et al., 2014; HUANG et al., 2022a). In contrast, High-Performance Fiber-Reinforced Concrete (HPFRC) refers to a broader category of fiber-reinforced concretes that exhibit the mechanical characteristics of High-Strength Concrete (HSC) combined with SCC-like workability. HPFRC typically reaches compressive strength values ranging from 100 MPa to 150 MPa (KAIKEA; KARIHALOO, 2014; WALRAVEN, 2009; SOHAIL et al., 2021).

The application of HPFRC and UHPFRC jackets in retrofitting strategies has proven effective in preventing shear failure. These advanced materials offer a promising solution for enhancing the structural performance of beam-column joints, particularly in terms of stiffness, shear capacity, and energy dissipation (SCHMIDT; FEHLING, 2005; BAHRAQ et al., 2021; MATSAGAR, 2015).

In addition, with the advance of computational tools, numerical analysis using the Element Finite Method (MEF) has been used more frequently to study the shear response in beam-column joints (MOURLAS et al., 2017; DEATON, 2010). Up to now, numerical simulations of beam-column joints strengthened with UHPFRC jackets have been conducted only by Bahraq et al. (2021) and Fayaz et al. (2022). Through numerical simulations, it is possible to consider the non-linearity of the materials, which helps determine the cracking behavior of the elements and the key parameters that influence the joint's shear behavior, both with and without retrofit.The

advantages of this method are the low cost and short computation time to obtain results.

Thus, due to the lack of analysis on this topic, the present work studies the structural behavior of exterior joints under cyclic load, strengthened and non-strengthened with HPFRC/UHPFRC jackets. For this, diverse analytical models of RC BCJs were investigated, and a new methodology to determine the shear force and shear strength of exterior BCJs retrofitted with a UHPFRC jacket was developed, which is also presented in Palomo et al. (2024). Furthermore, numerical models of exterior BCJs retrofitted and non-retrofitted with UHPFRC also were developed.

1.1 Objectives

1.1.1 Main Objective

The main objective of this research is to study the shear behavior of exterior beam-column joints (BCJs) both unretrofitted and retrofitted with UHPFRC jackets under cyclic loading conditions through novel analytical methodology and numerical simulations using the Finite Element Method (FEM), which are validated with experimental results available in the literature.

1.1.2 Specifics Objectives

- To develop a bibliographic revision of analytical models that determine the shear strength of exterior reinforced concrete BCJs subjected to cyclic load, available in literature.
- To propose an analytical model to predict the ultimate bending moment in the beam and the shear strength of exterior BCJs retrofitted with UHPFRC jackets subjected to cyclic load, considering the confinement effect of UHPFRC jacket on the concrete and geometric and mechanical parameters of the elements.
- To simulate exterior BCJs both unretrofitted and retrofitted with UHPFRC jacket, using the Finite Element Method under cyclic loads, implementing constitutive laws to represent the non-linear behavior of the materials.
- To develop a parametric study to verify the influence of the beam's reinforcement ratio, compressive strength and thickness of UHPFRC material on the shear capacity of exterior beam column joints retrofitted with UHPFRC jackets.

1.2 Research significance

The significance of this research lies in its contribution to understanding the shear behavior of beam-column joints (BCJs), particularly those strengthened with UHPFRC jackets. Given the increasing demand for more efficient and durable structural solutions, this study provides a comprehensive analysis, including a review of available experimental tests, numerical model simulations, and the development of a new analytical model. The findings of this research not only expand knowledge on the performance of strengthened BCJs but also offer valuable guidelines for structural design, fostering advancements in civil engineering and contributing to the improvement of structural safety and longevity.

1.3 Organization of research

This work investigates the shear behavior of beam-column joints (BCJs), focusing on those strengthened with UHPFRC jackets. This study includes a summary of experimental tests available in literature, simulation of numerical models, and the purpose of a new analytical model. Figure 1.2 outlines the research structure and activities conducted throughout the thesis.

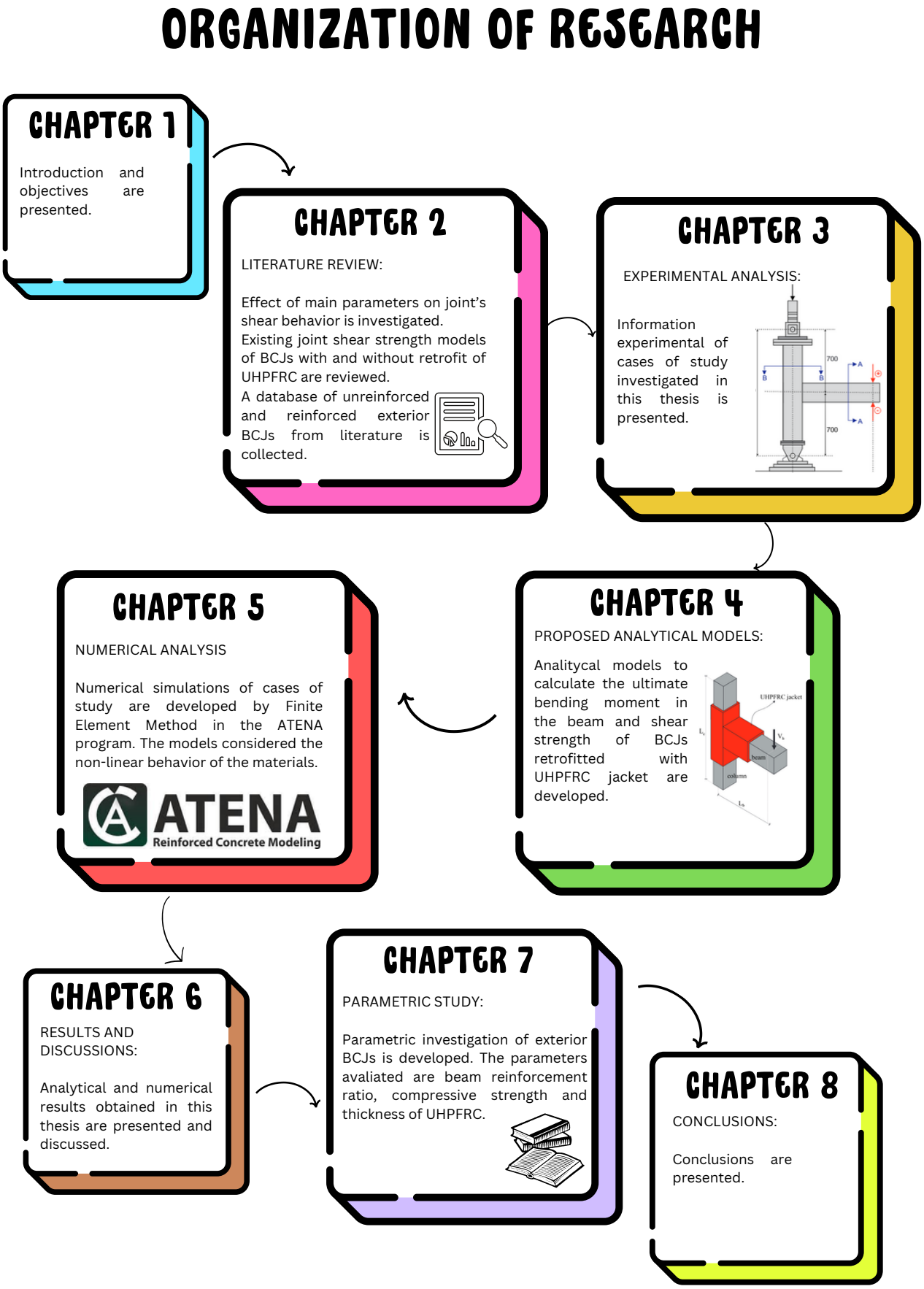

Figure 1.2 – Flowchart of research.

2 Literature Review

Reinforced concrete (RC) beam-column joints play a crucial role in the structural behavior of buildings. This connection is an essential factor in providing ductility to structural frames, ensuring the effective transfer of loads between beams and columns (Figure 2.1). Cases where gravity loads, wind loads, earthquake loads, or other forces induce moments in the connections must be considered in the resulting shear force and, consequently, in the joint design (ACI 318, 2019).

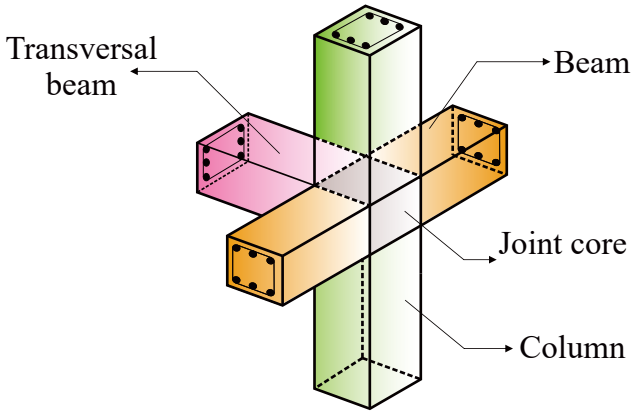

Figure 2.1 – Scheme of beam-column joint (BCJ).

ACI 352R (2002) defines a beam-column joint (BCJ) as the portion of the column located within the depth of the deepest beam. In contrast, transverse beams are orthogonal to the direction of the applied seismic load. Similarly, ACI 318 (2019) defines a BCJ as the common region at the intersection of structural elements.

The beam-column joints can be classified according to their geometry. They are labeled as exterior, interior, and corner joints, as shown in Figure 2.2. Other researchers also have analyzed the joints with transversal joints and slabs to obtain results closer to reality.

The standard ACI 352R (2002) classifies the beam-column joints in two categories, which are based on the load conditions and element's strains:

- Type 1: connections without significant inelastic deformation, *e.g.*, joints subjected to gravity loads and wind loads (without seismic loading).
- Type 2: connections designed to resist deformation reversal into the inelastic range, with energy dissipation, *e.g.*, beam-column joints subjected to cyclic loads, which are derived from earthquake loads.

Old constructions designed without seismic requirements have caused total or partial collapse in diverse structures worldwide. For this reason, diverse studies have been necessary to

predict the shear strength of joints, proposing diverse alternatives that help enhance the structural response of the joints subjected to cyclic loads.

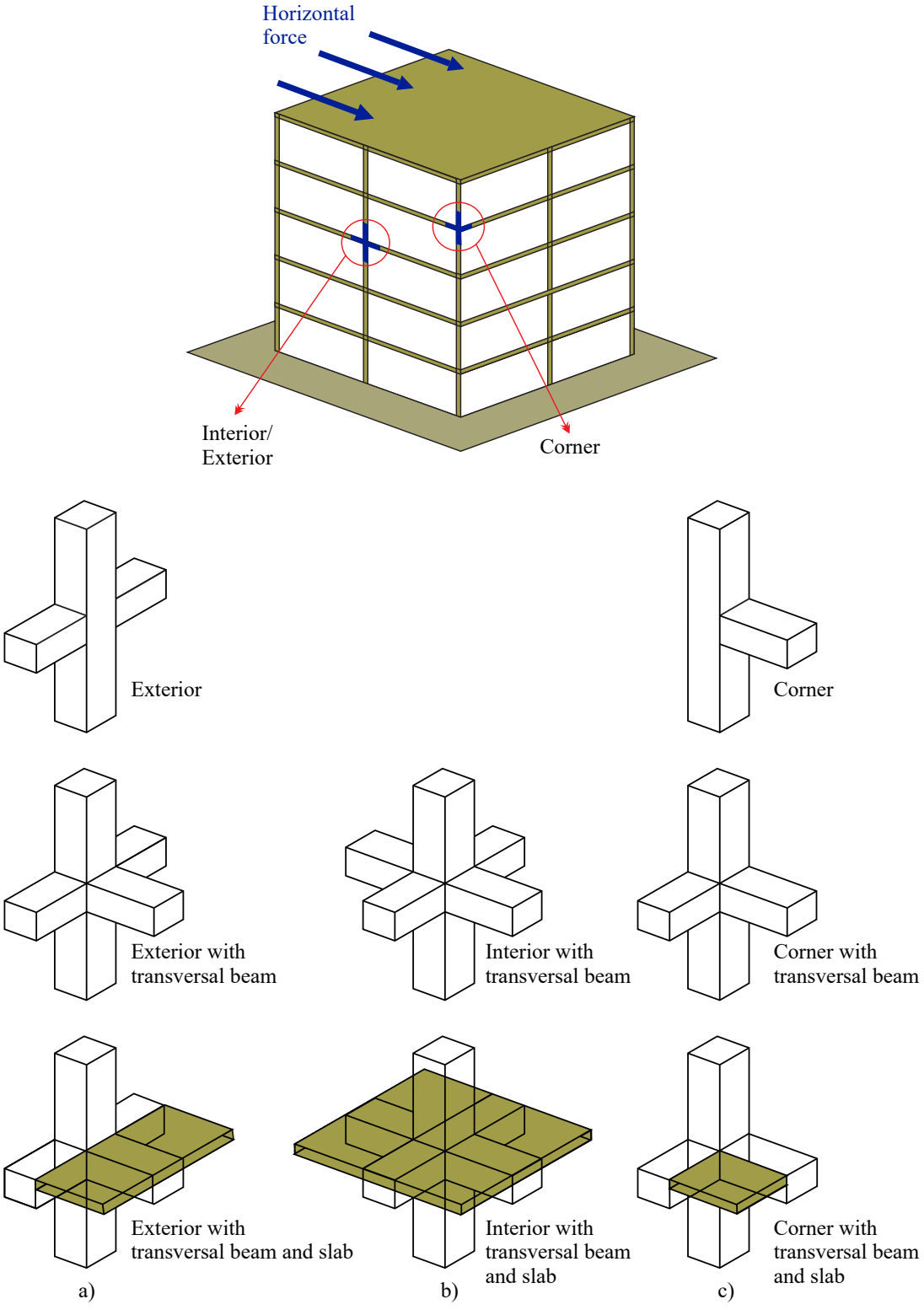

Figure 2.2 – Classification of beam-column joints a) Exterior, b) Interior, c) Corner.
Font: Obtained from ACI 352R (2002)

2.1 Connections in frames subjected to monotonic load

Over the years, researchers have studied the behavior of reinforced concrete (RC) to develop adequate formulations that guarantee the safety and reduction of cost in structures. Some of these studies have focused on beam-column joints, since they frequently control the behavior of frames subjected to seismic loads. The joints can be analyzed from a general or local point of view (frames or isolated joints). The structural response of both cases can be studied through non-linear analysis, which considers the material's cracking and plasticity, which are essential properties to obtain results closer to reality.

Initial studies of elements subject to shear forces have been evidenced in reinforced concrete frames under incremental lateral monotonic load conditions. Guner (2008) restructured and verified the numerical algorithm of Vector5 software, used for the non-linear analysis of frames based on Modified Compressive Field Theory (MCFT) (VECCHIO; COLLINS, 1986b). This new methodology allowed a better capture of the shear behavior and bending in the elements. Moreover, it could be applied to different conditions, such as monotonic loads, cyclic loads, dynamic loads, impact loads, and others. On the other hand, the work of Alfarah (2017) studied the performance of reinforced concrete frames subjected to monotonic load, proposing an analytical methodology with damaged models in tension and compression, as a function of their strains. This methodology was applied in numerical simulations using the ABAQUS software.

2.2 Beam-column joints subjected to cyclic load

The study of beam-column joints (BCJs) under cyclic loading, particularly in seismic conditions, has been extensively investigated in the pursuit of structural resilience. Researchers have evaluated various parameters influencing joint behavior, aiming to enhance performance and prevent failure. The following section presents a historical review of key parameters studied in past research.

2.2.1 Historic review of reinforced concrete BCJs

One of the first studies on BCJs was performed by Wallace (1996), who analyzed interior joints subjected to seismic loads with splices in the plastic region of the beam; since there were no requirements to use splices in critical regions of plastic hinges by that time. The authors tested the connections using both smooth (typical constructions in the 1960s) and deformed steel bars, following the recommendations of NZS 3101 (1982). The results showed that the connections with deformed bars presented low ductility and loss in load capacity during the first negative displacements and observed a significant reduction in the horizontal capacity load in joints with high-length splices (in the tensile longitudinal reinforcement). In contrast, connections with smooth bars presented bond loss during the first cycles, due to insufficient anchorage, low stiffness, and low ductility.

Liu and Park (1998) and Liu (2001) studied the joint behavior (interior and exterior) of typical 1950s constructions in New Zealand, with smooth bars and a small quantity of transverse

reinforcement. Results showed a significant loss in stiffness and bending strength, which could be attributed to the slipping of the smooth bars into the joint core. However, it was evidenced improvements in the shear strength of the BCJs.

Hakuto et al. (2000) studied the behavior of exterior joints (typical constructions before the 1970s) with deformed bars and small quantities of transverse reinforcement (stirrups) in the joint core. In this work, the authors evidenced the influence of the hooks regarding the joint's behavior, since beam bars bent in the joint region presented higher values of shear strength, bending strength, and ductility.

Pantelides et al. (2002) studied BCJs' exterior behavior with smooth steel bars, with beam bars bent away from the joint region, and small quantities of transverse reinforcement (stirrups) in the joint core (typical Italian constructions between the 1590s and 1970s). The results evidenced shear failure due to the opening of the hooks, showing again the influence of the hooks on the joint's structural response.

Dhakal and Maekawa (2002) observed that joints designed based only on gravity loads can present a reduction in the shear capacity up to 20% during three consecutive cycles. In addition, Braga et al. (2009) and Vaghani et al. (2015) stated that old structures (designed only for gravity loads) have typical characteristics: smooth beam bars, insufficient transverse reinforcement, and inadequate anchorage. These features can cause brittle shear failures, slipping in the beam's bars, loss in the load capacity, and degradation in the ductility and stiffness, which occur frequently more in exterior than interior joints.

Shafaei et al. (2017) observed that the absence of transverse reinforcement in the joint and poor bond between the bars and concrete decreased the stiffness as the cyclic displacements increase, due to insufficient confinement and inadequate anchorage at the bottom longitudinal reinforcement of the beam. These tests represented typical Iranian constructions in the 1970s. Furthermore, the hysteresis curve evidenced a significant "pinching" effect and low capacity of energy dissipation, Figure 2.3.

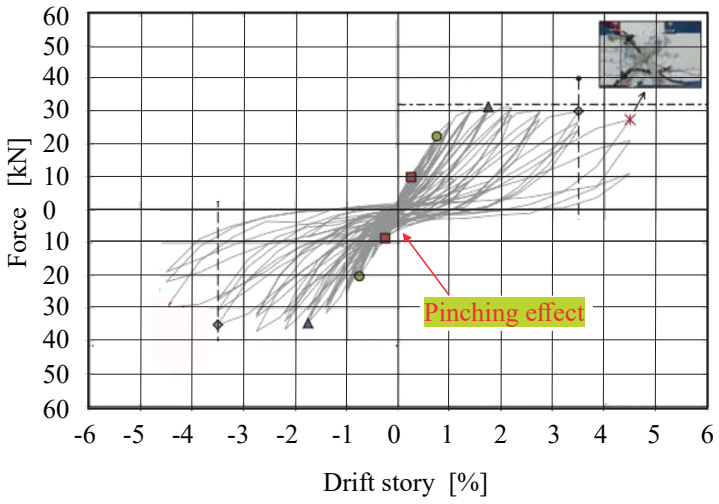

Figure 2.3 – Example of hysteresis curve with pinching effect.
Font: Adapted from Shafaei et al. (2017)

Authors such as Anderson et al. (2008) and Wong (2005) claimed that joint's strength and failure mode depended on joint shear stress demand or the amount of beam reinforcement rather than joint shear capacity. Sabah and Harba (2021) described the failure modes that can occur in RC BCJs of old buildings, as shown in Table 2.1. In addition, Park and Mosalam (2012b) described that exterior joints also can fail by beam flexural failure (BF) and column flexural failure (CF).

Table 2.1 – Summary of failure modes in BCJs

Failure mode	Brief description
J - Failure Mode	Occurs when the connection reaches maximum shear force before the longitudinal reinforcement of the column or beam yields.
BJ - Failure Mode	Occurs when the bottom or top longitudinal reinforcement of the beam yields, followed by reaching the maximum resisting shear force in the connection.
P - Failure Mode	In this case, the maximum shear force is not reached due to the pullout of the bottom reinforcement of the beam. This mechanism is typical of inadequate joints because of the straight and short anchorage inside the joint (without hook anchorage). This situation is evidenced when the forces acting on the bottom reinforcement of the beam on the face of the column are greater than the bond strength (bond-slip failure).

2.2.2 Principal parameters studied in experimental tests of BCJs

This section investigated the influence of diverse parameters on the joint's behavior.

2.2.2.1 Transverse reinforcement

The presence of stirrups (transverse reinforcement) in the joint core has many advantages in the joint's cyclic behavior, such as the beneficial effect in the confinement of concrete, improvements of the anchorage in the longitudinal beam bars, and post-peak behavior (MEINHEIT; JIRSA, 1977; DURRANI, 1982; GAO et al., 2021). The first studies that investigated the influence of stirrups in the joints were developed by Hanson and Connor (1967) and Kaku and Asakusa (1991), which affirmed that exterior joints with small quantities of stirrups had a reduced ductility.

Meinheit and Jirsa (1977) observed that an adequate number of stirrups in the joints improved the shear strength and cyclic behavior and helped to delay the shear cracking. Uzumeri (1977) considered the transverse reinforcement as an essential parameter to increase the shear strength and help in the anchorage of the beam's bars. Transverse reinforcement was also needed to resist the shear and torsion caused by the transversal beams (DURRANI, 1982). Nevertheless, Ehsani and Wight (1985) concluded that transverse reinforcement did not cause a significant improvement in joints with transversal beams and slabs.

According to Durrani (1982), three layers of horizontal stirrups in the joint core were considered as minimum quantity of reinforcement. Kim et al. (2020) stated that non-seismic exterior joints, with hooks bent at 90 degrees and stirrups spaced every h/3 (h: height of the beam), contributed to preventing diagonal cracking in the concrete and increasing shear strength. Alameddine (1990) showed that by increasing transverse reinforcement the concrete

deterioration decreased; however, when joints were subjected to high shear stresses, a high quantity of stirrups did not necessarily prevent the BCJs deterioration. Durrani and Wight (1985) noted that in interior joints, stirrups were more effective when they had low ductility levels (less than two), defined as the relation between the yield and ultimate displacement of the joint, helping to maintain the joint's strength rather than reducing stiffness loss. Other researchers like Kamimura et al. (2000) argued that by increasing stirrups slightly the bond behavior between the reinforcement and concrete improved, and it had a low influence on the level of story drift.

Alameddine (1990) observed in exterior joints with High Strength Concrete (HSC) and low shear stresses that only a few stirrups must be used to not affect the structure's ductility. Hwang et al. (2005) described that stirrups worked as a tension tie and helped restrict crack opening. Other research considered even a transverse reinforcement ratio of 0.4% was a beneficial value in hysteresis behavior and shear strength of exterior joints with seismic deficiency (KAUNG; WONG, 2011). Authors like Choi et al. (2017) noticed a slight improvement in lateral load capacity. However, they evidenced a reduction in shear strains. Gao et al. (2021) noted that a transverse reinforcement ratio of 0.687% prevented brittle shear failures in seismic exterior joints.

2.2.2.2 Hooks and anchorage length of the beam's bars

Megget (1974) observed the ineffectiveness of the horizontal anchorage length of the beam's bars in cycles after reaching the maximum load joint. Uzumeri (1977) described that the quality of anchorage had a greater influence on energy dissipation. Joh et al. (1991) observed improvements in hysteresis behavior and energy absorption capacity when hooks were bent at 90 degrees, as seen in Figure 2.4. Pampanin et al. (2002) studied the joint's behavior with different types of anchorage using smooth bars. They observed, in contribution to studies performed by Hakuto et al. (2000), that smooth bars with end-hooks could cause bond deterioration, slipping of beam bars in the initial stages of loading, and an additional concentrated force at the compressed bars, which, after reaching the first diagonal crack in exterior joints, could cause the expulsion of a "wedge" of concrete. This situation was also evidenced in experimental tests developed by Risi and Verderame (2017).

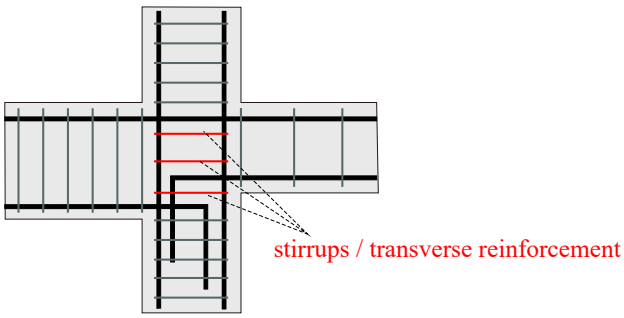

Figure 2.4 – Beam-column joints with 90 hooks.
Font: Obtained from Joh et al. (1991)

Hakuto et al. (2000) and Kuang and Wong (2006) observed low shear strength in exterior

joints with seismic deficiency and hooks bent away from joint core (Figure 2.5.a), or with hooks in the compressed bar bent away from joint core and tensile bar bent in joint region (Figure 2.5.b). Nevertheless, this situation can be improved by using hooks bent in the joint core, Figure 2.5.c. Other authors like Cosgun et al. (2020), described the anchorage type as an essential factor in both the capacity and failure mode of joints, mostly in the case of exterior joints.

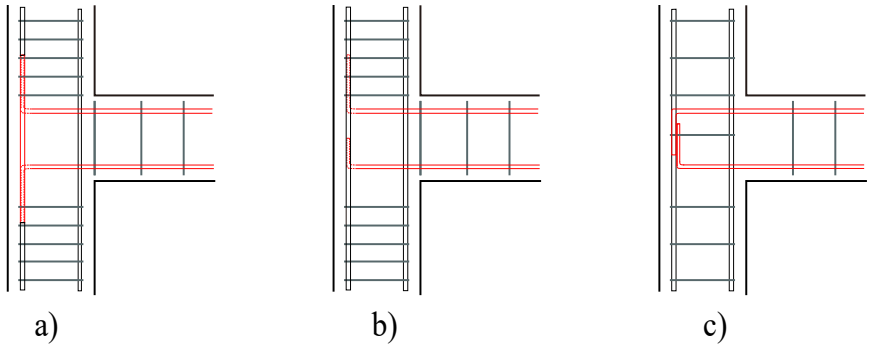

Figure 2.5 – Types of anchorage in BCJs a) Beam bars bent away from joint core, b) Tension beam bars bent away from the joint and compression beam bars bent in the joint core, c) Beam bars bent in the joint.
Font: Obtained from Kuang and Wong (2006) and Hakuto et al. (2000)

2.2.2.3 Slipping in the beam and column longitudinal bars

Slippage in beam bars influences the behavior of joints. Soleimani et al. (1979) described the loss of bond between the beam bars and concrete as one cause of premature anchorage failure and inelastic strains concentrated at the beam fixed-ends of interior joints. Beckingsale (1980) considered this phenomenon as one of the reasons for reducing the capacity to absorb energy. Meanwhile, Ehsani et al. (1987) affirmed that slippage caused stiffness degradation in both interior and exterior joints. However, Alameddine (1990) said that transverse reinforcement in the joint core reduced slippage in exterior BCJs.

On the other hand, Zerbe (1985) found that bond loss in the longitudinal bars during the initial cyclic loads may occur due to loss of cover in the column, which is caused by plastic hinges in the column's interface.

2.2.2.4 Axial compressive force in the column

In recent years, the effect of the axial force applied in the column on the joints has been a topic of study in diverse investigations. Authors as Beckingsale (1980), Birss (1978), Park and Milburn (1983), and Paulay (1989), considered beneficial the presence of axial force in the joint's compression behavior, increasing its shear strength. However, Liu (2001) observed insignificantly beneficial effects in the shear strength for interior joints with smooth bars and few column bars. Experimental tests conducted by Clyde et al. (2002), Pantelides et al. (2002), and Park (1988) observed improvements in the shear capacity of non-seismic exterior connections with high values of axial force; however, it was unfavorable for energy dissipation and ductility.

This same phenomenon was evidenced in the study developed by Gao et al. (2021) in exterior joints designed with seismic criteria.

Park and Mosalam (2012b) claimed that in the case of weak column–strong beam design, increasing the column axial load up to the balanced point improved the joint shear strength because the column moment capacity was positively affected by the axial load. Conversely, in the case of strong column–weak beam design (case of most tests), high values of column axial load given joint shear strength both favorable and unfavorable effects to the joint's shear strength.

From the strut mechanism in the joint region, it is known that the compressive diagonal strut width is determined by the compression block depth of the column and the beam. Thus, the column compression block depth increases with the increase of the column axial load, which has a positive effect on improving joint strength. In addition, high column axial load improves bond strength between the beam reinforcing bars and the surrounding concrete, leading to improvements in the joint shear strength because the horizontal shear force is transferred into the joint by bond and anchorage of the beam reinforcement, (PARK; MOSALAM, 2012b).

However, because most joint shear failures occur after cracking in the joint, the crack width is usually transformed into an average principal tensile strain to be used in softening a concrete constitutive, such as the Modified Compression Field Theory (MCFT) (VECCHIO; COLLINS, 1986a). Thus, the acceleration in the crack propagation is caused by Poisson's effect as the column axial load increases, and consequently, the joint has less shear strength (PARK; MOSALAM, 2009). In a similar way, Minami and Nishimura (1985) evidenced increments in the anchorage strength of the hooked bar in the joint region with column axial load, which was rapidly deteriorated under high axial load.

2.2.2.5 Transversal beam and compressive strength of concrete

Studies affirm that transverse beams helped to improve the joint's confinement (MEINHEIT; JIRSA, 1977; JOH; GOTO, 2000; KUSUHARA; SHIOHARA, 2008; KAM et al., 2010), increasing significantly their shear capacity with lateral beams on two sides (PARK et al., 2012). In addition, the research conducted by Hanson and Connor (1967) and Durrani (1982) emphasized the need for transverse reinforcement in joints confined only on two faces, as they asserted that connections with transverse beams on a minimum of three of their faces would not require stirrups. Transverse beams caused plastic hinges in the principal beam, delays in the concrete deterioration, and delays in the joint core cracking (MEGGET, 1974; ALAMEDDINE, 1990).

Regarding concrete compressive strength (f_c), Melo et al. (2015) observed improvements in the shear capacity for non-seismic interior joints, as the compressive strength increased. Meanwhile, the studies of Vandana and Bindhu (2017) described other beneficial effects in connections with high values of f_c, such as shear strength, stiffness, and energy dissipation capacity.

2.2.2.6 Shear strength

Many studies have been conducted to propose analytical, numerical, and experimental models to determine the joint's shear strength (V_{jh}). One of the first works on this was developed by Paulay (1989) and Paulay and Priestley (1992), in which a beneficial effect on strength was observed when intermediate bars in the column were considered. Alva et al. (2007) observed that the concrete compressive strength had a bigger influence than the amount of transverse reinforcement in the core in joints with equal cross-sectional dimensions. Other more recent research conducted by Meas et al. (2014), De Risi et al. (2016), and Verderame et al. (2018) evidenced an increase in V_{jh} when the joints had high longitudinal beam bars ratios.

Alameddine (1990) observed a significant delay in the deterioration of the joint concrete and stability in the cyclic load-carrying capacity in joints with low shear stress, which was caused by the members connected to the joint and the load intensity. Otherwise, early joint shear failure could happen before the yielding of the beam's bars.

Kim and LaFave (2007) reported that the joint aspect ratio ($h \ \ h_c$) from 1.0 to 1.6 for exterior joints, had little influence on the joint shear stresses and strains for the case of joint failure following beam yielding. Moreover, Kim and LaFave (2007) stated that the increase of the joint aspect ratio slightly reduced the joint shear strength for the case of joint shear failure without beam reinforcement yielding.

However, Chun and Shin (2014) analyzed BCJs with a joint aspect ratio (beam depth to column depth ratio) greater than 1.5. The results showed flexural yielding in the beam bars and extensive diagonal cracking within the joint, producing spalling of the joint cover concrete only at the end of testing. This happened due to an increase in the joint ratio that promoted severe distortions in the joints and a reduction in the beam's damage. For this, the authors proposed a reduction factor in the joint's shear strength ( ). Hence, the shear strength of unreinforced exterior joints was inversely proportional to its aspect ratio.

2.2.2.7 Type of load

Numerous studies have examined the behavior of the BCJ to better understand its structural response to seismic events. In experimental tests, the horizontal loads applied to the connections are typically modeled using either incremental monotonic forces or cyclic forces that simulate the effects of earthquakes.

The experimental investigation developed by Yang et al. (2018) analyzed BCJs subjected to cyclic loading in both the column and the beam. The results showed greater shear force transfer capacity in joints with cyclic loading applied at the beam than in the column, with smaller diagonal cracks in the joint core; however, with faster yielding beam bars. The joint's strains varied depending on the position of the cyclic load, as observed in Figure 2.6. Although the deformed position of BCJ with load applied to the column exhibits a more realistic behavior, the experimental method under cyclic loading on the beam is easier to develop. However, the authors asserted that BCJs with cyclic forces on the column are more recommended for studying

their behavior under seismic conditions.

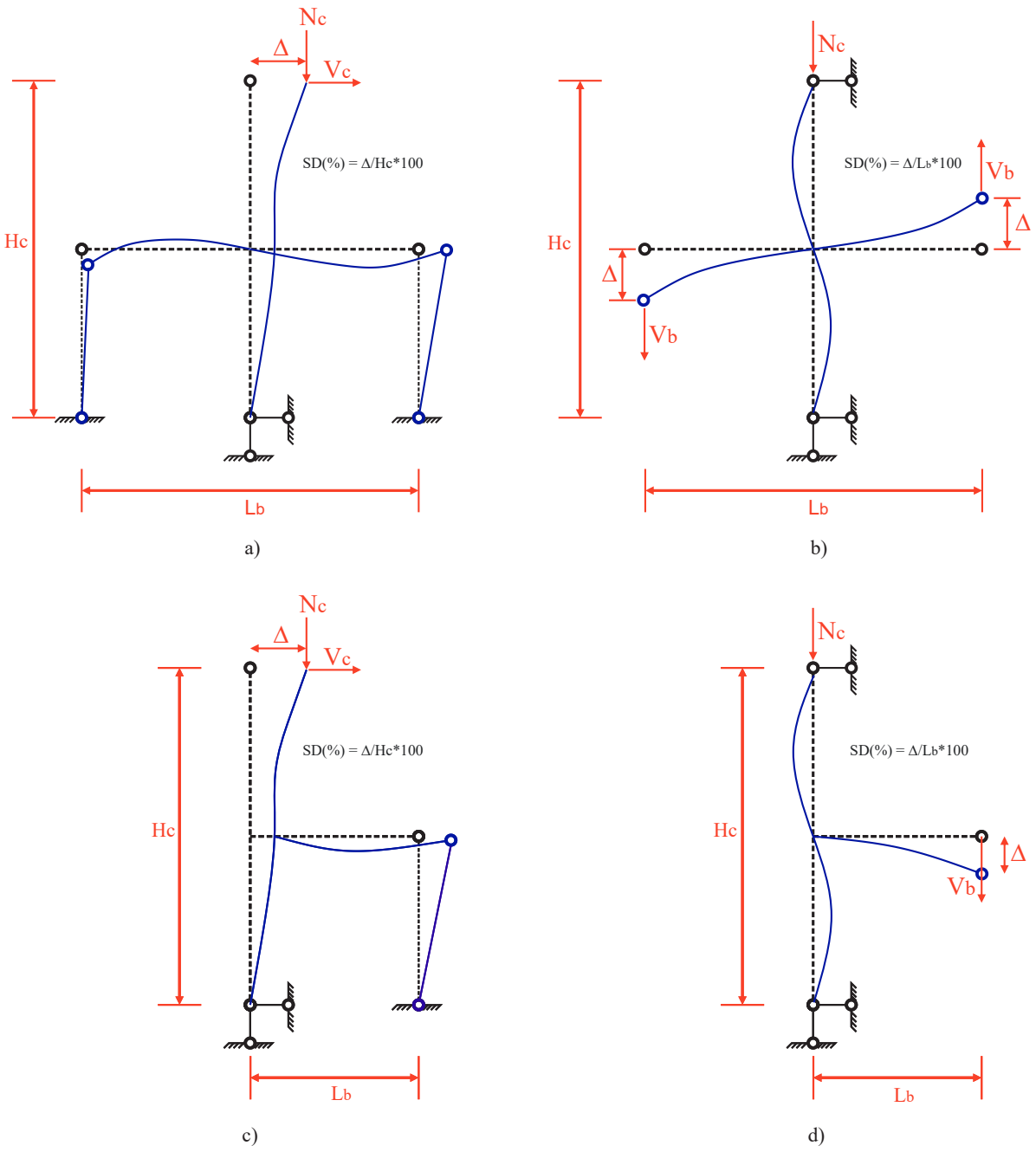

Figure 2.6 – Beam-column joint deformed configuration: Interior with cyclic load a) In the column, b) In the beam; Exterior subjected with cyclic load c) In the column, and d) In the beam.
Font: Adapted from Yang et al. (2018), Ma et al. (2020), and Bahraq et al. (2021)

Consequently, several analytical methodologies have been developed to determine the joint shear strength V_{jh}. Frequently, the models consider V_{jh} as the sum of two contributions, derived from concrete V_{ch} and steel V_{sh}, Equation 2.1.

$$V_{jh} \quad V_{sh} \quad V_{ch} \tag{2.1}$$

One of the earliest studies is attributed to the work of Paulay and Priestley (1992), in which they proposed the mechanism of strut and tie. The strut acted diagonally between the edges of the joint core, while the tie mechanism depended on the horizontal and vertical reinforcement of the joint, as presented in Figures 2.7 and 2.8. Thus, the formation of plastic hinges in the beams connected to the edges of the columns was expected in exterior beam-column joints under seismic actions. Therefore, high shear stresses from the longitudinal bars of the column and the beam occurred in the joint core.

Where T corresponded to the resultant force of the tensile reinforcement in the beam, C_s the resultant force of the compressive reinforcement in the beam, T and T the resultant forces of the tensile reinforcements in the column, C_s and C_s the resultant forces of the compressive reinforcements in the column, C_c the resultant of the compressive stress in the concrete, V_c the shear force acting on the column, N_c the axial force applied to the column, and V_b the shear force acting on the beam.

Through the equilibrium of horizontal forces, it was possible to calculate V_{jh} for exterior beam-column joints by Equations 2.2 and 2.3. The parameter $_o$ was an over-strength factor governed by the yield strength of the beam bars f_{yb}, with values of 1.25 and 1.40 for f_{yb} of 275 MPa and 400 MPa, respectively.

$$V_{jh} \quad T \quad V_c \tag{2.2}$$

$$V_{jh} \quad A_{sb,sup} \quad _o f_{yb} \quad V_c \tag{2.3}$$

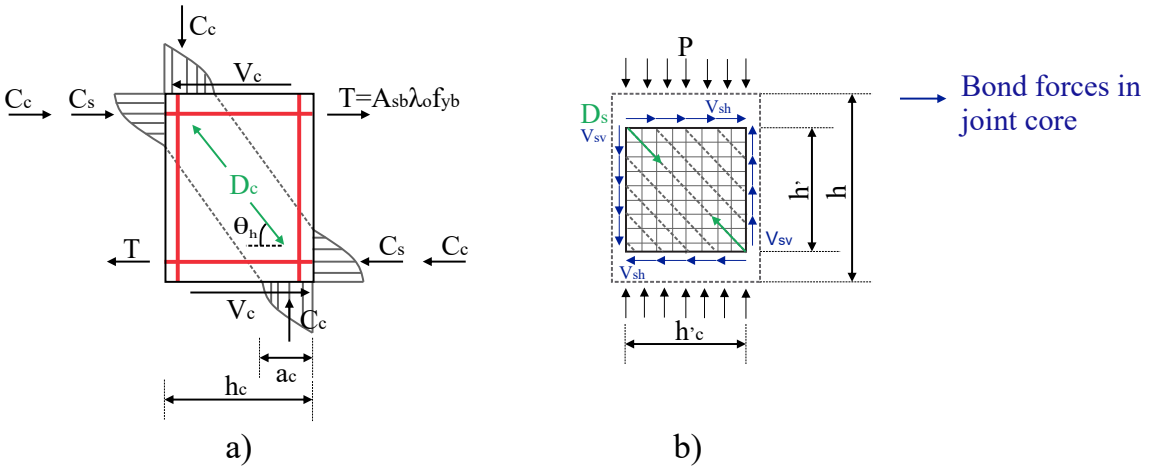

Figure 2.7 – a) Strut mechanism, b) Truss mechanism (Interior BCJ).
Font: Adapted from Paulay and Priestley (1992)

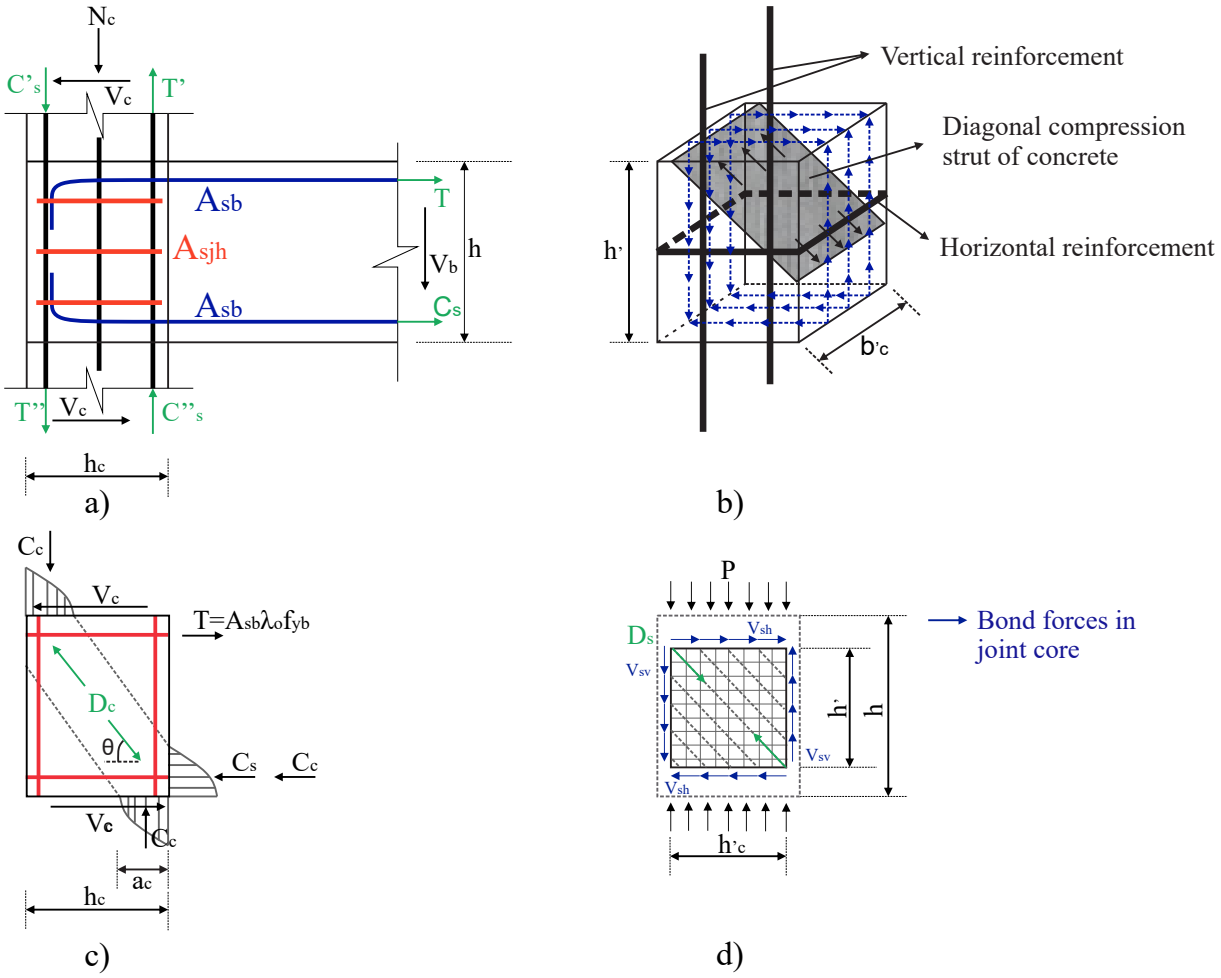

Figure 2.8 – a) Idealization of distribution of seismic and gravity loads, b) Diagonal strut mechanism, c) Strut mechanism, and d) Truss mechanism (exterior joint).
Font: Adapted from Paulay and Priestley (1992), Tsonos (2008), and Kassem (2016)

2.3 Joint shear strength models

A review of joint shear strength models with and without retrofitting was developed to be used as a background for creating a new analytical shear methodology of strengthened joints with UHPFRC. The following methods were developed through empirical and/or analytical equations obtained from experimental results, which depended on the geometric and mechanical properties of the elements.

2.3.1 Paulay and Priestley (1992) Model

The theoretical model of Paulay and Priestley (1992) adopted the strut-and-tie mechanism, expressed by Equations 2.4 and 2.7 that were governed by the contribution of concrete and the stirrups at the joint, respectively. The analytical proposal considered the influence of various parameters such as concrete compressive strength (f_c), column geometry (b_c, h_c), axial force of the column (N_c), beam and joint reinforcement (A_{sb}, A_{sjh}), as well as mechanical properties of the steel. The parameter represented the ratio between the bottom and top reinforcement of

beam $A_{s,bot}$ $A_{s,top}$, and $_o$ can range from 1.25 to 1.40.

$$V_{ch} \quad T \quad 1 \quad \frac{}{_o} \quad \frac{1.4 \quad a_c T}{_o h_c} \quad V_c \tag{2.4}$$

$$a_c \quad 0.25 \quad \frac{0.85 N_c}{A_g f_c} \quad h_c \tag{2.5}$$

$$T \quad A_{sb,sup} \quad _o f_{yb} \tag{2.6}$$

$$V_{sh} \quad \frac{T}{_o} \quad 0.7 \quad \frac{N_c}{A_g f_c} \quad A_{sjh} f_{yjh} \tag{2.7}$$

2.3.2 NZS 3101 (1995) Model

The standard NZS 3101 (1995) presented a model to determine the shear strength based on the truss mechanism, Equation 2.8. This model can be applied to joints subjected to seismic (cyclic) loads and gravity forces or both.

$$V_{jh} \quad \frac{A_{sjh} f_c}{6 \quad 0.7 \quad \frac{C_j N_c}{f_c A_g}} \frac{f_{yh} b_j h_c}{f_{yb} A_{sb}} \tag{2.8}$$

$$A_{jh} \quad \frac{0.4 V_{jh}}{f_{yh}} \tag{2.9}$$

$$0.85 \quad \frac{6 V_{jh}}{f_c} \quad 1.20 \tag{2.10}$$

$$A_j \quad b_j h_c \tag{2.11}$$

$$b_c \quad b_b \quad b_j \quad b_b \quad 0.5 h_c ; h_c \quad b_c \quad b_b \quad b_j \quad b_b \quad 0.5 h_c ; h_c \tag{2.12}$$

In exterior joints 1, C_j was a non-dimensional factor expressed as $C_j \quad V_{jh} \quad V_{jx} \quad V_{jy}$.

2.3.3 Priestley (1997) Model

Priestley (1997) studied the seismic performance of RC elements, such as beam-column joints. In this model, the width and height of the column (b_c, h_c), axial force of the column (Nc), compressive strength of concrete (f_c), and axial stress of the column ($N_c \quad A_g$) were considered, as shown in Equation 2.13.

$$V_{jh} \quad 0.42 \quad \overline{f_c} A_g \quad \overline{1 \quad \frac{N_c}{0,42 A_g \quad \overline{f_c}}} \tag{2.13}$$

The value of 0.42 referred to the principal tension stress (p_t), where the hooks of the longitudinal beam bars were bent into the joint.

2.3.4 Tsonos (1999) Model

Tsonos (1999) proposed an equation to predict the shear strength in the joints. The shear forces acting on the joint core were resisted by the strut mechanism (which acted between opposite edges diagonally across the joint) and by the truss mechanism (formed by vertical and horizontal reinforcement and a compression strut). Both mechanisms depended on the strength of the concrete. It assumed that the concrete was subjected to biaxial stress (Mohr's Circle), and the confinement effect in the concrete was considered through the model developed by Scott et al. (1982), as follows:

$$\frac{h_b V_{jh}}{2 b_j h_c^2 f_c} \quad 1 \qquad \sqrt{1 \quad \frac{4h_c}{h_b}}^{\,5} \qquad \frac{5h_b V_{jh}}{2 b_j h_c^2 f_c} \quad 1 \qquad \sqrt{1 \quad \frac{4h_c}{h_b}} \qquad 1.0 \tag{2.14}$$

$$f_c \quad k f_c \tag{2.15}$$

$$k \quad 1 \quad \frac{{}_s f_{yjh}}{f_c} \tag{2.16}$$

The parameter ${}_s$ refered to the horizontal reinforcement ratio of the joint.

2.3.5 Pampanin et al. (2002) Model

Pampanin et al. (2002) proposed a new analytical method as a sequence of Priestley (1997) work. This method considered the principal tension stress p_t, which was a function of the story drift or the shear strain joint. The shear strength of exterior joints with seismic deficiency can be determined through Equation 2.17.

$$V_{jh} \quad 0.20 \quad \sqrt{f_c} A_g \quad \sqrt{1 \quad \frac{N_c}{0,20 A_g \quad \sqrt{f_c}}} \tag{2.17}$$

2.3.6 Hwang and Lee (2002) Model

Hwang and Lee (2002) proposed a simplified model to calculate the shear strength of joints subjected to diagonal compression failure mode. The proposed formulation was associated with the work developed by Hwang and Lee (1999), which considered force equilibrium, compatibility of strains, and constitutive laws of materials when the ultimate load was reached. The model was governed by the diagonal strut mechanism, horizontal truss mechanism (horizontal tie), and vertical truss mechanism (vertical tie), as shown in Figure 2.9. Thus, the model considered the loss of bond between the reinforcement of the beam and the column, where its principal stress was concentrated in the diagonal strut, causing shear failure. The shear strength can be determined by Equation 2.18.

$$V_{jh} \qquad K f_c A_{str} \cos \quad {}_h \tag{2.18}$$

$$\frac{3.35}{\overline{f_c}} \quad 0.52 \tag{2.19}$$

$$K \quad K_h \quad K_v \tag{2.20}$$

$$_h \quad \frac{2tan \quad _h \quad 1}{3} \quad 1.0 \tag{2.21}$$

$$_v \quad \frac{2cot \quad _h \quad 1}{3} \quad 1.0 \tag{2.22}$$

$$\overline{K_h} \quad \frac{1}{1 \quad 0.2 \quad _h \quad \frac{2}{h}} \tag{2.23}$$

$$\overline{K_v} \quad \frac{1}{1 \quad 0.2 \quad _v \quad \frac{2}{v}} \tag{2.24}$$

$$F_{yh} \quad A_{sjh} f_{yjh} \tag{2.25}$$

$$F_{yv} \quad A_{sjv} f_{yjv} \tag{2.26}$$

$$\overline{F_h} \quad _h \overline{K_h} \quad f_c A_{str} cos \quad _h \tag{2.27}$$

$$\overline{F_v} \quad _v \overline{K_v} \quad f_c A_{str} sin \quad _h \tag{2.28}$$

$$K_h \quad 1 \quad \frac{F_{yh} \quad \overline{K_h} \quad 1}{\overline{F_h}} \quad \overline{K_h} \tag{2.29}$$

$$K_v \quad 1 \quad \frac{F_{yv} \quad \overline{K_v} \quad 1}{\overline{F_v}} \quad \overline{K_v} \tag{2.30}$$

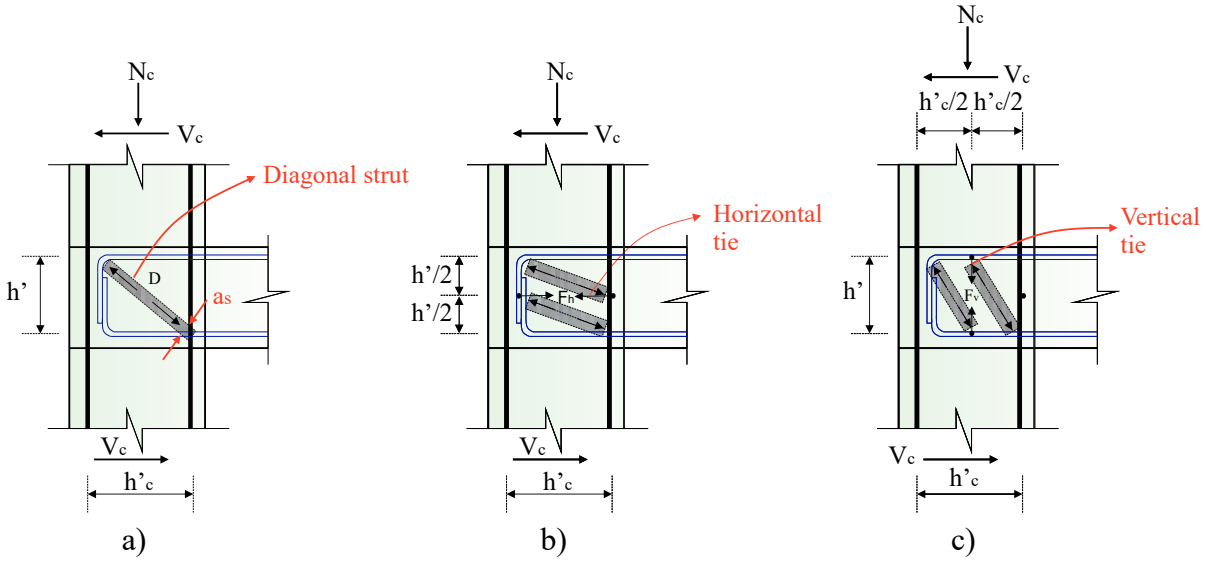

Figure 2.9 – Joint shear resisting mechanisms: (a) Diagonal mechanism, (b) Horizontal mechanism (horizontal tie), and (c) Vertical mechanism (vertical tie).
Font: Adapted from Hwang and Lee (1999)

Where corresponded to a softening factor, and K was a factor that considered the favorable effect of vertical and horizontal reinforcement in the joint (HWANG; LEE, 1999; TRAN et al., 2014). A_{str} was the effective area of the diagonal strut determined by the product of the width of the compression diagonal strut (assuming that a_s a_c, depending on the joint geometry, axial force in the column N_c, and compressive strength of concrete f_c, Equation 2.5), and the width of the diagonal strut, which was equal to the effective width of the joint, following the criteria of ACI 318 (1995). The parameter $_h$ was the fraction of diagonal compression transferred by the horizontal tie in the absence of a vertical tie and $_v$ corresponded to the fraction of diagonal compression taken by the vertical tie in the absence of a horizontal tie. $\overline{K_h}$ and $\overline{K_v}$ were the indices of the horizontal and vertical ties of the joint. F_{yh} and F_{yv} were the yielding forces of the horizontal and vertical ties of the joint, where K_h and K_v were determined by Equations 2.29 and 2.30. $_h$ was the angle of the diagonal compression strut.

2.3.7 ASCE SEI/41 (2007) Model

The joint shear model proposed by the standard ASCE SEI/41 (2007) is expressed in Equation 2.31. Where was 0.75 for lightweight aggregate concrete and 1.0 for normal weight aggregate concrete, and the parameter b_j was the effective joint width, following the recommendations of ACI 318 (2002).

$$V_{jh} \qquad \overline{f_c} A_j \tag{2.31}$$

$$A_j \quad b_j h_c \tag{2.32}$$

$$b_j \quad b_b \quad h_c; b_b \quad 2x \tag{2.33}$$

Where A_j was the effective area of the joint, was equal to 0.062 and 0.083 for concrete with lightweight and normal aggregate, respectively. The parameter x was the orthogonal length from the longitudinal axis of the beam to the exterior face of the column. The parameter was determined from Table 2.2.

Table 2.2 – Values of (Joint shear strength)

$_{sjh}$	Value of				
	Interior Joint with Transverse Beams	Interior Joint without Transverse Beams	Exterior Joint with Transverse Beams	Exterior Joint without Transverse Beams	Knee Joint with or without Transverse Beams
0.003	12	10	8	6	4
0.003	20	15	15	12	8

$_{sjh}$ = volume ratio of horizontal confinement reinforcement in the joint.

Font: Obtained from ASCE SEI/41 (2007)

2.3.8 Kim et al. (2009) Model

Kim et al. (2009) developed an analytical model to assess the shear capacity in joints of both old and new structures. The method used an experimental database of both exterior and interior joints (reinforced and unreinforced). The authors used a probabilistic method to predict the joint shear strength (Equation 2.34). The model considered the influence of beam width (b), column width (b_c), beam depth (h), column depth (h_c), concrete compressive strength (f_c), longitudinal reinforcement beam (A_{sb}), reinforcement ratio of beam ($_b$), and volumetric joint horizontal reinforcement ratio ($_{sjh}$), obtained from the relationship between the volume of transverse reinforcement of the joint located between the top and bottom reinforcement of the beam and the joint volume (product of column height, beam width, and the distance between the longitudinal beam reinforcements), Equations 2.38 and 2.39, respectively. The method can be applied to joints with eccentricity, inadequate confinement, and out-of-plane elements. However, the effect of the axial load was not considered.

$$_{jh} \quad \frac{V_{jh}}{b_j h_c} \quad _t \; _t \; _t \; _t \; JI^{\,0.15} \; BI^{\,0.30} \; f_c^{\,0.75} \quad MPa \tag{2.34}$$

$$b_j \quad b_c \quad ; \quad \frac{b \quad b_c}{2} \tag{2.35}$$

$$JI \quad \frac{_{sjh} f_{yjh}}{f_c} \quad 0.0139 \tag{2.36}$$

$$BI \quad \frac{_b f_{yb}}{f_c} \tag{2.37}$$

$$_b \quad \frac{A_{sb,bottom} \quad A_{sb,top}}{h_b b_b} \tag{2.38}$$

$$_{sjh} \quad \frac{A_{sjh}h_c}{h_b \quad 2 \ _{sb} \ h_c b_c} \tag{2.39}$$

The parameter $_t$ described the in-plane geometry in the joint (equals 1.0, 0.7, and 0.4 for interior, exterior, or corner joints, respectively). $_t$ considered the out-of-plane geometry (equal to 1.0 for joints with up to one transverse beam and 1.18 for joints with two transverse beam, $_t$ expressed as $_t \quad 1 \quad e \ b_c \ ^{0.67}$, corresponding to a value of 1.0 for joints without eccentricity, and $_t$ was equal to 1.31. The joint transverse reinforcement index JI and the beam reinforcement index BI were determined by Equations 2.36 and 2.37.

2.3.9 Wang et al. (2012) Model

The methodology proposed by Wang et al. (2012) can be used in joints with transverse reinforcement in the joint core and intermediate bars in the column. A special feature of the model was the consideration of the bi-dimensional rupture envelope of Kupfer-Gerstle to determine the shear strength, expressed in Equation 2.40.

$$V_{jh} \quad \frac{1 \quad _y \ sin \quad _h \ ^2 \ f_{tn} \quad 0.8cos \quad _h \ ^2 \ f_c}{\frac{1}{f_{tn}} \quad \frac{0.8}{f_c} \quad sin \ 2 \ _h} b_j h_c \tag{2.40}$$

$$f_{tn} \quad f_{tc} \quad _s f_{yjh} cos \quad ^2 \quad _{sv} f_{yjv} sin \quad _h \ ^2 \tag{2.41}$$

$$_y \quad \frac{N_c}{A_g} \tag{2.42}$$

$$f_{ct} \quad 0.556 \quad \overline{f_c} \tag{2.43}$$

$$_{sjh} \quad \frac{A_{sjh}}{b_j h} \qquad _{sjv} \quad \frac{A_{sjv}}{b_j h_c} \tag{2.44}$$

The value of was equal to 1.0 or 0.8 for interior or exterior joints, respectively. $_h$ was the inclination of the concrete strut, $_y$ was the axial stress of column, b_j was the effective width of the joint following the criteria of NZS 3101 (1995), $_s$ and $_{sv}$ were the horizontal and vertical reinforcement ratio of the joint, respectively, and f_{ct} was the contribution of concrete to nominal tensile strength. In the model, the authors assumed that both the concrete tensile strength and the yield strength of the steel were reached, which is considered an unlikely scenario.

2.3.10 Park and Mosalam (2012a) Model

The model by Park and Mosalam (2012a) determined the shear capacity only in unreinforced exterior joints (without transverse reinforcement), governed by the mechanism of two diagonal struts, truss analogy, and deterioration of bond strength. The simplified model considered the influence of geometric parameters of the beam and the column, as well as some mechanical properties of the reinforcements, Equation 2.45:

$$V_{jh} \quad k \quad _{ext} \quad \overline{f_c} b_j h_c \frac{cos \quad _h}{cos \quad 4} \tag{2.45}$$

$$k \quad 0.4 \quad 0.6 \quad \frac{SI_J \quad X_1}{X_2 \quad X_1} \quad 1.0 \tag{2.46}$$

$$SI_J \quad \frac{A_{sb} f_{yb}}{b_j h_c \quad \overline{f_c}} \quad 1 \quad \frac{0.85h}{H} \tag{2.47}$$

$$X_1 \quad _{ST1} \frac{cos \quad _h}{cos \quad 4} \tag{2.48}$$

$$X_2 \quad _{ext} \frac{cos \quad _h}{cos \quad 4} \tag{2.49}$$

$$b_j \quad \frac{b \quad b_c}{2} \tag{2.50}$$

Where k was a resistance factor, $_{ext}$ was the upper limit of shear strength normalized to a ratio of $h_b \ h_c \quad 1.0$ (equals to 12 $Psi^{0.5}$ or 1.0 $MPa^{0.5}$), b_j was the width of the joint, $_h$ was the angle of the diagonal compression strut, and SI_J was the shear index of the joint, representing the shear demand of the joint at the onset of yielding of the tension reinforcement in the beam. The factor $_{ST1}$ had a value of 4 $\overline{f_c} Psi^{0.5}$ or 0.33 $\overline{f_c} MPa^{0.5}$.

2.3.11 ACI 318 (2014) Model

The proposal given by the standard ACI 318 (2014) did not consider the contribution of the truss mechanism (V_{sh}). Therefore, the shear strength was governed only by the geometry of the joint and the compressive strength of the concrete (f_c), Equation 2.51.

$$V_{jh} \quad \overline{f_c} A_j \quad MPa \tag{2.51}$$

$$A_j \quad b_j h_c \tag{2.52}$$

$$b_j \quad b_b \quad h_c; b_b \quad 2x \tag{2.53}$$

Where A_j was the effective area of joint, and was defined as the factor considering the confinement effect on the joint, Table 2.3 . The variable was equal 0.062 and 0.083 for lightweight and normal aggregate concrete, respectively. x was the horizontal distance measured between the beam's outer face and the column's outer face.

2.3.12 Tran et al. (2014) Model

The empirical model of Tran et al. (2014) can be applied to interior and exterior connections without slabs, transverse beams, and eccentricity. The model was based on the strut-and-tie mechanism, where the bond conditions was considered through the parameter $_b$, which depended on the number of beam bars the beam and the diameter of tensile beam reinforcement (n_b, d_{sb}), Equation 2.54:

$$V_{jh} \quad _1 \quad \frac{N_c}{b_c h_c f_c} \quad 1.2 \; _b \quad A_j f_c^{0.5} \quad _2 \; A_{sjh} f_{yjh} \quad A_{sjv} f_{yjv} \tag{2.54}$$

$$A_j \quad b_j h_c \tag{2.55}$$

$$b_j \quad \frac{b_c \quad b_b}{2} \tag{2.56}$$

$$_b \quad \frac{_b d_{sb} h_c}{b_b h_b} \quad 0,4 \tag{2.57}$$

The factor $_1$ was equal to 0.81 and 0.34 for interior and exterior joints, respectively. $_2$ was equal to 0.34 for interior and 0.22 for exterior joints.

2.3.13 Metelli et al. (2015) Model

Metelli et al. (2015) proposed two analytical models for predicting V_{jh} for exterior beam-column joints without seismic criteria, labeled PSLM and SSTM. The PSLM model (Principal Stress Limitation Model) was limited by the tensile stress of the joint, while the SSTM model (Modified Softened Strut-and-Tie Model) was governed by the strut-and-tie mechanism. The shear strength using the PSLM model was determined by Equation 2.58.

$$V_{jh} \quad K_1 \quad \overline{f_c} \quad \sqrt{1 \quad \frac{f_a}{K_1 f_c}} \quad h_c b_b \tag{2.58}$$

Where f_a corresponded to the average compressive stress in the column, and k_1 was equal to 0.2 for joints with smooth bars and no transverse reinforcement.

2.3.14 Pauletta et al. (2015) Model

Pauletta et al. (2015) developed an analytical model for exterior joints subjected to seismic loading, considering the strut-and-tie mechanism. The model considered the contribution of two diagonal struts, horizontal joint reinforcement, and intermediate bars in the column. The formulation was governed by both geometric and mechanical parameters of the exterior joint (Equation 2.59).

$$V_{jh} \quad 0.71 \quad \frac{f_c b_j a_c cos \quad _h}{} \quad 0.079 A_{sjh} f_{yjh} \quad \frac{0.52 A_{sjv} f_{yjv}}{tan \quad _h} \tag{2.59}$$

$$\frac{2L_cL_b}{2L_cL_b \quad 2L_b \quad h_c \;\; j_{db}} \quad 1 \quad \frac{4k}{b}\frac{l_h}{f_b}\frac{\overline{f_c}}{} \qquad 1,0 \tag{2.60}$$

Where b_j was the width of the ST1 diagonal strut determined as the minimum value between the width of the beam and the column (b and b_c), $_h$ was the slope of the first ST1 strut, a_c corresponded to the height of the compressed zone in the column (Equation 2.5), was a non-dimensional interpolating function accounting for concrete softening, and was a factor that depends on the tensile stress f_b. The horizontal projection of the ST2 diagonal strut was l_h, and j_{bd} was the internal moment arm of the beam's cross-sectional area.

2.3.15 Kassem (2016) Model

Kassem (2016) developed a shear capacity prediction model for interior and exterior joints using the strut-and-tie model. The shear strength can be determined by the generalized Equation 2.61, or specifically for exterior and interior joints through Equations 2.62 and 2.63, respectively. The proposed method considered parameters such as the geometry of the joint, effective width of the joint (b_j b_c), and axial force in the column (N_c).

$$V_{jh} \quad h_c b_j \;\; _c \quad a_c f_c cos \;\; _h \qquad _h \; A_{sjh} f_{yjh} \qquad A_{sb,bot} \quad A_{sb,top} \;\; f_{yb} \qquad _v \; A_{sjv} f_{yjv} \quad cot \;\; _h \tag{2.61}$$

$$V_{jh} \quad h_c b_j 0.21 \quad a_c f_c cos \;\; _h \quad 0.09 \; A_{sjh} f_{yjh} \qquad A_{sb,bot} \quad A_{sb,top} \;\; f_{yb} \quad 0.22 \; A_{sjv} f_{yjv} \quad cot \;\; _h \tag{2.62}$$

$$V_{jh} \quad h_c b_j 0.26 \quad a_c f_c cos \;\; _h \quad 0.44 \; A_{sjh} f_{yjh} \qquad A_{sb,bot} \quad A_{sb,top} \;\; f_{yb} \quad 0.07 \; A_{sjv} f_{yjv} \quad cot \;\; _h \tag{2.63}$$

$$1 \quad \frac{f_c}{250} \tag{2.64}$$

The parameter was equal to 0.6 or 0.48 for interior or exterior joints, respectively. In exterior joints, $_c$ had a value of 0.21, $_h$ of 0.09, of 3.47, and $_v$ of 0.22.

2.3.16 Parate and Kumar (2018) Model

The proposal developed by Parate and Kumar (2018) may be used for both exterior and interior joints, where the transverse reinforcement can be in horizontal or diagonal (A_{sinc}) direction. The model considered geometric parameters of the elements and mechanical properties of the materials 2.65.

$$V_{jh} \quad \frac{\overline{f_c} \;\; \frac{b}{c} \;\; 0.15 \quad 1 \quad N_c \;\; A_g f_c}{\frac{h_b}{h_c} \;\; 0.15} A_j \qquad A_{sjh} f_{yjh} \tag{2.65}$$

$$A_j \quad b_j h_c \tag{2.66}$$

$$\begin{array}{ll} {}_s \quad 1.0 & 0.15 \\ 1.0 \quad {}_s \quad 2.0 & 0.20 \\ {}_s \quad 2.0 & 0.25 \end{array} \tag{2.67}$$

was a factor that depends on the horizontal reinforcement ratio of the BCJ $_s$.

2.3.17 Hassan and Moehle (2018) Model

Hassan and Moehle (2018) developed two prediction proposals for exterior joints without transverse reinforcement. The first one used the strut-and-tie model, while the second one was determined based on empirical analyses. According to ACI 318 (2014), the strut-and-tie model required the consideration of the concrete softening factor, denoted as $_s$, with values of 0.6 for struts that had bottle-shaped. This proposal considered the joint geometry, the steel ratio for compressive and tensile reinforcement beam (,), and the distances from the extreme compressed concrete fiber to the centroid of the compressed and tensioned longitudinal reinforcement ($_{sb}$, d_b), respectively, (Equation 2.68). The second proposal was an empirical model, which was considered as an alternative to the first proposal for joints that exhibit shear failure before the reinforcement in the column or beam yields (*J - failure*) (Equations 2.73-2.74).

$$V_{jh} \quad f_{cu} a_s b_j \cos \quad {}_h \tag{2.68}$$

$$b_j \quad b; \quad \frac{b \quad b_c}{2}; \quad b_b \quad \sum \frac{m h_c}{2} \tag{2.69}$$

$$f_{cu} \quad 0.85 \quad {}_s f_c \tag{2.70}$$

$${}_h \quad \tan^{1} \frac{d_b \quad {}_{sb}}{d_c \quad d_c} \qquad a_s \quad \overline{a_b^2 \quad a_c^2} \tag{2.71}$$

$$a_b \quad k d_b \qquad \frac{}{{}^{2\ 2} \quad 2 \qquad \frac{{}_{sb}}{d_b}} \qquad d_b \tag{2.72}$$

$$V_{jh} \quad 11 \quad \overline{\frac{h_c}{h} k b_j h_c \quad \overline{f_c}} \qquad Psi \tag{2.73}$$

$$V_{jh} \quad 0.91 \quad \overline{\frac{h_c}{h} k b_j h_c \quad \overline{f_c}} \qquad MPa \tag{2.74}$$

$$k \quad 1 \quad \frac{4}{9} \quad \frac{N_c}{f_c A_g} \quad 0,15 \qquad 1,0 \quad k \quad 2,0 \tag{2.75}$$

The effective joint width b_j was calculated following the criteria of ACI 352R (2002), where f_{cu} was the effective strength of the compressed strut, $_h$ and a_s were the angle and depth of the diagonal compression strut, respectively. The height of the compressed zone in the column a_c must be less than $0.4h_c$ (a_c $0.4h_c$), and was the ratio between the elasticity modulus of the materials. The kappa factor (k) considered the influence of the axial force in the column, and the $_s$ factor was equal to 0.6.

2.3.18 Parate and Kumar (2019) Model

Parate and Kumar (2019) developed an analytical model to determine shear strength based on a hybrid approach. The model combined the strut-and-tie method with an empirical method. The authors considered that under diagonal compression, the action of the strut was derived using the strut-and-tie method, while under tension, the influence of the transverse reinforcement was obtained from experimental results, as shown in Equations 2.77 and 2.80.

$$V_{jh} \quad V_{ch} \quad V_{sh} \qquad k f_c^{0.6} A_{strut} cos \quad _h \qquad A_{sjh} f_{yjh} \quad A_{sjv} f_{yjv} \quad A_{sji} f_{yji} \tag{2.76}$$

$$V_{ch} \qquad k f_c^{0.6} A_{strut} cos \quad _h \tag{2.77}$$

$$A_{strut} \quad b_{ej} d_{strut} \tag{2.78}$$

$$d_{strut} \qquad \overline{a_c^2 \quad a_b^2} \tag{2.79}$$

The variables and were determined based on the longitudinal reinforcement of the beam and the column. The presence of a transverse beam and/or slab was represented by the parameter (equal to 1.2 for joints with a transverse beam and 1.0 without a transverse beam), and the factor k encompassed the effect that joints with wide beams may have on strength (k b b_c).

$$V_{sh} \qquad A_{sj} \quad f_{yj} \qquad A_{sjh} f_{yjh} \quad A_{sjv} f_{yjv} \quad A_{sji} f_{yji} \tag{2.80}$$

$$\frac{100 A_{sb}}{A_b} \quad ^{0.321} \qquad \frac{100 A_{sco}}{A_g} \quad ^{0.505} \tag{2.81}$$

$$\begin{array}{l} b_c \quad b \quad b_j \quad b \quad h_c; b \quad 2x \\ \qquad b_c \quad b_b \quad b_j \quad b_c \end{array} \tag{2.82}$$

To consider the contribution of transverse reinforcement in the joint strength, the authors proposed a formulation based on experimental results (empirical model), where A_{sj} represented the area of reinforcement located in the joint core in the horizontal (A_{sjh}) and vertical (A_{sjv})

directions. The factor represented the influence of joint reinforcement with empirical values of 0.2 for a reinforcement ratio less than 0.5%, 0.3 for a reinforcement ratio between 0.51% and 1.0%, 0.3 for a reinforcement ratio between 1.0% and 2.0%, or 0.35 for a reinforcement ratio greater than 2.0%.

2.3.19 Other guidelines

The standards ACI 352R (2002), Eurocodigo 8-Part I 1998 (2004), and FEMA 273 (1997) also provided formulations to calculate the joint shear strength. Most of them are based on the strut-and-tie model (HAACH, 2005).

The American standard ACI 352R (2002) may be applied for joints localized in seismic and non-seismic regions. It considers the action of multidirectional forces that the members transmit to the joint, including axial load, bending, torsion, and shear. The model can be applied to joints of high-strength concrete, with slabs, eccentric beams, and beams wider than the column (Equation 2.83).

$$V_{jh} \quad 0.083 \quad \overline{f_c} b_j h_c \qquad MPa \tag{2.83}$$

$$b_j \qquad b; \quad \frac{b \quad b_c}{2}; \quad b \quad \sum \frac{m h_c}{2} \tag{2.84}$$

Where is determined by the classification of the joint, as shown in Table 2.3. The parameter m is equal to 0.3 for joints with eccentricity between the beam and the column higher than b_c 8, and 0.8 for other cases.

Table 2.3 – Values of $[MPa^{0.5}]$

Classification	**Joint type**	
	1	**2**
A. Joints with a continuous column		
A.1. Joints effectively confined on all four vertical faces	24	20
A.2. Joints effectively confined on three vertical faces or on two opposite vertical faces	20	15
A.3. Other cases	15	12
B. Joints with a discontinuous column		
B.1. Joints effectively confined on all four vertical faces	20	15
B.2. Joints effectively confined on three vertical faces or on two opposite vertical faces	15	12
B.3. Other cases	12	8

Font: Obtained from ACI 352R (2002)

Due to the axial force of the column, the ACI 352R (2002) recommends an adequate confinement in the joint core, which can be provided by transverse reinforcement or transverse elements. The transverse reinforcement for Type 1 joints must have at least two layers of stirrups

(located between the top and bottom reinforcement of the beam) and spacing less than 30 cm (300 mm). For Type 2 joints, the transverse reinforcement must be at least equal to:

$$A_{sjh} \quad 0.3\frac{s_h b_c f_c}{f_{yjh}} \quad \frac{A_g}{A_c} \quad 1 \tag{2.85}$$

However, it should not be less than:

$$A_{sjh} \quad \frac{0.09 s_h b_c f_c}{f_{yjh}} \tag{2.86}$$

Where A_c is the area of the joint core of the connection confined by the stirrups, s_h is the spacing between hoops, and b_c is the joint width.

The FEMA 273 (1997) considers the presence of plastic hinges in the elements adjacent to the connection. However, without exceeding the design values obtained by the combination of gravity force and seismic force. It uses the same expressions as the ACI 318 (1995) (Equations 2.51 and 2.53).

Eurocodigo 8-Part I 1998 (2004) allows to calculate the shear strength for interior and exterior joints through Equations 2.87 and 2.91, respectively.

$$V_{jh,int} \quad f_{cd} \quad \overline{1 \quad \frac{d}{}} b_j h_j \tag{2.87}$$

$$0.6 \;\; 1 \quad f_{ck} \;\; 250 \qquad MPa \tag{2.88}$$

$$_d \quad \frac{N_c}{A_g f_{cd}} \tag{2.89}$$

$$\begin{array}{llll} b_c & b & b_j & b_c; b \quad 0.5 h_c \\ b_c & b & b_j & b; b_c \quad 0.5 h_c \end{array} \tag{2.90}$$

$$V_{jh,ext} \quad 0.8 V_{jh,int} \tag{2.91}$$

where f_{cd} is the design compressive concrete strength, and h_{jc} is the distance between the faces of the longitudinal bars of the column.

Currently, the Brazilian Standard, Associação Brasileira de Normas Técnicas - ABNT (2023) does not have any analytical prediction model for the joint shear strength. It only specifies requirements for the bond strength between concrete f_{bd} (item 9.3.2.1) and the anchorage length of longitudinal bars of the beam l_b (item 9.4.2.4).

A database of experimental tests was built and applied to the previous analytical models (see Appendix A). Table 2.4 summarizes the contribution of geometric and mechanical parameters of the models above mentioned.

Table 2.4 – Parameters used in analytical models to determine the joint shear strength V_{jh}

Model	*LT*	*CT*	*Reinf.*	f_c	b	b_c	h	h_c	N_c	A_{sb}	A_{sco}	A_{sjh}	A_{sjv}	f_{yjh}	f_{yjv}	f_{yb}	N_c A_g	$_c$	$_b$
Paulay and Priestley (1992)	C	E	R - UR		–		–				–		–	–	–			–	–
NZS 3101 (1995)	C	E	R				–				–		–		–			–	–
Priestley (1997)	C	E	UR		–		–			–	–	–	–	–	–	–		–	–
Tsonos (1999)	C	E - I	R - UR			–			–	–	–		–		–	–	–	–	–
Pampanin et al. (2002)	C	E	UR		–		–			–	–	–	–	–	–	–		–	–
Hwang and Lee (2002)	C	E - I	R							–	–					–		–	–
ASCE SEI/41 (2007)	C	E - I	R - UR				–		–	–	–	–	–	–	–	–	–	–	–
Kim et al. (2009)	C	E - I	R - UR						–		–		–		–		–	–	
Wang et al. (2012)	C	E - I	R - UR							–	–					–		–	–
Park and Mosalam (2012a)	C	E	UR						–		–	–	–	–	–		–	–	–
ACI 318 (2014)	C	E - I	R - UR						–	–	–	–	–	–	–	–	–	–	–
Tran et al. (2014)	C	E - I	R - UR							–	–					–	–	–	–
Metelli et al. (2015) - PSLM	C	E	UR			–	–			–	–	–	–	–	–	–	–	–	–
Pauletta et al. (2015)	C	E	R - UR								–							–	–
Kassem (2016)	C	E- I	R - UR								–							–	
Parate and Kumar (2018)	C	E - I	R - UR												–	–			
Hassan and Moehle (2018) -STM	C	E	UR								–	–	–	–	–	–		–	–
Hassan and Moehle (2018) -EMPIR	C	E	UR							–	–	–	–	–	–	–		–	–
Parate and Kumar (2019)	C	E - I	R - UR											–					–

LT: Load type; *C*: Cyclic load; *CT*: Connection type; *E*: Exterior Joint; *I*: Interior Joint; *R*: Reinforced joint; *UR*: Unreinforced joint; f_c: Compressive concrete strength; b: beam width; b_c: Column width; h: Beam depth; h_c: Column height; N_c: axial force in the column; A_{sb}: Area of the beam longitudinal; A_{sco}: Area of the column longitudinal; A_{sjh}: Area of horizontal joint reinforcement; A_{sjv}: Area of vertical joint reinforcement; f_{yjh}: Yield strength of horizontal joint reinforcement; f_{yjv}: Yield strength of vertical joint reinforcement; f_{yb}: Yield strength of beam tensile reinforcement; N_c A_g: Axial stress in the column; $_c$: Reinforcement ratio of column; $_b$: reinforcement ratio of beam.

2.4 Beam-column joints retrofitted with UHPFRC subjected to cyclic load

Numerous retrofit techniques for strengthening and repairing BCJs have been developed, enhancing their shear capacity during seismic events. Such as RC jacketing (KARAYANNIS et al., 2008); epoxy resin injections (KARAYANNIS et al., 1998); steel jacketing (NOYAN, 2014); steel plates (LI et al., 2017; EBANESAR et al., 2022); steel braces (SAID; NEHDI, 2008); fiber-reinforced polymers (FRP) (MUKHERJEE; JOSHI, 2005; PAMPANIN et al., 2007; BEYDOKHTY; SHARIATMADAR, 2016; MA et al., 2017; POHORYLES et al., 2018; OBAIDAT et al., 2019; ILIA et al., 2020; LEE et al., 2010; ATTARI et al., 2010; PARVIN et al., 2010; ILKI et al., 2011; SEZEN, 2012; CHOUDHURY et al., 2013; REALFONZO et al., 2014; VECCHIO et al., 2014); High-Performance Fiber Reinforced Concrete (HPFRC) (SHANNAG; ALHASSAN, 2005; SHANNAG et al., 2002; BESCHI et al., 2015); and Ultra High-Performance Fiber Reinforced (UHPFRC) (KHAN et al., 2018; SHARMA; BANSAL, 2019; SAHARAN et al., 2023)

The Ultra-High Performance Concrete (UHPC) is characterized by its exceptional compressive and tensile strength, as well as its high stiffness. However, due to its brittle nature, fibers are often added to improve its ductility, resulting in what is known as Ultra-High Performance Fiber-Reinforced Concrete (UHPFRC) (FEHLING; SCHMIDT, 2014). UHPFRC combines the superior mechanical properties of UHPC with enhanced ductility and crack resistance provided by the fibers. It is also highly flowable, comparable to or even exceeding the workability of Self-Compacting Concrete (SCC), and typically achieves compressive strengths of no less than 150 MPa (AFGC, 2002; NF P 18-710, 2016; WILLE et al., 2014; HUANG et al., 2022a). In contrast, High-Performance Fiber-Reinforced Concrete (HPFRC) refers to a broader category of fiber-reinforced concretes that exhibit the mechanical characteristics of High-Strength Concrete (HSC) combined with SCC-like workability. HPFRC typically reaches compressive strength values ranging from 100 MPa to 150 MPa (KAIKEA; KARIHALOO, 2014; WALRAVEN, 2009; SOHAIL et al., 2021). UHPFRC material has higher tensile strength compared with the HPFRC, due to the higher fiber volume (usually higher than 2%). However, both HPFRC and UHPFRC develop the hardening and microcracking states, represented by a trilinear stress-strain tensile curve (elastic-hardening-softening branches) (AL-OSTA et al., 2017; NAAMAN; REINHARDT, 1996; WILLE et al., 2014; NAAMAN; REINHARDT, 2006).

The French Building Code NF P 18-710 (2016) defines UHPFRC as a material with high post-cracking tensile strength and high compressive strength, which guarantee a ductile behavior in tension. This results in structural elements with higher energy absorption capacity, durability, flexural strength, and shear strength (HUANG et al., 2022a). Whereas the AFGC (2002), describes the UHPFRC as a material with tensile strength values between 7 and 15 MPa.

The strengthening with HPFRC and UHPFRC jackets not only helps to shift the failure region away from the typical shear failure region but also improves the joint's behavior with seismic deficiency in terms of stiffness, shear strength, and energy dissipation capacity (FEHLING; SCHMIDT, 2014; BAHRAQ et al., 2021; MATSAGAR, 2015). Several experimental studies on BCJs retrofitted with HPFRC/UHPFRC jackets have been carried out in the last decades. Table

2.5 summarizes some experimental tests of beam-column joints strengthened with UHPFRC.

Table 2.5 – Summary of experimental tests of BCJs retrofitted with UHPFRC/HPFRC under conditions of cyclic load

Author	Brief description
Shannag and Alhassan (2005) and Shannag et al. (2002)	BCJs retrofitted with HPFRC jackets of thickness 15 mm and 25 mm were investigated. In the retrofitted joints, the authors observed a ductile failure mode, increase in the load capacity, energy dissipation and ductility, and less stiffness degradation.
Beschi et al. (2015)	The effectiveness of a HPFRC jacket with thickness of 30 mm in the beam and 40 mm in the column as retrofit intervention for exterior non-seismic BCJs was investigated. The results showed increase of the joint shear strength, lateral displacement capacity and energy dissipation capacity, and ductile flexural failure at the beam.
Sharma and Bansal (2019)	Exterior BCJs retrofitted with Ultra-High Performance Hybrid Fiber Reinforced Concrete (UHP-HFRC) jackets of thickness 25 mm were analyzed, obtaining improvements in the load capacity, ductility, energy dissipation, and stiffness.
Saharan et al. (2023)	BCJs were exteriorly retrofitted with a UHPFRC jacket of thickness 25 mm. It was verified the increase in the lateral load, ductility, and energy absorption.
Khan et al. (2018)	BCJs were exteriorly retrofitted with 30 mm thick UHPFRC plates. Two different alternatives for the bond between the concrete and the retrofit material were tested. The first one consisted of using sandblasting (Figure 2.10.a) and the second one was carried out attaching pre-fabricated UHPFRC plates using epoxy resin and special fillers (Figure 2.10.c). The experimental results showed improvement in the shear capacity, stiffness, energy dissipation capacity, and ductility. In addition, a change from diagonal cracks in the joint core to flexural vertical cracks at the interface between the beam and the joint was observed, a desired configuration, Figure 2.11.

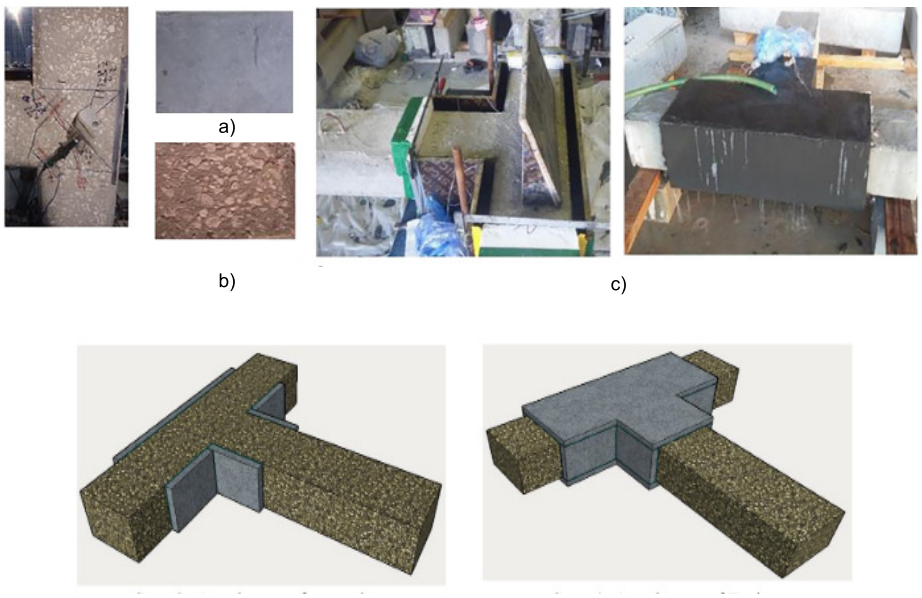

Figure 2.10 – Scheme of exterior BCJ retrofitted with UHPFRC a) Before sandblasting, b) After sandblasting, c) Demolding of UHPFRC in the conventional concrete, d) Attachment of pre-fabricated UHPFRC plates in the conventional concrete.
Font: Obtained from Khan et al. (2018)

a) b) c)

Figure 2.11 – Cracks at rupture load in a) Unretrofitted BCJ, b) BCJ retrofitted with UHPFRC, and c) BCJ retrofitted with pre-fabricated UHPFRC plates.
Font: Obtained from Khan et al. (2018)

2.5 Shear strength models of joints retrofitted with UHPFRC

Despite the effectiveness of UHPFRC as a retrofit material, there is a lack of analytical models to predict the shear strength of exterior joints retrofitted with UHPFRC jackets. Below is presented the only analytical model available to determine the shear capacity of joints strengthened with UHPFRC, which was developed by Bahraq et al. (2021).

In this model, the joint shear strength is a function of the contribution of the concrete V_{jhc} and UHPFRC V_{jhR}, (Equation 2.92). The authors assumed that the contribution of the UHPFRC jacket to the BCJ shear strength could be determined with the formula provided by ACI 352R (2002) for normal concrete (Equation 2.94). The contribution of the concrete may be determined through the empirical model developed by Sarsam et al. (1985), even though the model was proposed for joints subjected to monotonic loading (Equation 2.93). However, the simplification of using the formulation of normal concrete for UHPFRC may not lead to reliable results, instead an analytical expression specific for UHPFRC retrofit should be used.

$$V_{jh} \quad V_{jc} \quad V_{jhR} \tag{2.92}$$

$$V_{jhc} \quad 2.4 f_{cu}^{0.33} b_c h_c \qquad f_{cuR} \quad 70N \ \ mm^2 \tag{2.93}$$

$$V_{jhR} \quad 0.083 \quad \overline{f_{cR}} A_j \tag{2.94}$$

where f_{cR} is the compression strength of UHPFRC, is determined using Table 2.3, and A_j is the effective area of UHPFRC, as shown in Figure 2.12.

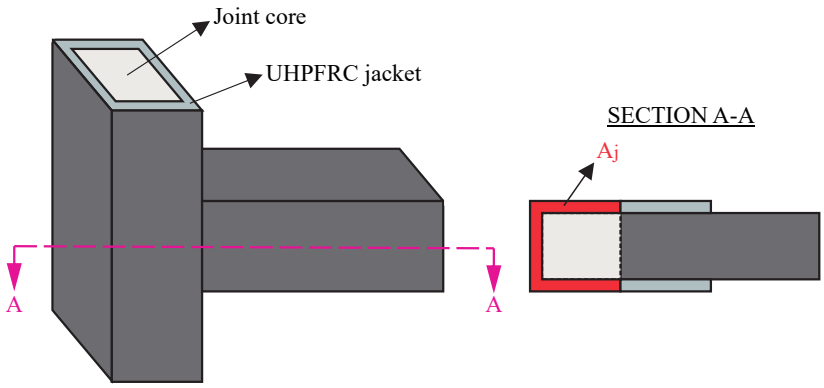

Figure 2.12 – Scheme of effective area of UHPFRC jacket.
Font: Obtained from Bahraq et al. (2021)

2.6 Numerical simulations of BCJs

2.6.1 Reinforced concrete BCJs

To represent the nonlinear behavior of the materials, various numerical techniques and constitutive models have been implemented through commercial software developed via the Finite Element Method (FEM), such as ATENA, DIANA, ABAQUS, ANSYS, and others. The use of computational simulations to study the behavior of RC joints is considered an important tool in cases involving cyclic loading.

Experimental analyses have helped to understand the behavior of RC joints; however, these studies require a high cost and time. Nevertheless, in many cases, they do not capture the influence of many variables that can affect the behavior of the connections. Therefore, the implementation of numerical simulations is considered an effective alternative to complement experimental research and expand the knowledge on joints.

In many cases, simulating RC BCJs is considered complex due to the need for calibrated models and the consideration of the bond between reinforcement and concrete. A review of the most important studies related to numerical strategies to simulate the behavior of BCJs under conditions of cyclic load is presented in Table 2.6.

Table 2.6 – Summary of studies with FE analysis of BCJs under conditions of cyclic load

Author	Brief description
Sharma et al. (2008)	The behavior of non-seismic exterior joints under cyclic and monotonic loading was studied. The results showed that models with cyclic loading and using a bond-slip relationship were more critical in obtaining good calibration in terms of cracking patterns and failure modes. The authors considered a specific formulation to represent the bond-slip relationship of the reinforcements. (ABAQUS SOFTWARE)
Haach et al. (2008)	The influence of the axial force of the column on the behavior of exterior joints, through numerical analyses with monotonic horizontal loading was investigated. The results showed large deformations in the transverse reinforcement with low axial force, higher shear strength with high axial force values, and no significant effect on the joint stresses when the applied load is eccentric. The modeling considered a perfect bond between reinforcement and concrete. (ABAQUS SOFTWARE)
Najafgholipour et al. (2017)	The behavior of exterior BCJs (ductile and non-ductile) was investigated to evaluate the influence of shear failure mode on shear strength, ductility, and stability in reinforced concrete frames. Shear failures in connections without seismic criteria were efficiently simulated. (ABAQUS SOFTWARE)
Arowojolu and Ibrahim (2020)	Simulations of exterior joints with secondary reinforcement in the critical regions of plastic hinges. The results showed that the addition of horizontal stirrups in the joint core was not sufficient to prevent its failure because the plastic hinges still occur in the interface beam-joint core, and yielding of longitudinal reinforcement causes loss of bond. However, the methodology used to shift the plastic hinge region was satisfactory, with improvement in the ductility, energy dissipation, load capacity, and stiffness degradation. (ABAQUS SOFTWARE)
Shirai (2006)	Bi-dimensional (2D) and three-dimensional (3D) simulations of interior BCJs with shear failure mode were carried out. The 3D results showed a good representation of damage distribution in the elements and joint failure. The authors used the bond model proposed by fib Model Code (1990). However, some models showed higher shear capacity than the ones experimentally obtained. (DIANA SOFTWARE)
Li and Kulkarni (2010)	Joints with wide beams was analyzed to assess the influence of the concrete strength, axial force in the column, and anchorage length of beam reinforcement. The results showed that compressive concrete strength did not have a significant effect on this type of connection. In addition, due to the beam width, shear stresses are lower, hence the need for transverse reinforcement is reduced. However, the axial force had an advantageous effect on the shear strength. The reinforcement bond was simulated according to the criteria of *fib* Model Code (1990). (DIANA SOFTWARE)
Deaton (2010)	Numerical simulations of exterior BCJs were developed. The author studied the seismic performance of exterior (corner) joints with slabs and seismic deficiencies subjected to cyclic loading in two directions (bi-axial loading). The results exhibited the hysteresis characteristics (*e.g.*, pinching effect) of the joints and rupture modes close to experimental ones. However, it was recommended to introduce new models for the bond-slip relationship because the relationship used did not show significant effects on the behavior of the joints. (DIANA SOFTWARE)
Sasmal et al. (2011)	Exterior BCJs designed only for gravity loads were simulated. Numerical results displayed anchorage failure in the reinforcement beam and shear cracks in the joint core. The bond model used was the one proposed by *fib* Model Code (1990).(ATENA SOFTWARE)
Haris and Roszevák (2019)	The seismic behavior of corner joints subjected to cyclic loading was simulated. The authors highlighted that it is necessary to consider the real characteristics of the reinforcement as, in some cases, linear models of reinforcement are not close to experimental results. However, the proposed methodology can be applied only up to story drifts of 1%. The bond between reinforcement and concrete was simulated using the relationship of *fib* Model Code (1990). (ATENA SOFTWARE)

2.6.2 Reinforced concrete elements retrofitted with UHPFRC

Table 2.7 summarizes finite element analysis of columns and BCJs retrofitted with UHPFRC jackets.

Table 2.7 – Summary of studies with FE analysis of elements retrofitted with UHPFRC

Author	Brief description
Sakr et al. (2020)	The behavior of RC columns retrofitted with UHPFRC jackets was investigated through finite element analysis. The authors observed the increase in the load capacity with the increase of the UHPFRC jacket thickness. In this model, the interface between the concrete and the jacket was simulated by multi-zero-length connectors, which are two-node connectors placed at the interface, with one node on the concrete and the other on the jacket. (ABAQUS SOFTWARE)
Fayaz et al. (2022)	Numerical analyses of BCJs retrofitted with 30 mm thick UHPFRC jacket confined by CFRP sheets were developed. The models considered the perfect bond between concrete and UHPFRC, while the bond between UHPFRC and CFRP was modeled as a tie-bond. The numerical results displayed the improvement in the shear strength, energy dissipation capacity, and structural stiffness, due to the retrofits. (ABAQUS SOFTWARE)
Bahraq et al. (2021)	Numerical investigations of exterior BCJs strengthened with UHPFRC jackets, through finite element analysis were carried out. The contact between the concrete and the UHPFRC jacket was simulated with cohesive elements, using the constitutive model *Traction-Separation Approach*, which can be used for materials of thin thickness. The results showed increments in the load-bearing capacity and failure mode in the interface beam-joint core, as obtained in the experimental tests. (ABAQUS SOFTWARE)

3 Experimental Tests Used in Reference

3.1 Case studies

This thesis was developed using the following experimental tests as a reference, which consist of one low-high reinforced concrete frame under monotonic load and four beam-column joints subjected to cyclic loading.

3.1.1 Case 1 - Reinforced concrete frame: Vecchio and Emara (1992)

The first case corresponds to a reinforced concrete frame, tested by Vecchio and Emara (1992) at the University of Toronto. The authors studied the influence of the shear effects on the frame's structural behavior, specifically on parameters such as frame strain, load capacity, and rupture mode.

The frame had two stories 1800 mm and 1600 mm high and a span of 3100 mm. The beams and columns had cross-sections of 300x400 mm^2 and 400x300 mm^2, respectively. The structure was fixed to a rigid base represented by hinge support in the column base, as shown in Figures 3.1 and 3.2.

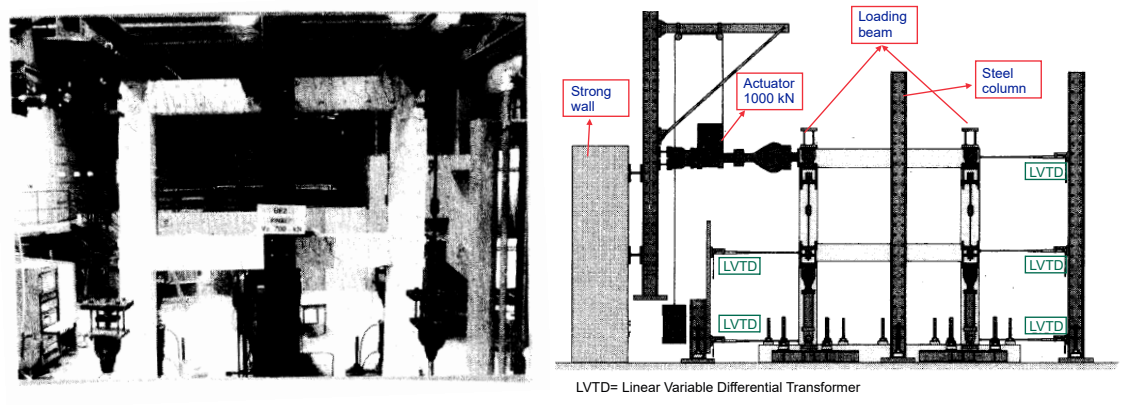

Figure 3.1 – a) Experimental test of frame, b) Test setup.
Font: Adapted from Vecchio and Emara (1992)

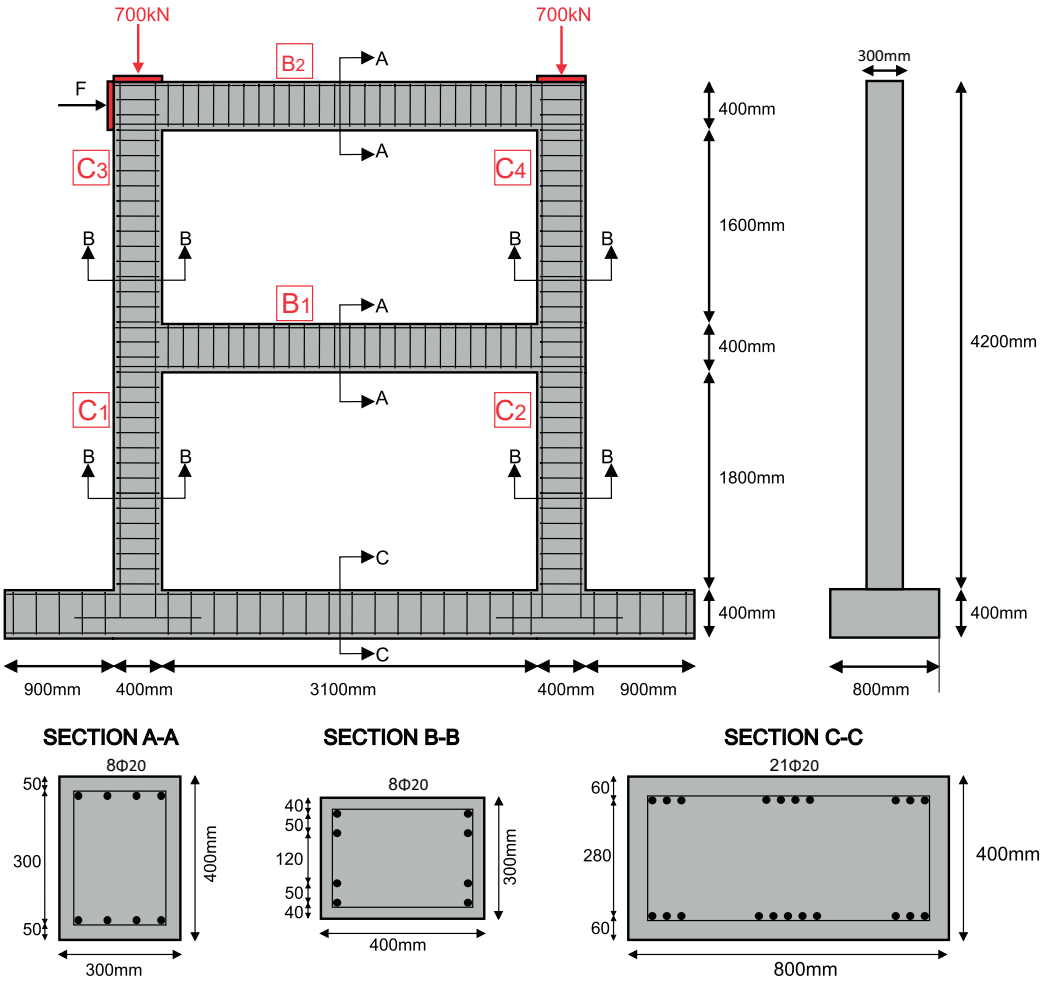

Figure 3.2 – Details of the reinforced concrete frame.
Font: Adapted from Vecchio and Emara (1992)

The variables V_1 and V_2 correspond to the beams of the first and second floor, while C_1-C_3 and C_2-C_4 correspond to the columns of the left and right face, respectively. The beams and columns were reinforced with eight bars of 20 mm diameter, four at the top and four at the bottom face. In addition, the structure was reinforced with stirrups of 10 mm diameter, spaced by each other by 125 mm. The rigid base was reinforced with 21 bars of 20 mm diameter and stirrups, placed at each 250 mm.

A constant vertical load of 700 kN was applied to the top of the columns C_3 and C_4, which represents the weight of the upper floors (gravity forces). Subsequently, a monotonic horizontal loading was applied through a hydraulic actuator, until reaching the ultimate capacity of the frame, starting with load intervals of 25 kN and ending with intervals of 10 kN. To measure horizontal displacements and strains, displacement transducers (LVDTs) and electrical strain gauges located at different points of the structure were used.

The concrete had a compressive strength f_c of 30 MPa (Figure 3.3.a) and a tensile strength f_t of 1.81 MPa. The 20 mm steel bars had a yield strength of 418 MPa, an ultimate strength of 454 MPa, a Young's modulus of 192500 MPa, and a hardening modulus of 3100 MPa, as shown in Figure 3.3.b. The stirrups of 10 mm diameter had a yield strength of 454 MPa and

an ultimate strength of 690 MPa.

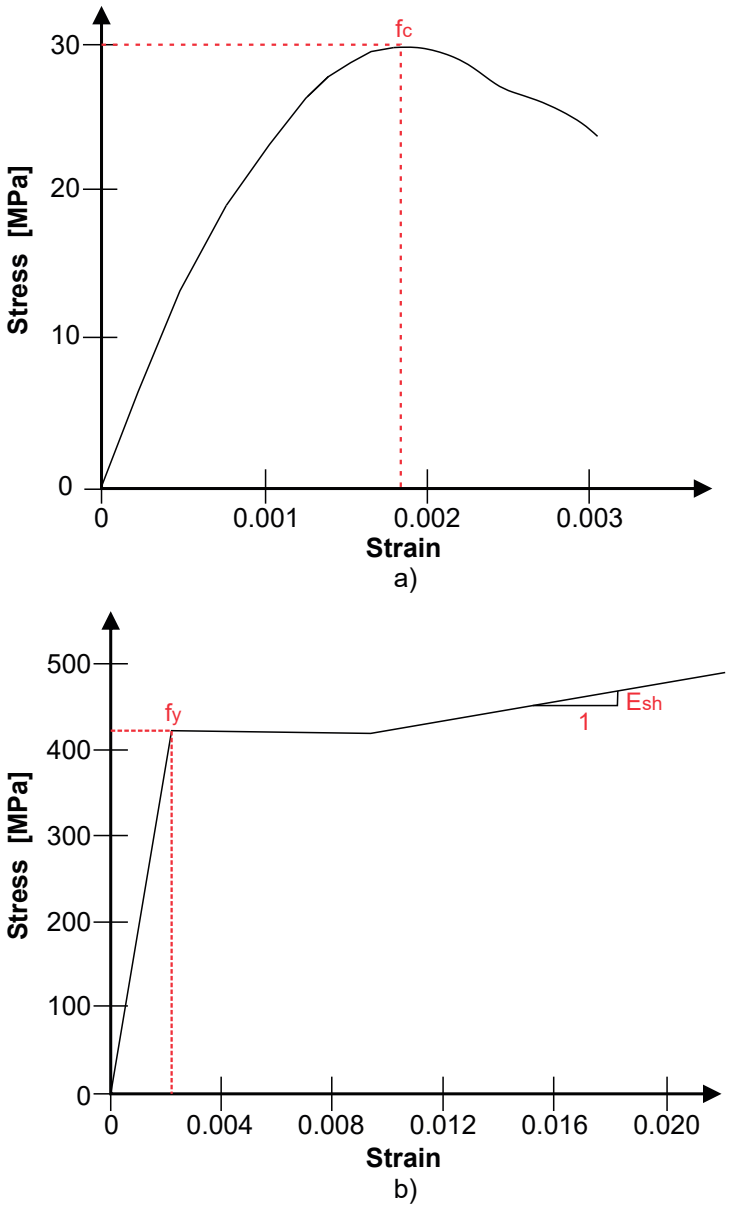

Figure 3.3 – Stress-strain curve in a) Compression of concrete and b) Tensile of reinforcement. Font: Adapted from Vecchio and Emara (1992)

3.1.2 Case 2 - Exterior beam-column joint: Kusuhara and Shiohara (2008)

This case corresponds to an exterior beam-column connection tested by Kusuhara and Shiohara (2008) at the University of Toronto (Canada). The test investigated the joint's strength, ductility, and failure mode when subjected to a significant demand of seismic forces. The authors used the theoretical model proposed by Kusuhara and Shiohara (2006) to calculate the relative displacements at the ends of the elements, rotations in beams and columns, and stresses in the longitudinal steel bars.

The exterior BCJ, named A2, had a cross-section of 300x300 mm^2, as observed in Figure 3.4. The beam was divided into two sections: the first vertically supported at its end, and the second in cantilever. During the experimental test, the displacements at the base of the column

were restricted in all directions, leaving only the rotations free. The base for the column and the end of the beam had hinge and roller supports, respectively.

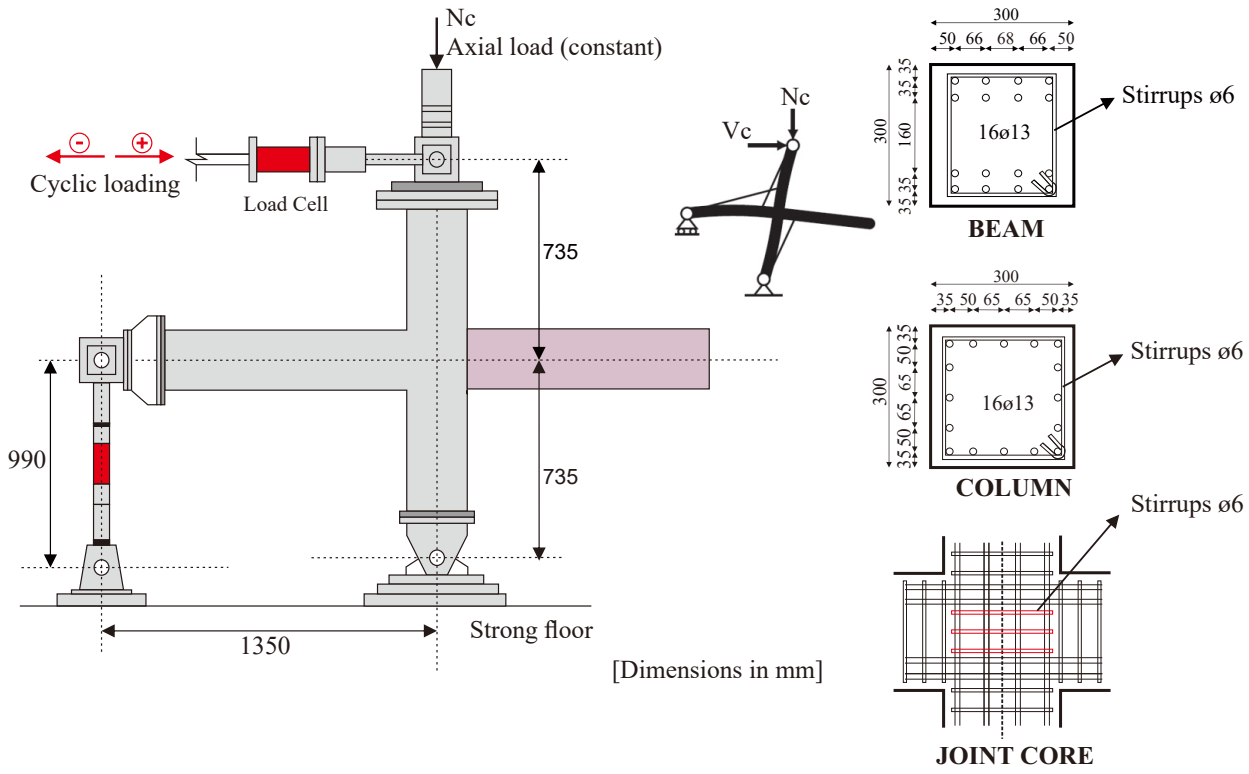

Figure 3.4 – Details of BCJ A2.
Font: Adapted from Kusuhara and Shiohara (2008)

The beam was reinforced with sixteen longitudinal bars of 16 mm diameter, eight localized at the bottom and eight at the top. The column was reinforced with sixteen longitudinal bars of 16 mm diameter. The beam and the column had stirrups of diameter of 6 mm, spaced each 50 mm. The joint core had a transverse reinforcement of 6 mm diameter, composed of three horizontal layers corresponding to the minimum value required by AIJ Structural Committee (1990).

The top of column was initially loaded with a constant vertical axial force on the column of 216 kN, through a hydraulic actuator of capacity 500 kN. Subsequently, a cyclic and quasi-static horizontal load was applied to the top of the column, through a hydraulic actuator with a capacity of 200 kN. The applied load gradually increased until reaching a story drift (SD) of 6%, determined by Equation 3.1.

$$SD_c \quad \frac{100\Delta}{L_c} \tag{3.1}$$

where L_c represents the total height of the column and Δ is the horizontal displacement measured at the top of the column.

In the experimental test, BCJ A2 was subjected to a cyclic displacement history, as shown in Figure 3.5, demonstrating a progressive increase in displacement with each cycle.

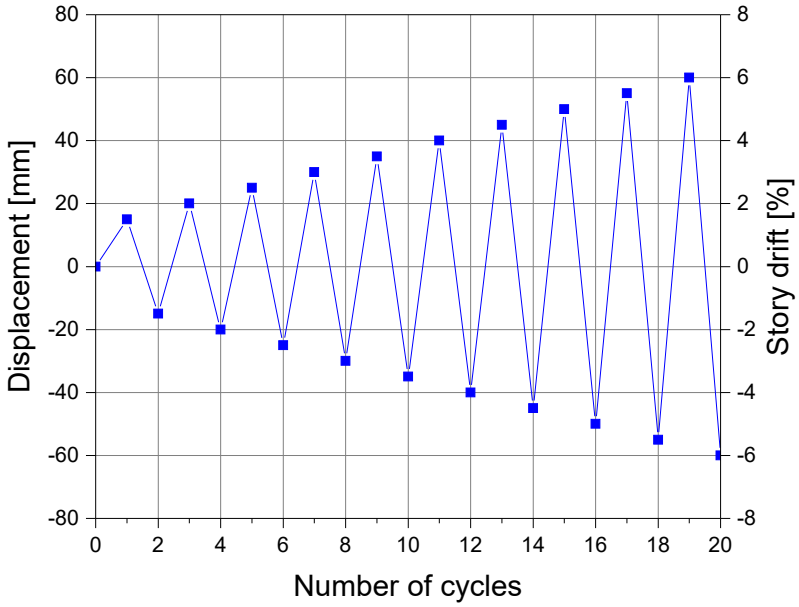

Figure 3.5 – Cyclic displacement history BCJ A2.
Font: Adapted from Kusuhara and Shiohara (2008)

The concrete material had a cylindrical compressive strength of 28 MPa, a Young's modulus of 25900 MPa, and a tensile strength of 2.67 MPa. The longitudinal reinforcement of the beam and the column had a Young's modulus of 176000 MPa, hardening modulus of 962 MPa, yield strength of 456 MPa and 357 MPa, and ultimate strength of 582 MPa and 493 MPa, respectively. The transverse reinforcement had a Young's modulus of 151000 MPa, hardening modulus of 3775 MPa, yield strength of 326 MPa, and ultimate strength of 488 MPa.

3.1.3 Case 3 - Exterior beam-column joint: Tsonos (2005)

The third case corresponds to the exterior joint tested by Tsonos (2005) at the structural engineering laboratory of the Aristotle University of Thessaloniki (Greece), labeled as A1. The study aimed to evaluate the seismic behavior of beam-column connections designed with seismic criteria from recent standards. The authors considered that, in some cases, the safety of framed structures can be compromised during strong seismic events, such as earthquakes, due to premature shear failures that occur in the joint core.

The beam and column had cross-sections of 200x300 mm^2 and 200x200 mm^2, respectively, Figure 3.6. Like the previous case, at the base of the column, displacements were restricted in all directions while their rotations were free. Thus, the top and base of the column were restrained with roller and hinge support, respectively.

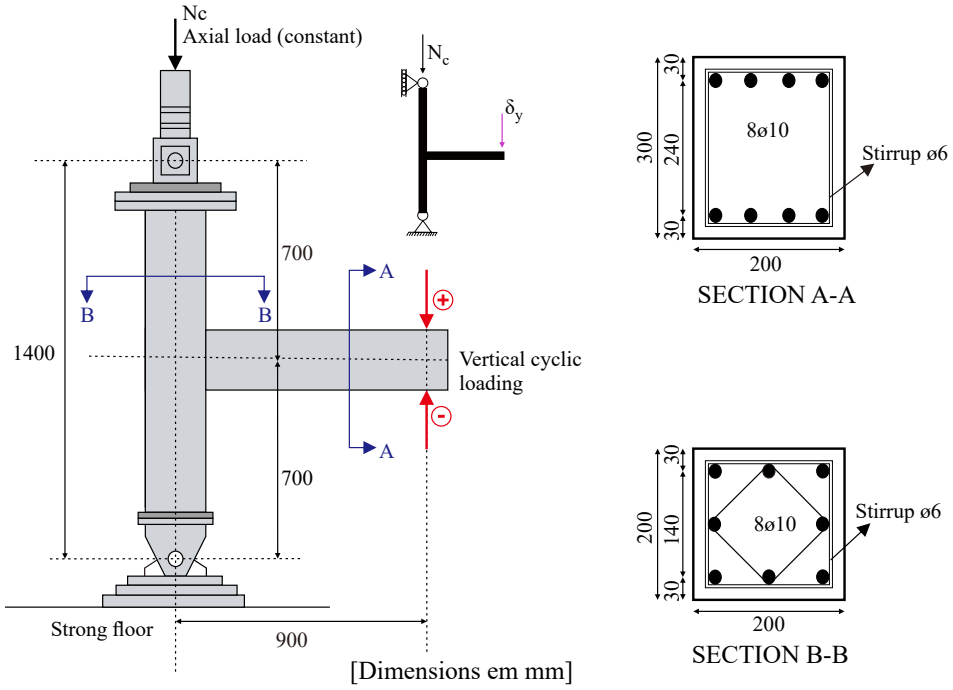

Figure 3.6 – Details of BCJ A1.
Font: Adapted from Tsonos (2005)

The beam was reinforced by eight longitudinal bars of 10 mm diameter, four localized at the top and four at the bottom. The longitudinal reinforcement of the column was composed of eight bars of diameter 10 mm. The beam and column were reinforced with stirrups of diameter 6 mm, spaced each 65 mm and 50 mm, respectively. In the less confined region of the beam, a spacing of 200 mm was used. Similarly, the joint core was reinforced by five layers of closed stirrups. In addition, the column and the joint core had 45deg rotated closed stirrups, as shown in Figure 3.6. The joint A1 was designed following the requirements of standards ACI 352R (2002) and ACI 318 (2005).

A vertical axial force of 200 kN was applied to the top of the column, which was constant throughout the test. Afterward, a cyclic load at the end of the beam was applied until reaching a story drift of 6%, determined by Equation 3.2. L_b represents the total length of the beam and Δ is the vertical displacement measured at the end of the beam.

$$SD_b \quad \frac{100\Delta}{L_b} \tag{3.2}$$

Figure 3.7 exhibits the history displacement of the cyclic load, with displacements of 15, 20, 25, 30, 35, 40, 45, 50, 55, and 60 mm, and story drifts of 1.5%, 2.0%, 2.5%, 3.0%, 3.5%, 4.0%, 4.5%, 5.0%, 5.5% e 6.0%.

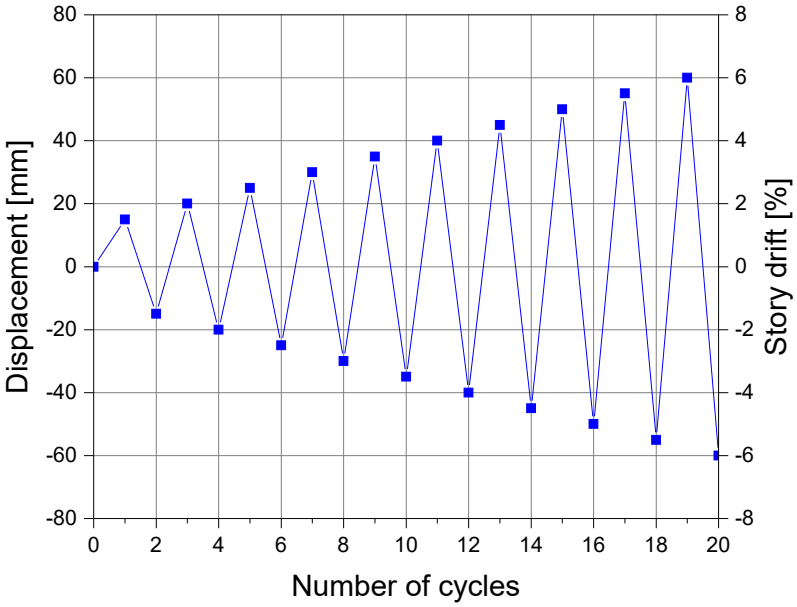

Figure 3.7 – Cyclic displacement history BCJ A1.
Font: Adapted from Tsonos (2005)

The concrete had a compressive strength of 35 MPa at 28 days. The longitudinal reinforcement of the beam and column had a yield strength of 500 MPa, while the transverse reinforcement presented a yield strength of 540 MPa.

3.1.4 Case 4 - Exterior beam-column joint: Beschi et al. (2015)

The next specimen analyzed in the current thesis corresponds to the exterior beam-column joint tested by Beschi et al. (2015). The authors tested two identical joints, one without retrofit and the other retrofitted with an HPFRC jacket named specimens CJ2 and RCJ2, respectively. Both specimens had the same geometry but with different concrete compressive strengths.

The dimensions of the beam and column cross-sections were 300x500 mm^2 and 300x300 mm^2, respectively. The total height for the column (L_c) and the length of the beam (L_b) corresponding to the contra-flexure points placed in the beam mid-span and column mid-height of a real building frame, were 3000 mm and 2100 mm, respectively, as observed in Figure 3.8.

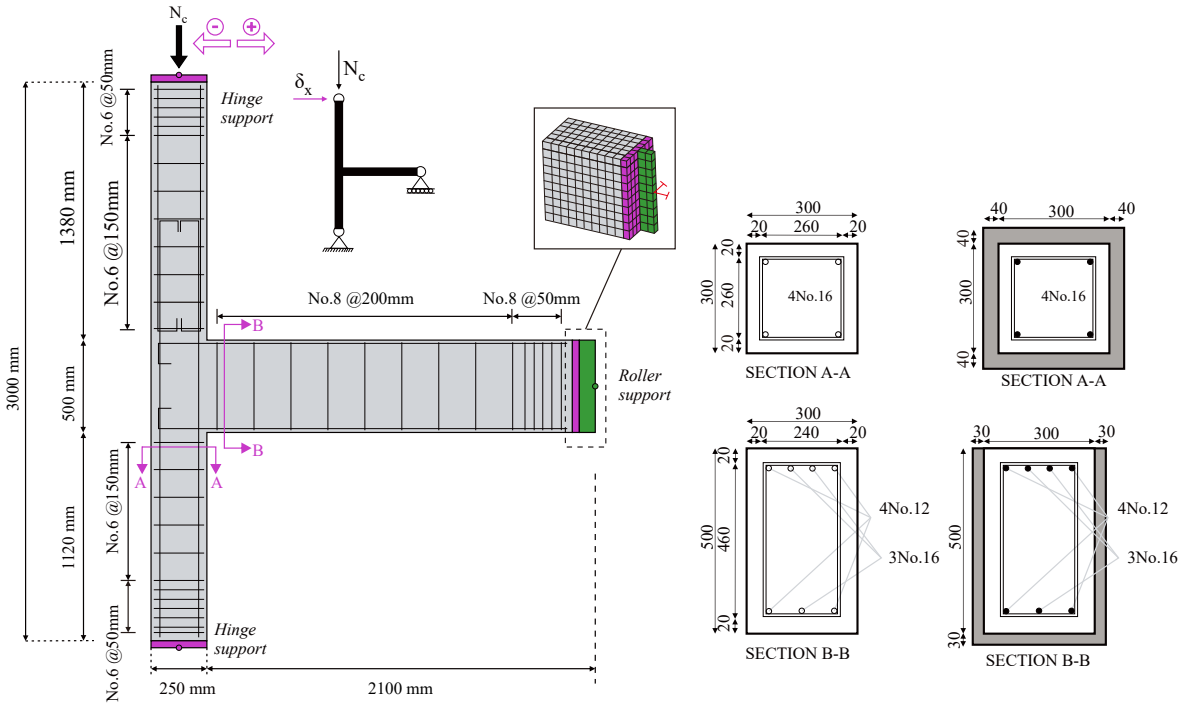

Figure 3.8 – Geometrical details of: a) Beam-column joint, b) Sections of joint CJ2, and c) Sections of joint RCJ2.
Font: Adapted from Beschi et al. (2015)

The longitudinal reinforcement of the beam was composed by four smooth steel bars of diameter 12 mm (two localized at the bottom and two at the top) and three bars of diameter 16 mm with end-hooks in the region of the joint core, as shown in Figure 3.8. The longitudinal reinforcement of the column was composed of four steel bars of 12 mm diameter with a lap-splice in the superior column. Regarding the transverse reinforcement, the beam had stirrups of diameter 8 mm, spaced 200 mm (50 mm in the beam end), and the column had stirrups of diameter 6 mm, spaced 150 mm (50 mm in the column ends). No transverse reinforcement was placed in the joint core.

Two hydraulic jacks were used to apply a vertical load of 210 kN to the column top to simulate the gravity load. The horizontal cyclic displacement was applied using an electromechanical jack fixed to a strong wall and the column top. The load was considered positive in the left-to-right direction. The beam-column joint presented free rotation at the top and the base of the column (hinge supports). The beam end was restricted only vertically through a roller support. These boundary conditions were applied to both specimens. The history displacement applied during the experimental test, with horizontal displacements of 15, 22.5, 30, 45, 60, and 75 mm, corresponding to story drifts of 0.5%, 0.75%, 1.0%, 1.5%, 2.0%, and 2.5,% as shown in Figure 3.9.

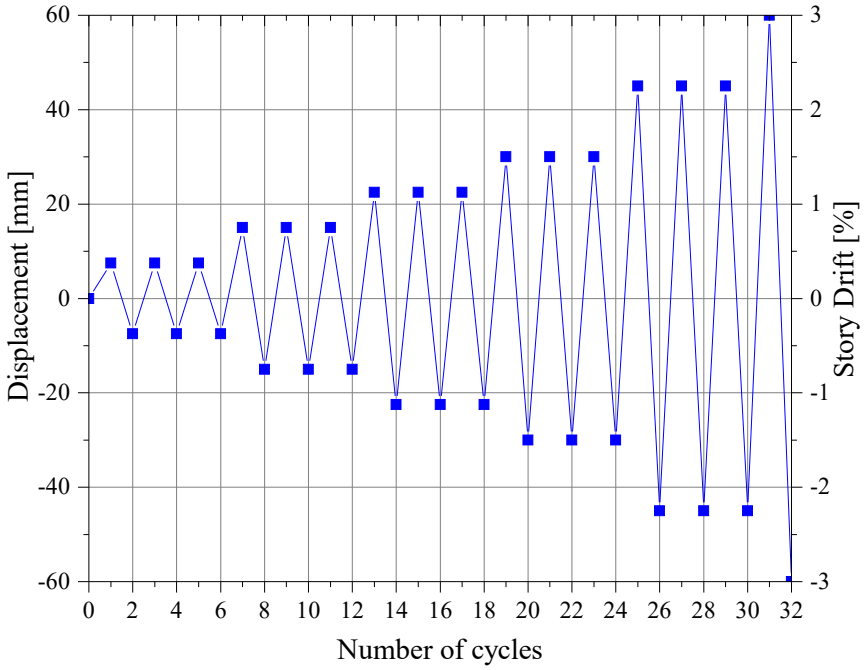

Figure 3.9 – Cyclic displacement history of BCJs CJ2 and RCJ2.
Font: Adapted of Beschi et al. (2015)

The steel bars of 12 mm and 16 mm diameters presented yield strengths of 365 MPa and 445 MPa, ultimate strengths of 558 MPa and 546 MPa, and ultimate strains of 15.9% and 13.7%, respectively. Stirrups with 6 mm and 8 mm diameter had yield strengths of 493 MPa and 337 MPa, ultimate strengths of 556 MPa and 440 MPa, and ultimate strains of 16.1% and 21%, respectively. The Young's modulus of steel was assumed to be equal to 200000 MPa.

The normal concrete of CJ2 and RCJ2 specimens had a cylinder compressive strength of 38.7 MPa and 27 MPa, respectively, and a Young's modulus of 29238 MPa and 24421 MPa, respectively. The HPFRC material had a compression strength of 110.5 MPa, a Young's modulus of 36000 MPa, and a tensile strength of 6.6 MPa. The thickness of the HPFRC jacket was 30 mm in the beam and 40 mm in the column (Figure 3.8).

4 Proposed analytical models

In this chapter, an analytical model to calculate the beam flexural strength of RC BCJs retrofitted with UHPFRC jacket, called flexural model, and an analytical model to calculate the shear strength of exterior BCJs retrofitted with UHPFRC jackets, named shear model, are proposed. These methods were published by Palomo et al. (2024).

4.1 Flexural model

The proposed flexural model is used to calculate the beam ultimate bending moment converging to exterior RC BCJs retrofitted with UHPFRC jackets. It is based on the model of Bahraq et al. (2021), assuming a different stress distribution on the cross-section and a different failure mode. In the proposed model the distribution of the tensile stresses in the jacket is continuous along the height and the failure is due to UHPFRC crushing. Conversely, in Bahraq et al. (2021), the distribution of the tensile stresses in the jacket is not continuous along the jacket's height and the failure is due to both UHPFRC crushing and UHPFRC behavior under tension. The proposed analytical model's value lies in the possibility of calculating the ultimate bending moment of the retrofitted cross-section without using software.

The proposed equations can be easily implemented in a spreadsheet or using programming in software such as MathCad or Matlab. Once this is done, the design of the UHPFRC jacket for the flexural strengthening of a beam can be quickly carried out. The model does not apply to BCJs with pre-deformations before the construction of the strengthening jacket. This methodology is based on the assumption of plane sections, as the condition of perfect bond between UHPFRC and plain concrete can be achieved by using different techniques of substrate surface preparation, as shown in Habel et al. (2006), Safdar et al. (2016), Paschalis and Lampropoulos (2021), Huang et al. (2022b), Nagib et al. (2022), and Al-Osta et al. (2020).

Three possible intervals for the neutral axis depth (x_c) in the beam cross-section were considered, corresponding to Cases 1, 2, and 3. Case 1 occurs when the neutral axis falls within the UHPFRC layer (Figure 4.1), of thickness $_R$; Case 2 occurs when the neutral axis is localized between the inner face of the retrofit layer and the centroid of the top longitudinal reinforcement. Finally, Case 3 occurs when the neutral axis is localized below the centroid of the top longitudinal reinforcement.

The equations proposed in this methodology were derived for the case in which the flexural failure in the cross-section is due to UHPFRC crushing. Accordingly, it must be checked that, at UHPFRC crushing the strains, in the plain concrete and in steel reinforcements do not exceed the ultimate strains. In the following formulation, subscript c refers to the conventional concrete, while R to the retrofit material.

Figure 4.1 shows the distributions of stresses, strains and internal forces on the beam

cross-section at joint interface for Case 1. In this case, for convenience of calculation the tensile resultant force is divided in seven components, labelled T_{R1} - T_{R7}. The meaning of the symbols used in Figure 4.1 is the following: $_{cuR}$ is the maximum compressive strain in the UHPFRC layer (Equation 4.1), $_{ut,crack}$ is the strain corresponding to the tensile cracking strength f_{ut} of UHPFRC (Figure 4.2); the strains $_{ut}$ and $_{ut}$ and stresses f_{ut} and f_{ut} correspond to the horizontal edges of the beam original cross-section (Figure 4.2), expressed by Equations (4.2)-(4.3) and (4.8)-(4.9) reported in Table 4.1, respectively.

The parameters $_{ut1}$ and f_{ut1} correspond to the ultimate tensile strain and stress in UHPFRC. The strains $_{sc}$ and $_{sc}$ represent those in the bottom and top longitudinal reinforcements, respectively, as given by Equations (4.4) and (4.5). The distance y denotes the distance from the neutral axis to the strain $_{ut,crack}$ (Equation 4.7). The parameter d refers to the distance between the centroid of the top longitudinal reinforcement and the extreme compressed concrete fiber in the beam section without the jacket. The parameters b and h are the width and depth of the beam section without the jacket, while B and H are the beam's width and depth with the jacket. CR_1 represents the compressive force in the UHPFRC layer (Equation 4.11). The internal tensile and compressive forces acting on the UHPFRC material can be calculated through Equations (4.14)-(4.25). The forces, strains, and areas of the bottom and top longitudinal steel reinforcements are represented by C_{sc} (Equation (4.26)), C_{sc} (Eq. (4.27)), $_{sc}$, $_{sc}$, A_{sc}, and A_{sc} , respectively. The parameter $_{ut,crack}$ can be determined directly from the tensile strain-stress diagram of UHPFRC, while $_{ut1}$ corresponds to the strain associated with f_{ut1}.

The yield strength and Young's modulus of steel bars are indicated with symbols f_{sy} and E_s, respectively. Regarding the tensile behavior of UHPFRC, the simplified stress-strain diagram shown in Figure 4.2 was adopted, which does not consider the hardening branch, represented as a bi-linear diagram composed by a linear and softening stage. This simplification was adopted also in other analytical models developed by other researchers (AL-OSTA et al., 2017; BAHRAQ et al., 2021; LAMPROPOULOS et al., 2016).

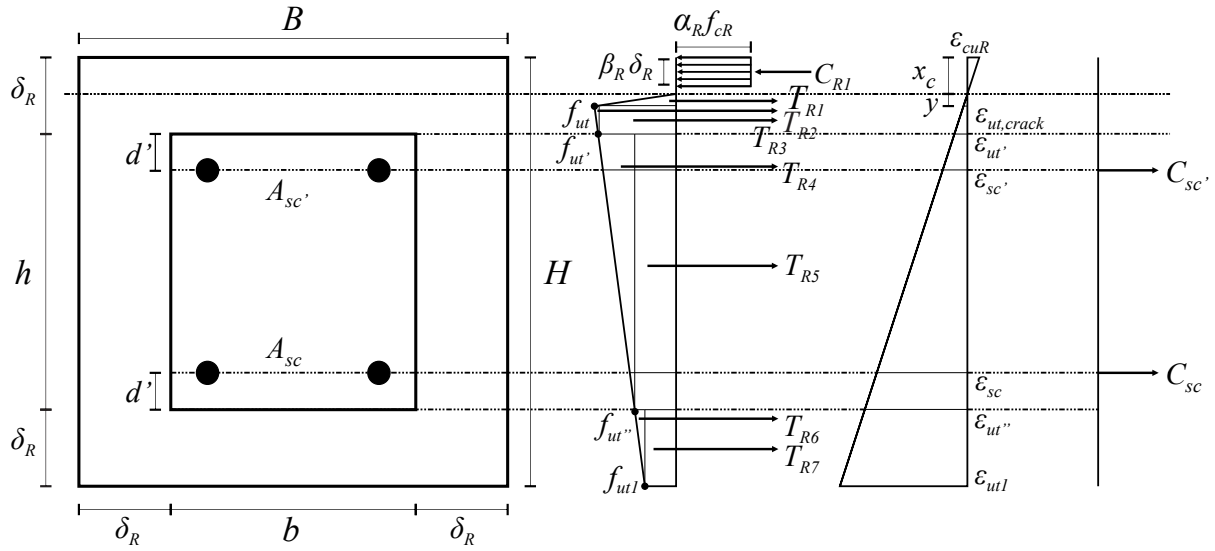

Figure 4.1 – Distributions of stresses, strains, and forces on the beam cross-section at the interface with the joint retrofitted with UHPFRC jacket – Case 1: x_c $_R$.
Font: Obtained from Palomo et al. (2024)

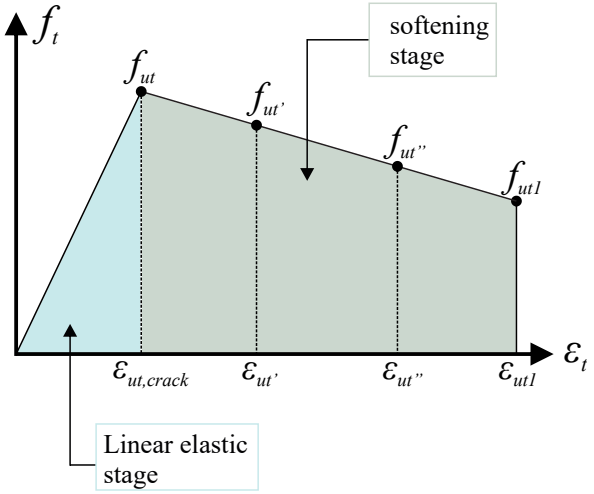

Figure 4.2 – UHPRFC tensile stress-strain diagram.
Font: Adapted from Palomo et al. (2024)

Table 4.1 – Analytical equations for strains and stresses in Cases 1, 2, and 3

Case 1 (x_c $_R$)		Case 2 ($_R$ x_c $_R$ d)		Case 3 (x_c $_R$ d)	
$_{cuR}$ $\frac{_{ut1}}{H\ x_c}x_c$	(4.1)	As case 1		As Case 1	
$_{ut}$ $\frac{_{ut1}}{H\ x_c}$ $_R$ x_c	(4.2)	$_{ut}$ $_{ut}$ (Case 1)		As case 2	
$_{ut}$ $\frac{_{ut1}}{H\ x_c}$ H x_c $_R$	(4.3)	Not present		Not present	
$_{sc}$ $\frac{_{ut1}}{H\ x_c}$ H x_c $_R$ d	(4.4)	As Case 1		As Case 1	
$_{sc}$ $\frac{_{ut1}}{H\ x_c}$ $_R$ x_c d	(4.5)	As Case 1		$_{sc}$ $\frac{_{ut1}}{H\ x_c}$ x_c $_R$ d	(4.6)
y $\frac{_{ut,crack}}{_{ut1}}$ H x_c	(4.7)	As Case 1		As Case 1	
f_{ut} f_{ut} $\frac{f_{ut1}\ f_{ut}}{_{ut1}\ \ _{ut,crack}}$ $_{ut}$ $_{ut,crack}$	(4.8)	As Case 1		As Case 1	
f_{ut} f_{ut} $\frac{f_{ut1}\ f_{ut}}{_{ut1}\ \ _{ut,crack}}$ $_{ut}$ $_{ut,crack}$	(4.9)	Not present		Not present	
Not present		C_c $_c$ x_c $_R$ f_c $_c b$	(4.10)	As Case 2	
C_{R1} $_R$ $_R$ $_R f_{cR} B$	(4.11)	C_{R1} $_R$ $_R f_{cR} B$	(4.12)	As Case 2	
Not present		C_{R2} $_R x_c$ R $_R f_{cR} 2$ $_R$	(4.13)	As Case 2	
T_{R1} $\frac{f_{ut} y}{2} B$	(4.14)	T_{R1} $f_{ut} y$ $_R$	(4.15)	As Case 2	
T_{R2} $\frac{f_{ut}\ f_{ut}}{2}$ $_R$ x_c y B	(4.16)	T_{R2} f_{ut} f_{ut} H $_R$ x_c y $_R$	(4.17)	As Case 2	
T_{R3} f_{ut} $_R$ x_c y B	(4.18)	T_{R3} f_{ut} H $_R$ x_c y 2 $_R$	(4.19)	As Case 2	
T_{R4} f_{ut} f_{ut} H 2 $_R$ $_R$	(4.20)	T_{R4} $\frac{f_{ut}\ f_{ut1}}{2}$ $_R B$	(4.21)	As Case 2	
T_{R5} f_{ut} H 2 $_R$ 2 $_R$	(4.22)	T_{R5} f_{ut1} $_R B$	(4.23)	As Case 2	
T_{R6} $\frac{f_{ut}\ f_{ut1}}{2}$ $_R B$	(4.24)	Not present		Not present	
T_{R7} f_{ut1} $_R B$	(4.25)	Not present		Not present	
C_{sc} $_{sc} E_s A_{sc}$ $A_{sc} f_{sy}$	(4.26)	As Case 1		As Case 2	
C_{sc} $_{sc}$ $E_s A_{sc}$ A_{sc} f_{sy}	(4.27)	As Case 1		As Case 2	

Font: Obtained from Palomo et al. (2024)

The factors $_R$ and $_R$ appearing in the equivalent rectangular compressive stress block of UHPFRC are expressed by Equations 4.28 and 4.29 (MERTOL et al., 2008), respectively.

$$_R \quad 0.85 \quad 0.0029 \ f_{cR} \quad 69 \qquad \begin{matrix} _R & 0.85 & for & f_{cR} & 69MPa \\ 0.75 & & for & f_{cR} & 69MPa \end{matrix} \tag{4.28}$$

$$_R \quad 0.85 \quad 0.007252 \ f_{cR} \quad 28 \qquad \begin{matrix} _R & 0.85 & for & f_{cR} & 28MPa \\ 0.65 & & for & f_{cR} & 28MPa \end{matrix} \tag{4.29}$$

where f_c and f_{cR} are the cylindrical compressive strength of normal concrete and of UHPFRC material. The depth of the beam cross-section referents to Figure 4.1 can be determined from the equilibrium of the internal and external axial forces, expressed as:

$$N \quad 0 \quad C_{R1} \quad T_{R1} \quad T_{R2} \quad T_{R3} \quad T_{R4} \quad T_{R5} \quad T_{R6} \quad T_{R7} \quad C_{sc} \quad C_{sc} \tag{4.30}$$

the values of each term can be calculated through Table 4.1.
Consequently, the beam flexural capacity can be obtained with the equilibrium of internal and external bending moments calculated respect to the neutral axis, as follows:

$$M \quad C_{R1} \quad \frac{x_c}{2} \quad T_{R1} \quad \frac{2y}{3} \quad T_{R2} \quad \frac{_R \quad x_c \quad y}{3} \quad y \quad T_{R3} \quad \frac{_R \quad x_c \quad y}{2} \quad y \quad T_{R4}$$
$$\frac{H \quad 2 \quad _R}{3} \quad _R \quad x_c \quad T_{R5} \quad \frac{H \quad 2 \quad _R}{2} \quad _R \quad x_c \quad T_{R6} \quad \frac{2 \quad _R}{3} \quad H \quad x_c \quad _R \quad (4.31)$$
$$T_{R7} \quad \frac{_R}{2} \quad H \quad x_c \quad _R \quad C_{sc} \; H \quad x_c \quad _R \quad d \quad C_{sc} \quad _R \quad x_c \quad d$$

The illustrations of Cases 2 and 3 are presented in Figures 4.3 and 4.4, respectively. The parameter f_c is the cylindrical compressive strength of normal concrete and C_c is the compressive force in the normal concrete, determined by Equation 4.10; C_{R1} and C_{R2} are the compressive forces in the UHPFRC, determined by Equations (4.12) and (4.13), respectively; and the internal tensile forces of UHPFRC (T_{R1} T_{R7}) are estimated by Equations (4.15)-(4.23). Finally, the factors $_c$ and $_c$ are determined through Equations (4.32) and (4.33), respectively, following the recommendations of ACI 318 (2019).

$$_c \quad 0.85 \tag{4.32}$$

$$\begin{array}{lll} _c \quad 0.85 & for \quad 17MPa \quad f_c \quad 28MPa \\ _c \quad 0.85 \quad \frac{0.05 \; f_c \quad 28}{7} & for \quad 28MPa \quad f_c \quad 55MPa \\ _c \quad 0.65 & for \quad f_c \quad 55MPa \end{array} \tag{4.33}$$

For Case 2 (Figure 4.3), the neutral axis depth and the ultimate bending moment of the cross-section can be determined by Equations (4.34) and (4.35), respectively.

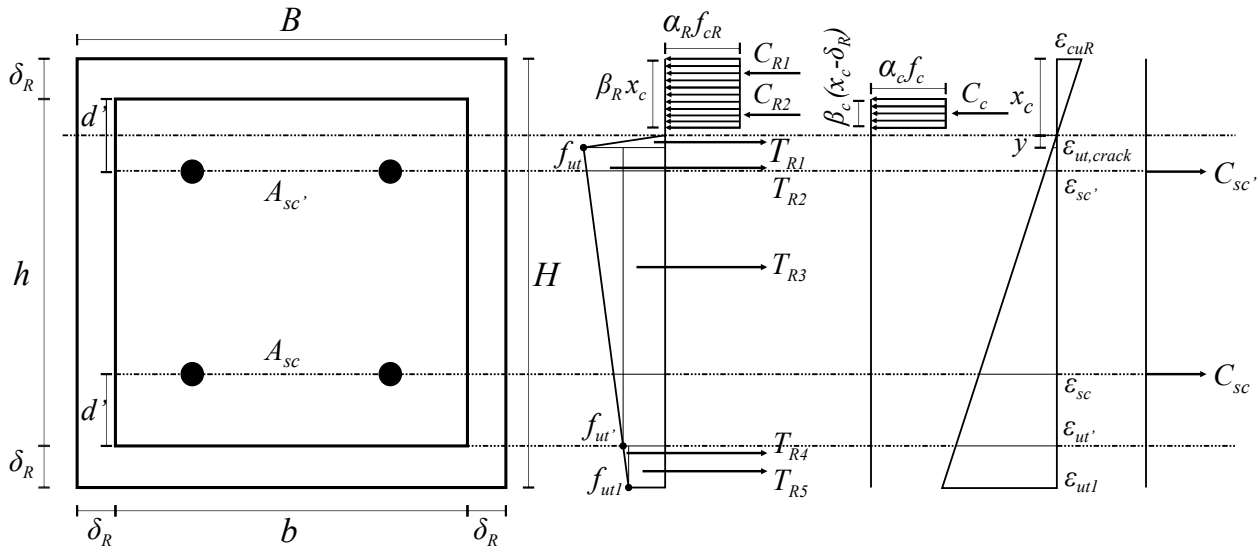

Figure 4.3 – Distributions of stresses, strains, and forces on the beam cross-section at the interface with the joint retrofitted with UHPFRC jacket – Case 2: $_R \quad x_c \quad _R \quad d$.
Font: Obtained from Palomo et al. (2024)

$$N \quad 0 \quad C_c \quad C_{R1} \quad C_{R2} \quad T_{R1} \quad T_{R2} \quad T_{R3} \quad T_{R4} \quad T_{R5} \quad C_{sc} \quad C_{sc} \tag{4.34}$$

$$M \quad C_c \quad x_c \quad _R \quad \frac{_c\, x_c \quad _R}{2} \quad C_{R1} \quad x_c \quad \frac{R}{2} \quad C_{R2} \quad x_c \quad _R \quad \frac{_R x_c \quad _R}{2} \quad T_{R1}$$
$$\frac{2y}{3} \quad T_{R2} \quad \frac{H \quad _R \quad x_c \quad y}{3} \quad y \quad T_{R3} \quad \frac{H \quad _R \quad x_c \quad y}{2} \quad y \quad T_{R4}$$
$$\frac{R}{3} \quad H \quad _R \quad x_c \quad T_{R5} \quad \frac{R}{2} \quad H \quad _R \quad x_c \quad C_{sc} \; H \quad x_c \quad _R \quad d$$
$$C_{sc} \quad _R \quad x_c \quad d \tag{4.35}$$

For Case 3 (Figure 4.4), the neutral axis depth and the ultimate bending moment of the cross-section are given by Equations (4.36) and (4.37), respectively. In this case, is important to highlight that the strain $_{sc}$ is a compressive strain, differently from that of other cases, expressed by Equation 4.6.

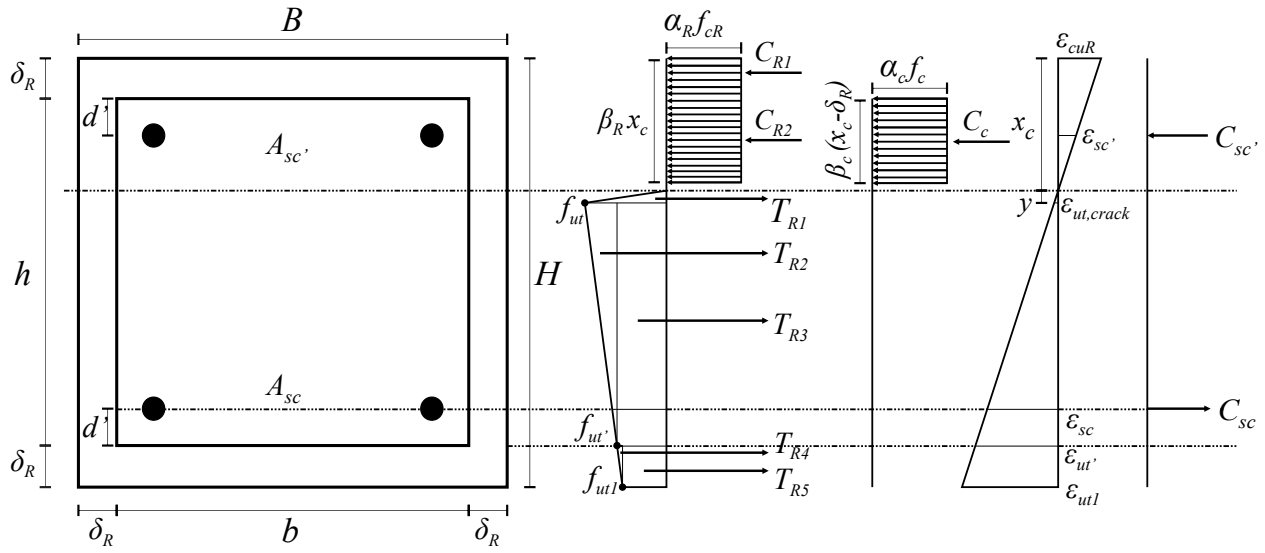

Figure 4.4 – Distributions of stresses, strains, and forces on the beam cross-section at the interface with the joint retrofitted with UHPFRC jacket – Case 3: $x_c \quad _R \quad d$.
Font: Obtained of Palomo et al. (2024)

$$N \quad 0 \quad C_c \quad C_{R1} \quad C_{R2} \quad T_{R1} \quad T_{R2} \quad T_{R3} \quad T_{R4} \quad T_{R5} \quad C_{sc} \quad C_{sc} \tag{4.36}$$

$$M \quad C_c \quad x_c \quad _R \quad \frac{_c\, x_c \quad _R}{2} \quad C_{R1} \quad x_c \quad \frac{R}{2} \quad C_{R2} \quad x_c \quad _R \quad \frac{_R x_c \quad _R}{2} \quad T_{R1}$$
$$\frac{2y}{3} \quad T_{R2} \quad \frac{H \quad _R \quad x_c \quad y}{3} \quad y \quad T_{R3} \quad \frac{h \quad _R \quad x_c \quad y}{2} \quad y \quad T_{R4} \quad \frac{R}{3} \quad H \quad _R \quad x_c$$
$$T_{R5} \quad \frac{R}{2} \quad H \quad _R \quad x_c \quad C_{sc} \; H \quad x_c \quad _R \quad d \quad C_{sc} \quad _R \quad x_c \quad d$$
$$\tag{4.37}$$

The previous formulations allow to determine the ultimate bending moment and consequently the acting shear load in the beam (V_b) and the column (V_c). The results obtained for the analyzed specimens are presented in Chapter 6.

4.2 Shear model

This section presents the proposed shear model, which aims to estimate the shear strength of exterior RC BCJs strengthened with UHPFRC jacket. The model assumes that joint failure is due to the attainment of the peak compressive stress in the joint core, taking into account the confinement effect produced by the UHPFRC jacket on the joint core through the confined concrete strength (f_{cc}), as shown in Figure 4.5. By considering a strut and tie resisting mechanism for the joint, the principal direction of the compression stresses is along the concrete strut, which develops inside the joint core inclined by an angle $_h$ with respect to the horizontal plane (Figure 4.5.a). Thus, the compressive strain in the confined concrete at the peak stress ($_{c2,c}$) is attained along this direction.

To calculate the strength f_{cc} according to the requirements of the Italian Building Code (NTC, 2018) and Eurocode 2 EN 1992-1-1 (Eurocode 2, 2004) an iterative process was developed, shown in the flowchart of Figure 4.6. Since the UHPFRC jacket is in contact with the joint vertical surfaces, to determine the effective mean lateral (horizontal) confining pressure produced by the jacket on the concrete core ($_2$), the horizontal component of the confined concrete strain ($_{th}$) is considered.

The iterative process starts by assuming an initial value of $_{c2,c}$, which can be made equal to the unconfined ultimate compressive strain of normal concrete at peak stress $_{c2}$ ($_{c2}$ = 2.0‰ for NTC (2018), Eurocode 2 (2004)). The transverse strain of the confined concrete strut in the presence of the UHPFRC jacket ($_t$), is determined by using Poisson's ratio. For concrete under compression at peak stress, the adopted value of the Poisson's ratio, $_0$ was 0.5, as suggested by Samani and Attard (2014). This value was obtained considering that the axial compressive strain at the instant of zero volumetric strain is approximately equal to the axial compressive strain at which the concrete reaches its peak compressive axial stress.

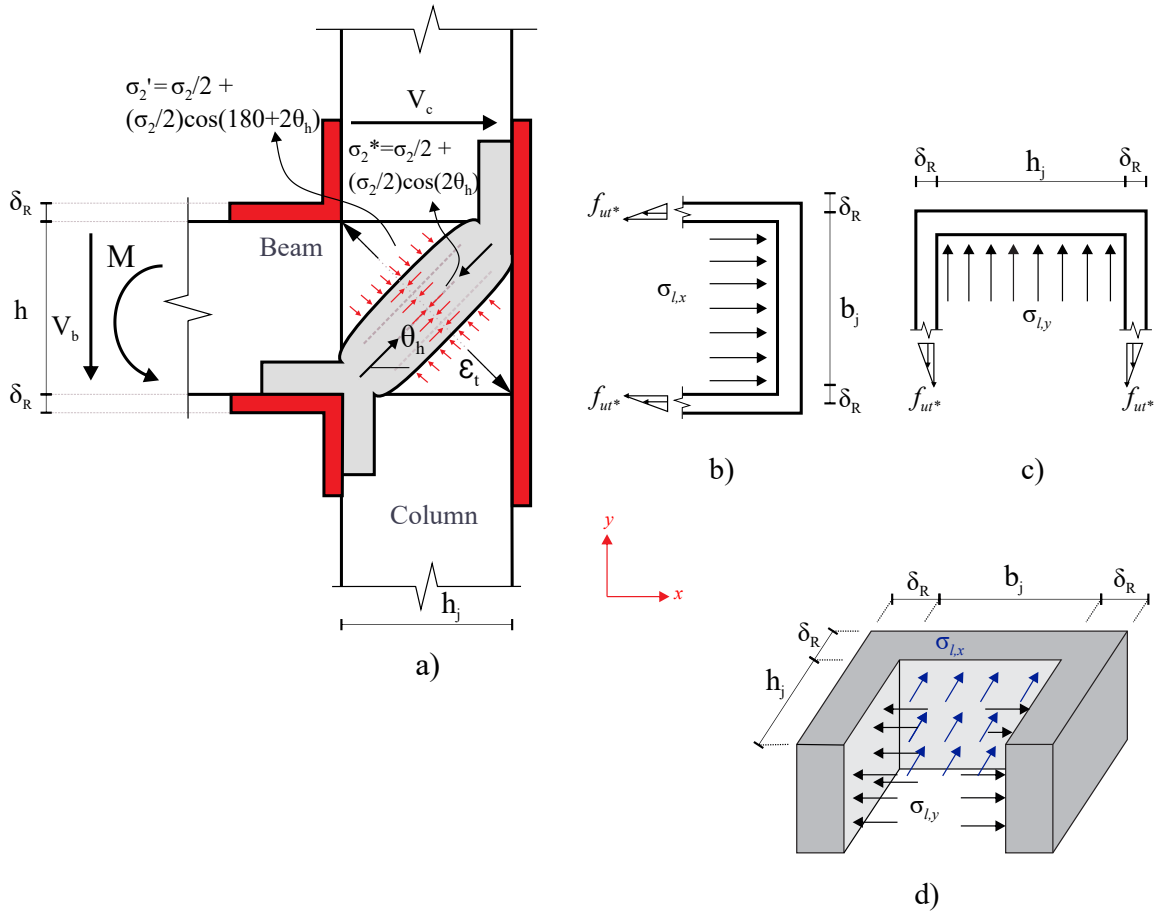

Figure 4.5 – Confining pressure exerted by UHPFRC jacket on exterior RC beam-column joint: a) Front view, b) X-direction, c) Y-direction, and d) 3D-view of confinement produced by the UHPFRC jacket.
Font: Adapted from Palomo et al. (2024)

By assuming a perfect bond at the interface between the joint core and the external jacket, the horizontal strain in the jacket is equal to the normal strain of the confined concrete strut in the horizontal plane ($_{th}$). Consequently, the tensile stress in the UHPFRC jacket at the interface with the joint core is obtained from the tensile curve of UHPFRC with the strain value $_{th}$.

Since the value of tensile stress on the external surface is unknown and the real distribution of tensile stresses across the UHPFRC jacket is also unknown, to account for the fact that tensile stress decreases across the jacket thickness, it is assumed that tensile stress linearly decreases from the inner to the outer surface of the jacket, becoming null on the outer surface. Hence, a triangular distribution of tensile stresses within the jacket thickness was adopted. The value of tensile stress in the jacket at the interface with the joint core (f_{ut}) can be calculated from the experimental tensile strain-stress curve.

Figure 4.5.a represents the scheme of confining caused by the lateral pressures exerted by the UHPFRC jacket on the joint core, which depends on pressures $_{l,x}$ and $_{l,y}$, acting in x and y horizontal directions, respectively, which can be determined by the following expressions:

$$_{l,x} \quad \frac{f_{ut} \quad R}{b_j} \tag{4.38}$$

$$_{l,y} \quad \frac{f_{ut} \quad R}{h_j} \tag{4.39}$$

where b_j and h_j are the width and the depth of the joint core, respectively.

Equations 4.38 and 4.39 are derived assuming that the confinement provided by the UHPFRC jacket and by the beam is uniform on each side of the joint core.

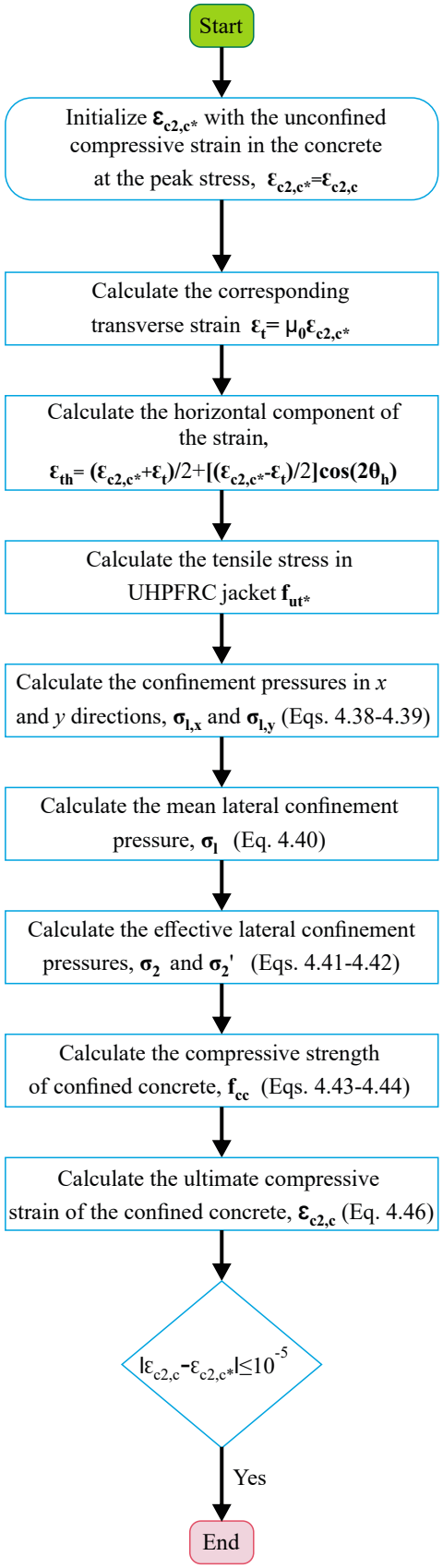

Figure 4.6 – Iterative process to determine the confined compressive strength of the diagonal strut in exterior BCJs retrofitted with UHPFRC jackets.
Note: f_{ut} is the tensile stress corresponding to the strain $_{th}$, which is obtained from the tensile curve of UHPFRC.
Font: Adapted from Palomo et al. (2024)

According to NTC (2018) and Eurocode 2 (2004), the mean lateral confinement pressure, $_l$, can be calculated as the geometrical mean between the two above lateral stresses, following:

$$l \quad \overline{l,x \;\; l,y} \tag{4.40}$$

The effective mean lateral confining pressure is calculated by

$$2 \quad l; \qquad n \;\; s \tag{4.41}$$

where the coefficients $_n$ and $_s$ can be assumed equal to 1, being the UHPFRC jacket continuous and uniform in thickness on the lateral surfaces of the joint.

To calculate the confining pressure orthogonal to the direction of the concrete diagonal strut ($_2$) showed in Figure 4.5.a, the Mohr's circle was used:

$$2 \quad \frac{2}{2} \quad \frac{2}{2} cos \; 180 \quad 2 \; _h \tag{4.42}$$

The confined concrete strength can be calculated following the standards of NTC (2018) and Eurocode 2 (2004), expressed as:

$$f_{cc} \quad f_{ck} \quad 1.0 \quad \frac{5.0 \; _2}{f_{ck}} \qquad \text{for} \quad _2 \quad 0.05 f_{ck} \tag{4.43}$$

$$f_{cc} \quad f_{ck} \quad 1.125 \quad \frac{2.5 \; _2}{f_{ck}} \qquad \text{for} \quad _2 \quad 0.05 f_{ck} \tag{4.44}$$

where f_{ck} is the characteristic value of the compressive strength of concrete.

The Mohr's circle was also used to determine the compressive stress arising along the axis of the diagonal concrete strut ($_2$), due to the confining action of the jacket:

$$2 \quad \frac{2}{2} \quad \frac{2}{2} cos \; 2 \; _h \tag{4.45}$$

This stress is added to that induced by the lateral load, reducing the maximum stress bearable by the joint. To take account of this, the compressive strength of the strut is calculated by subtracting $_2$ to the compressive strength of the strut confined concrete f_{cc}, as observed in Equation 4.47 .

Finally, the compressive strain in the confined concrete strut at the peak stress ($_{c2,c}$) was determined by the following equation (NTC, 2018; Eurocode 2, 2004):

$$_{c2,c} \qquad _{c2} \quad \frac{f_{cc}}{f_{ck}} \tag{4.46}$$

The iterative procedure represented in Figure 4.6 ends when the absolute value of the difference between $_{c2,c}$ and $_{c2,c}$ is 10^{-5}.

Thus, the shear strength of the retrofitted joint (V_{jh}) was calculated as the sum of the joint core contribution (V_{jhc}) and the UHPFRC jacket. The parameter V_{jh} is obtained by the formulation of Pauletta et al. (2015), replacing the concrete strength f_c by the confined concrete strength f_{cc} (MPa) and the presence of stress $_2$

$$V_{jhc} \quad 0.71 \quad \frac{f_{cc} \quad _2 \; b_j a_c \cos \quad _h}{} \quad 0.79 A_{sjh} f_{yjh} \quad 0.52 \frac{A_{sjv} f_{yjv}}{tan \quad _h} \tag{4.47}$$

where

$$0.74 \quad \left(\frac{f_{cc}}{105}\right)^3 \quad 1.28 \quad \left(\frac{f_{cc}}{105}\right)^2 \quad 0.22 \quad \frac{f_{cc}}{105} \quad 0.87 \tag{4.48}$$

$$a_c \quad 0.25 \quad 0.85 \frac{N}{A_g f_{cc}} \quad h_c \tag{4.49}$$

$$\frac{2L_c L_b}{2L_c L_b \quad 2L_b \quad h_c \; j_{bd}} \quad 1 \quad \frac{4kl_h \quad \overline{f_{cc}}}{_b f_{bi}} \quad 1.0 \tag{4.50}$$

where is a non-dimensional interpolation function that accounts for concrete softening (PAULETTA et al., 2015), a_c is the depth of the compression zone in the column; A_{sjh} and f_{yjh} are the area and the yield strength of joint horizontal longitudinal reinforcement, respectively; A_{sjv} and f_{yjv} correspond to the area and the yield strength of joint vertical reinforcement, respectively. A_g is the gross area of the column section; h_c is the height of the column cross-section; j_{bd} is the internal moment arm of the beam cross-section, which can be calculated as suggested in Pauletta et al. (2015); l_h is the horizontal projection of the diagonal concrete strut, which is equal to $h_c \quad a_c$; k is a experimental factor equals to 0.25; $_b$ is the mean diameter of beam longitudinal bars in tension; and f_{bi} is he stress of beam bars in tension, given in MPa.

In this condition, the acting shear force V_{jh}^A is distributed between the joint core and the UHPFRC jacket in relation to their shear stiffness, expressed as:

$$V_{jhc}^A \quad V_{jh}^A \quad \frac{G_c A_c}{G_c A_c \quad G_R A_R} \tag{4.51}$$

$$V_{jhR}^A \quad V_{jh}^A \quad \frac{G_R A_R}{G_c A_c \quad G_R A_R} \tag{4.52}$$

where G_c and G_R are the shear modulus of the normal concrete and UHPFRC material, respectively; A_c is the joint core horizontal area and A_R is the UHPFRC jacket horizontal area at mid-height in the joint, as shown in Figure 4.7.b. The shear moduli of normal concrete, G_c, and UHPFRC, G_R, can be calculated by means of Equation (4.53), using the values of the Young's modulus and Poisson's ratio of the materials. Concrete and UHPFRC Young's modulus, E_c and E_R, respectively, can be obtained from experimental results. Alternatively, E_c can be calculated according to the recommendations of ACI 318 (2019) (Equation (4.54)), while E_R through the formula developed by Guo et al. (2018), expressed by Equation (4.55) (f_c and f_{cR} in MPa).

Regarding the Poisson's ratios ( ), the value of 0.2 is adopted both for normal concrete and UHPFRC, as recommended by ACI 318 (2019), NF P 18-710 (2016) and in the studies of Russell et al. (2013).

$$G \quad \frac{E}{2\ 1} \tag{4.53}$$

$$E_c \quad 4700 \quad \overline{f_c} \tag{4.54}$$

$$E_R \quad 3837 \quad \overline{f_{cR}} \tag{4.55}$$

The contribution of the UHPFRC jacket to shear strength is determined in function of the contribution provided by the concrete strut, assuming that both the jacket and the concrete core are in the elastic field. Assuming that the jacket percentage contribution to joint shear strength is that considered in Equations (4.51) and (4.52), the joint shear strength is calculated as follows:

$$V_{jh} \quad V_{jhc} \quad V_{jhc}\frac{G_R A_R}{G_c A_c} \tag{4.56}$$

In order to avoid joint shear failure, the joint shear strength must be greater than the shear force on the joint acting at beam flexural failure. In this condition, the acting shear force (V_{jh}^A) can be calculated from the equilibrium of the top half part of the joint, as shown in Figure 4.7.a. Considering that a negative bending moment acts on the beam cross-section, V_{jh}^A is given by the sum of the tensile force on the retrofit material (T_R), the tensile force on the top reinforcement (T_s), and the shear force on the column (V_c), following:

$$V_{jh}^A \quad T_R \quad T_s \quad V_c \tag{4.57}$$

where

$$T_s \quad A_s f_y \tag{4.58}$$

$$V_c \quad \frac{L_b V_b}{L_c} \tag{4.59}$$

where A_s is the area of the top steel reinforcement; $_s$ is the tensile strain in the top steel reinforcement (at the ultimate bending moment); V_b is the shear acting on the beam; L_b and L_c are the lengths of the beam and the column, respectively (Figure 4.8).

To provide adequate ductility to the joint, the UHPFRC layer should be designed to promote the beam's flexural failure. For this, the value of shear force acting in the beam (V_b) shown in Equation (4.59) can be determined considering the attaining of the ultimate bending moment in the beam, calculated as described in Section 4.1.

The total shear force acting in the joint can also be expressed as the sum of two contributions: the joint shear force acting in the joint core (V^A_{jhc}), and the joint shear force acting in the UHPFRC jacket (V^A_{jhR}), expressed as:

$$V^A_{jh} \quad V^A_{jhc} \quad V^A_{jhR} \tag{4.60}$$

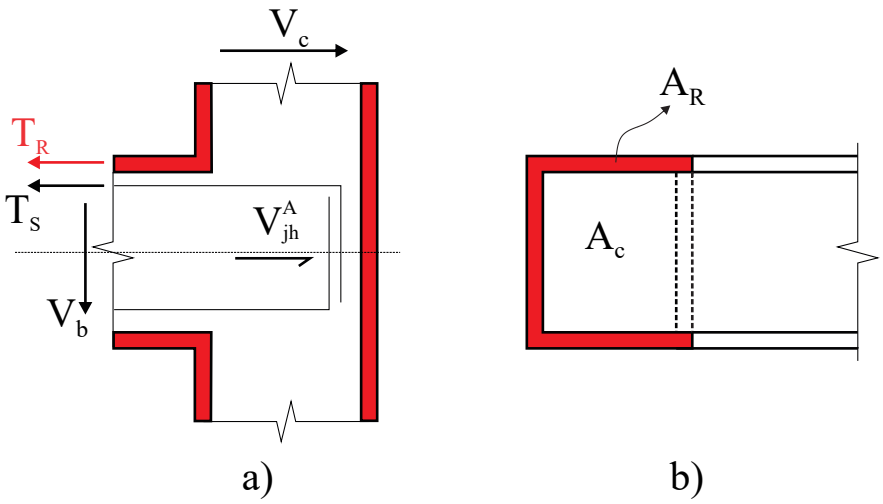

Figure 4.7 – Scheme of the retrofitted joint: a) Vertical section, b) Horizontal section at mid-height.
Font: Obtained from Palomo et al. (2024)

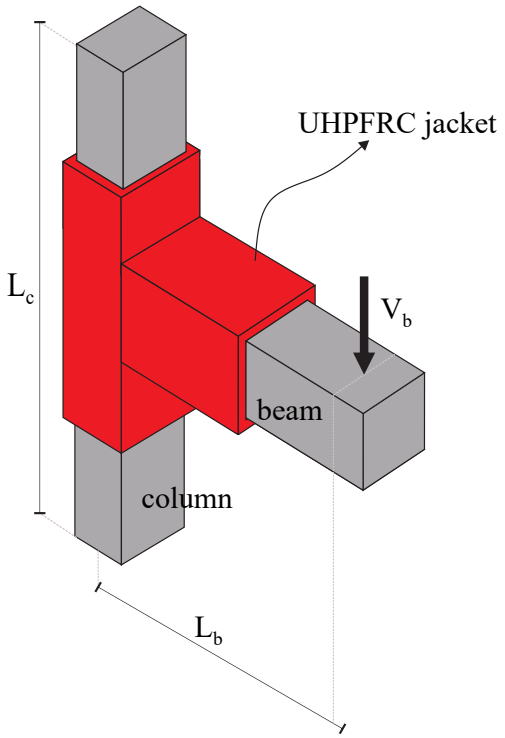

Figure 4.8 – Scheme of exterior beam-column joint retrofitted with UHPFRC.
Font: Obtained from Palomo et al. (2024)

Thus, the previously mentioned methodology allows the calculation of the shear strength

of exterior BCJs strengthened with UHPFRC layer. The results obtained are presented in Chapter 6.

5 Numerical analyses

Two-dimensional (2D) and three-dimensional (3D) numerical analyses were developed in this work. The structure's geometry and its preprocessing were performed in the GID program Version (version 10.0.9), which easily adapts to numerical simulations and transfer information to the numerical program. The processing and post-processing of the models were carried out using the ATENA program (version 5.9.1) through Finite Element Method (FEM) (ČERVENKA et al., 2021).

The numerical models developed in this thesis correspond to one reinforced concrete frame subjected to incremental monotonic horizontal load and four exterior BCJs subjected to cyclic loading. Below are described the constitutive models used in the simulations, available in the ATENA program.

5.1 Constitutive Models of materials

5.1.1 Constitutive model for concrete

The constitutive models represents the nonlinear mechanical behavior of concrete elements through stress-strain relationships as a function of applied loads. The nonlinear behavior for a biaxial stress state is described by effective stress σ_c^{ef} and equivalent uniaxial strain ε^{eq}. The latter is considered to avoid the Poisson effect on the plane stress state. Figure 5.1 presents the stress-strain relationship of concrete subjected to uniaxial load, where for the linear regime, strain and stress is a fuction of Young's modulus, expressed in Equation 5.1.

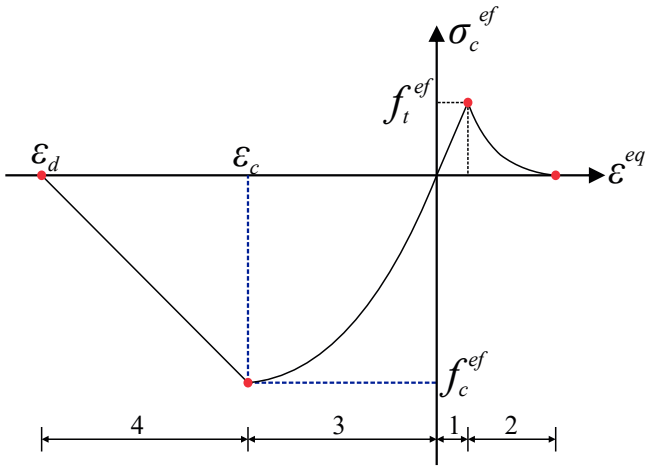

Figure 5.1 – Uniaxial stress-strain curve of concrete.
Font: Adapted from Červenka et al. (2021)

5.1.1.1 Tensile pre-cracking

The tensile behavior of concrete with the absence of cracks can be considered an elastic linear material, as shown in Equation 5.1.

$$\begin{matrix} ef \\ c \end{matrix} \quad E_c \; ^{eq} \qquad 0 \leqslant \; _c \leqslant f_t^{ef} \tag{5.1}$$

where f_t^{ef} corresponds to the effective tensile stress, which can be determined from the curve of Kupfer for concrete under biaxial loading (KUPFER et al., 1969), as observed in Figure 5.4.

5.1.1.2 Tensile post-cracking

After reaching its maximum tensile strength, indicated by cracks, concrete is introduced in the post-cracking regime. In this phase, the tensile strength begins to decrease as the strain increases, which is governed by the crack opening w . In uniaxial state, the first cracks appear when the tensile stress reaches its maximum strength f_t. However, for a multi-axial stress study, the first cracks occur when it reaches the effective tensile strength f_t^{ef} , (ČERVENKA et al., 2021).

The ATENA program presents two types of formulations to consider crack opening. The first one consists of a fictitious crack model related to the fracture energy G_f . In this formulation, it is possible to simulate crack propagation in concrete through the crack band theory proposed by Bazant and Oh (1983). The second formulation corresponds to a stress-strain relationship given at a point in the material, used in unusual cases to describe crack propagation in concrete, such as in the case of Steel Fiber Reinforced Concrete (SFRC). In this work, the fictitious crack model was used, described by the softening function developed by Hordijk (1991), as shown in Figure 5.2.

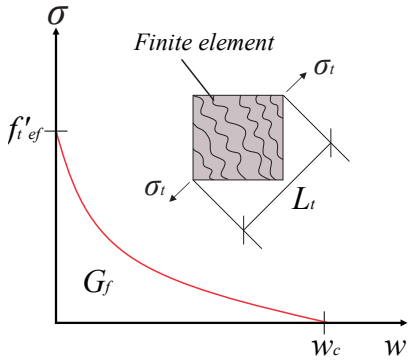

Figure 5.2 – Softening curve developed by Hordijk (1991).
Font: Adapted from Červenka et al. (2021)

Figure 5.2 shows the energy dissipated until the material reaches the crack opening w_c , where the area under the curve corresponds to the fracture energy G_f . The curve is described by Equation 5.2, where cracks are numerically represented in the finite element mesh through the smeared crack formulation developed by Bazant and Oh (1983).

$$\overline{f_t} \qquad 1 \qquad c_1 \frac{w}{w_c} \quad ^3 \qquad exp \qquad c_2 \frac{w}{w_c} \qquad \frac{w}{w_c} \; 1 \qquad c_1^3 \; exp \qquad c_2 \tag{5.2}$$

where is the tensile stress normal to the crack band, f_t^{ef} is the effective tensile strength, w is the crack opening, and w_c is the crack opening when the energy has been completely dissipated. The variables c_1 and c_2 are coefficients obtained from experimental tests, with values of 3 and 6.93, respectively. The parameter w_c can be determined by Equation 5.3, showing that the energy dissipated in cracking does not depend on the finite element mesh used in the models, (ČERVENKA et al., 2021).

$$w_c \quad 5.14\frac{G_f}{f_t} \tag{5.3}$$

Different methods have been developed to determine the crack band width, initially proposed by Bazant and Oh (1983). In the ATENA program, the crack band width in tension L_t is calculated as the projection of the finite element in a direction parallel to the crack. This calculation method is recommended for analyses with linear elements, as shown in Figure 5.2, (ČERVENKA et al., 2021).

5.1.1.3 Compression before reaching the maximum stress (pre-peak)

Just before the concrete reaches its maximum compressive strength f_c^{ef} (ascending branch), the stress-strain relationship of the material can be represented by Equation 5.4, a formulation proposed by *fib* Model Code (2013), as shown in Figure 5.3.

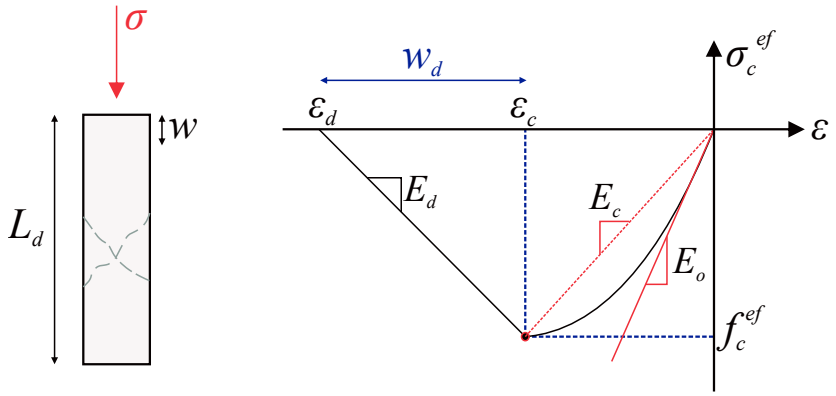

Figure 5.3 – Stress-strain curve of concrete in compression.
Font: Adapted from Červenka et al. (2021)

$$\begin{matrix} ef \\ c \end{matrix} \quad f_c^{ef} \frac{kx \quad x^2}{1 \quad x \; k \quad 2} \qquad x \qquad c \qquad k \quad E_o \; E_c \tag{5.4}$$

where $\begin{matrix} ef \\ c \end{matrix}$ is the effective "stress" of concrete, f_c^{ef} is the effective "stress" of concrete in compression, x is normalized strain, $_c$ is the strain at peak stress f_c^{ef}, k is a shape parameter, E_o is the initial elastic modulus, and E_c is the secant elastic modulus at peak stress, Equation 5.5.

$$E_c \quad \frac{f_c^{ef}}{c} \tag{5.5}$$

5.1.1.4 Compression after reaching the maximum stress (post-peak)

After reaching the maximum strength of concrete, the post-peak behavior can be represented by a linear softening curve (descending branch), as shown in Figure 5.3. ATENA presents two models to represent softening in compression: one based on dissipated energy and the other based on local strain (ČERVENKA et al., 2021).

In this work, the analyses conducted were elaborated using the model based on dissipated energy, known as *Fictitious Compression Plane Model*. In this model, compression failure is located on a plane normal to the direction of the principal compression stress. In addition, displacements are independent of the structure size, as assumed in the experiments developed by Van Mier (1986).

Figure 5.3 shows that the softening curve is conditioned by a plastic displacement w_d (a recommended value of 0.5 mm for conventional concrete) (Van Mier, 1986). Furthermore, the slope of the softening branch in the stress-strain curve is composed of two specific points, the maximum peak stress and the plastic displacement w_d, reached when the compressive stress is zero. The displacement w_d can be calculated through Equation 5.6.

$$w_d \quad L_c \quad _d \quad _c \tag{5.6}$$

where w_d is the post-peak plastic displacement, L_c is the crack band width in compression, $_d$ is the strain limit when stress is zero, and $_c$ is the strain corresponding to the peak compressive stress.

5.1.1.5 Criteria of rupture under biaxial stress

(a) Compressive failure

When concrete material is in a biaxial state, the failure criteria will be conditioned by the failure envelope proposed by Kupfer et al. (1969), as shown in Figure 5.4.

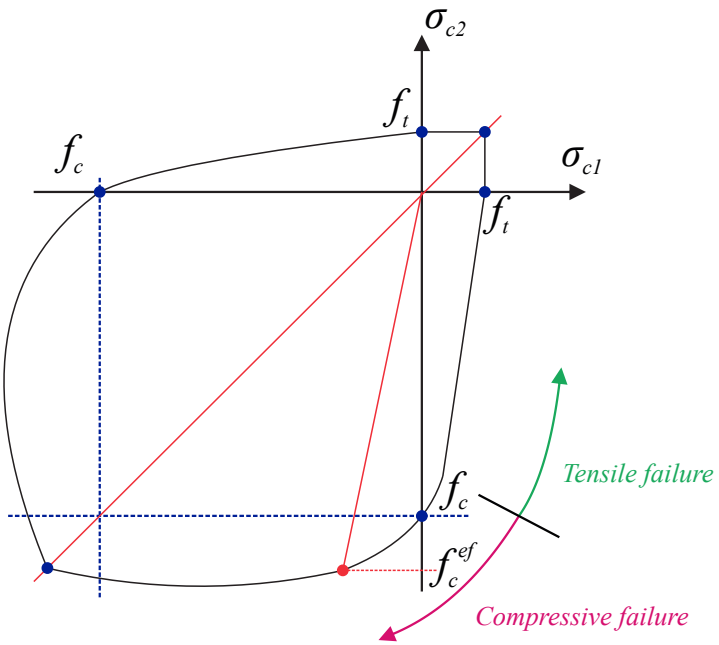

Figure 5.4 – Biaxial failure function for concrete.
Font: Adapted from Červenka et al. (2021)

In the compression-compression state, the effective compressive concrete strength is determined by Equation 5.7. Here, $_{c1}$ and $_{c2}$ correspond to the principal stresses of the concrete, and f_c is the cylindrical uniaxial strength of the material.

$$f_c^{ef} \quad \frac{1 \quad 3.65a}{1 \quad a^{\ 2}} f_c \qquad a \quad \frac{_{c1}}{_{c2}} \tag{5.7}$$

For the compression-compression state, the rupture function has a linear behavior represented by Equation 5.8.

$$f_c^{ef} \quad f_c r_{ec} \qquad r_{ec} \quad 1 \quad 5.3278 \frac{_{c1}}{f_c} \tag{5.8}$$

where r_{ec} is a reduction factor applied in the concrete compression stress, which can vary between 0.9 and 1.0.

(b) Tensile rupture

In a state of tension-tension, the effective stress of concrete in tension will be equal to the uniaxial tensile stress f_t, as presented by Equation 5.9. On the other hand, for the biaxial state of tension-compression, the tensile strength will be reduced and may vary linearly or hyperbolically (as shown in Figure 5.5), using the reduction factor r_{et}, Equation 5.10. The factor r_{et} can be determined by Equations 5.11 and 5.12, corresponding to a linear or hyperbolic function, respectively. The parameters K and A will define the hyperbolic function, see Table 5.1.

$$f_t^{ef} \quad f_t \tag{5.9}$$

$$f_t^{ef} \quad f_t r_{et} \tag{5.10}$$

$$r_{et} \quad 1 \quad 0.95\frac{c2}{f_c} \tag{5.11}$$

$$r_{et} \quad \frac{A \quad A \quad 1 \; B}{AB} \qquad B \quad Kx \qquad x \quad \frac{c2}{f_c} \tag{5.12}$$

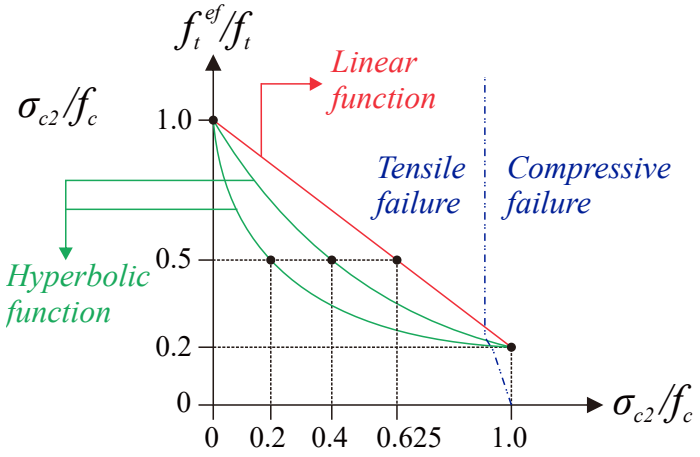

Figure 5.5 – Tension-compression failure function for concrete.
Font: Adapted from Červenka et al. (2021)

Two predefined shapes of the hyperbola are given by the position of an intermediate point r, x. Constants K and A define the shape of the hyperbola. The values of the constants for the two positions of the intermediate point are given in the following table:

Table 5.1 – Parameters that define the hyperbola shape of failure function in tension-compression failure function for concrete

Type	**Point**		**Parameters**	
	r	**x**	**A**	**K**
a	0.5	0.4	0.75	1.125
b	0.5	0.2	1.0625	6.0208

Font: Adapted from Červenka et al. (2021)

5.1.1.6 Failure criteria in triaxial state

One of the constitutive models available in ATENA is the Fracture-Plastic Constitutive Model. This model considers the material's fracture under tension and plasticity under compression (ČERVENKA; PAPANIKOLAOU, 2008).

The concrete fracture model under tension is based on the smeared crack model formulation and the crack band model proposed by Bazant and Oh (1984). It uses the Rankine failure

criterion and a cohesive model represented by the exponential softening curve of Hordijk (1991), which can be used with either a fixed or rotated crack model. Regarding concrete behavior under compression, it uses a hardening/softening plastic model based on the Menétrey-William rupture surface (MENETREY; WILLIAM, 1995).

Many material models are available in the ATENA software. All the material models described are based on the fracture-plastic constitutive model. In this thesis, the concrete was simulated with the *CC3DNonLinCementitious2* model. The model assumes that strains are composed of an elastic component ($^{e}_{ij}$), plastic component ($^{p}_{ij}$), and fracture component ($^{f}_{ij}$), as shown in Equation 5.13 (DEBORST, 1986).

$$ij \quad \overset{e}{ij} \quad \overset{p}{ij} \quad \overset{f}{ij} \tag{5.13}$$

$$f_{co} \quad f_c \quad f_{co} \quad 1 \quad \frac{c \quad \overset{p}{c}}{c}^{2} \tag{5.14}$$

where f_c is the compressive stress, f_{co} is the compressive stress at the onset of material plasticity, and $^{p}_{c}$ corresponds to the plastic strain. Červenka et al. (2021) states that the plastic strain $^{p}_{c}$ can be determined by subtracting the elastic strain $_{el}$ (f_c E) from the total strain, Equation 5.15. The strain $_1$ corresponds to the compression strain when the compressive strength f_c is reached.

$$\overset{p}{c} \quad 1 \quad \frac{f_c}{E} \tag{5.15}$$

The behavior of concrete after reaching its maximum compressive strength exhibits softening, as observed in Figure 5.6.b., where the area under the curve represents the energy dissipated during compression failure. The parameter w_d is the plastic displacement, which governs the brittleness of the material after its rupture. Similarly to uniaxial concrete, a value of 0.5 mm for w_d is considered appropriate for normal strength concretes (Van Mier, 1986).

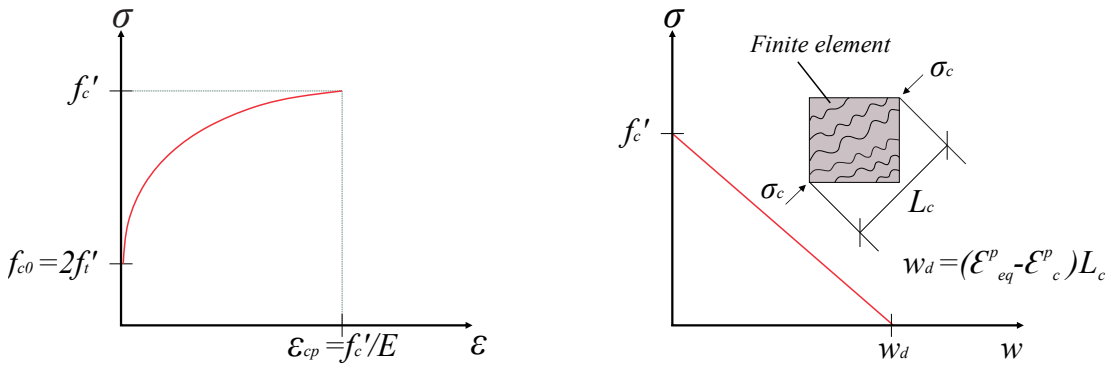

Figure 5.6 – Compressive models of concrete a) Hardening b) Softening based on experimental tests of Van Mier and Vonk (1991).
Font: Adapted from Červenka et al. (2021)

The parameter f_{co} corresponds to the stress at the onset of nonlinear behavior, and L_c is the crack band width in compression. As above mentioned, the concrete plasticity model is based on the Menétrey-William failure criterion (MENETREY; WILLIAM, 1995), which depends on the level and state of the applied stress, described by Equation 5.16.

$$f^p \quad , \quad , \qquad \overline{1,5}\frac{}{k \quad f_c}^{\,2} \qquad m \quad \frac{}{\overline{6}k \quad f_c} r \quad ,e \quad \frac{}{\overline{3}k \quad f_c} \qquad c \qquad 0 \tag{5.16}$$

$$m \quad 3\frac{k \quad f_c \;^2 \qquad {}_t f_t \;^2}{k \quad f_c \quad {}_t f_t} \frac{e}{e \quad 1} \tag{5.17}$$

$$r \quad ,e \quad \frac{4\ 1 \quad e^2\ cos \quad ^2 \quad 2e \quad 1\ ^2}{2\ 1 \quad e^2\ cos \qquad 2e \quad 1 \quad \overline{4\ 1 \quad e^2\ cos \quad ^2 \quad 5e^2 \quad 4e}} \tag{5.18}$$

where:

- $\quad , \quad , \quad$: coordinates of Haigh-Westergaard to describe the rupture surface (Figure 5.7)
- f_c: compressive concrete strength
- f_t: tensile concrete strength
- m: cohesion parameter of material (Equation 5.17)
- ${}_t$: parameter that helps to intersect the surface failure of Rankine and Menetrey-William in the fracture and plastification state.
- e: describes the roundness of the rupture surface $\quad 0.5 \quad and \quad 1.0$
- $\quad$: coefficient that denotes the softening/hardening law.
- $r \quad ,e$: elliptic function (Equation 5.18)

When eccentricity e is equal to 0.5, deviatory cross-section of failure surface is in the shape of an equilateral triangle, while for a value equal to 1.0, curves forming the deviator cross section take on a shape of circle, as shown in Figure 5.7.c.

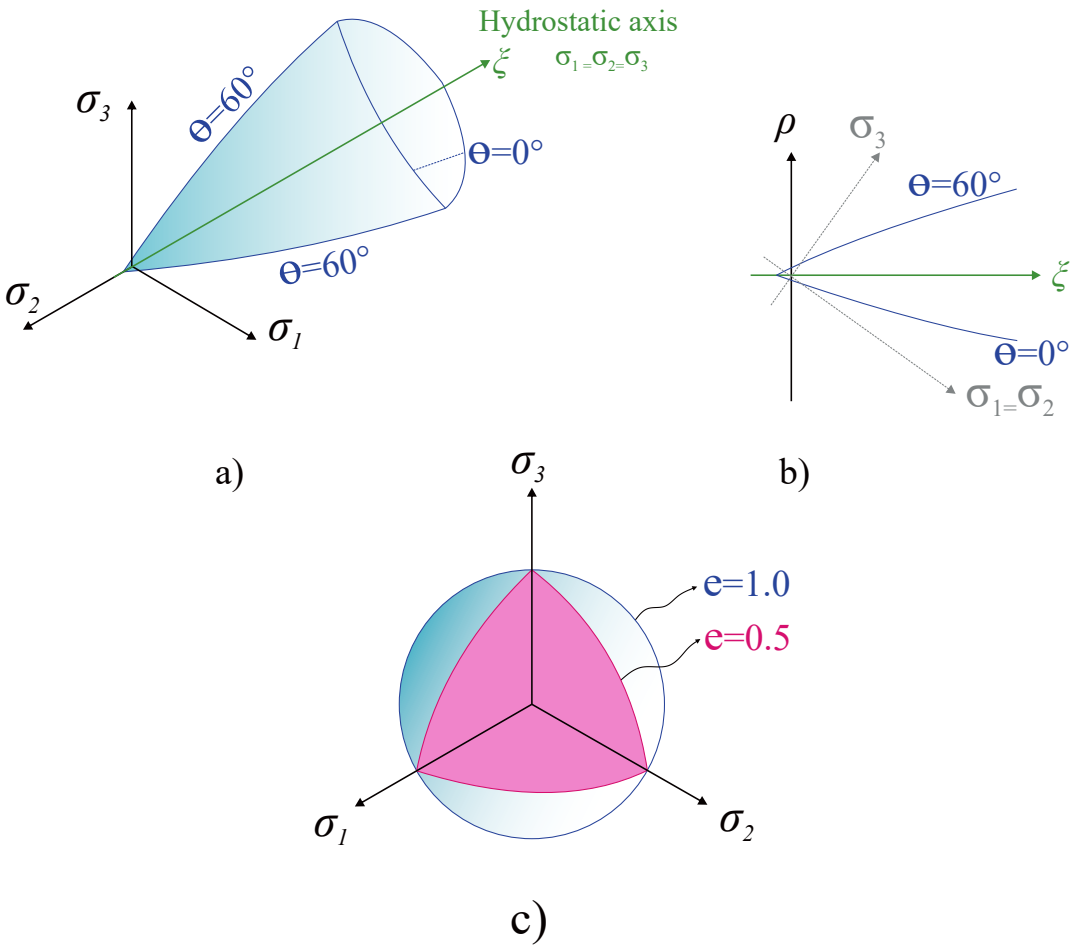

Figure 5.7 – Failure surface of Menétrey-William: a) 3D view of stresses b) Axial view of stresses c) Deviatoric sections.
Font: Adapted from Červenka et al. (2021) and Menetrey and WillIam (1995)

5.1.2 Constitutive model for reinforcement

The reinforcement constitutive model is based on the multilinear stress-strain relationship, where the steel behavior is defined by several points on the stress-strain curve, as shown in Figure 5.8. This same function can be adopted for bars subjected to compressive stress. The points in the curve define whether only reinforcement yield stress is considered or if there is also hardening behavior. The bars behavior is defined by three parameters: Young's modulus E_s , the yield stress f_y , and the coordinates of the rupture point, which will define the hardening modulus of the material E_{sh} . In the ATENA program, this model is named *Reinforcement*.

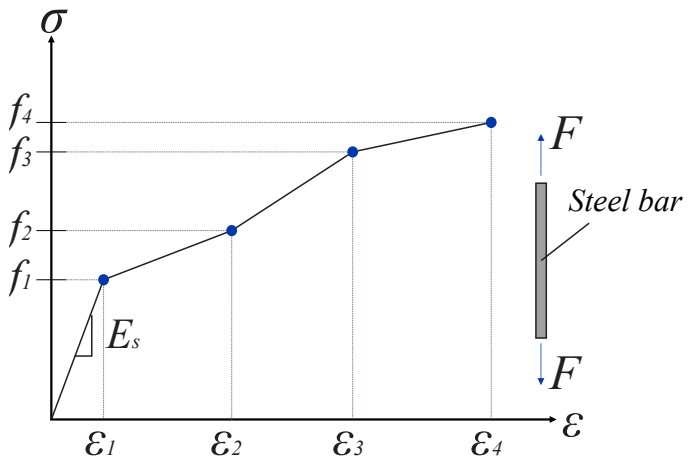

Figure 5.8 – Stress-strain relationship of steel.
Font: Adapted from Červenka et al. (2021)

5.1.2.1 Constitutive model of cyclic reinforcement

In addition to considering the multilinear stress-strain curve in the reinforcement, the models under seismic conditions used the constitutive model based on the work by Menegotto (1973). In the ATENA program, this model is named *CCCyclingReinforcement*, which represents a uniaxial material model that can be used for reinforcement within concrete, and its formulation is suitable for cyclic loading. The normalized material model is described by Equation 5.19 (GIUFFRÈ, 1970).

$$b \qquad \frac{1 \quad b}{1 \qquad R \ \frac{1}{R}} \tag{5.19}$$

where and correspond to the normalized strain and stress, determined by Equations 5.20 e 5.21, respectively.

$$\frac{r}{0 \quad r} \tag{5.20}$$

$$\frac{r}{0 \quad r} \tag{5.21}$$

Equation 5.19 determines the stress for a given strain from the transition curve of the asymptotic line with slope E_0 to another asymptotic line with slope $E_1 \quad bE_0$, corresponding to the lines and in Figure 5.9, respectively. The parameters $_0$ and $_0$ are the stress and strain at the point where the two asymptotes of the considered region intersect (point A in Figure 5.9), similarly, $_r$ and $_r$ correspond to the stress and strain at the point where the last reversal of strain with the same sign of stress occurred (point B in Figure 5.9). The parameter b represents the strain hardening ratio, expressed as the ratio between the slopes E_0 and E_1. The shape of the transition curve represents the Bauschinger effect. This relationship is also a function of the curvature parameter R, which depends on the difference in strain between the current asymptotic

intersection point and the previous load reversal point. The values of $_0$, $_0$, and $_r$, $_0$ are updated after each strain reversal, as shown in Figure 5.9.

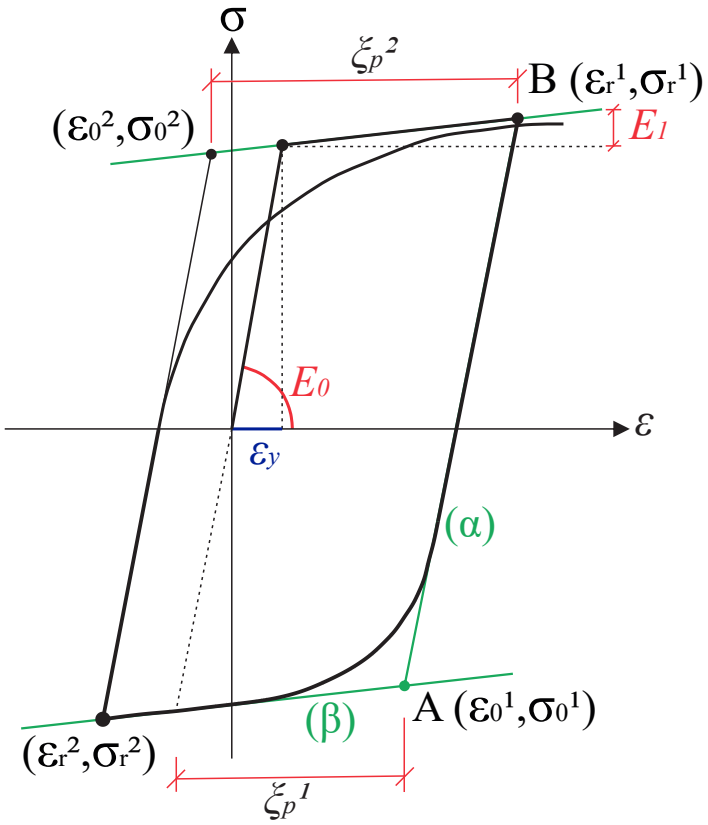

Figure 5.9 – Stress-strain relationship of Menegotto-Pinto.
Font: Adapted from Menegotto (1973)

The value of R can be determined by Equation 5.22, where ^n_p is the plastic precursor of the current semicircle defined by Equation 5.23. Additionally, the factor R_0 represents the value of R during the first loading, and c_1 and c_2 are experimentally determined parameters. The hardening relationships are functions of three parameters: yield stress $_y$, Young's modulus E_0 , and hardening rate b . In ATENA, the *CCCyclingReinforcement* model is a function of the parameters R, c_1, and c_2.

$$R \quad R_0 \quad \frac{a_1 \ ^n_p}{a_2 \quad ^n_p} \tag{5.22}$$

$$^n_p \quad ^n_r \quad ^n_y \tag{5.23}$$

5.1.3 Bond-slip constitutive model

An adequate formulation of the bond-slip relationship between reinforcement and concrete under monotonic and/or cyclic loads is of great importance to obtain results closer to reality. The bond-slip relationship defines the bond stress ($_b$), which is a function of slip (s) between the steel and surrounding concrete. In the ATENA program, the bond-slip relationships proposed by *fib* Model Code (1990), *fib* Model Code (2013), and Bigaj (1999) are available.

The bond-slip relationship described in *fib* Model Code (1990) is determined by Equations 5.28 - 5.31, as shown in Figure 5.10.

$$_{max}\ s\ \ s_1 \qquad for \quad 0 \leqslant s \leqslant s_1 \tag{5.24}$$

$$_{max} \quad for \quad s_1 \leqslant s \leqslant s_2 \tag{5.25}$$

$$_{max} \qquad _{max} \quad _{f} \quad \frac{s \quad s_2}{s_3 \quad s_2} \qquad for \quad s_2 \leqslant s \leqslant s_3 \tag{5.26}$$

$$_{f} \quad for \quad s_3 \quad s \tag{5.27}$$

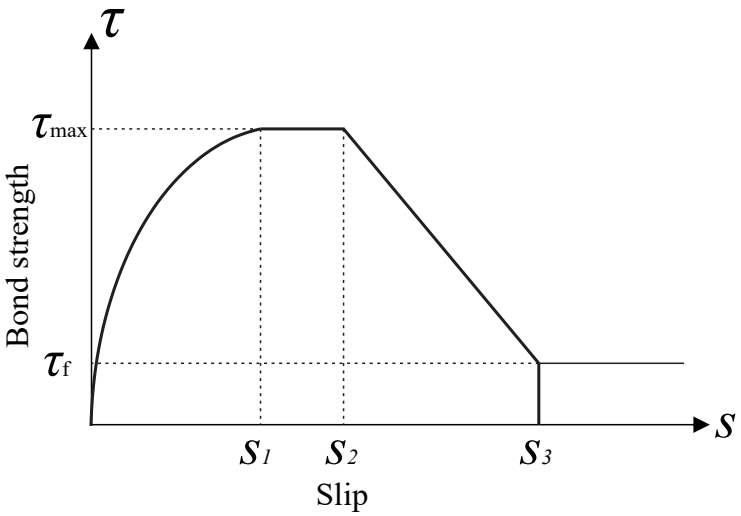

Figure 5.10 – Bond-slip diagram (monotonic load).
Font: Adapted from *fib* Model Code (1990)

The bond-slip relationship is obtained from the cubic compressive concrete strength f_{cu}, the diameter, and type of reinforcement, as well as the confinement conditions and concrete quality, according to the parameters presented in Tables 5.2 and 5.3.

Table 5.2 – Parameters used in the bond stress-slip relationship for ribbed bars

	2	**3**	**4**	**5**
Value	**Unconfined concrete**		**Confined concrete**	
	Bond condition		**Bond condition**	
	Good	**ther cases**	**Good**	**Other cases**
s_1	0.6 mm	0.6 mm	1.0 mm	
s_2	0.6 mm	0.6 mm	3.0 mm	
s_3	1.0 mm	2.5 mm	Clear rib spacing	
	0.4		0.4	
$_{max}$	2.0 $\overline{f_{cu}}$	1.0 $\overline{f_{cu}}$	2.5 $\overline{f_{cu}}$	1.25 $\overline{f_{cy}}$
$_{f}$	0.15 $_{max}$		0.40 $_{max}$	

Font: Adapted from *fib* Model Code (1990)

Table 5.3 – Parameters used in the bond stress-slip relationship for smooth bars

	2	3	4	5
Valor	**Cold drawn wire**		**Hot rolled bars**	
	Bond condition		**Bond condition**	
	Good	**Other cases**	**Good**	**Other cases**
$s_1 = s_2 = s_3$	0.01 mm		0.1 mm	
	0.5		0.5	
$_{max} =$ $_f$	0.1 $\sqrt{f_{cu}}$	0.05 $\sqrt{f_{cu}}$	0.3 $\sqrt{f_{cu}}$	0.15 $\sqrt{f_{cu}}$

Font: Adapted from *fib* Model Code (1990)

The bond-slip relationship described in *fib* Model Code (2013) is determined by Equations 5.28 - 5.31, as shown in Figure 5.11.

$$_b \quad _{bmax} \; s \; s_1 \qquad for \quad 0 \leqslant s \leqslant s_1 \tag{5.28}$$

$$_b \quad _{bmax} \quad for \quad s_1 \leqslant s \leqslant s_2 \tag{5.29}$$

$$_b \quad _{bmax} \quad _{bmax} \quad _{bf} \quad \frac{s \quad s_2}{s_3 \quad s_2} \qquad for \quad s_2 \leqslant s \leqslant s_3 \tag{5.30}$$

$$_b \quad _{bf} \quad for \quad s_3 \quad s \tag{5.31}$$

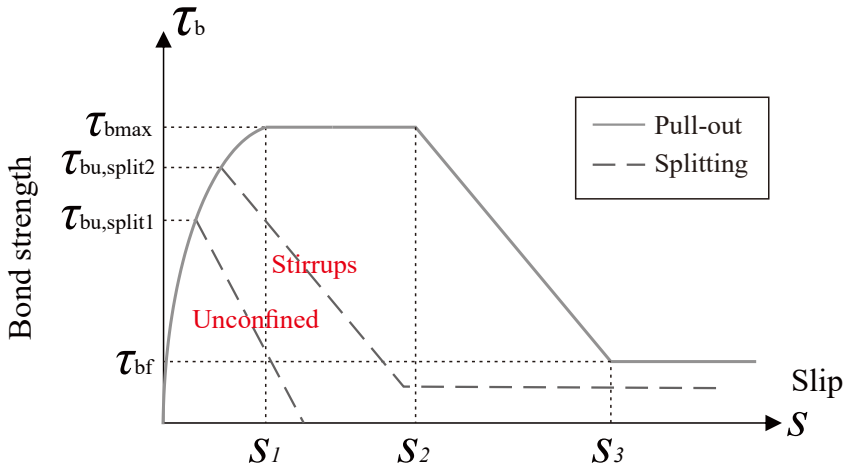

Figure 5.11 – Bond-slip diagram (monotonic load).
Font: Adapted from *fib* Model Code (2013)

The bond stresses between the concrete and reinforcement bar for pull-out and splitting failure are calculated as a function of relative displacement, mean cylinder compressive concrete strength f_{cm}, and bond and confinement conditions, as presented in Table 5.4.

Table 5.4 – Parameters used in the bond stress-slip relationship for ribbed bars

	1	2	3	4	5	6
	Pull-out (OP)		**Splitting (SP)**			
	$_{s,y}$		$_{s,y}$			
	Good boundary conditions	**All other boundary conditions**	**Good boundary conditions**		**All other boundary conditions**	
			Unconfined	**Stirrups**	**Unconfined**	**Stirrups**
$_{bmax}$	2.5 $\overline{f_{cm}}$	1.25 $\overline{f_{cm}}$	2.5 $\overline{f_{cm}}$	2.5 $\overline{f_{cm}}$	1.25 $\overline{f_{cm}}$	1.25 $\overline{f_{cm}}$
$_{bu,split}$	–	–	7.0 $\frac{f_{cm}}{25}^{0.25}$	8.0 $\frac{f_{cm}}{25}^{0.25}$	5.0 $\frac{f_{cm}}{25}^{0.25}$	5.5 $\frac{f_{cm}}{25}^{0.25}$
s_1	1.0 mm	1.8 mm	s $_{bu,split}$	s $_{bu,split}$	s $_{bu,split}$	s $_{bu,split}$
s_2	2.0 mm	3.6 mm	s_1	s_1	s_1	s_1
s_3	c_{clear}	c_{clear}	$1.2s_1$	$0.5c_{clear}$	$1.2s_1$	$0.5c_{clear}$
	0.4	0.4	0.4	0.4	0.4	0.4
$_{bf}$	0.4 $_{max}$	0.4 $_{max}$	0	0.4 $_{bu,split}$	0	0.4 $_{bu,split}$

Font: Adapted from *fib* Model Code (2013)

where c_{clear} is the distance between ribs *fib* Model Code (2013), and $_{bu,split}$ is the peak value of bond strength function in a splitting failure mode.

The equations of columns 1-2 are applied for well-confined concrete (concrete cover 5 $_b$, clear spacing between bars 10 10 $_b$).

On another hand, the equations of columns 3-6 are applied assuming a uniform bond stress over the length l_b $_b$ 5, with a diameter bar $_b$ 25mm, c_{max} c_{min} 2.0, c_{min} $_b$, and K_{tr} 0.02 or K_{tr} 0.0 for cases where the bars are confined by stirrups or where no stirrups are provided, respectively. For other conditions, the value of $_{bu,split}$ is determined by the Equation 5.32:

$$_{bu,split} \quad _2 6.5 \quad \frac{f_{cm}}{25}^{0.25} \quad \frac{25}{_b}^{0.2} \quad \frac{c_{min}}{_b}^{0.33} \quad \frac{c_{max}}{c_{min}}^{0.1} \quad K_m K_{tr} \tag{5.32}$$

where l_b is the bond length, $_2$ is 1.0 and 0.7 for good and all other bond conditions, K_m express the efficiency of the confinement derived from transverse reinforcement (this value is 12 when bars are confined within bend bars circulating them in an angle of at least 90 , and 0 when no confining reinforcement is provided), $_b$ is the diameter of the anchored bar, c_{min} is the lowest value between c_s 2, c_x, and c_y, and c_{max} is the highest value between c_s 2, and c_x (Figure 5.12).

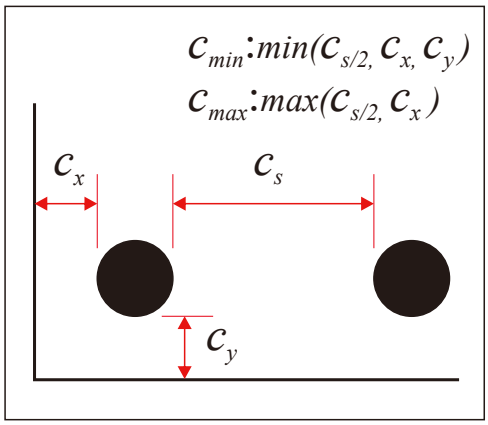

Figure 5.12 – Details of covers and bar spacing.
Font: Adapted from *fib* Model Code (2013)

In numerical simulations with cyclic loading, the adhesion model between reinforcement and concrete was simulated with the *Memory Bond material* model, which can more efficiently capture the response during loading and unloading cycles. This model can be used in conjunction with the bond-slip relationship proposed for *fib* Model Code (1990), *fib* Model Code (2013), or Bigaj (1999). The model's response differs from these previous relationships only when the bond stress changes direction.

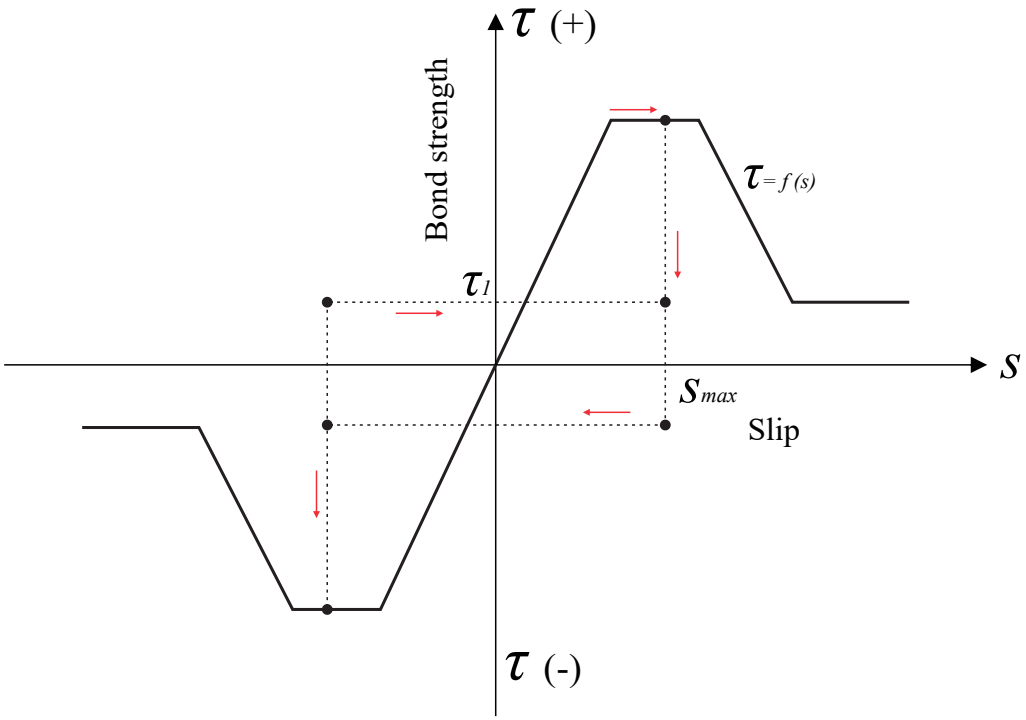

Figure 5.13 – Bond stress-slip relationship with *Memory Bond* model.
Font: Adapted from Červenka et al. (2021)

In the model described, the allowed values are restricted to $_{res} \leqslant _1 \leqslant _{max}$, where $_{res}$ is the residual bond stress (the last value of the bond-slip function), $_{max}$ corresponds to the maximum bond stress (the highest value of the bond-slip function), and $f\ s$ represents

the bond stress function. The simulation of the reinforcement was discretely performed, where the elements were embedded within the concrete elements. Finally, perfect bond between the concrete and transverse reinforcement (stirrups) was considered in all analyses.

5.2 Numerical simulation of frame - Vecchio and Emara (1992)

To study the structural response of beam-column connections in a frame structure, the first numerical simulation developed in this work corresponds to a reinforced concrete frame subjected to a monotonic horizontal displacement, representing the initial cyclic behavior stage. The analysis was carried out using a two-dimensional (2D) model in the ATENA program and compared to the experimental results obtained by Vecchio and Emara (1992). The numerical results not only allow the observation of vulnerable regions but also enable the identification of cracking pattern of the structure.

5.2.1 Finite element - Vecchio and Emara (1992)

The choice of the finite element is an important step to obtaining closer results to the experimental ones. The concrete was simulated with the material model *CC3DNonlinCementitious2*, using a linear quadrilateral finite element called *CCIsQuad<xxxx>*. The finite element is composed of four nodes with three degrees of freedom, integrated through the Gauss integration technique with four integration points, as illustrated in Figure 5.14.a. Regarding the longitudinal and transverse reinforcement of the frame, the material model *CCReinforcement* and a linear truss-type finite element named *CCIsoTruss<xx>* were used. The truss element is composed of two nodes and one integration point, as shown in Figure 5.14.b. The steel plates were simulated using the material model *CC3DElastIsotropic* and the finite element *CCIsQuad<xxxx>*.

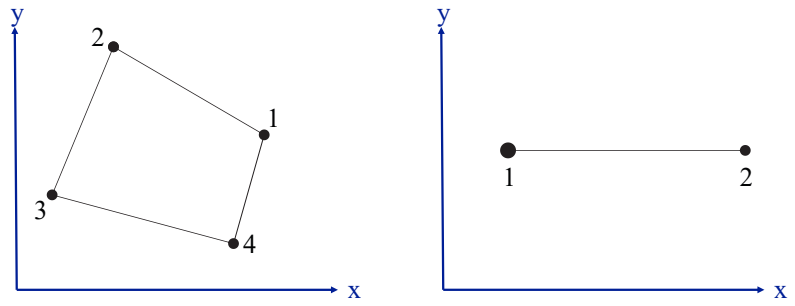

a) b)

Figure 5.14 – a) Concrete: finite element CCIQuad<xxxx> b) Reinforcement: finite element CCIsoTruss<xx>.
Font: Adapted from Červenka et al. (2021)

To assess the sensitivity of finite element size and obtain an adequate size to represent the experimentally obtained results, three models were developed, corresponding to coarse, medium, and fine meshes. The coarse mesh model used elements with a size of 100x100 mm^2, corresponding to 824 quadrilateral elements, 994 linear elements, and 2186 nodes. The medium mesh model was simulated with elements of size 80x80 mm^2, composed of 1262 quadrilateral

elements, 994 linear elements, and 2670 nodes. The fine mesh had finite elements of size 50x50 mm^2, generating 3272 quadrilateral elements, 994 linear elements, and 4845 nodes. The final model with the fine mesh was adopted, which presented better the results, as seen in Chapter 7. The mesh of the structure's reinforcement is presented in Figure 5.15.

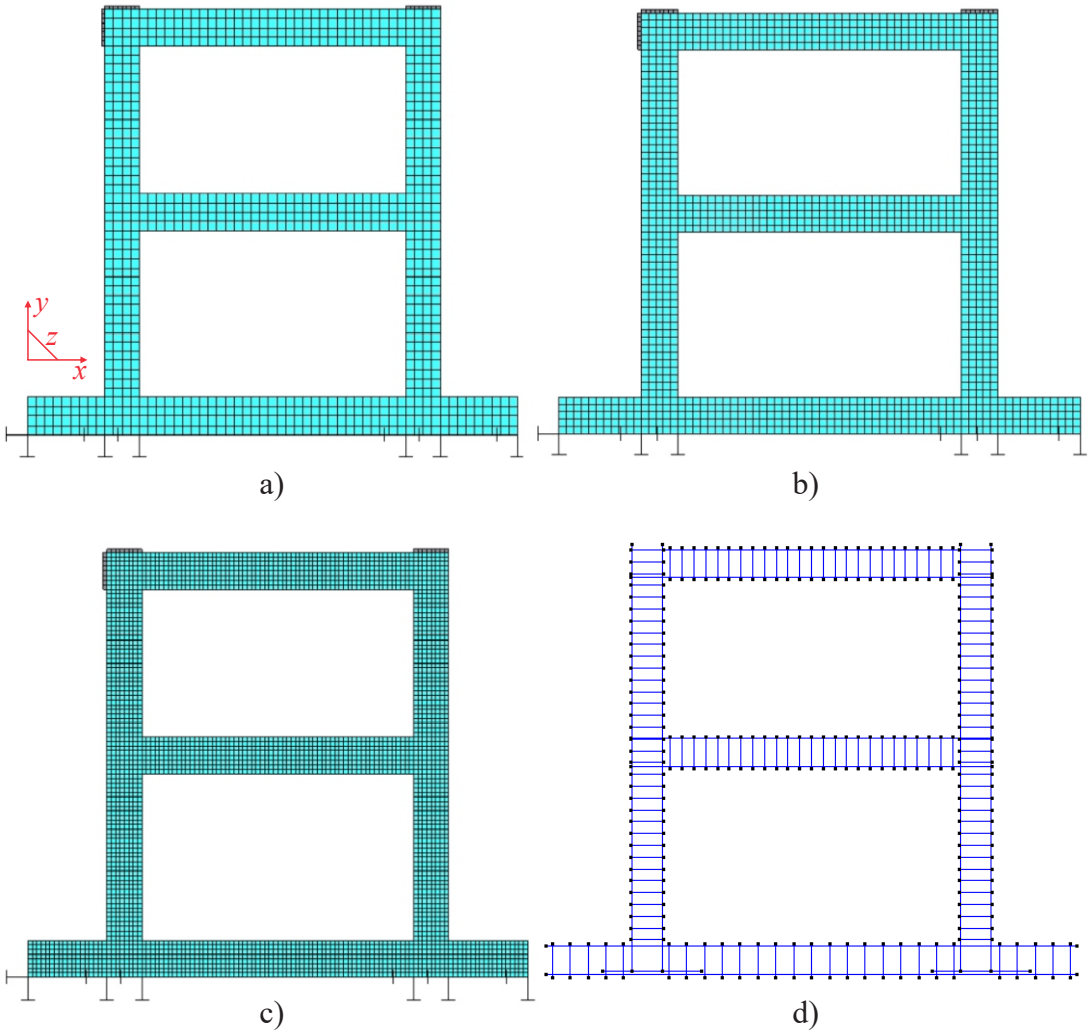

Figure 5.15 – Finite element discretization a) Coarse mesh b) Medium mesh c) Fine mesh, and d) Reinforcement.

5.2.2 Boundary conditions - Vecchio and Emara (1992)

Two load intervals were used to simulate the experimental test's boundary conditions. In the first interval, two vertical loads of 700 kN were applied to the upper face of columns C_3 and C_4, respectively, through a force-controlled static analysis. For this, two steel plates of thickness 40 mm were used. In the second interval, incremental lateral displacement was applied to the metal plate connected to column C_3, through a quasi-static displacement-controlled analysis. The applied horizontal displacement was 140 mm, with a step of 0.8 mm for each iteration. The steel plates were fixed to the concrete surface using the master-slave condition, as shown in Figure 5.16.

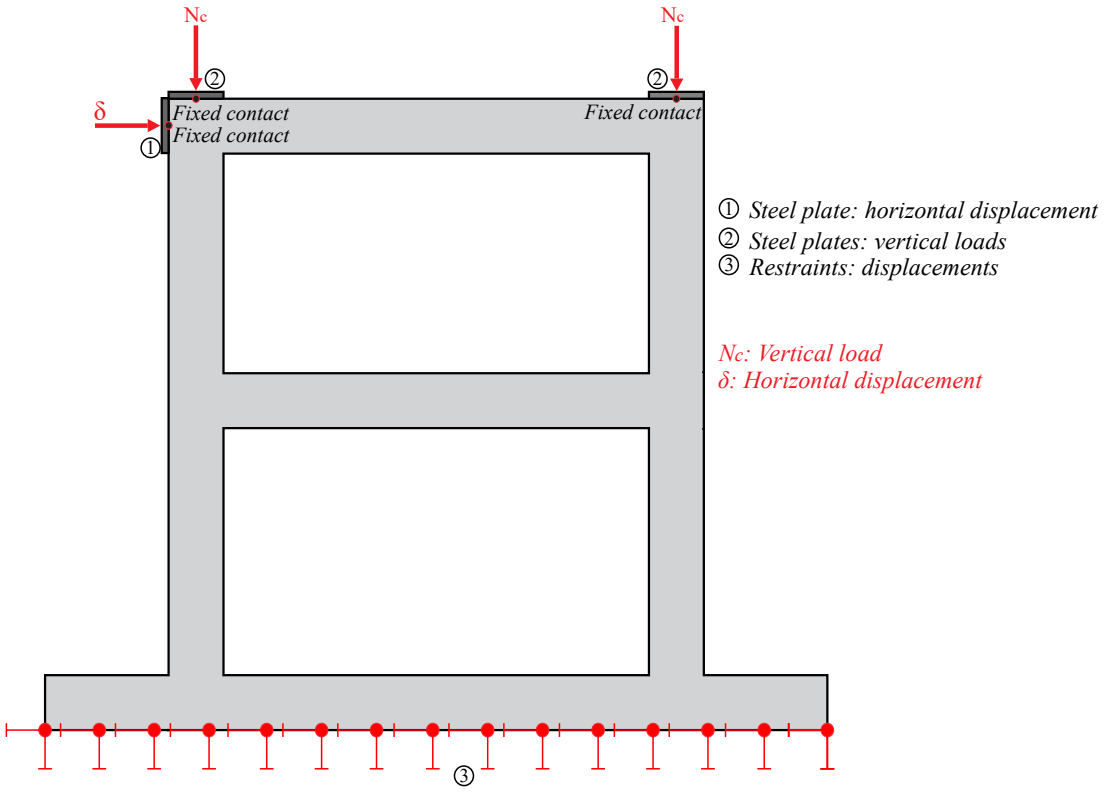

Figure 5.16 – Scheme of boundary conditions used in the numerical model.

The iterative procedures of the numerical simulation were carried out following the Modified Newton-Raphson method. In addition, several convergence parameters were considered during the nonlinear analysis. In the ATENA program, four convergence criteria are available:

- Relative error in displacement: 0.01
- Relative error in residual forces: 0.01
- Absolute error in residual forces. 0.01
- Relative error in energy: 0.0001

The error value corresponds to the maximum value that each criterion can reach in the numerical simulation. Therefore, if any of the criteria have their smallest error greater than 10% (0.01), the numerical analysis will be terminated.

5.2.3 Materials' properties - Vecchio and Emara (1992)

To achieve a good approximation of the real behavior in the numerical simulation of the frame, various parameters were utilized, such as: the shear factor S_f , which defines the relationship between normal stiffness and shear stiffness; the plastic strain at peak compressive stress $_{cp}$; and the bond-slip relationship between concrete and reinforcement, following the relationship presented in Figure 5.11 (*FIB* MODEL CODE, 2013). The values of the shear strength reduction factor and the onset stress of nonlinear behavior f_{co} correspond to those

recommended by the ATENA program, (ČERVENKA et al., 2021). Tables 5.5 and 5.6 present the parameters used in the numerical simulation.

Table 5.5 – Concrete properties used in the numerical model of RC frame

Parameter	**Concrete**	**Reference**
Young's modulus E_c	23674 MPa	Vecchio and Emara (1992)
Fracture energy G_f	90 N/m	*fib* Model Code (2013)
Shear factor S_f	50	–
Compressive strength f_c	30 MPa	Vecchio and Emara (1992)
Tensile strength f_t	1.81 MPa	Vecchio and Emara (1992)
Poisson coefficient	0.20	–
Strength at the onset of nonlinear behavior f_{co}	3.6 MPa	–
Plastic strain at compressive strength $^{p}_{c}$	0.00185	Van Mier (1986)
Reduction factor of compression r_c	0.8	Dyngeland (1989)
Crack orientation	Fixed	Cervenka (1985)

Table 5.6 – Steel properties used in the numerical model of RC frame

Parameter	**Long. Reinf.**	**Transv. Reinf.**	**Reference**
Young's modulus E_s	192500 MPa	200000 MPa	Vecchio and Emara (1992)
Hardening modulus E_{sh}	3100 MPa	3100 MPa	Vecchio and Emara (1992)
Yield strength f_y	418 MPa	596 MPa	Vecchio and Emara (1992)
Ultimate strength f_u	454 MPa	640 MPa	Vecchio and Emara (1992)
Yield strain $_s$	0.00217	0.00298	Vecchio and Emara (1992)
Hardening strain $_{sh}$	0.0095	0.0095	Vecchio and Emara (1992)
Ultimate strain $_u$	0.0669	0.0695	Vecchio and Emara (1992)

The condition of good bond and confined by stirrups was adopted in the model. The bond strength curves for beam and columns used in the model are presented in Figure 5.17 , with values of maximum bond strength by splitting failure ($_{b,split}$) of 9.52 MPa and 9.16 MPa for the beams and columns, respectively.

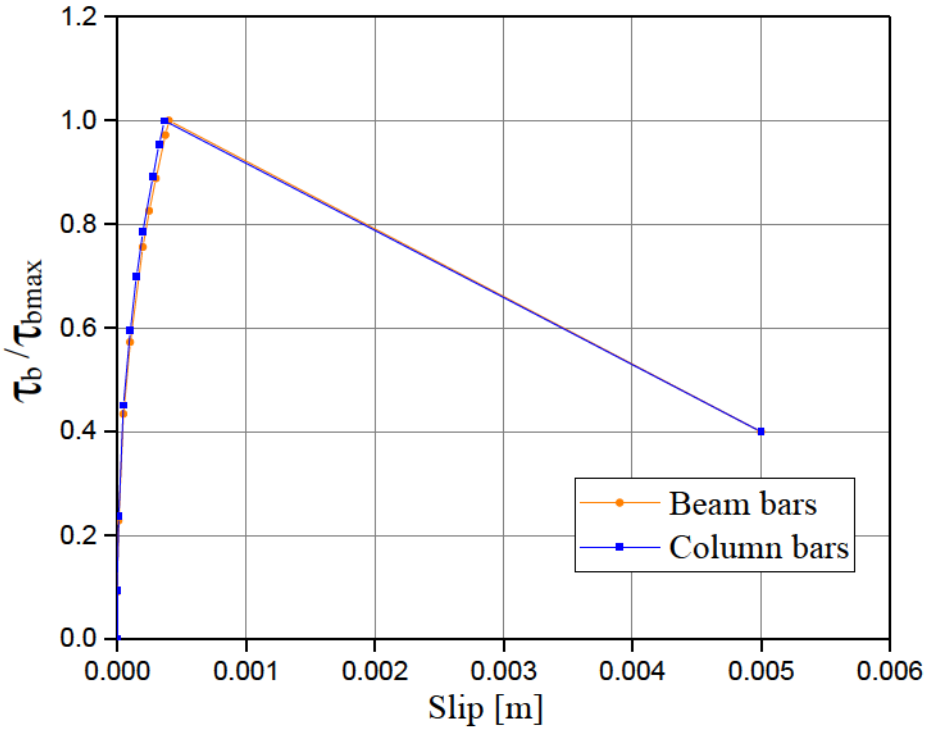

Figure 5.17 – Bond-slip relationship used in the frame.

5.3 Numerical simulation of BCJ A2 - Kusuhara and Shiohara (2008)

The second numerical simulation refers to an exterior beam-column joint subjected to cyclic loading, denoted as A2. The experimental results were obtained from the work conducted by Kusuhara and Shiohara (2008). For this, a three-dimensional (3D) numerical model was developed.

5.3.1 Finite element - Kusuhara and Shiohara (2008)

In the numerical analysis, concrete elements were simulated using the material model *CC3DNonlinCementitious2*, employing the linear hexahedral finite element *CCIsoBrick<xxxxxxxx>* (where each *x* represents a node). It is composed of eight nodes and integrated using Gauss integration with eight integration points, as observed in Figure 5.18.a. Due structure's cyclic behavior, the longitudinal and transverse reinforcement of the beam and column were simulated with the material model *CCCyclingReinforcement* and linear finite elements type truss (*CCIsoTruss2*), which is composed of two nodes and one integration point (Figure 5.18.b). The steel plates were simulated using the material model *CC3DElastIsotropic* and the finite element *CCIsoBrick<xxxxxxxx>*.

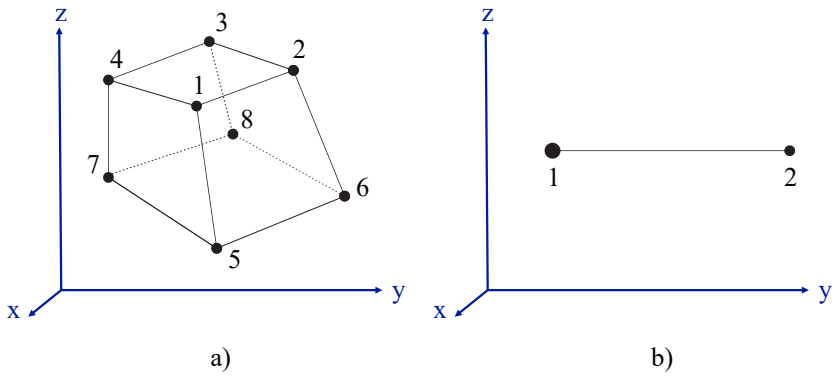

Figure 5.18 – a) Concrete: finite element CCIBrick<xxxxxxxx> b) Reinforcement: finite element CCIsoTruss<xx>.
Font: Adapted from Červenka et al. (2021)

The simulation of the beam and the column had a mesh size of 30x50 mm^2. However, a finer discretization was performed in the joint core, and elements of 30x30 mm^2 were used. Thus, the numerical simulation had 8500 hexahedral elements, 580 linear elements, and 11381 nodes, as shown in Figure 5.19.

5.3.2 Boundary conditions - Kusuhara and Shiohara (2008)

The boundary conditions of the BCJ A2 were modeled to represent the same experimental setup used by Kusuhara and Shiohara (2008). In this model, the column base had a hinge support (displacement restriction in all directions but free rotation). There was a roller support restricting vertical displacement at one end of a section of the beam, while the other section of the beam was left free. To avoid stress concentration and premature cracking in the connection, 40 mm thick steel plates were added both at the point of load application and the support reaction, which were fixed to the concrete through the master-slave condition, as observed in Figure 5.19.a.

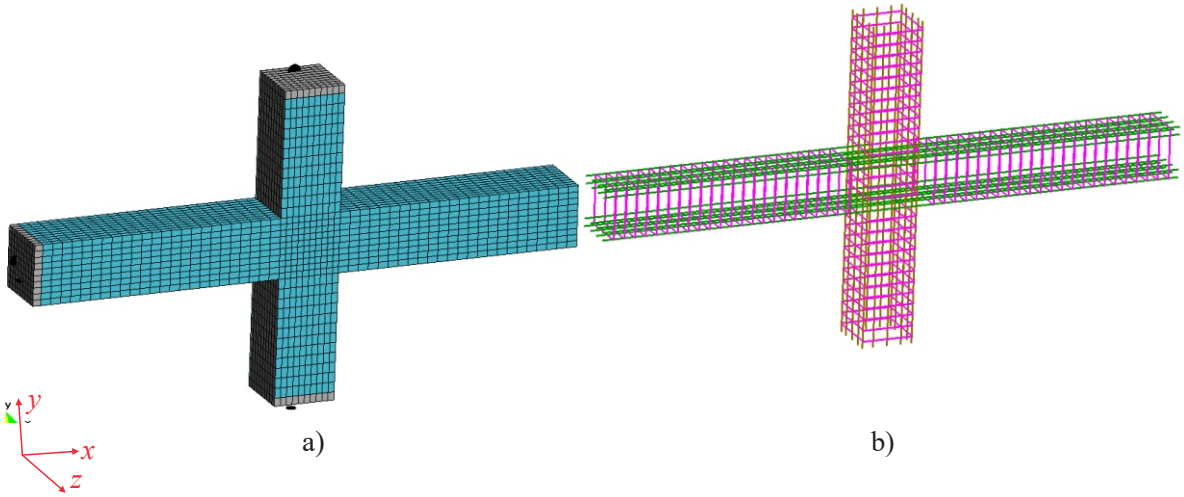

Figure 5.19 – Finite element discretization a) Concrete b) Reinforcement.

To represent cyclic behavior, 20 load intervals were used. In the first interval, a vertical

load of 216 kN was applied at the top of the column, which was constant throughout of simulation. In the other 19 intervals, horizontal cyclic displacements were applied at the top of the column, following the displacement history shown in Figure 3.5. Steps of 0.1 mm and 1.0 mm were applied to the first and last displacement cycles, respectively.

The modified Newton-Raphson method was used in the analysis, limited to 200 iterations in each load interval. The convergence criteria used in the model were:

- Relative error in displacement: 0.01
- Relative error in residual forces: 0.01
- Absolute error in residual forces: 0.01
- Relative error in energy: 0.0001

5.3.3 Materials' properties - Kusuhara and Shiohara (2008)

Tables 5.7 and 5.8 present the parameters used in the numerical simulation.

Table 5.7 – Concrete properties used in the numerical model of BCJ A2

Parameter	Value	Reference
Young's modulus E_c	30400 MPa	Kusuhara and Shiohara (2008)
Fracture energy G_f	133 N/m	*fib* Model Code (2013)
Shear factor S_f	20	Červenka et al. (2021)
Compressive strength f_c	28.30 MPa	Kusuhara and Shiohara (2008)
Tensile strength f_t	2.23 MPa	Kusuhara and Shiohara (2008)
Poisson coefficient	0.20	–
Strength at the onset of nonlinear behavior f_{co}	4.6 MPa	–
Plastic strain at compressive strength $^{p}_{c}$	0.00134	Van Mier (1986)
Reduction factor of compression r_c	0.8	Dyngeland (1989)
Eccentricity	0.52	Červenka et al. (2021)
Plastic flow	0.5	–
Unloading factor	0.2	–
Crack orientation	Fixed	Cervenka (1985)

Table 5.8 – Steel properties used in the numerical model of BCJ A2

Parameter	Long. Reinf.	Transv. Reinf.	Reference
Young's modulus E_s	176000 MPa	151000 MPa	Kusuhara and Shiohara (2008)
Yield strength f_y	456/357 MPa	326 MPa	Kusuhara and Shiohara (2008)
Ultimate strength f_u	582/485 MPa	488 MPa	Kusuhara and Shiohara (2008)
Yield strain $_s$	0.0026/0.002	0.0022	Kusuhara and Shiohara (2008)
Hardening strain $_{sh}$	0.029/0.027	0.0022	Kusuhara and Shiohara (2008)
Ultimate strain $_u$	0.16	0.045	Kusuhara and Shiohara (2008)
Menegotto-Pinto	R 20 C_1=0.925 C_2=0.15		Menegotto (1973)
Bond-slip model	*Memory bond*	*Perfect*	Červenka et al. (2021)

The interaction between the longitudinal bars was simulated through the bond-slip relationship of Memory Bond material of *fib* Model Code (2013) (Figure 5.11), adopting the condition of good bond and confined by stirrups. Figure 5.20 presents the bond-slip laws used for longitudinal beam and column bars. The values of $\tau_{b,split}$ for beam and column bars was 11.61 MPa 12.26 MPa, respectively.

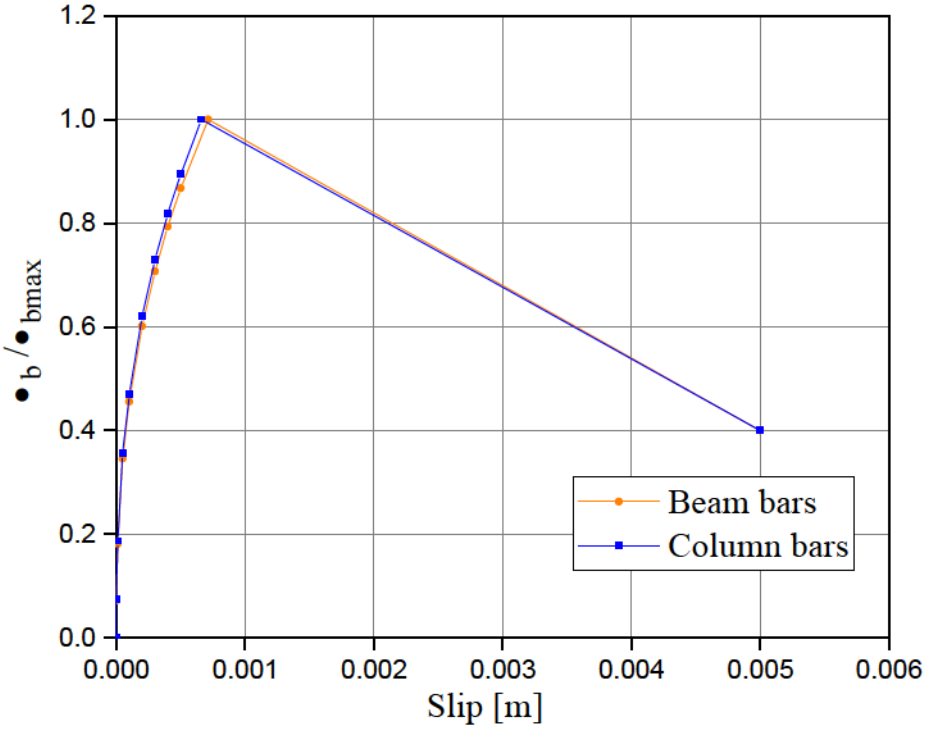

Figure 5.20 – Bond-slip relationship used in the BCJ A2.

5.4 Numerical simulation BCJ A1 - Tsonos (2005)

This simulation corresponds to an exterior beam-column joint under cyclic loading conditions, denoted as A1. The beam-column joint was experimentally tested by Tsonos (2005) and compared with the numerical results developed in this study.

5.4.1 Finite element - Tsonos (2005)

The finite elements used to simulate the concrete material and the reinforcement of the beam-column connection are the same as those used in the A2 joint, corresponding to linear hexahedral finite element *CCIsoBrick<xxxxxxxx>* and *CCIsoTruss2*, respectively, as shown in Figure 5.18.

The mesh size used in the simulation was 25x25 mm^2, corresponding to 7552 hexahedral elements, 2170 linear elements, and 11768 nodes, as presented in Figure 5.21.

5.4.2 Boundary conditions - Tsonos (2005)

Regarding the support conditions of joint A1, at the base of the column hinge support was applied (displacement restriction in all directions but free rotation), at the top of the column roller support was applied (displacement restriction in the horizontal direction), and end-beam

was left free. The cyclic load was applied at the end of the beam through a metal plate rigidly connected to the concrete using the master-slave condition, as shown in Figure 5.21.

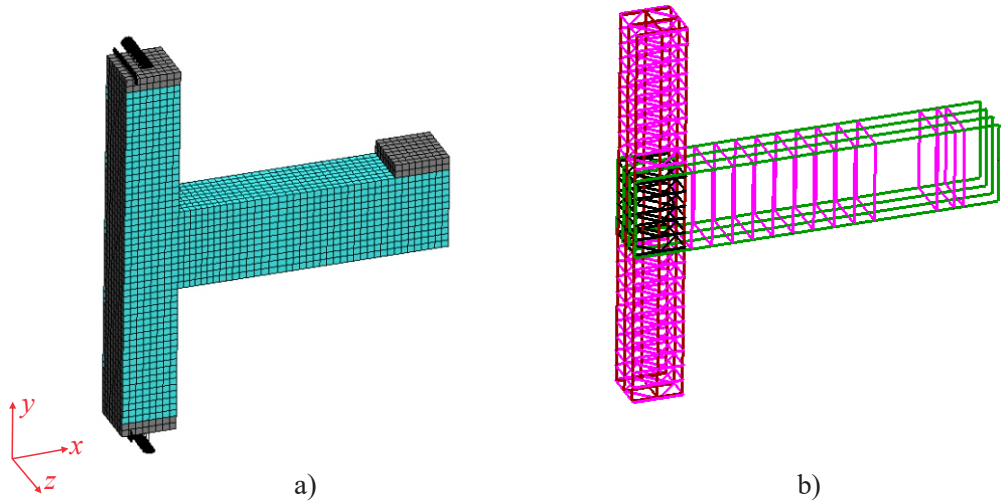

Figure 5.21 – Finite element discretization a) Concrete b) Reinforcement.

In the numerical simulation, 22 load intervals were used. In the first interval, a constant vertical load of 200 kN was applied at the top of the column. In the subsequent intervals, displacements were applied according to the displacement history shown in Figure 3.7, with step displacements of 0.1 mm. The iterative procedure used in the model was the Modified Newton-Raphson method, limited to 300 iterations in each load interval. The convergence criteria used were:

- Relative error in displacement: 0.01
- Relative error in residual forces: 0.03
- Absolute error in residual forces: 0.01
- Relative error in energy: 0.0001

5.4.3 Materials' properties - Tsonos (2005)

Tables 5.9 and 5.10 present the values adopted in the simulation of BCJ A1.

Table 5.9 – Concrete properties used in the simulation of BCJ A1

Parameter	**Concrete**	**Reference**
Young's modulus E_c	32600 MPa	Tsonos (2005)
Fracture energy G_f	138 N/m	*fib* Model Code (2013)
Compressive strength f_c	35 MPa	Tsonos (2005)
Tensile strength f_t	2.7 MPa	–
Poisson coefficient	0.20	–
Strength at the onset of nonlinear behavior f_{co}	5.6 MPa	–
Plastic strain at compressive strength $^{p}_{c}$	0.00133	Van Mier (1986)
Reduction factor of compression r_c	0.8	Dyngeland (1989)
Excentricity	0.52	Červenka et al. (2021)
Plastic flow	0.5	–
Crack orientation	Fixed	Cervenka (1985)

Table 5.10 – Steel properties used in the simulation of BCJ A1

Parameter	**Long. Reinf.**	**Transv. Reinf.**	**Reference**
Young's modulus E_s	210000 MPa	210000 MPa	–
Yield strength f_y	500 MPa	540 MPa	Tsonos (2005)
Ultimate strength f_u	700 MPa	540 MPa	Tsonos (2005)
Yield strain $_s$	0.0024	0.0026	Tsonos (2005)
Ultimate strain $_u$	0.16	0.025	Tsonos (2005)
Menegotto-Pinto	R 20 C_1=0.925 C_2=0.15		Menegotto (1973)
Bond-slip model	*Memory bond*	*Perfect*	Červenka et al. (2021)

The interface between reinforcement and concrete was simulated with the *Memory bond* material of *fib* Model Code (2013) (Figure 5.11), assuming good bond conditions and confined concrete by stirrups. In addition, a perfect bond between the stirrups and the concrete was considered. Figure 5.22 shows the bond-slip curves used in the reinforcement material for the beam and column. The $_{b,split}$ values for beam and column bars were 11.00 MPa and 11.23 MPa, respectively.

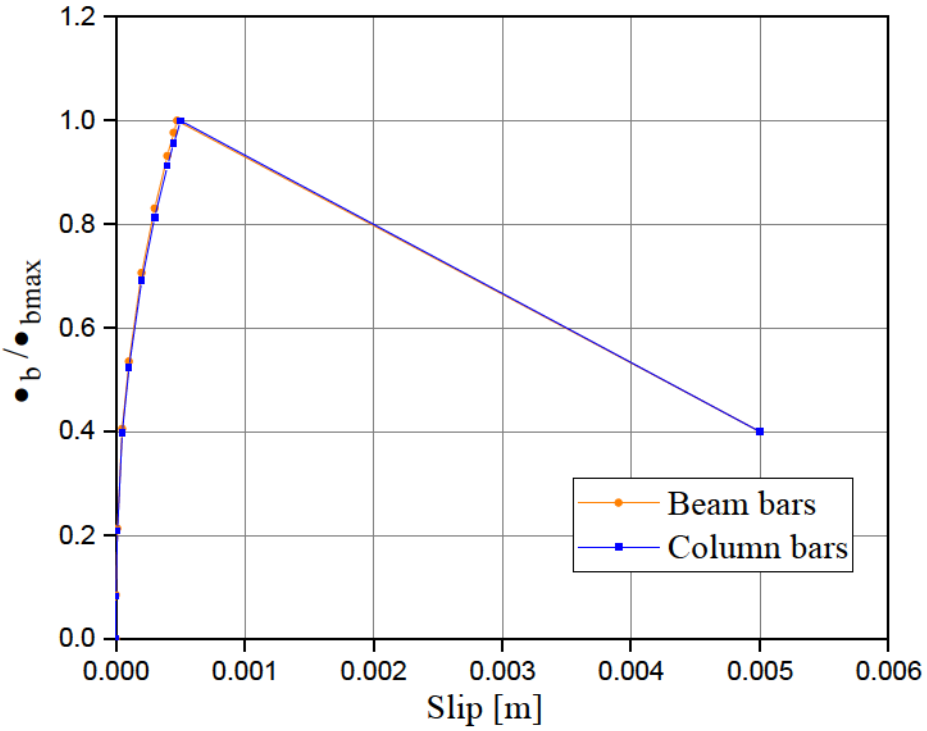

Figure 5.22 – Bond-slip relationship used in the BCJ A2.

5.5 Numerical simulation of retrofitted BCJ - Beschi et al. (2015)

In order to provide a numerical model of BCJs retrofitted with UHPFRC jackets, a numerical simulation of the exterior beam-column joints (corner) studied by Beschi et al. (2015) was performed. As Beschi et al. (2015) tested two identical joints, one without retrofit and the other retrofitted with an HPFRC jacket, specimens CJ2, and RCJ2, respectively, two models corresponding to these specimens were implemented in this work. Both the BCJs' numerical models were subjected to the same cyclic displacement history, applied to the column during the tests. In addition, to check the reliability of the simplified stress-strain diagram used to describe the HPFRC tensile behavior, the tensile direct test of the material was simulated in the ATENA program, through a 3D simulation of the "dog-bone" specimen.

5.5.1 Finite element - Beschi et al. (2015)

The concrete beam and column were modeled using hexahedral finite elements with eight nodes and eight integration points (Figure 5.18.a). The steel longitudinal bars and stirrups were modeled using truss finite elements with two nodes and two integration points. The steel plates were modeled through the *CC3DElastIsotropic* material model, using linear hexahedral finite elements with four nodes and four integration points (Figure 5.18.b.). To model the HPFRC material, the *CC3DNonLinearCementitious2user* model was used, which specifies defined relationships for tensile and compression behaviors, combining the fracture and the plasticity models of the material (ČERVENKA et al., 2021).

The beam-column joints and the HPFRC jacket had a mesh of 50x50x50 mm^3 composed of 5085 and 16825 elements for CJ2 and 6885 elements and 20016 nodes for RCJ2, as shown

in Figure 5.23. In the interface beam-joint was applied a finer mesh with the aim of obtaining results with better accuracy in the cracking state and hysteresis behavior, Figure 5.23.a.

5.5.2 Boundary conditions - Beschi et al. (2015)

Two hydraulic jacks were used in the experimental test to apply a vertical load of 210 kN at the column top to simulate the gravity load. The horizontal cyclic displacement was applied using an electromechanical jack fixed to a strong wall and the column top. The load was considered positive in the left-to-right direction. The beam-column joint presented free rotation at the top and the base of the column (hinge supports). The beam end was restricted only vertically through a roller support. In these points, steel plates of thickness 40 mm were applied, which were fixed through the master-slave condition. These boundary conditions were applied to both specimens, Figure 5.23.

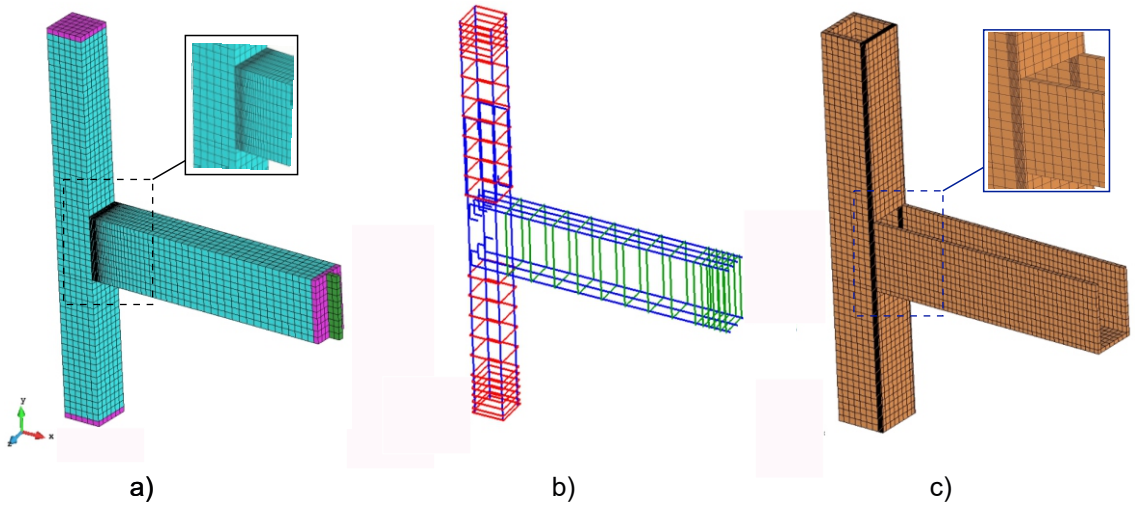

Figure 5.23 – Discretization mesh of a) Concrete and restraints of CJ2, b) Reinforcement of CJ2, and c) HPFRC of RCJ2.

In the simulation of CJ2 and RCJ2 joints, 13 interval loads were used. In the first step was applied the axial load at the top of the column, and subsequently, the horizontal displacements following the historic load of Figure 3.5, resulting in 3151 and 3401 steps for the CJ2 and RCJ2 joints, respectively. A high number of steps were used in the simulation of RCJ2 to obtain a better model discretization with the UHPFRC jacket. The computational time for running the CJ2 model was approximately 1.5 days (33 hours), while the RCJ2 simulation took approximately 13 days (319 hours).

In the same way as the previous models, the Modified Newton-Raphson iterative solver was used for simulations, with a maximum number of 300 iterations. Regarding convergence, the next error criteria were fixed during the simulations:

- Relative error in displacement: 0.01
- Relative error in residual forces: 0.01

- Absolute error in residual forces: 0.01
- Relative error in energy: 0.0001

5.5.3 Materials' properties - Beschi et al. (2015)

Tables 5.11, 5.12, and 5.13 present the material properties used in the numerical simulations of CJ2 and RCJ2 joints.

Table 5.11 – Concrete properties used in the numerical models of BCJ CJ2

Parameter	**Value**	**Reference**
Compressive strength (f_c)	38.7 MPa	Beschi et al. (2015)
Young's modulus (E_c)	4700 $\sqrt{f_c}$	ACI 318 (2019)
Poisson's ratio	0.2	ACI 318 (2019)
Tensile strength (f_t)	0.23 $f_c^{2/3}$	Committee et al. (2010)
Fracture energy (G_f)	$73 f_c^{0.18}$	*fib* Model Code (2013)
Tension stiffening	0.05	*fib* Model Code (2013)
Aggregate size	20 mm	–
Shear factor (S_f)	60	–
Plastic strain at compressive strength (^p_c)	0.00115	Červenka et al. (2021)
Strength at the onset of nonlinear behavior (f_{co})	5.6 MPa	Červenka et al. (2021)
Reduction factor of compression	0.8	Červenka et al. (2021)
Eccentricity (e)	0.5	Červenka et al. (2021)
Flow plastic ( )	0.5	Červenka et al. (2021)
Crack orientation	Fixed	Cervenka (1985)

Table 5.12 – Concrete properties used in the numerical models of BCJ RCJ2

Parameter	**Value**	**Reference**
Compressive strength (f_c)	27 MPa	Beschi et al. (2015)
Compressive strength of HPFRC (f_{cR})	110.5 MPa	Beschi et al. (2015)
Young's modulus of HPFRC (E_{cR})	36000 MPa	Beschi et al. (2015)
Young's modulus (E_c)	4700 $\sqrt{f_c}$	ACI 318 (2019)
Poisson's ratio	0.2	ACI 318 (2019)
Tensile strength (f_t)	0.23 $f_c^{2/3}$	Committee et al. (2010)
Fracture energy (G_f)	$73 f_c^{0.18}$	*fib* Model Code (2013)
Tension stiffening	0.05	*fib* Model Code (2013)
Aggregate size	20 mm	–
Shear factor (S_f)	60	–
Plastic strain at compressive strength (^p_c)	0.00137	Červenka et al. (2021)
Strength at the onset of nonlinear behavior (f_{co})	4.50 MPa	Červenka et al. (2021)
Reduction factor of compression	0.8	Červenka et al. (2021)
Eccentricity (e)	0.5	Červenka et al. (2021)
Flow plastic ( )	0.5	Červenka et al. (2021)
Crack orientation	Fixed	Cervenka (1985)

Table 5.13 – Steel properties used in the numerical models of BCJs CJ2 and RCJ2

Parameter	**Long. Reinf. =12mm/16mm**	**Transv. Reinf. =6mm/8mm**	**Reference**
Young's modulus (E_s)	200000 MPa	200000 MPa	–
Yield strength (f_y)	365 MPa / 445 MPa	493 MPa / 337 MPa	Beschi et al. (2015)
Ultimate strength (f_u)	558 MPa / 546 MPa	556 MPa / 440 MPa	Beschi et al. (2015)
Ultimate strain ($_u$)	0.159 / 0.137	0.161 / 0.21	Beschi et al. (2015)
Menegotto-Pinto	R=20, C1=0.925, C2=0.15		Menegotto (1973)

The cyclic behavior of steel reinforcement was reproduced through the Menegotto-Pinto model (MENEGOTTO, 1973), which considers Bauschinger's effect. Three parameters govern the Menegotto-Pinto model: the curvature R, and the experimental coefficients c_1 and c_2 (ČERVENKA et al., 2021). These parameters are presented in Table 5.13.

In addition, a good bond between concrete and steel, and a maximum bond strength $_{max}$ of 1.6 MPa, determined according to the design criteria of *fib* Model Code (2013) was adopted. For the stirrups, a perfect bond with the concrete was assumed.

5.5.4 Tensile behavior of HPFRC - Beschi et al. (2015)

In the experimental test of Beschi et al. (2015) two direct tensile tests known as 'dog-bone' tests of dimensions 160x330x15 mm^3 were performed on HPFRC material to obtain the tensile behavior of the material (Figure 5.24). These tests provided maximum tensile strength values of 7.5 MPa and 5.7 MPa, with an average tensile strength of 6.6 MPa and a strain-hardening up to 0.15% strain (BESCHI et al., 2015). Thus, to obtain good calibration in the simulation of the retrofitted joint, the 'dog-bone' model was also simulated in the ATENA program.

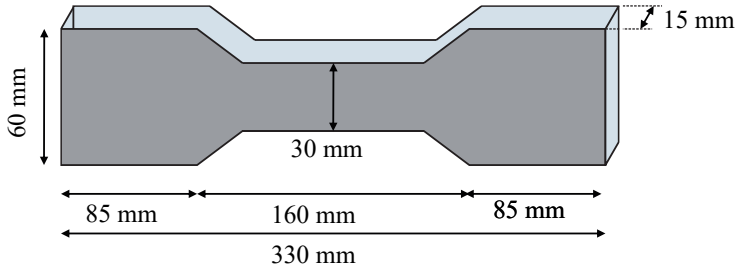

Figure 5.24 – Dimensions of the 'dog-bone' specimen.

The 'dog-bone' model was simulated through *CC3DNonLinearCementitious2user* material model, with a mesh size of 80x15x15 mm^3, as shown in Figure 5.25. Regarding boundary conditions, the displacements at the bottom edge of the 'dog bone' model were restrained. In contrast, a vertical displacement was applied to the top edge, similar to the experimental test. In addition, two 5 mm thick steel plates were simulated and fixed in the top and bottom edge of the specimen through the master-slave condition, Figure 5.25.

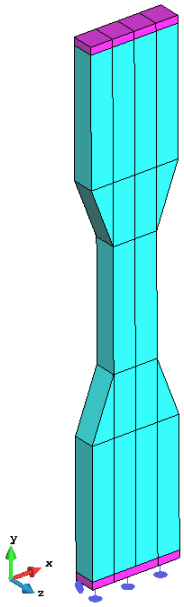

Figure 5.25 – Discretization mesh of 'dog-bone' specimen.

Figure 5.26 presents the comparison of the numerical and experimental tensile behavior curves of the 'dog-bone' of HPFRC. The numerical model was able to predict the peak load quite well, maintaining the safe side and a very good softening behavior, despite a little stiffer behavior than the experimental specimen in the elastic regime. Thus, the function used in ATENA to implement HPFRC can be considered satisfactorily reliable.

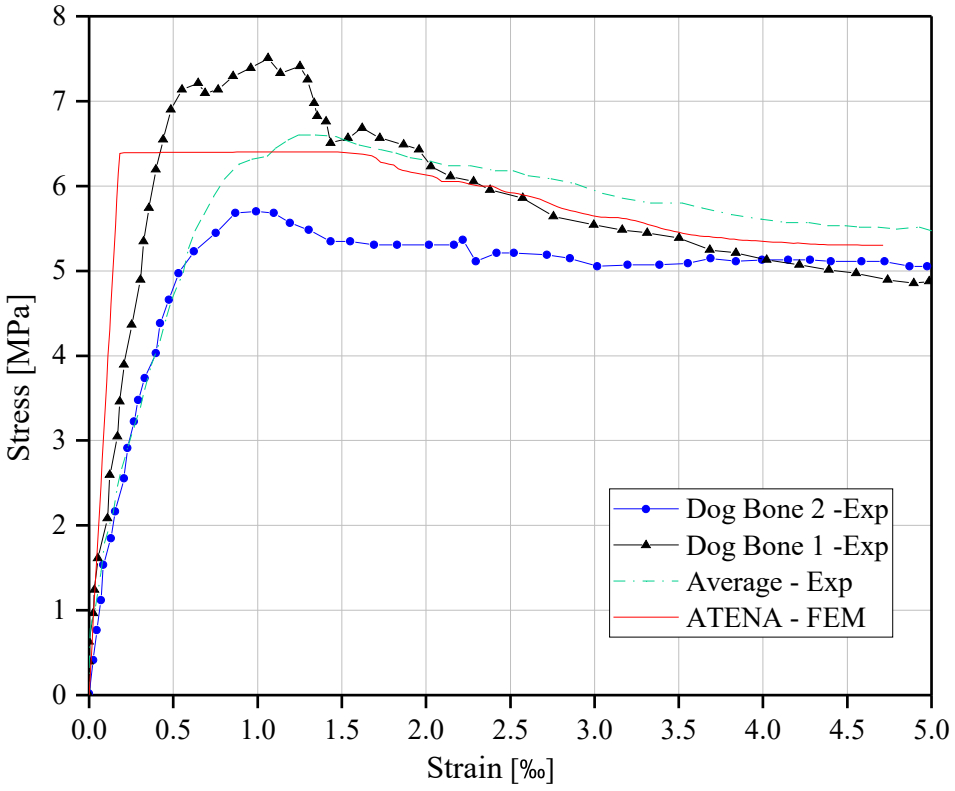

Figure 5.26 – Strain-stress curve of 'dog-bone' simulation compared with the experiment tests.
Font: Experimental results obtained from Beschi et al. (2015)

The fracturing strain describes this function, $\epsilon_1^{f'}$, which is calculated as shown by Equation 5.33, where: ϵ_1^f is the fracturing strain calculated from the strain tensor at the finite element integration points, ϵ_{loc}^f is the strain after which strain localization can be expected, L_t is the crack band size, and L_{ch}^t is the characteristic length. In the model, L_{ch}^t was taken to be equal to 80 mm.

$$\begin{aligned} \epsilon_1^{f'} &= \epsilon_1^f && for \quad \epsilon_1^f < \epsilon_{loc}^f \\ \epsilon_1^{f'} &= \epsilon_{loc}^f + (\epsilon_1^f - \epsilon_{loc}^f)\frac{L_t}{L_{ch}^t} && for \quad \epsilon_1^f > \epsilon_{loc}^f \end{aligned} \tag{5.33}$$

The stress-strain curve presented in Figure 5.27 corresponds to the function used in ATENA to simulate the tension behavior of HPFRC. This methodology has also been used by Lampropoulos et al. (2016). However, in this thesis, the hardening branch was not considered, since a significant hardening behavior was not observed in the experimental curves.

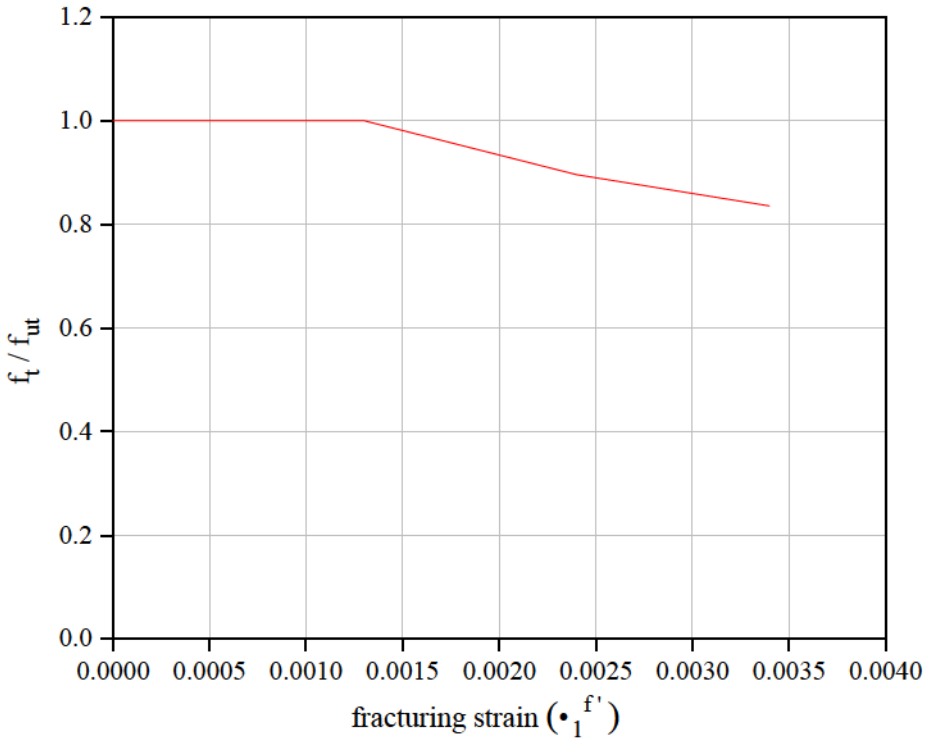

Figure 5.27 – Tensile stress-strain curve adopted in the numerical model for the simulation of UHPFRC material.

5.5.5 Concrete-HPFRC interface

In the numerical model of RCJ2 joint, the contact between concrete and HPFRC was simulated through the *Interface* material model, which is formulated to reproduce both monotonic and cyclic load conditions (PASCHALIS et al., 2018; SASMAL et al., 2011) (Figure 5.28). This model is based on the Mohr-Coulomb criterion with a tension cut-off. After stress reaches this condition, the surface collapses to a residual surface, representing a dry condition between the materials (ČERVENKA et al., 2021).

The *Interface* model is governed by the initial normal and tangential stiffnesses, K_{nn} and K_{tt}, respectively, the minimal normal and tangential stiffnesses, K_{nn}^{min} and K_{tt}^{min}, respectively, the

friction coefficient, , the tensile strength, $f_{t,int}$, and the cohesion coefficient, c. The minimum stiffness values K_{nn} and K_{tt} are used only for numerical purposes after the element failure, to preserve the positive definiteness of the global system of equations. These stiffness values should be chosen approximately 0.001 times the initial stiffness values (ČERVENKA et al., 2021). In cases where no experimental information on the interface material is available, can be assumed between 0.3 and 0.5 (except for oiled surface), $f_{t,int}$ between 0.25 and 0.5 times the tensile strength of the material with the lowest strength and c between 1 and 2 times the interface's tensile strength (ČERVENKA et al., 2021). The parameters used in the numerical model presented herein are reported in Table 5.14.

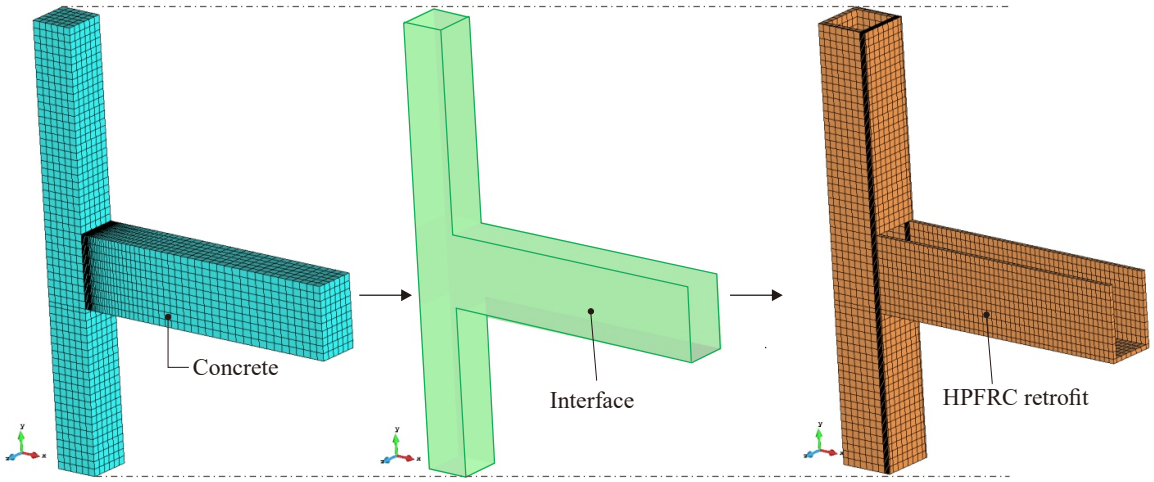

Figure 5.28 – Interface's elements of the joint retrofitted with HPFRC.

Table 5.14 – Properties of the interface material used in the numerical model of specimen RCJ2

Parameter	**3D interface**
Normal stiffness (K_{nn})	1.4x10^6 MN/m^3
Tangential stiffness (K_{tt})	1.4x10^6 MN/m^3
Minimal Normal stiffness (K_{nn}^{min})	1.4x10^3 MN/m^3
Minimal Tangential stiffness (K_{tt}^{min})	1.4x10^3 MN/m^3
Friction coefficient ( )	0.5
Tensile strength ($f_{t,int}$)	1.0 MPa
Cohesion coefficient (c)	1.0 MPa

6 Results and Discussions

To validate the shear joint models presented in Chapter 2, the shear strength data from Appendix A (Table A) was evaluated. The database includes a total of 150 experimental tests; however, it was not possible to validate all of them using every analytical model due to the specific limitations of each model. Table A.2 presents the reference labels of the experimental tests used in each analytical model (the reference labels correspond to those provided in Table A).

Additionally, the results obtained from numerical simulations of both the reinforced frame and the exterior beam-column joints were compared with the corresponding experimental results.

6.1 Comparative study: Analytical models and experimental tests

The joint shear strength comparison obtained in each analytical model ($V_{jh,model}$) and experimental test ($V_{jh,exp}$) is presented in Figure 6.1, showing that some models had a better approximation with the experimental results. The model with the best accuracy was the model proposed by Hassan and Moehle (2018)-STM with a R^2 of 0.97578. However, this model has the disadvantage of being applied only for unreinforced joints, not considering the contribution of joint transverse and vertical reinforcement (Figure 6.1.q.)

The models of Tran et al. (2014) and Pauletta et al. (2015) presented a good correlation with R^2 of 0.97148 and 0.96419, respectively, (Figures 6.1.l and 6.1.n). Those can be applied for reinforced and unreinforced joints. However, the defect of the model of Tran et al. (2014) does not consider the beam reinforcement, considered as a main parameter in the joint shear behavior (discussed in Chapter 2). For this reason, it could be noted that the model Pauletta et al. (2015) remains the better option, showing good results in the shear strength of the joint and the possibility of including the main parameters that influence the joints' shear behavior.

Regarding models applied only for unreinforced joints, the model of Hassan and Moehle (2018)-EMPIR had a R^2 of 0.95807, underestimating the joint shear strength. This model does not consider the contribution of reinforcement of the beam and the column (Figure 6.1. r). The models of Priestley (1997), Pampanin et al. (2002), Park and Mosalam (2012a), and Metelli et al. (2015) showed a lower correlation, which could be due to lack of not including the geometrical parameters of the beam and column, beam and column steel bars, and the axial force in the column (Figures 6.1.c, 6.1.e, 6.1.j, 6.1.m)

Standards criteria of ASCE SEI/41 (2007) and ACI 318 (2014) evidenced a good correlation compared with NZS 3101 (1995). However, in these models, the contribution of the joint reinforcement and the axial column force is not considered. In addition, the model of NZS 3101 (1995) underestimated the joint shear strength, as shown in Figures 6.1.b, 6.1.k, and 6.1.g.

Hwang and Lee (2002) developed an empirical model, which considers geometric param-

eters of the beam and column. However, this model does not include the beam reinforcement and it is applied only for reinforced joints. The results presented a R^2 of 0.90361, as shown in Figure 6.1.f.

The other models that can be applied for both reinforced and unreinforced joints presented a lower approximation in the Vjh values, where the axial column force, beam reinforcement, and column reinforcement were not included in their formulations. e.g., Tsonos (1999) and Kim et al. (2009) presented lower values of R^2 of 0.94976 and 0.93926, compared with the model proposed by Kassem (2016) with a R^2 value of 0.95232, which only did not include the column reinforcement (Figures 6.1.d, 6.1.h, and 6.1.o). However, despite that the models developed by Parate and Kumar (2018) and Parate and Kumar (2019) considered the contribution of diverse parameters, the results presented R^2 values of 0.94776 and 0.94751, respectively (Figures 6.1.p and 6.1.s).

Finally, the models (applied for reinforced and unreinforced joints) with the lowest correlation were those developed by Wang et al. (2012) and Paulay and Priestley (1992), with R^2 of 0.91982 and 0.90944, which can be caused by the absence of the beam reinforcement and beam geometry, respectively (Figures 6.1.i and 6.1.a).

Thus, can be considered that the best correlation was attributed to the model of Pauletta et al. (2015), while the lowest correlation corresponds to the model of Metelli et al. (2015), Figures 6.1.n and 6.1.m, respectively. Nevertheless, these empirical models were developed for joints without any retrofit material. For this reason, this thesis developed a new analytical model for exterior joints retrofitted with a UHPFRC jacket that can be applied to both reinforced (with stirrups in the joint) and unreinforced joints (no stirrups in the joint).

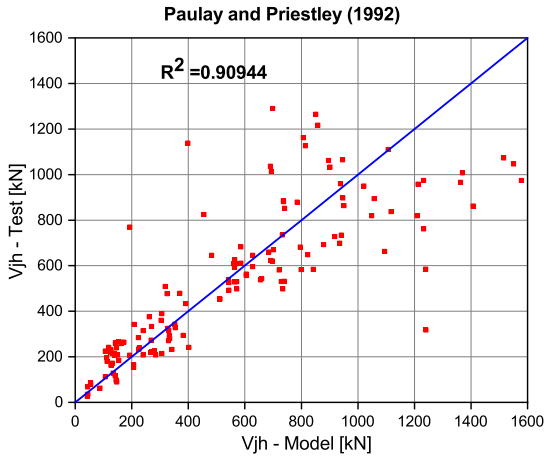

(a)

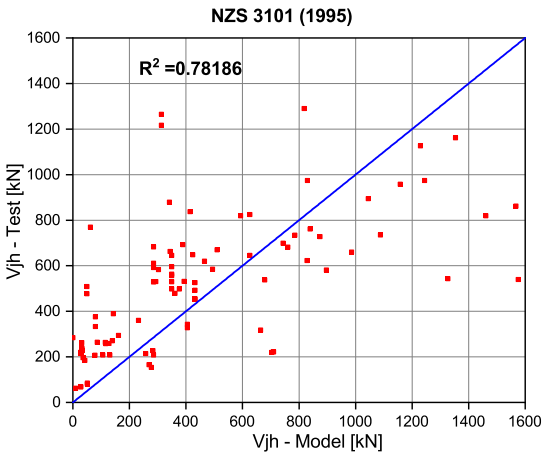

(b)

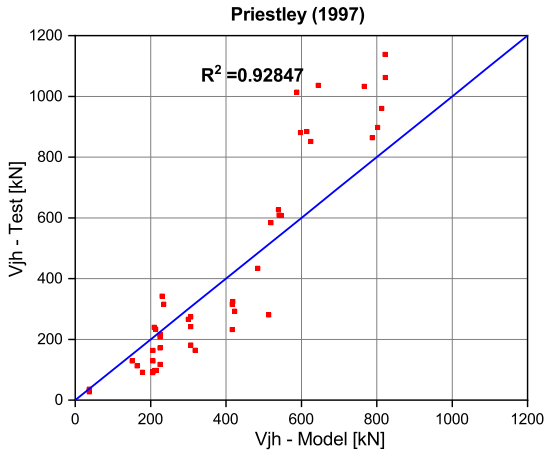
Priestley (1997)
R² =0.92847
Vjh - Test [kN]
Vjh - Model [kN]
0
200
400
600
800
1000
1200

(c)

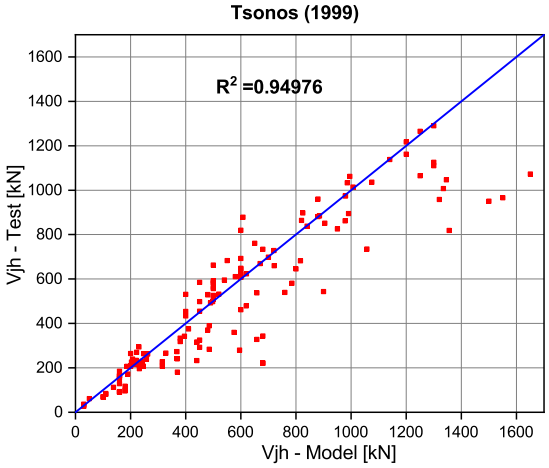
Tsonos (1999)
R² =0.94976
Vjh - Test [kN]
Vjh - Model [kN]
0
200
400
600
800
1000
1200
1400
1600

(d)

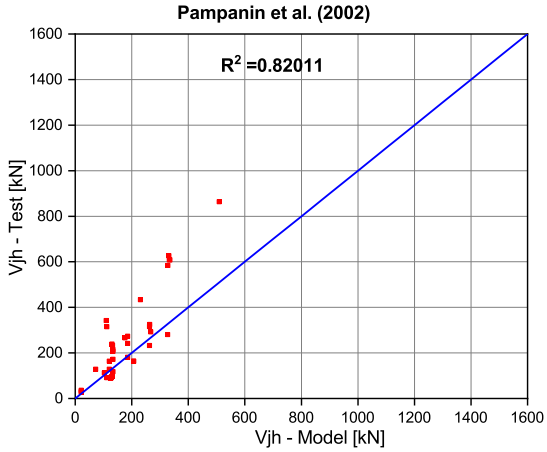
Pampanin et al. (2002)
R² =0.82011
Vjh - Test [kN]
Vjh - Model [kN]
0
200
400
600
800
1000
1200
1400
1600

(e)

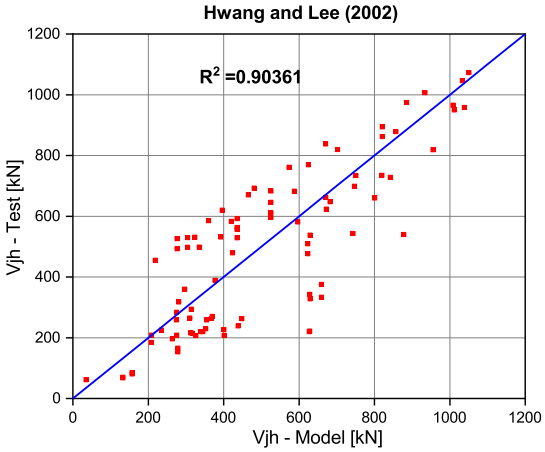
Hwang and Lee (2002)
R² =0.90361
Vjh - Test [kN]
Vjh - Model [kN]
0
200
400
600
800
1000
1200

(f)

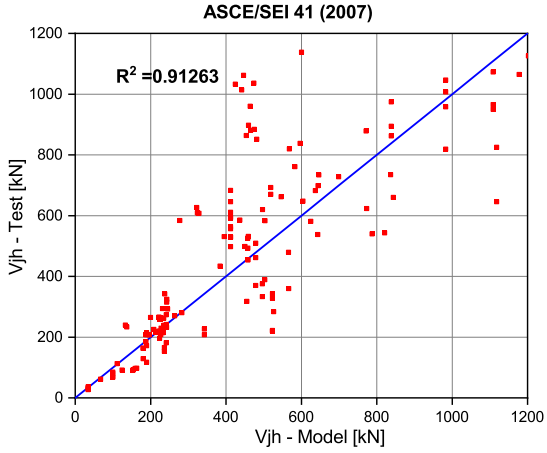
ASCE/SEI 41 (2007)
R² =0.91263
Vjh - Test [kN]
Vjh - Model [kN]
0
200
400
600
800
1000
1200

(g)

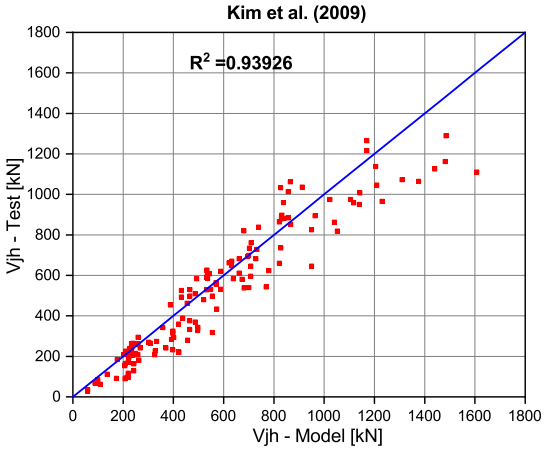
Kim et al. (2009)
R² =0.93926
Vjh - Test [kN]
Vjh - Model [kN]
0
200
400
600
800
1000
1200
1400
1600
1800

(h)

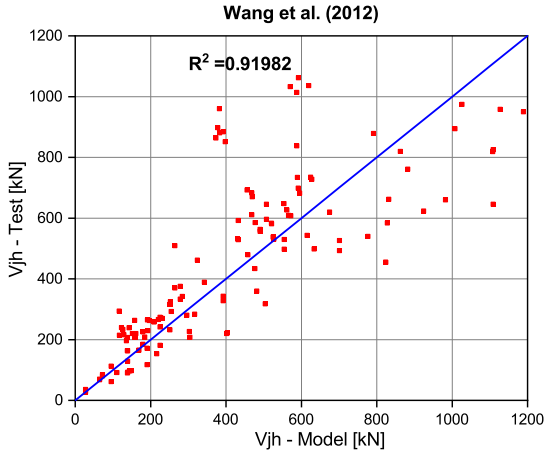
Wang et al. (2012)
R² =0.91982
Vjh - Test [kN]
Vjh - Model [kN]
0
200
400
600
800
1000
1200

(i)

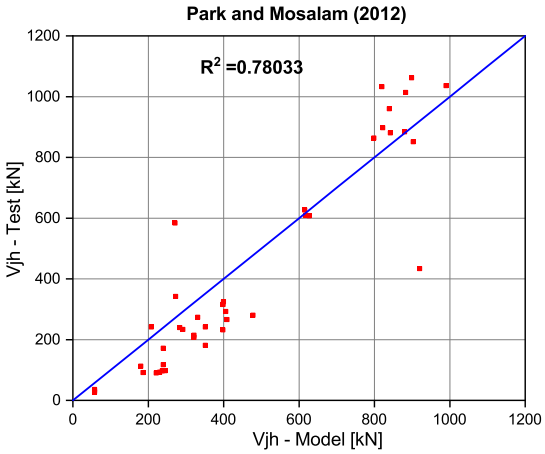
Park and Mosalam (2012)
R² =0.78033
Vjh - Test [kN]
Vjh - Model [kN]
0
200
400
600
800
1000
1200

(j)

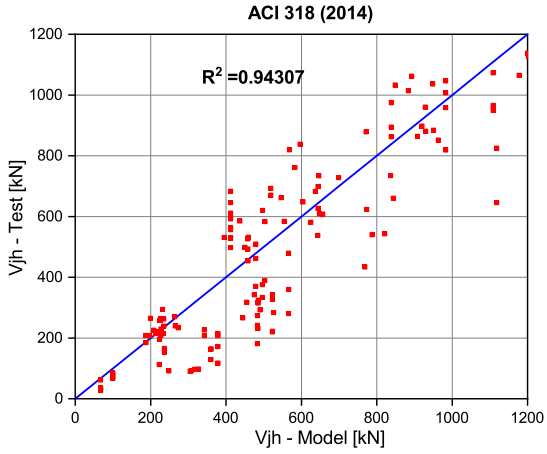
ACI 318 (2014)
R² =0.94307
Vjh - Test [kN]
Vjh - Model [kN]
0
200
400
600
800
1000
1200

(k)

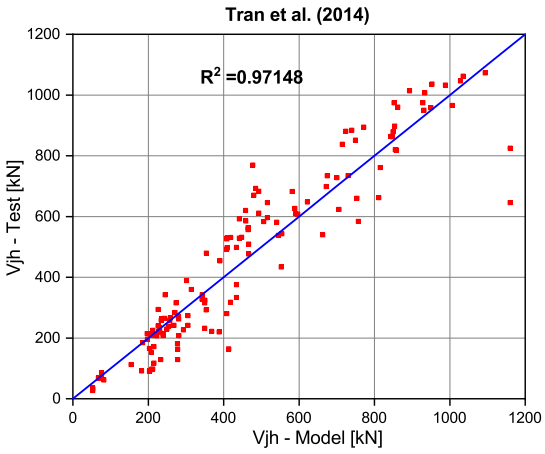
Tran et al. (2014)
R² =0.97148
Vjh - Test [kN]
Vjh - Model [kN]
0
200
400
600
800
1000
1200

(l)

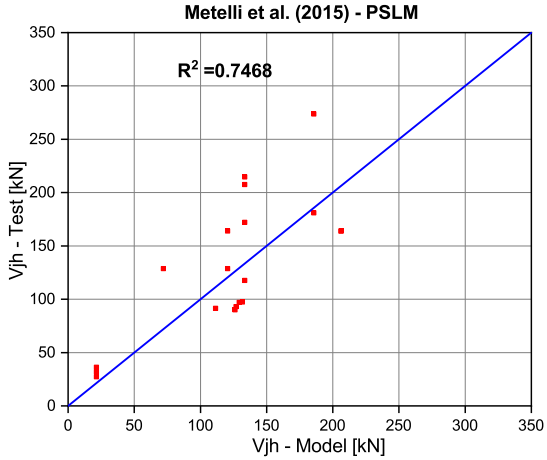
Metelli et al. (2015) - PSLM
R² =0.7468
Vjh - Test [kN]
Vjh - Model [kN]
0
50
100
150
200
250
300
350

(m)

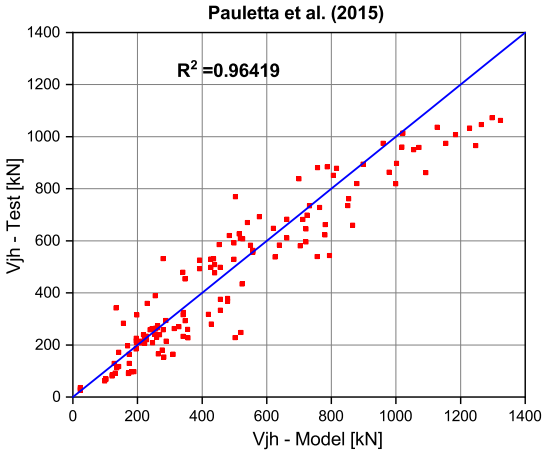
Pauletta et al. (2015)
R² =0.96419
Vjh - Test [kN]
Vjh - Model [kN]
0
200
400
600
800
1000
1200
1400

(n)

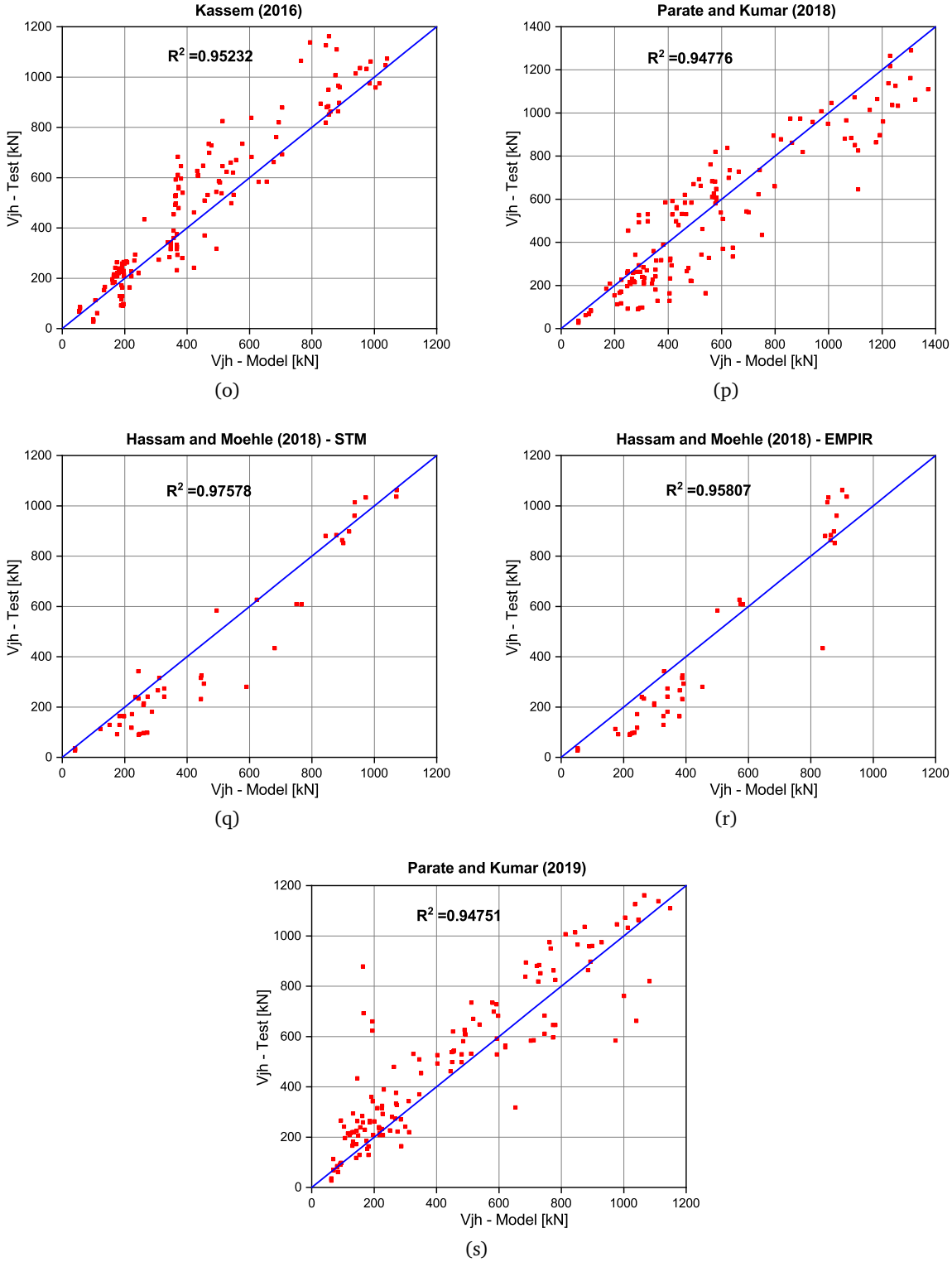

Figure 6.1 – Analytical models developed by: a) Paulay and Priestley (1992) b) NZS 3101 (1995) c) Priestley (1997) d) Tsonos (1999) e) Pampanin et al. (2002) f) Hwang and Lee (2002) g) ASCE SEI/41 (2007) h) Kim et al. (2009) i) Wang et al. (2012) j) Park and Mosalam (2012a) k) ACI 318 (2014) l) Tran et al. (2014) m) Metelli et al. (2015) n) Pauletta et al. (2015) o) Kassem (2016) p) Parate and Kumar (2018) q) Hassan and Moehle (2018) r) Hassan and Moehle (2018) s) Parate and Kumar (2019)

6.2 Comparative study: numerical and experimental

6.2.1 Reinforced concrete frame - Vecchio and Emara (1992)

This model represents the RC frames' joint subjected to monotonic load, which was tested by Vecchio and Emara (1992). This numerical model was analyzed using three different size mesh of 50 mm, 80 mm, and 100 mm.

Figure 6.2 presents the capacity curves obtained in each analysis. It can be observed that, in comparison to the experimental curve, the coarse mesh numerical model showed a higher maximum load, while the fine mesh model exhibited a better approximation with the experimental results. One reason for this could be attributed to the greater discretization of the connection between the beams and the columns. The maximum load values are presented in Table 6.1.

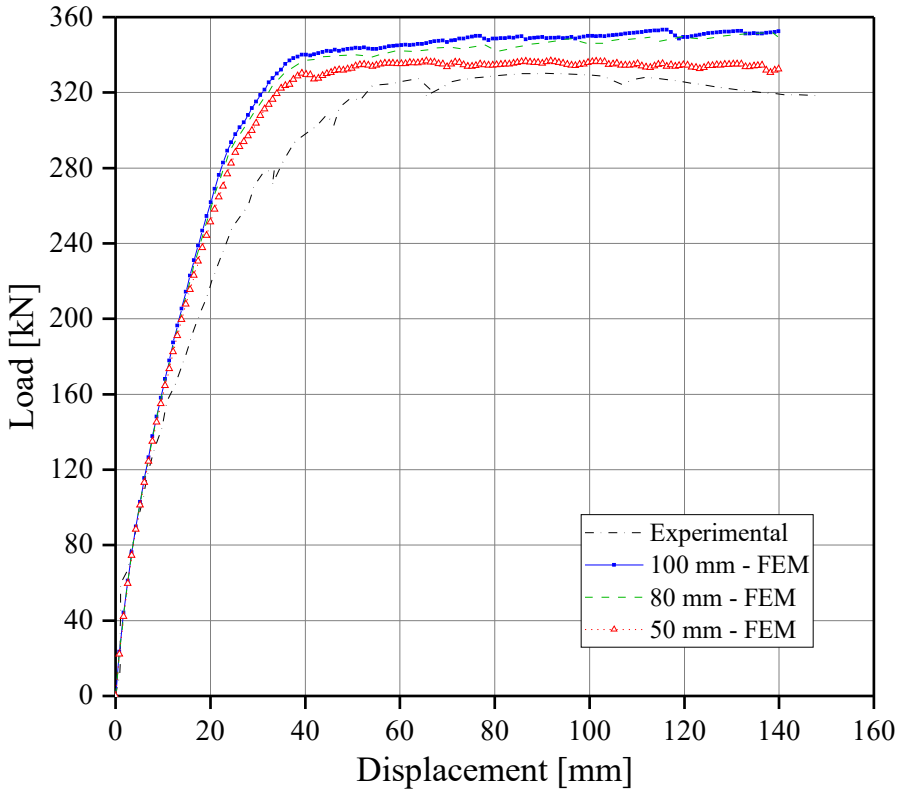

Figure 6.2 – Load-displacement curve obtained from experimental and numerical models with different size mesh.
Font: Experimental results adapted from Vecchio and Emara (1992)

Table 6.1 – Maximum loads obtained from numerical models and experimental test

Model	Mesh size	Load[kN]	Error [%]
Experimental test	–	332.0	–
Coarse mesh	100 mm	353.4	6.4
Medium mesh	80 mm	350.8	5.6
Fine mesh	50 mm	336.8	1.4

Figure 6.3 presents the comparison between the fine mesh model (50 mm) and numerical simulations developed by other authors where was possible to observe the good accuracy concerning the experimental results.

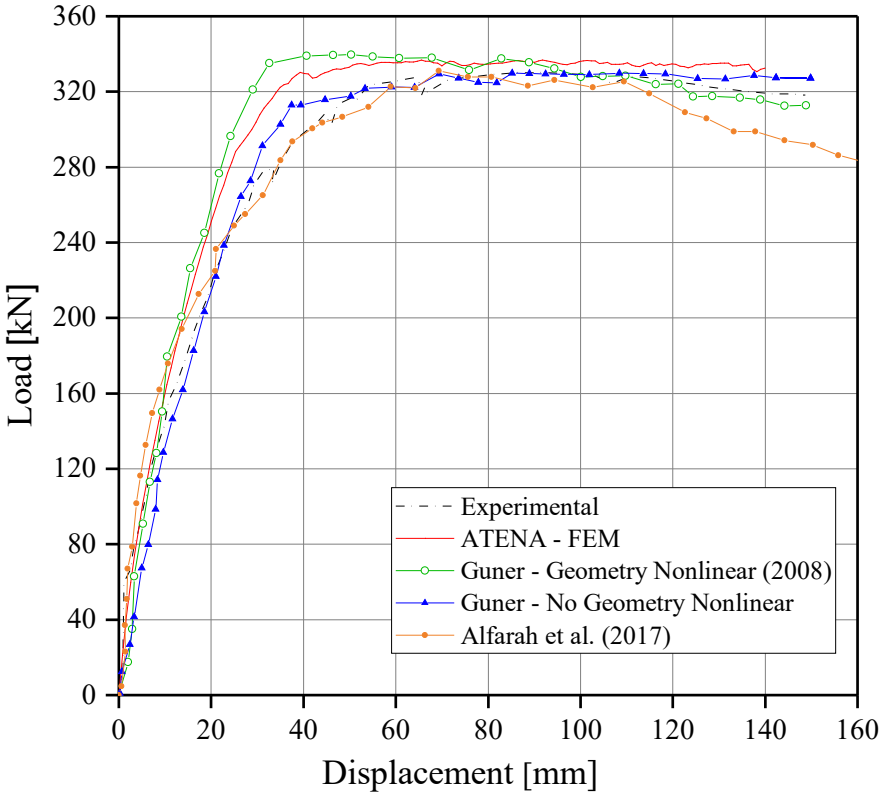

Figure 6.3 – Load-displacement curve using mesh a) Fine b) Medium and c) Coarse. (Horizontal displacement of 78 mm).
Font: Adapted from Vecchio and Emara (1992), Guner (2008), and Alfarah et al. (2017)

Figure 6.4 presents the cracking pattern for each mesh size when the ultimate load is reached, corresponding to a horizontal displacement of 78 mm. In these figures, a significant concentration of cracks is observed, both in the beam-column connections and at the base of the columns, highlighting the need for detailed joint analyses when subjected to horizontal loads.

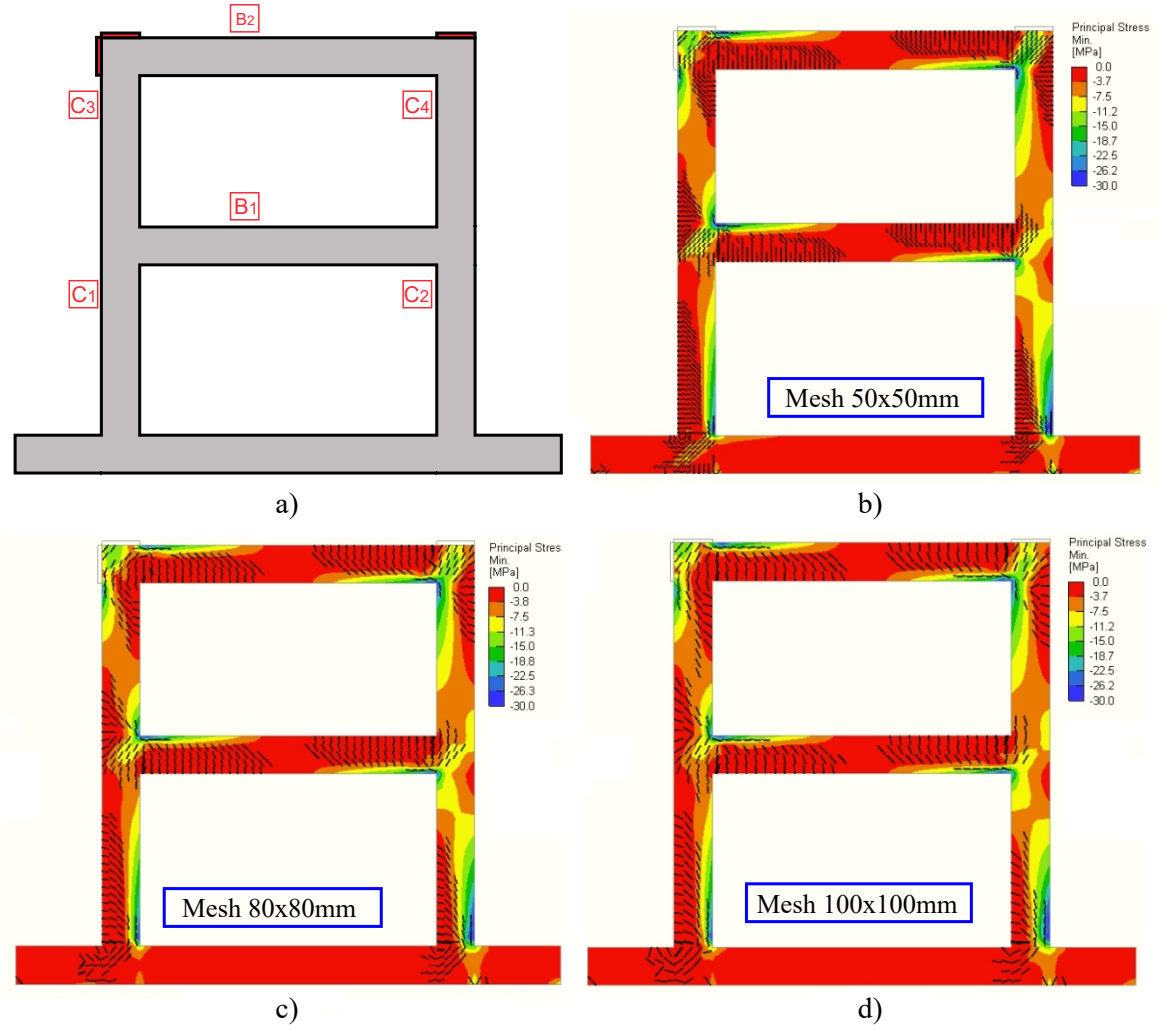

Figure 6.4 – Cracking at frame using mesh a) fine b) medium and c) coarse. (Horizontal displacement of 78 mm).

Comparisons of the numerical models with the experimental results were evaluated at the beam-column connection (B_2-C_3) and at the base of the column C_1, where it was possible to achieve experimental cracks in the numerical model, as observed in Figures 6.5 and 6.6.

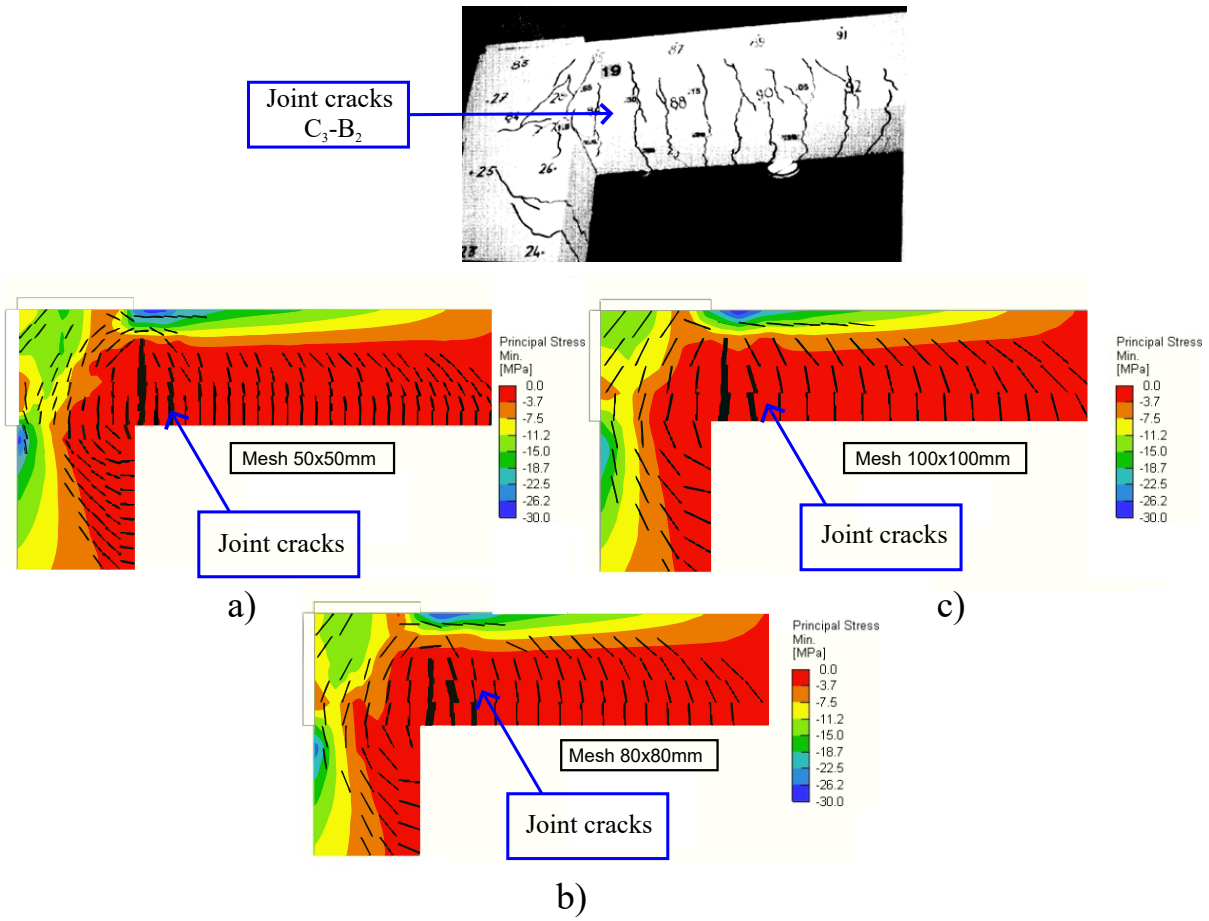

Figure 6.5 – Cracks at beam-column joint B_2-C_3 using mesh a) Fine b) Medium and c) Coarse. (Horizontal displacement of 78 mm).
Font: Experimental results obtained from Vecchio and Emara (1992)

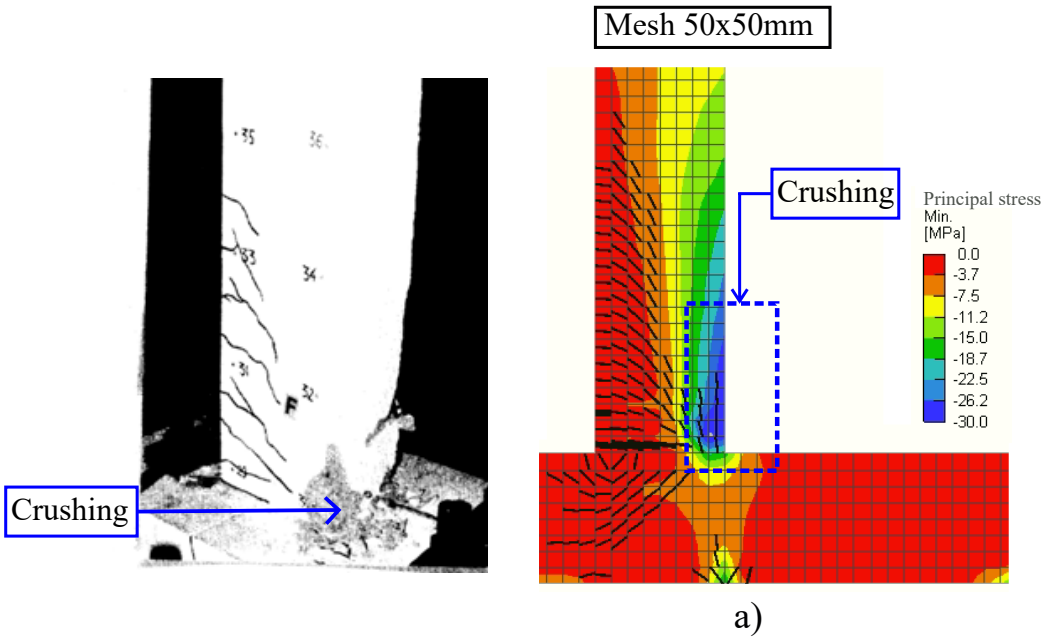

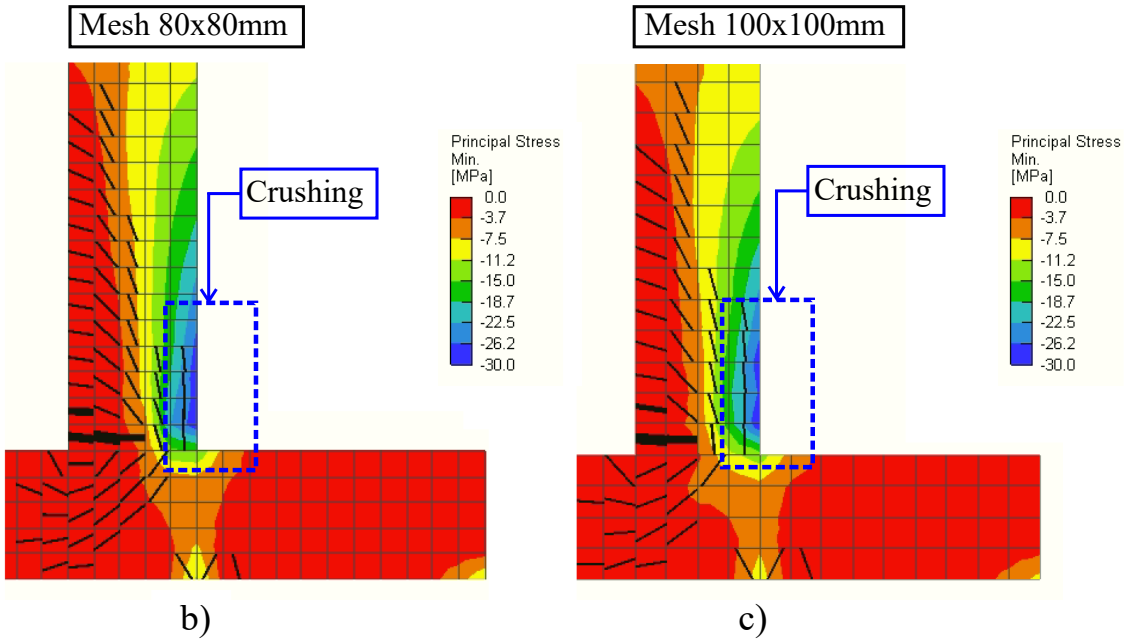

Figure 6.6 – Cracks at base column C_1 using mesh a) Fine b) Medium and c) Coarse. (Horizontal displacement of 78 mm).
Font: Experimental results obtained from Vecchio and Emara (1992)

In addition, analyses were conducted to highlight the level of cracking and yield stress of the reinforcement under different loadings. In Figure 6.7.a, the flexural cracking level due to a load of 52.5 kN on beam B_1 is presented, a situation observed in the experimental test at a load of 58.4 kN. Figure 6.7.b shows flexural cracks at the base of column C_1, in the numerical model they appeared at a load of 152.8 kN, while in the experimental test they occurred at a load of 145 kN, resulting in a difference of 4.9%. Regarding the reinforcement, in the experimental test, the top and bottom longitudinal reinforcement of beam B_1 yielded at loads of 264 kN and 287 kN, respectively. The numerical model exhibited the same behavior with a lateral load of 281.5 kN, as shown in Figure 6.7.c. The longitudinal reinforcement of columns C_1 and C_2 yielded at a horizontal load of 323 kN in the experimental test, a value similar to the numerical result of 326.1 kN, resulting in a difference of 0.9%, Figure 6.7.d.

The yielding in the reinforcement of the beam V2 was observed at a load of 326.1 kN and 329 kN for the numerical model and experimental test, respectively. Thus, there was a good similarity between the numerical and experimental results, as well as s similar concentration of cracks in the joint core, interface joint-beam, and at the base of the columns.

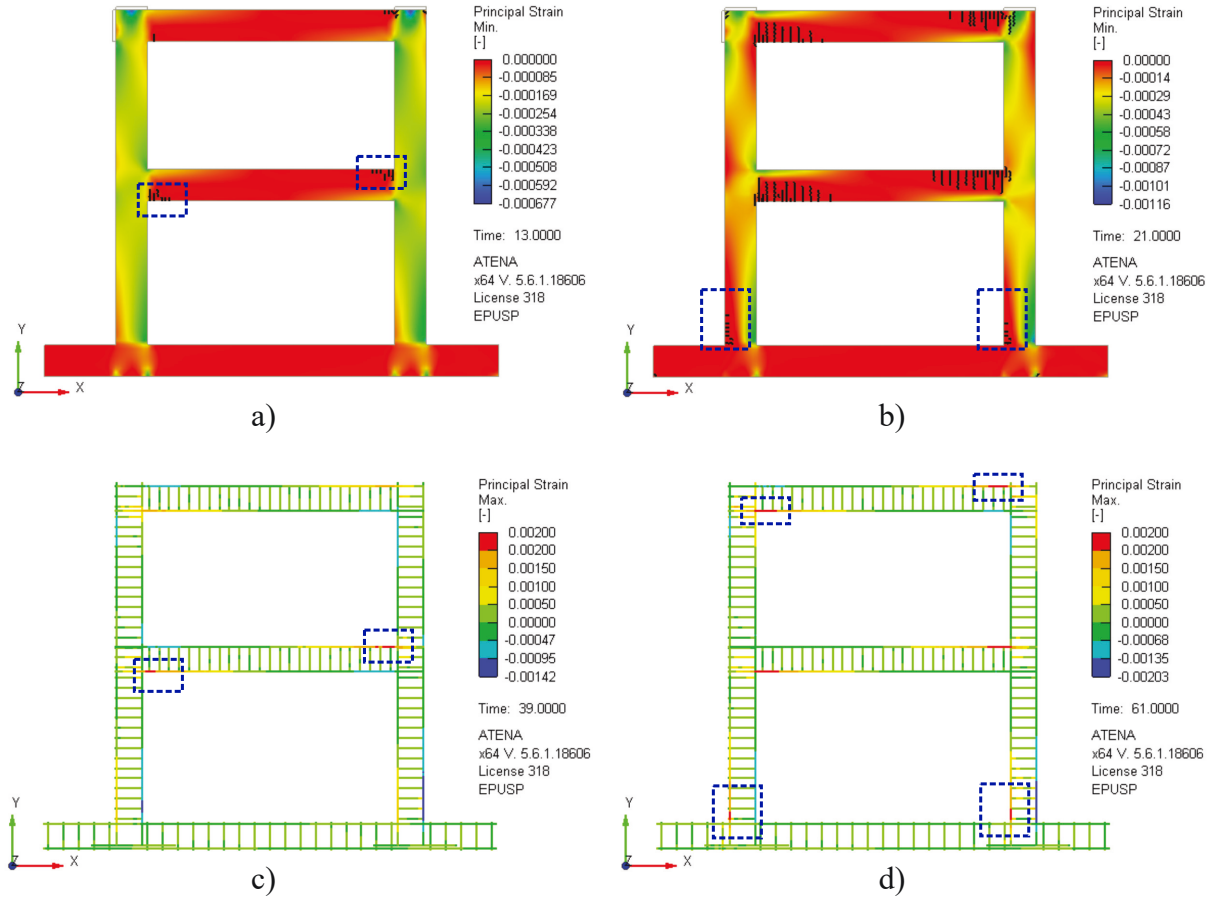

Figure 6.7 – Flexural cracks a) Beam ends B_1 b) Base column C_1. Yielding of the longitudinal steel bars c) Beam B_1 and d) Columns C_1 and C_2.

6.2.2 Model A2 - BCJ of Kusuhara and Shiohara (2008)

Figure 6.8 shows the load-displacement curve obtained in the numerical model and experimental test of the exterior BCJ A2, which presented a good fit and calibration between the hysteresis curves, reflecting the similarity between the experimental and numerical behaviors. In the numerical model, the maximum shear forces applied at the top of the column were of +76.0 kN and -72.21 kN, respectively, while for experimental test were of +77.9 kN and -77.1 kN, resulting in a difference of 2.5% in the positive direction (left to right) and 6.8% in the negative direction (right to left) of the load.

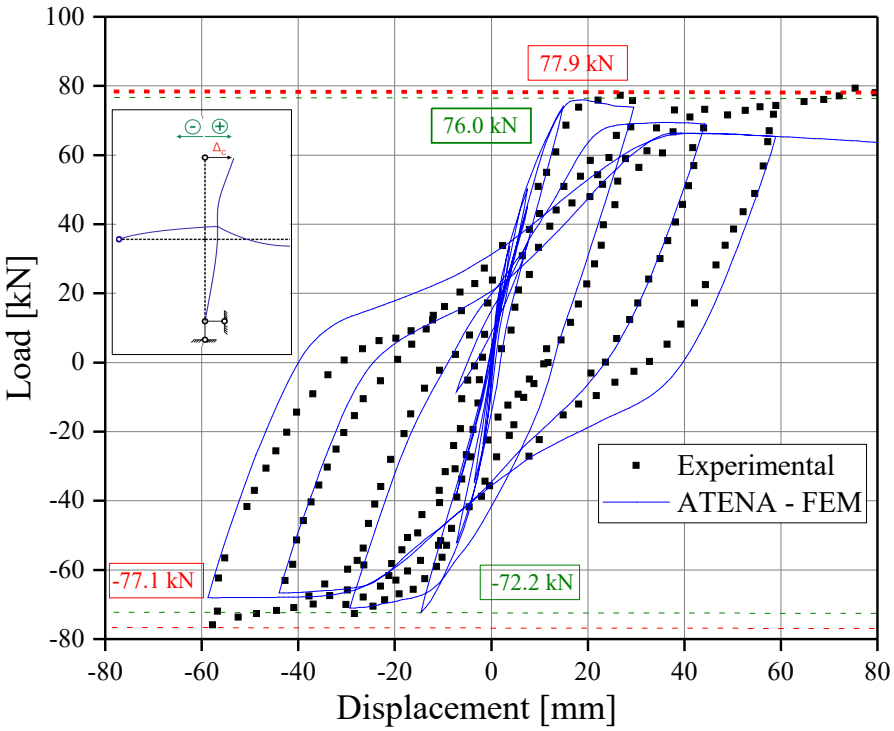

Figure 6.8 – Hysteresis curve BCJ A2.
Font: Experimental results obtained from Kusuhara and Shiohara (2008)

In Figures 6.9, 6.10, and 6.11, the crack patterns observed experimentally and numerically are presented. Figure 6.9 shows the cracking panorama of the joint A2 under cyclic displacement of 7.35 mm, corresponding to a SD (Story Drift) of 0.5%, with flexural cracks in the interface between the joint core and the beam. Figures 6.10.b and 6.10.c depict the cracking at a displacement of 29.4 mm (SD = 2.0%), showing diagonal cracks located in the joint core, similar to the experimental test. Figures 6.11.b and 6.11.c illustrate the cracks when the joint is under a displacement of 58.8 mm (SD = 4.0%). In the experimental test, at this load value, the concrete experienced crushing at the end of the beam (beam-joint interface), a situation also observed in the numerical simulation. Additionally, during the experimental test, the beam's right segment behaved as a rigid body as the displacement did not cause significant stresses, a situation also evidenced in the numerical model.

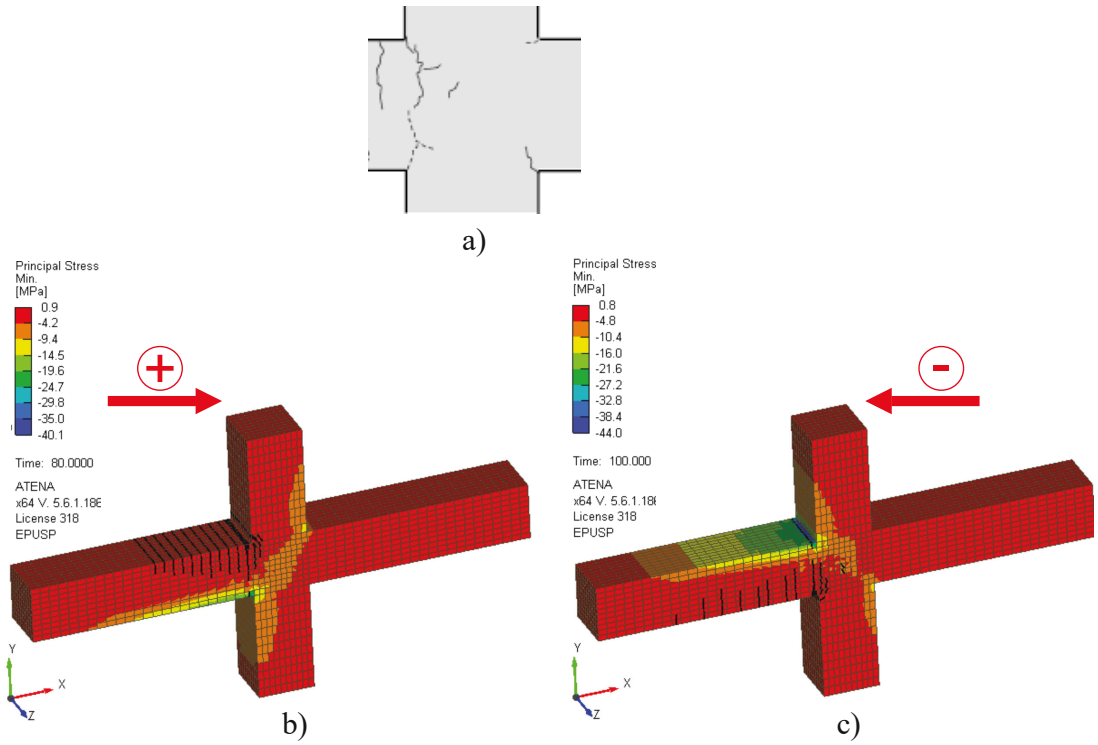

Figure 6.9 – Cracks at SD=0.5% BCJ A2 a) Experimental, numerical b) +7.35 mm c) -7.35 mm. Font: Experimental results obtained from Kusuhara and Shiohara (2008) and Tambusay et al. (2020)

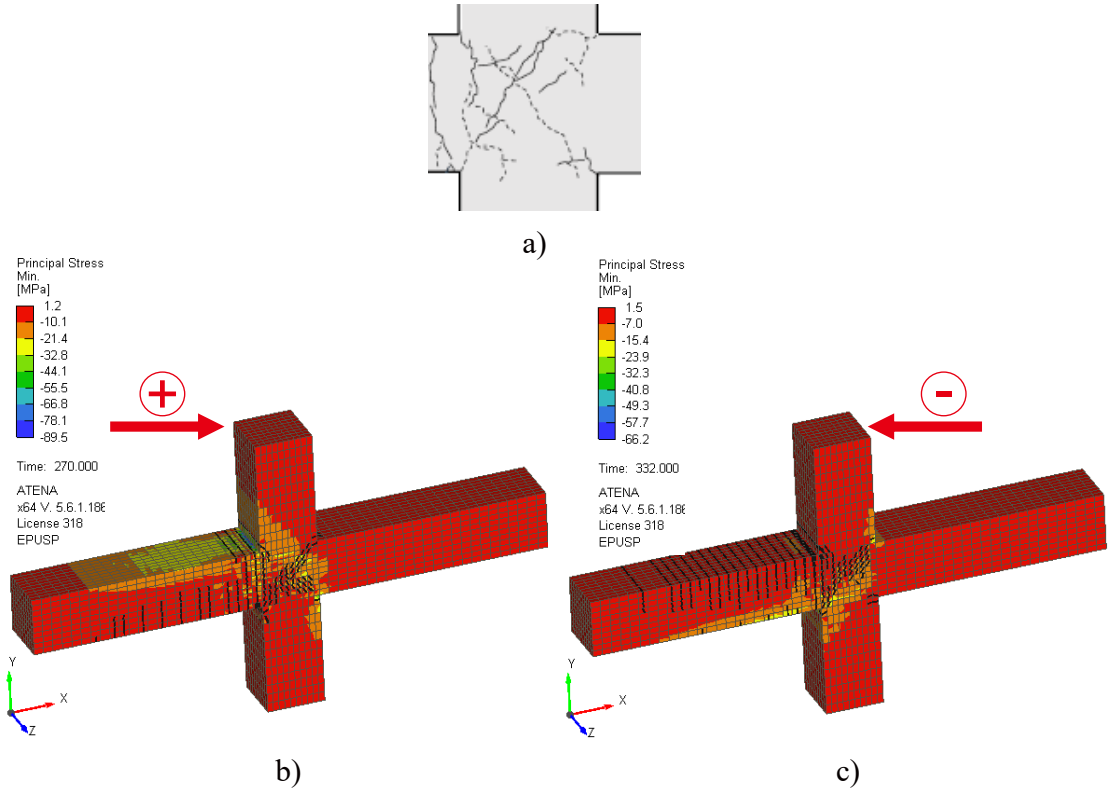

Figure 6.10 – Cracks at SD=2.0% BCJ A2 a) Experimental, numerical b) +29.4 mm c) -29.4 mm. Font: Experimental results obtained from Kusuhara and Shiohara (2008) and Tambusay et al. (2020)

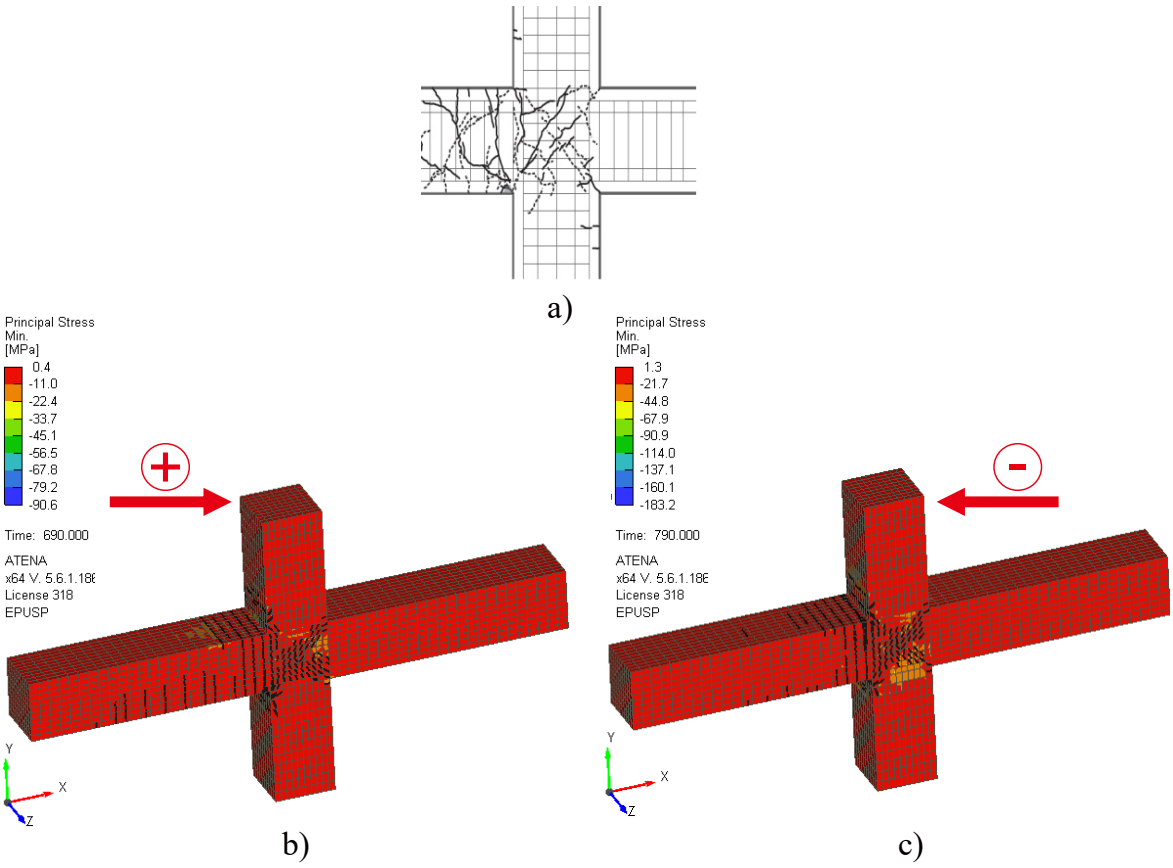

Figure 6.11 – Cracks at SD=4.0% BCJ A2 a) Experimental, numerical b) +58.8 mm c) -58.8 mm. Font: Experimental results obtained from Kusuhara and Shiohara (2008) and Tambusay et al. (2020)

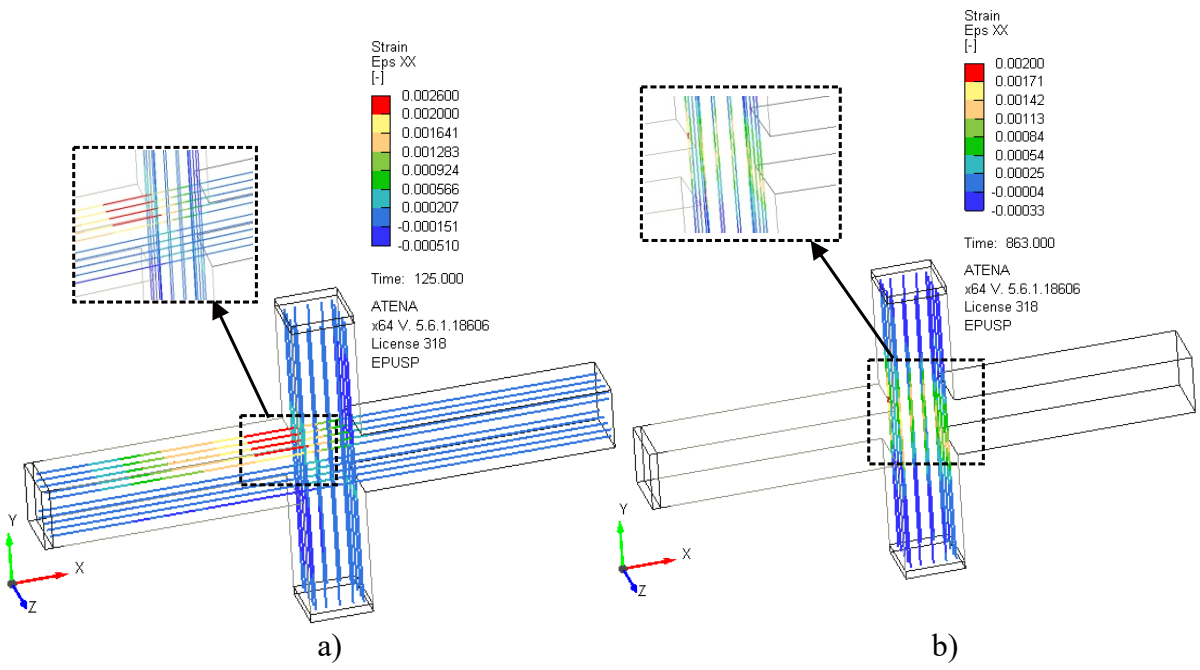

Figure 6.12 – Yielding of the longitudinal steel bars a) Beam b) Column (no yielding).

In the experimental test, the authors Kusuhara and Shiohara (2008) reported the yield of the longitudinal reinforcement of the beam at a horizontal force of 63.3 kN, situation obtained in the numerical model at a load of 63.5 kN, as observed in Figure 6.12.a. Thus, it is concluded that the longitudinal reinforcement yielding of the longitudinal reinforcement of the beam was first identified, followed by shear failure in the connection (BJ Failure mode – Joint failure after beam yielding). Furthermore, yielding in the column reinforcement was not observed in the numerical model, which follows the experimental test reported, as observed in Figure 6.12.b.

From the experimental results, was possible to observe the presence of mild damages, showing a more stable hysteresis behavior and a smaller "pinching" effect, reflected in the hysteresis curve being more diagonally extended. This same behavior was obtained in the response of the developed numerical model.

6.2.3 Model A1 - BCJ of Tsonos (2005)

The hysteresis behavior of the joint A1 is presented in Figure 6.13. For this model, a reasonable fit between the numerical and experimental curves is observed, although the displacements in the last cycles showed relatively higher values, possibly due to the lack of information about the real behavior of the reinforcement.

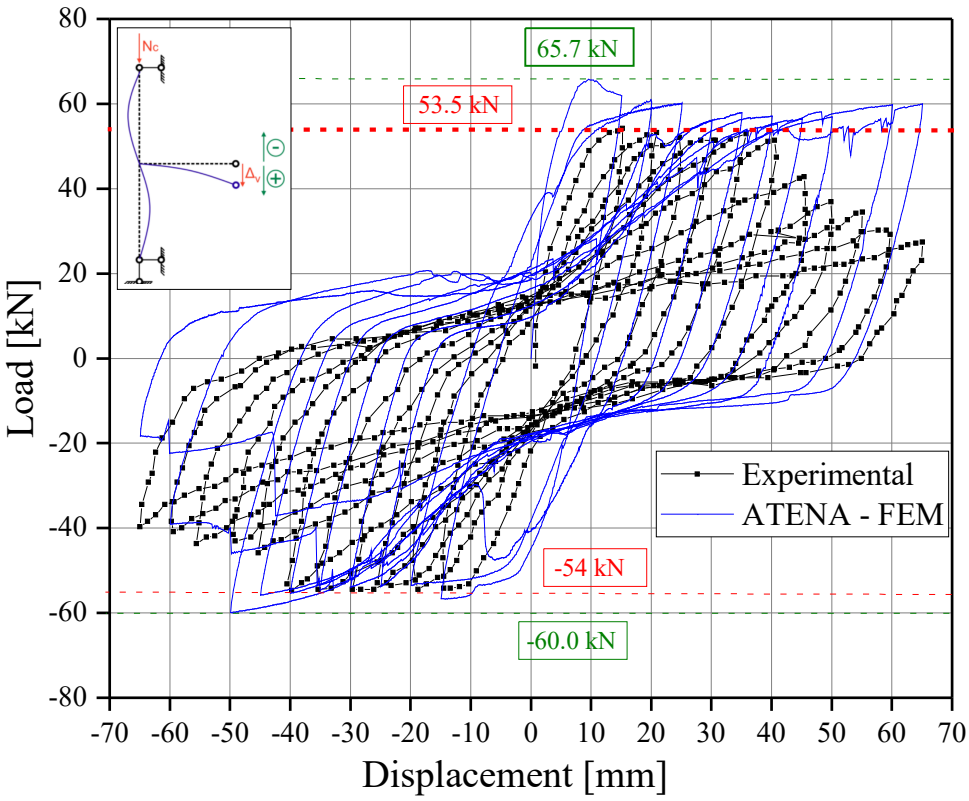

Figure 6.13 – Hysteresis curve BCJ A1.
Font: Experimental results obtained from Tsonos (2005)

In the experimental test, the cyclic loads resisted by the connection presented a value of 53.5 kN in the positive direction (left to right) and -54 kN in the negative direction (right to left). In the numerical model, the obtained result was 65.7 kN for the positive direction and -60 kN

for the negative direction. Figure 6.13 also highlights the similarity between the results of the numerical model and the results of the experimental model, indicating an adequate calibration of the modeling performed.

Figure 6.14 shows the cracking pattern obtained from the experimental test and the numerical modeling conducted for connection A2, corresponding to a horizontal displacement of 65 mm (SD=6.5%). The numerical model shows that, until the last cycles of applied displacement, no concrete crushing was evidenced in the joint core, which is consistent with the experimental report. Regarding the cracking pattern, a concentration of cracks was observed at the beam-joint interface, representing a behavior similar to that presented in the experimental test. In this case, the adequate structural behavior of the connection is highlighted, which can be attributed to the efficient design of the structural elements, carried out following the prescriptions of ACI 352R (2002) and ACI 318 (2005).

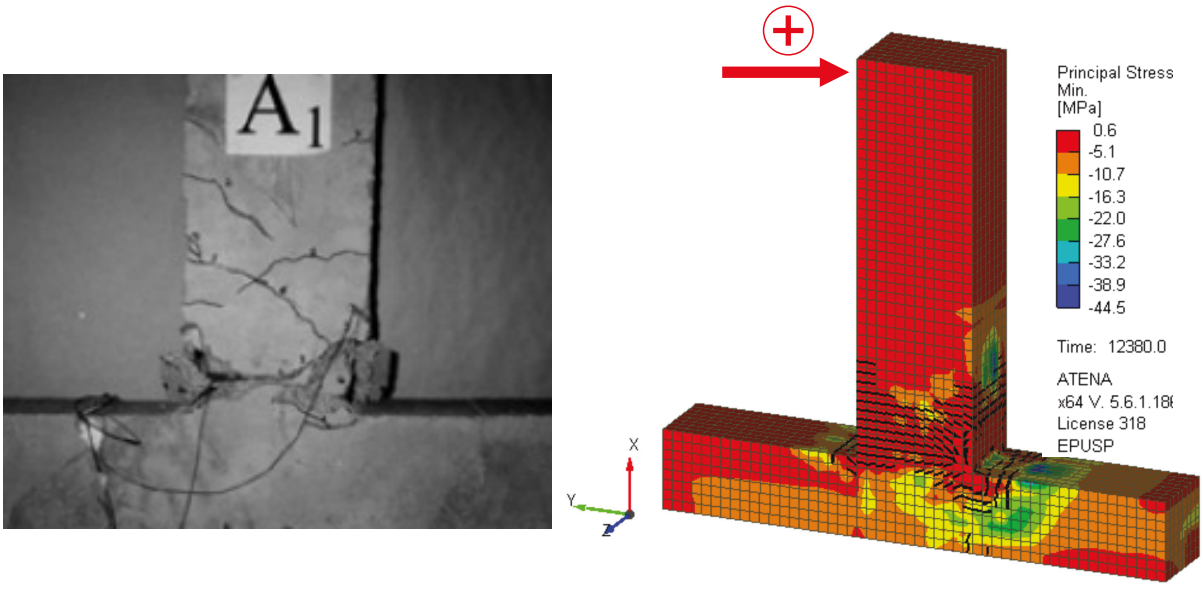

a) b)

Figure 6.14 – Cracks at SD of 6.5% BCJ A1 a) Experimental b) Numerical +65 mm.
Font: Experimental results obtained from Tsonos (2005)

Thus, it can be observed that the methodologies used in this work to simulate external beam-column connections under cyclic loading are suitable for achieving good calibration with experimental results.

6.2.4 Model CJ2 - BCJ of Beschi et al. (2015)

The numerical and experimental hysteresis curves of BCJ and CJ2 were compared in Figure 6.16, showing good accuracy with the experimental results. The numerical hysteresis curve shows that, with positive displacements, the force in the column had a trend almost constant after yielding, while, for negative displacements, the shear force decreases when the displacements increased due to the shear damage in the joint panel, as shown by the experimental curve. In addition, was observed that the pinching effect obtained in the experimental test was reproduced by the numerical model.

Regarding the prediction of the peak shear load in the column V_c, the numerical simulation provided a maximum value of 34.9 kN at a horizontal displacement of 45 mm and -43.1 kN at a horizontal displacement of -30 mm, while in the experimental test, the maximum load was 34.7 kN at a horizontal displacement of 75 mm. Although the maximum loads were reached at different displacements, their values were very close with a percentage difference of 0.6%.

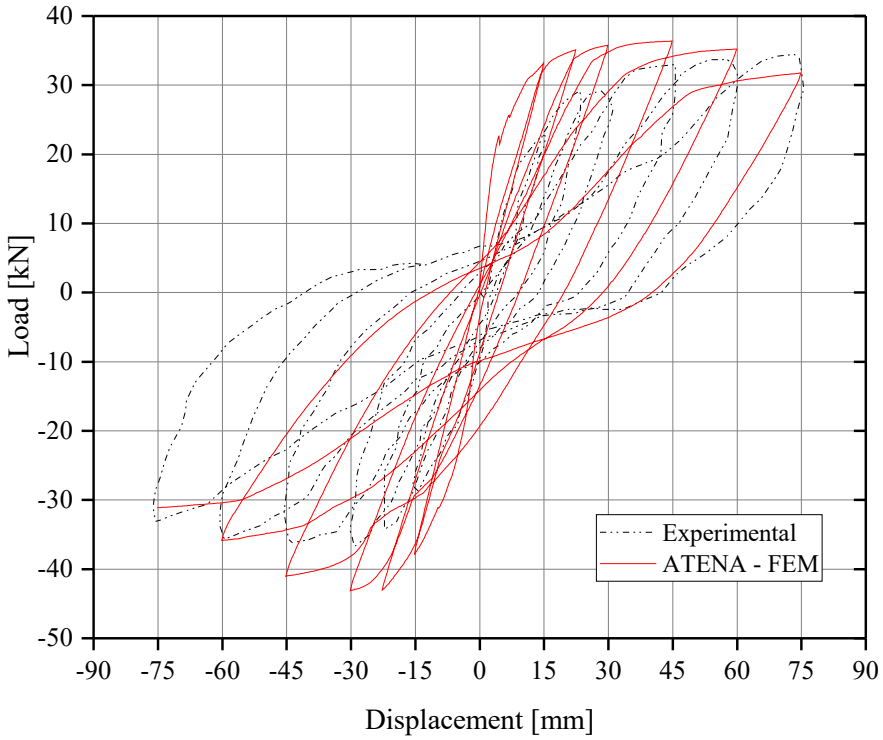

Figure 6.15 – Comparison between the experimental and numerical curve of the beam-column joint without retrofit (CJ2).
Font: Experimental results obtained from Beschi et al. (2015)

The cracking panorama obtained in the numerical model evidenced a good similarity with the experimental one. Figure 6.16 shows the cracks at story drifts of 0.5%, -1%, and 2%, corresponding to horizontal displacements of 15mm, -30mm, and 60mm, respectively. Figure 6.16.a evidenced flexural beam failure at positive horizontal displacement of +15mm (SD of 0.5%) with wide cracks in the beam-joint interface due to the slipping of the smooth bars.

On another hand, Figures 6.16.b and 6.16.c showed diagonal cracks at negative and positive horizontal displacement of -30mm (SD of -1.0%) and +60mm (SD of 2.0%), respectively, where at 1% was evidenced only one diagonal crack and, for 2%, two flexural cracks were developed, both for the experimental and numerical model.

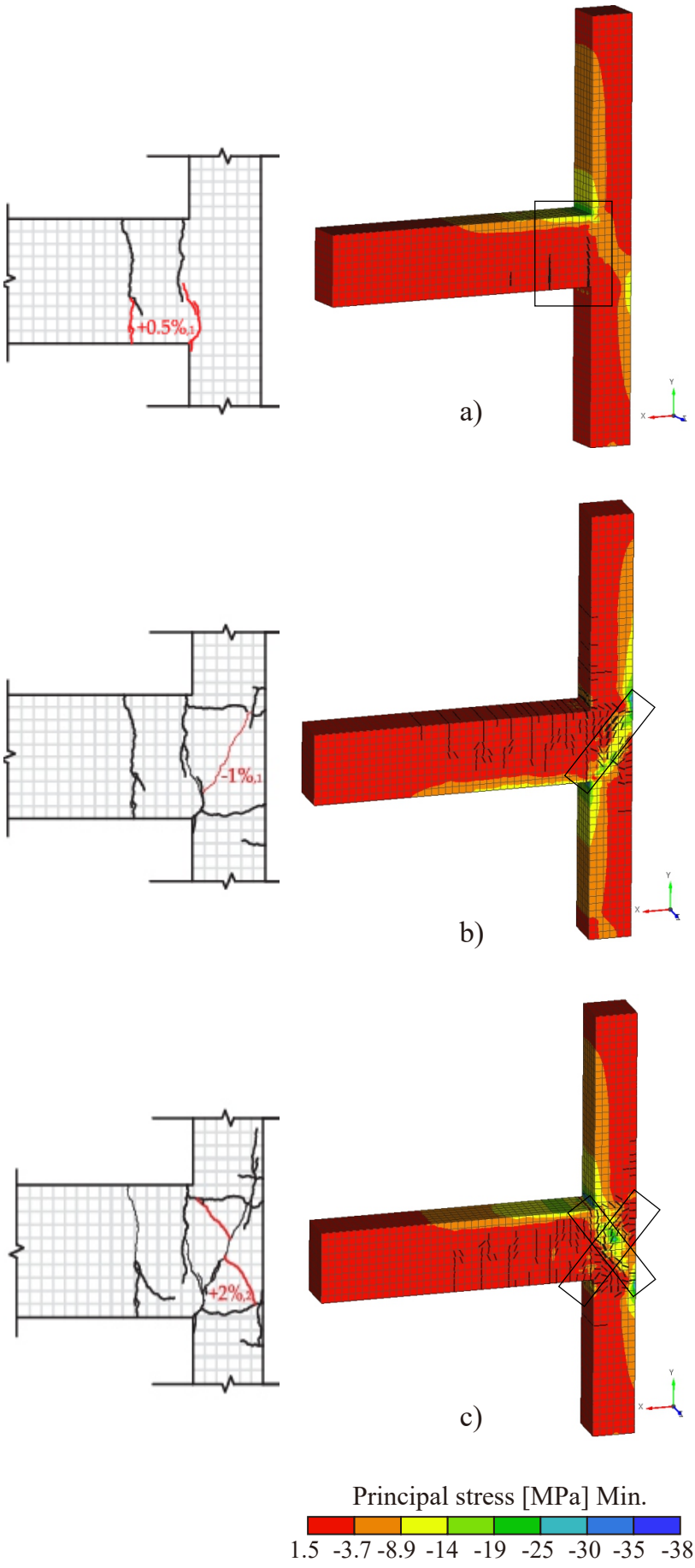

Figure 6.16 – Cracking panorama of BCJ CJ2 at SD of a) 0.5% +15mm, b) 1.0% -30mm, and c) 2.0% +60mm.
Font: Experimental results obtained from Beschi et al. (2015)

6.3 Analytical models validation

6.3.1 Flexural model

The analytical flexural model proposed was validated by comparison with experimental test results available in the literature. The model provides all the required data for applying the proposed model, particularly the experimental tensile stress-strain diagram of the retrofitting material. In this part, three RC columns (R-30, R-25, and Test 1) (MENNA et al., 2016; SAKR et al., 2020) and four RC beam-column joints (R-SED, RCJ2, TS1, and RS-UHPFRC-C) (SHARMA; BANSAL, 2019; BESCHI et al., 2015; KHAN et al., 2018; SAHARAN et al., 2023) were evaluated. All the joint specimens underwent flexural failure.

Table 6.2 summarizes the specimens' properties necessary for the application of the flexural model formulations (see section 2.1). Due to the insufficient experimental information about the UHPFRC tensile behavior of specimens tested by Sharma and Bansal (2019) and Saharan et al. (2023) (specimens R-SD and RS-UHPFRC-C, respectively), for these specimens it was assumed the same UHPFRC tensile strain-stress curve obtained by Khan et al. (2018). The tensile strength f_{ut} used in these specimens was similar to the formula of Graybeal et al. (2006) (Equation 6.1) and provisions given by the NF P 18-710 (2016) (f_{cR} in MPa).

$$f_{ut} \quad \frac{6.7 \quad \overline{f_{cR}}}{\overline{145}} \tag{6.1}$$

Table 6.2 – Specimens properties used for the flexural model validation

Specimen ID	$_R$ [mm]	B [mm]	H [mm]	L_b [mm]	L_c [mm]	f_c [MPa]	f_{cR} [MPa]	Reference
R-30	30	360	360	–	–	18	150	Sakr et al. (2020)
R-25	25	350	350	–	–	18	150	Sakr et al. (2020)
Test 1	60	280	280	–	–	13	107	Menna et al. (2016)
R-SED	25	125	225	950	1000	25.6	107	Sharma and Bansal (2019)
RCJ2	30	360	530	2100	3000	27	110.5	Beschi et al. (2015)
TS1	30	260	310	925	1025	30	145	Khan et al. (2018)
RS-UHPFRC-C	25	125	225	950	1000	122	26.3	Saharan et al. (2023)

Specimen ID	f_{sy} [MPa]	A_{sc} [mm^2]	A_{sc} [mm^2]	f_{ut} [MPa]	f_{ut1} [MPa]	$_{ut,crack}$	$_{ut}$
R-30	360	402.1	402.1	4.9	3.0	0.00012	0.009
R-25	360	402.1	402.1	4.9	3.0	0.00012	0.009
Test 1	450	226.2	226.2	3.8	0.6	0.000103	0.10
R-SED	415	235.6	157.1	7.5	4.4	0.00014	0.011
RCJ2	365	427.3	628.3	6.6	6	0.001	0.005
TS1	605	1256.3	1256.3	7.5	4.4	0.00014	0.011
RS-UHPFRC-C	415	235.6	157.1	7.5	4.4	0.00014	0.011

The ultimate bending moment values obtained from the analytical flexural model (M_{ana}) are reported in Table 6.3, together with the corresponding experimental values (M_{exp}). Due to the presence of axial force in the column of joints, the ultimate bending moment for the specimens R-30, R-25 and Test 1 has been calculated with respect to the axis passing through the geometric centroid of the column cross-section. Table 6.3 shows that all the analytical bending moment values were close to the experimental ones. The maximum moment differences were 10.3%

and 15.2%, for specimens R-SED (SHARMA; BANSAL, 2019) and RS-UHPFRC-C (SAHARAN et al., 2023), respectively, being that those correspond to the specimens with tensile strain-stress behavior of the UHPFRC unknown. For other specimens the absolute percentage error was lower than 9%.

Thus, it was concluded that, when all the required properties are known, the proposed flexural model guarantees good reliability in the prediction of the ultimate bending moment of RC beams intersecting the beam-column joints strengthened by UHPFRC jackets. When this moment acts on the beam cross-section-joint interface, the corresponding acting shear force (V_c) can be calculated through the equilibrium of the beam, expressed as M_{ana} L_b.

Table 6.3 – Analytical and experimental moments and shear actions

Specimen ID	x_c [mm]	M_{ana} [kN.m]	M_{exp} [kN.m]	Error - M [%]	Reference
R-30	9.4	72.1	74.2	2.8	Sakr et al. (2020)
R-25	8.8	65.7	67.7	3.0	Sakr et al. (2020)
Test 1	11.8	38.2	34.9	9.5	Menna et al. (2016)
R-SED	18.6	27.9	25.3	10.3	Sharma and Bansal (2019)
RCJ2	40.6	149.9	148.5	0.9	Beschi et al. (2015)
TS1	67.6	188.7	193.3	2.4	Khan et al. (2018)
RS-UHPFRC-C	18.9	27.9	32.9	15.2	Saharan et al. (2023)

6.3.2 Shear model

The analytical shear model proposed in this work was used to calculate the joint shear strength of specimens available in the literature tested under cyclic loads. The method was applied for three exterior beam-column joints subjected to cyclic load, corresponding to R-SED (SHARMA; BANSAL, 2019), RCJ2 (BESCHI et al., 2015), and RS-UHPFRC-C (SAHARAN et al., 2023) joints, respectively.

Table 6.4 summarizes the specimens' properties utilized to apply the shear model formulation (see section 2.2). This table also shows the analytically determined values of the acting shear force transferred by the beam to the joint core (V_{jh}^{A}) (Equation 4.57), and the contributions of this shear force distributed to the joint core and the UHPFRC jacket, V_{jhc}^{A} and V_{jhR}^{A} respectively. The analytical values for shear force in the column (V_c) are also presented, following Equation 4.59.

The effective mean lateral confining pressure ($_2$), and the confined concrete compressive strength (f_{cc}) are shown in Table 6.4, determined by Equations 4.41 and 4.43-4.44, respectively. Comparing the values of f_{cc} reported in Table 6.4 with the values of f_c reported in Table 6.2, it was possible to observe an increase of at least 9.4% in the compressive strength. The concrete contribution to the joint shear strength (V_{jhc}) and the total shear force (V_{jh}) shown in Table 6.4, were determined through Equations (4.47) and (4.56), respectively.

In addition, considering Equation (4.56) and the values presented, was possible to conclude that in 2 out of 3 cases, the main contribution to the joint shear strength was given by

the second term of the equation, expressed as V_{jhc} $G_R A_R$ $G_c A_c$, which is due to the UHPFRC retrofit. In fact, the percentage contributions of the jacket to joint shear strength were 65.6%, 28.6%, and 67.2% for specimens R-SED, RCJ2, and RS-UHPFRC-C, respectively.

By comparing the values of the acting shear force (V_{jh}^A) and the shear strength (V_{jh}) stated in Table 6.4, it was observed that, for all the strengthened specimens, the shear strength was higher than the acting shear force, with differences of 33.3%, 27.1% and 49.9%, for specimens R-SED, RCJ2 and RS-UHPFRC-C, respectively. Based on this comparison, no specimen undergoes joint shear failure, which corresponds to the results obtained in the experimental tests.

In the proposed shear model, the shear strength contribution of the jacket is quantified, in Equation 4.56, as the product between the shear strength of joint core and the ratio between the shear stiffness of the jacket and the shear stiffness of the joint core. In cases where the joint core is subjected to shear forces, and after of develop the first plastic damage, the shear force in the concrete diagonal strut continues to increase, until the peak shear stress is reached, and, then, decreases. Due to the plastic damage caused by cracking, the joint core shear stiffness reduces. According to Equation (4.56), if the shear modulus of the joint core, G_c, reduces, the second term of the equation, which represents the jacket contribution to joint shear strength, increases, until the peak load is reached. For this reason, the fact that the predicted shear strengths of specimens in Table 6.4 were always higher than the shear actions seem correct.

Being the BCJs shear strength unknown, since the specimens underwent beam flexural failure, this is the only possible comparison that can be made. It seems improbable that BCJs reinforced by UHPFRC jackets fail due to shear, since the jacket is used to increase the shear strength of joints to promote the beam flexural failure, preventing joint shear failure, which is an unwanted brittle mechanism. Moreover, the accuracy of the proposed model in predicting each of the two contributions to joint shear strength, V_{jhc} and V_{jh}^R, provided by the joint core and the jacket, respectively, have been checked. In particular, it has been observed that V_{jhc} and V_{jh}^R are always greater than the maximum shear force acting, respectively, in the core and in the jacket, V_{jhc}^A and V_{jhR}^A, respectively.

All these results suggest that the model can predict that the joint, both in the overall and in its components is subjected to actions lower than those producing shear failure. Moreover, they highlight the efficacy of UHPFRC as retrofitting material to avoid undesirable shear failure in non-seismic exterior beam-column joints subject to cyclic load.

Table 6.4 – Acting shear forces and shear strengths of BCJ specimens

Specimen ID	E_c [MPa]	E_R **[MPa]**	G_c **[MPa]**	G_R **[MPa]**	T_R **[kN]**	V_c **[kN]**	V_{jhc}^A **[kN]**	V_{jhR}^A **[kN]**	**Reference**
R-SED	23780	39614	9908	16505	38.3	27.9	38.9	74.1	Sharma and Bansal (2019)
RCJ2	24421	36000	10175	15000	158.6	49.99	194.4	77.9	Beschi et al. (2015)
RS-UHPFRC-C	23654	42381	9856	17658	38.3	32.8	35.5	72.7	Saharan et al. (2023)

Specimen ID	V_{jh}^A **[kN]**	2 **[MPa]**	f_{cc} **[MPa]**	V_{jhc} **[kN]**	V_{jh}^R **[kN]**	V_{jh} **[kN]**
R-SED	113.1	1.57	29.53	51.9	98.9	150.8
RCJ2	272.4	0.65	29.55	247.1	99.1	346.2
RS-UHPFRC-C	108.2	1.57	30.26	53.2	108.9	162.1

6.4 Comparative study: Numerical, experimental and analytical of retrofitted BJCs

6.4.1 Model RCJ2 - BCJ of Beschi et al. (2015)

Figure 6.18 shows the comparison between the numerical and experimental hysteresis curve of BCJ retrofitted with the HPFRC jacket (RCJ2), with a good accuracy between the results and the peak load. The numerical model predicted a peak shear load in the column (V_c) of 45 kN at a horizontal displacement of 15 mm, while, in the experimental test, the maximum load was 49.5 kN at a horizontal displacement of 22.5 mm, resulting in a percentage load difference of 9.1%. Since the ability of the numerical model to predict the maximum load is satisfying, the chosen interface relationship can well represent the real interaction between concrete and UHPFRC, when adequate values of the relationship parameters are used.

Based on the observations made about the implemented numerical models, it can be said that they simulate RC exterior BCJs behavior under cyclic loads sufficiently accurately, especially for the prediction of the maximum load, which is the main parameter of interest to verify the joint strength. This allows the use of numerical models to determine the acting shear force in BCJs.

Figure 6.18 also shows the shear load in the column (V_c), calculated through the analytical formulation of Equation (4.59). Since the specimens considered were subjected to beam flexural failure, the shear on the beam at failure (V_b) required by Equation (4.59) was calculated dividing the beam resisting bending moment, obtained from the flexural model (Equation 4.37), by the length . The acting force on the column obtained by Equation (4.59) had a value of 49.99 kN, showing a percentage difference of 0.8% compared to the experimental result.

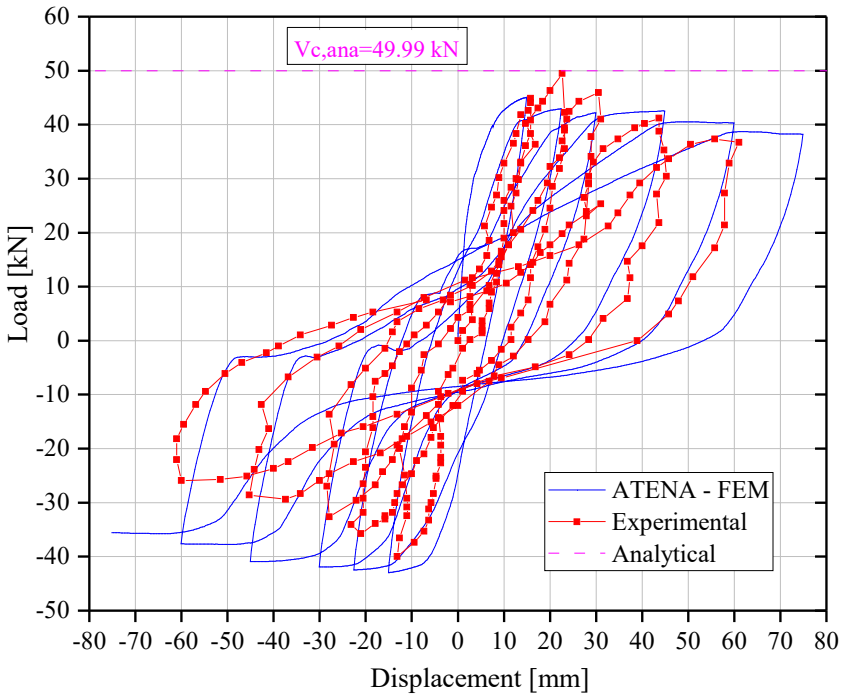

Figure 6.17 – Comparison between the experimental and numerical curve of the beam-column joint strengthened with HPFRC (RCJ2).
Font: Experimental results obtained from Beschi et al. (2015)

Table 6.5 summarizes the shear load values in the column obtained by the experimental test, analytical, and numerical models for both the specimens considered. Both analytical and numerical models predicted very well the maximum shear load on the column at the beam flexural failure. In particular, the proposed analytical model was the most accurate. This was a further validation of the proposed flexural model. It is stressed that the shear force in the column, was the maximum one, because, after the beam flexural failure, the shear in the column cannot increase anymore.

Table 6.5 – Values of the shear load in the column (V_c) obtained from the experimental test and the analytical and numerical models, and comparisons

Specimen ID	**Exp. [kN]**	**Ana. [kN]**	**FEM [kN]**	**Error [%] Exp/Ana**	**Error [%] Exp/FEM**
CJ2	34.7	–	34.9	–	0.6
RCJ2	49.5	49.9	45.0	0.8	9.1

This value of shear force is not reached if the shear failure occurs in the joint before the beam flexural failure. Knowing the joint shear strength from the shear model (Equation (4.56)) and comparing this value with the maximum joint shear force, obtained from Equation (4.57), at the beam flexural failure, was possible to establish if joint shear failure can occur or not. In this sense, the proposed flexural model, from which the maximum joint shear force can be derived, and the shear model, which provides the joint shear strength, appear as valuable tools for researchers and engineers to establish which type of failure will occur in BCJs retrofitted with UHPFRC jacket. If shear failure results from the design of the retrofitted joint, was possible to avoid this failure by increasing the UHPFRC jacket thickness until flexural failure occurs instead of shear one.

Figure 6.18 shows the evolution of the crack pattern of strengthened joint RCJ2. In the negative direction corresponding to a horizontal displacement of -15mm (SD= -0.5%), the joint developed vertical flexural cracks at the beam-joint interface, and small diagonal cracks in the top of the joint core, Figure 6.18.a. The increases to a negative horizontal displacement of -30mm (SD= -1%) showed bigger vertical flexural and diagonal cracks in the interface and inside the joint core, respectively, 6.18.b. And for a horizontal displacement of +60mm (SD= 2.0%), the numerical model displayed a higher stress concentration in the top side of the joint and diagonal cracks, as evidenced in the experimental test (Figure 6.18.c). The main difference observed in this research with the experimental results was the absence of higher vertical cracks in the top joint core. However, it could be considered that the numerical methodology used, displays a good accuracy in the joint's cracking panorama.

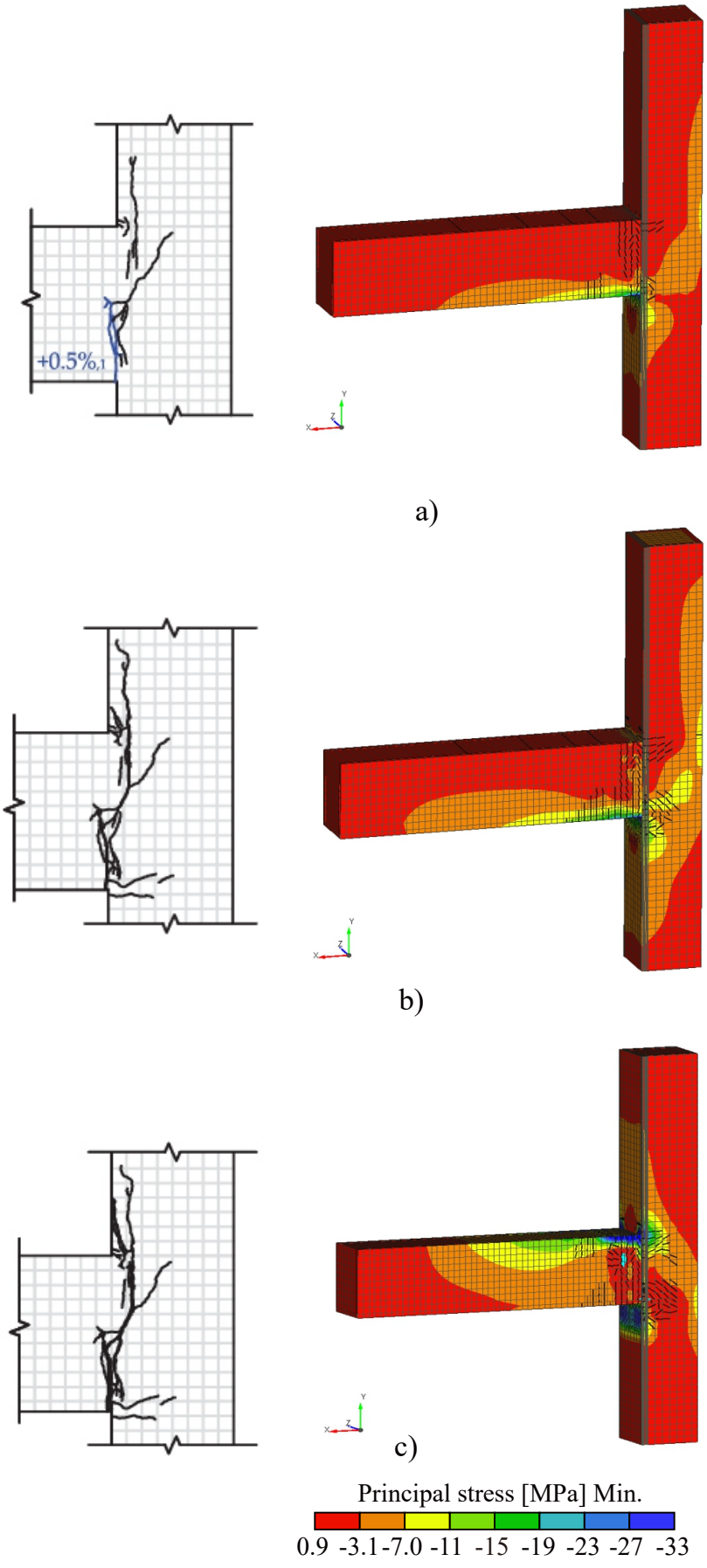

Figure 6.18 – Cracking panorama of BCJ RCJ2 at SD of a) 0.5% +15mm, b) 1.0% -30mm, and c) 2.0% +60mm.
Font: Experimental results obtained from Beschi et al. (2015)

7 Parametric Study

Comparisons between numerical, analytical, and experimental results of retrofitted joints were carried out. For this, a parametric study of strengthened joints with HPFRC jacket was developed in this chapter to verify the reliability of the methodologies previously given and to evaluate the influence on the shear response and optimization of parameters for construction. A series of retrofitted joints under cyclic were numerically modeled and validated analytically, where the retrofitted joint (RCJ2) tested by Beschi et al. (2015) was used as the control test.

Due to the high cost and computational time in the numerical model RCJ2, an optimization of the numerical simulation was developed. For this, a new numerical model for the joint RCJ2 was developed with a reduction of 43.5%, in the step numbers labeled in this work of $RCJ2_{red}$. The RCJ2 model was simulated with 3401 steps, while the $RCJ2_{red}$ model was simulated with 1921 steps, requiring a computational time of 6.5 days (156 hours). Numerical models processing was conducted on a system featuring an Intel(R) Core(TM) i7-12700 CPU operating at 2.1 GHz, with 32.0 GB of installed RAM. Figure 7.1 presents the hysteresis curves of RCJ2 and $RCJ2_{red}$ joints, where it is possible to observe a good accuracy between the models. Considering this beneficial effect on processing and the need to develop diverse numerical models, all the models presented here were simulated with 1921 steps.

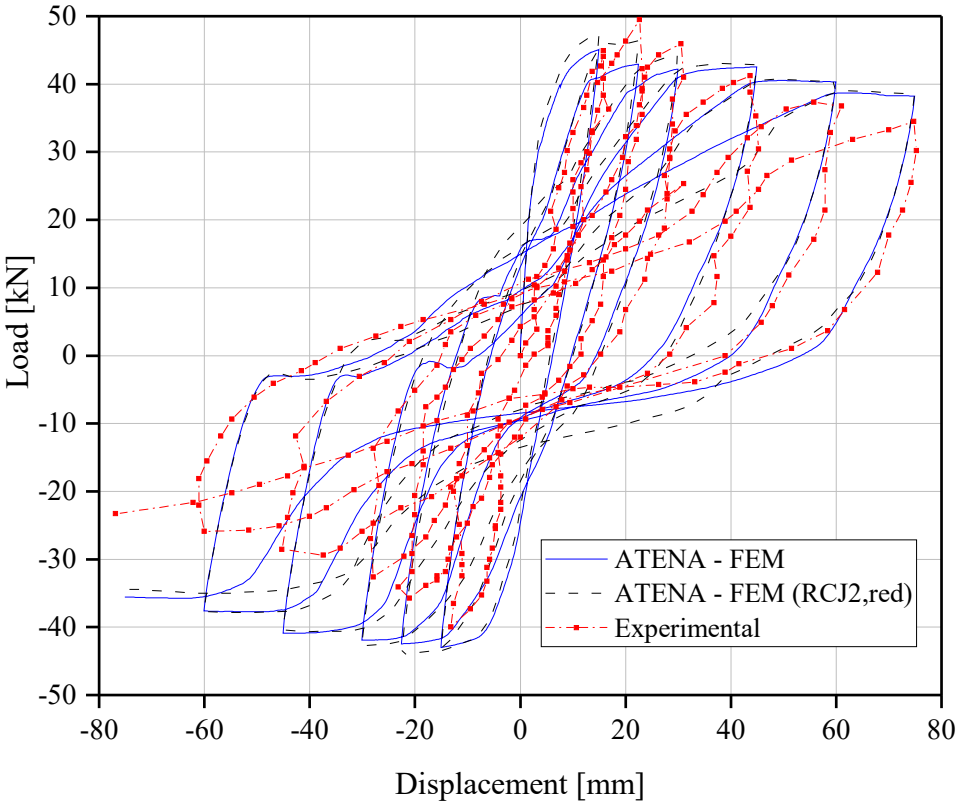

Figure 7.1 – Hysteresis curve comparative using reduction in steps number - RCJ2 joint.
Font: Experimental results obtained from Beschi et al. (2015)

This validation evaluated the influence of certain parameters on the performance of the retrofitting technique used in the present work. These parameters include HPFRC jacket thickness ($_R$), compressive strength of HPFRC (f_{cR}), and beam's reinforcement ratio ( ). For this were investigated: i) three different HPFRC thicknesses corresponding to 15 mm, 30 mm, and 45 mm (Figure 7.2); ii) three compressive strengths of HPFRC with values of 110.5 MPa, 165.8 MPa, and 221.0 MPa, named Models A, B, and C, respectively, and iii) three beam's reinforcement ratio with values 0.4%, 0.7%, and 1.2%, labeled as L(Low), M(Medium), and (High) ratios, respectively. Thus, the specimen's label depends on each value for the parameters analyzed (e.g. A15-L corresponds to the joint strengthened with a HPFRC jacket of thick 15 mm, compressive strength of 110.5 MPa, and beam's steel ratio of 0.4%) (Figure 7.3). In total were investigated 15 specimens and which were divided into six groups, where the specimens A15-M, 30-M, and A45-M, were the same as A15, A30, and A45, respectively (see Tables 7.1 and 7.2). All models had a concrete compressive strength (f_c) of 27 MPa, Figure 5.12

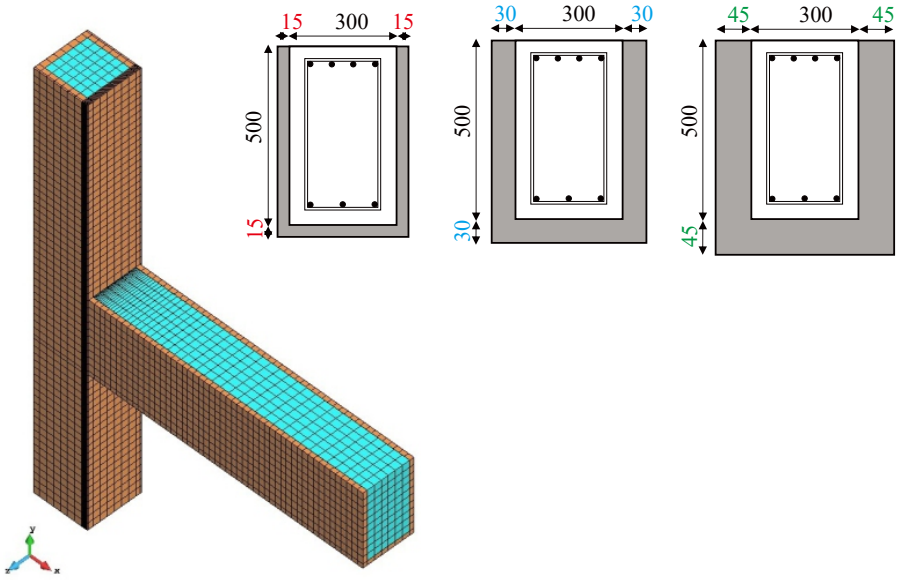

Figure 7.2 – Cross-sections of strengthened joints with HPFRC layers.

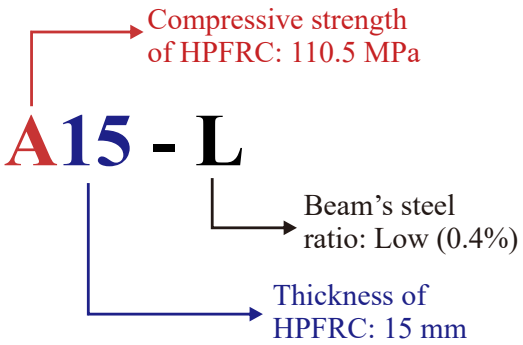

Figure 7.3 – Example of specimen for parametric study.

The beam's cross-sections of each ratio are presented in Figure 7.4, composed of steel

bars of diameter 10 mm, 12 mm, 16 mm, and 20 mm. Because this work wanted to study the influence of the bar diameter, the yield and ultimate strength adopted for the bar diameter of 10 mm were the same as those of 12 mm, and for 20 mm, they were the same as those of 16 mm.

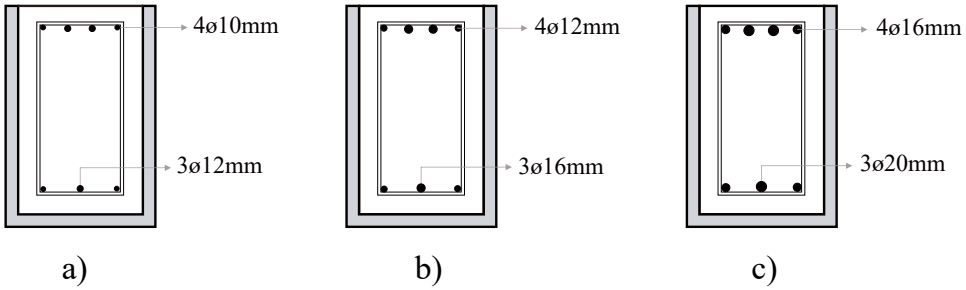

Figure 7.4 – Classification of beam's reinforcement ratio: a) 0.4% b) 0.7% and c) 1.2%.

It's known that when the compressive strength of retrofit material (f_{cR}) changes, the tensile strength of retrofit material of (f_{ut}) also changes. For this reason, Equation 7.1 proposed by (GRAYBEAL et al., 2006) was used to determine the new values of f_{ut} for each model. In the experimental test, the RCJ2 joint had a f_{ut} value of 6.6 MPa, while using Equation 7.1 was of 5.8 MPa. Tables 7.1 and 7.2 show the tensile strength of HPFRC for each specimen investigated.

$$f_{ut} \quad \frac{6.7 \quad \overline{f_{cR}}}{\overline{145}} \tag{7.1}$$

Table 7.1 – Parameters investigated of strengthened joints with different layers and compressive strengths

Specimen ID	**Group**	**HPFRC thickness** $_R$ [mm]	**Compressive strength of HPFRC** f_{cR} **[MPa]**	**Tensile strength of HPFRC** f_{ut1} **[MPa]**
A15	Group 1	15	110.5	5.8 (A)
B15			165.8	7.1 (B)
C15			221.0	8.2 (C)
A30	Group 2	30	110.5	5.8 (A)
B30			165.8	7.1 (B)
C30			221.0	8.2 (C)
A45	Group 3	45	110.5	5.8 (A)
B45			165.8	7.1 (B)
C45			221.0	8.2 (C)

Table 7.2 – Parameters investigated of strengthened joints with different layers and beam's reinforcement ratios

Specimen ID	**Group**	**HPFRC thickness** $_R$ [mm]	**Bar diameter** $_{b1}$ **[mm]**	**Bar diameter** $_{b2}$ **[mm]**	**Beam's reinf. ratio** $_b$ **[%]**
A15-L	Group 4	15	10	12	0.4
A15-M(A15)			12	16	0.7
A15-H			16	20	1.2
A30-L	Group 5	30	10	12	0.4
A30-M(A30)			12	16	0.7
A30-H			16	20	1.2
A45-L	Group 6	45	10	12	0.4
A45-M(A45)			12	16	0.7
A45-H			16	20	1.2

7.1 Numerical models

Figure 7.5 shows the mesh discretization of the joints retrofitted with a HPFRC jacket of thickness 15 mm, 30 mm, and 45 mm. All models were simulated with the same concrete compressive strength and constitutive models for the concrete and steel reinforcement.

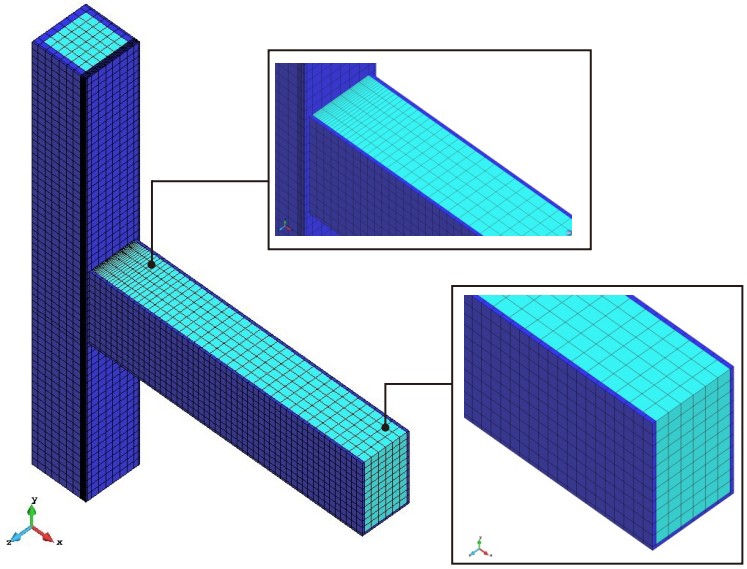

(a)

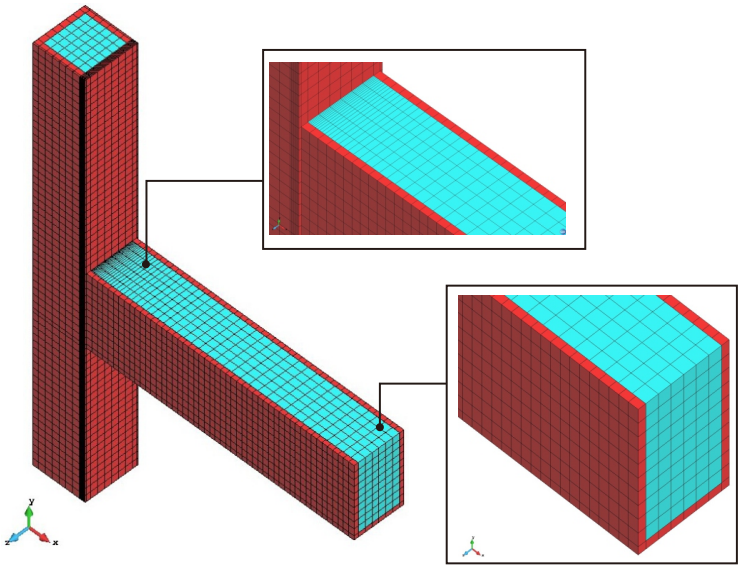

(b)

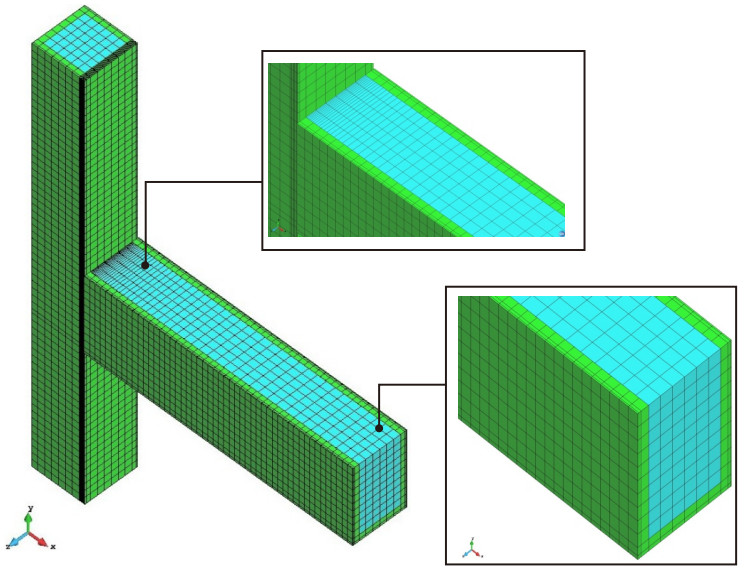

(c)

Figure 7.5 – Mesh discretization of strengthened joints with thickness layer of a) 15 mm, b) 30 mm, and c) 45mm.

To obtain the tension behavior of the joints for each model (A, B, C), three supplementary dog-bone models were developed, corresponding to the compressive strength of HPFRC of 110.5 MPa, 165.8 MPa, and 221.0 MPa, respectively. The tensile stress-strain curves of each case were obtained through the simplified model used by Xin et al. (2023), which is represented by a bilinear curve of strain-softening (Figure 7.6). Figures 7.7, 7.8, and 7.9 present the tensile strain-diagram for HPFRC material for A, B, and C models. Here, it is possible to observe the increase of the tensile strength f_{tu1} when the compressive strength f_{cR} also increases.

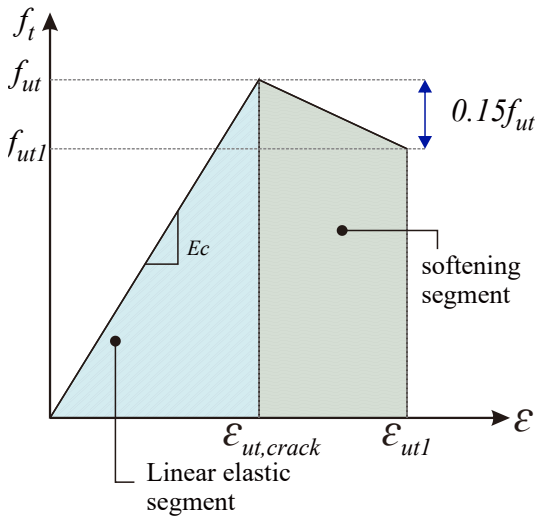

Figure 7.6 – Scheme of the envelope curve of strain softening UHPFRC.
Font: Adapted from Xin et al. (2023)

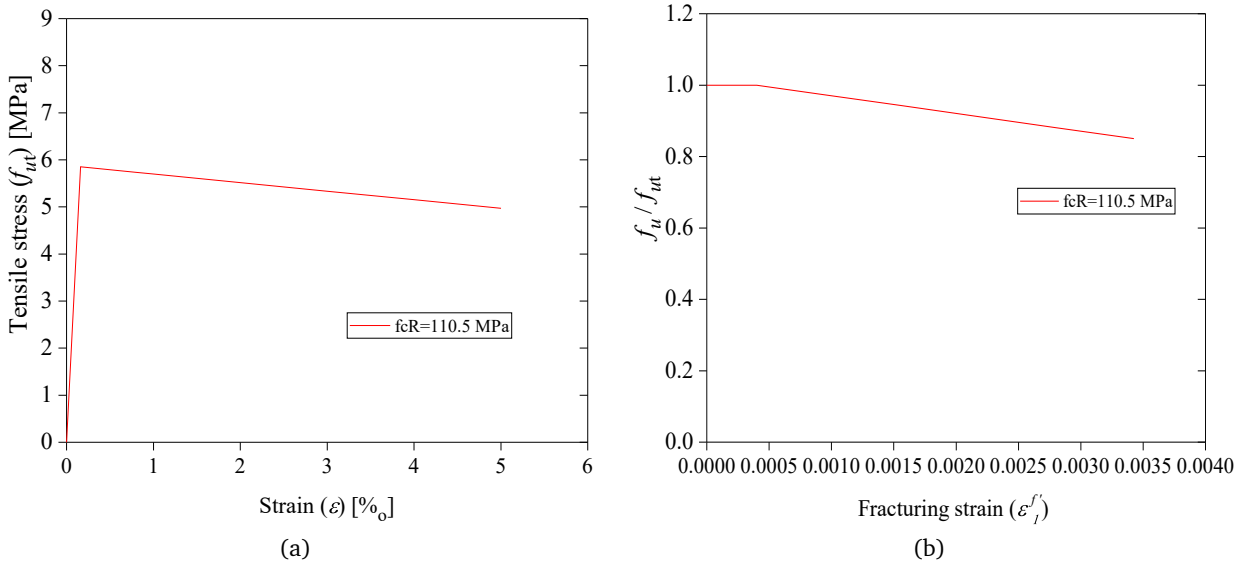

Figure 7.7 – Tensile stress-strain model of UHPFRC of A model represented by: a) Simplified diagram, b) Constitutive model in Atena.

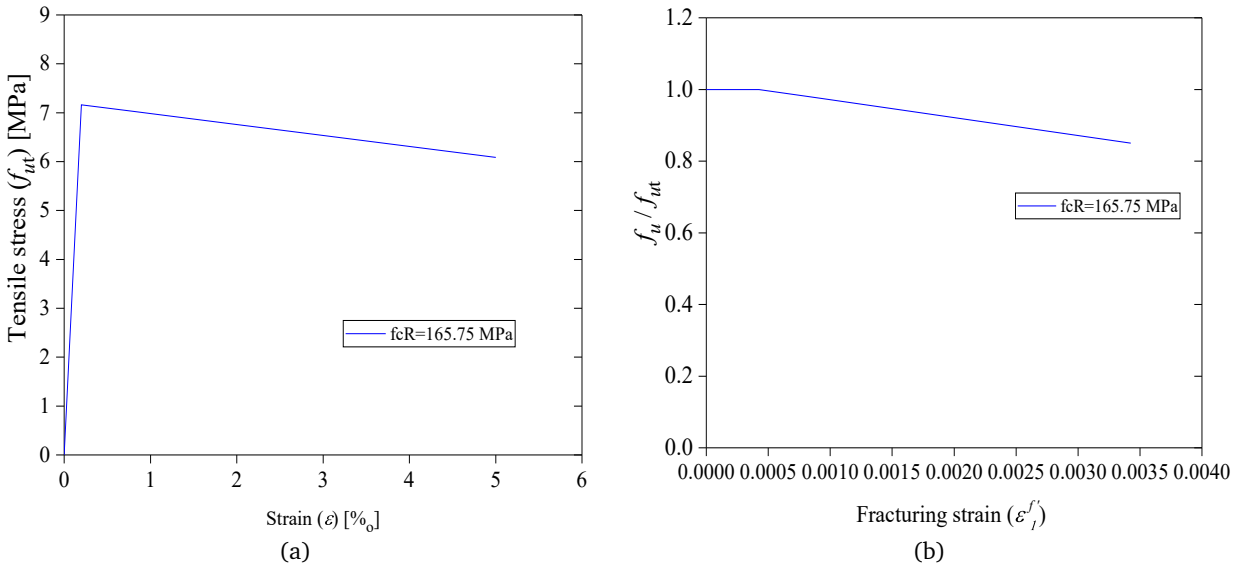

Figure 7.8 – Tensile stress-strain model of UHPFRC B model represented by: a) Simplified diagram, b) Constitutive model in Atena.

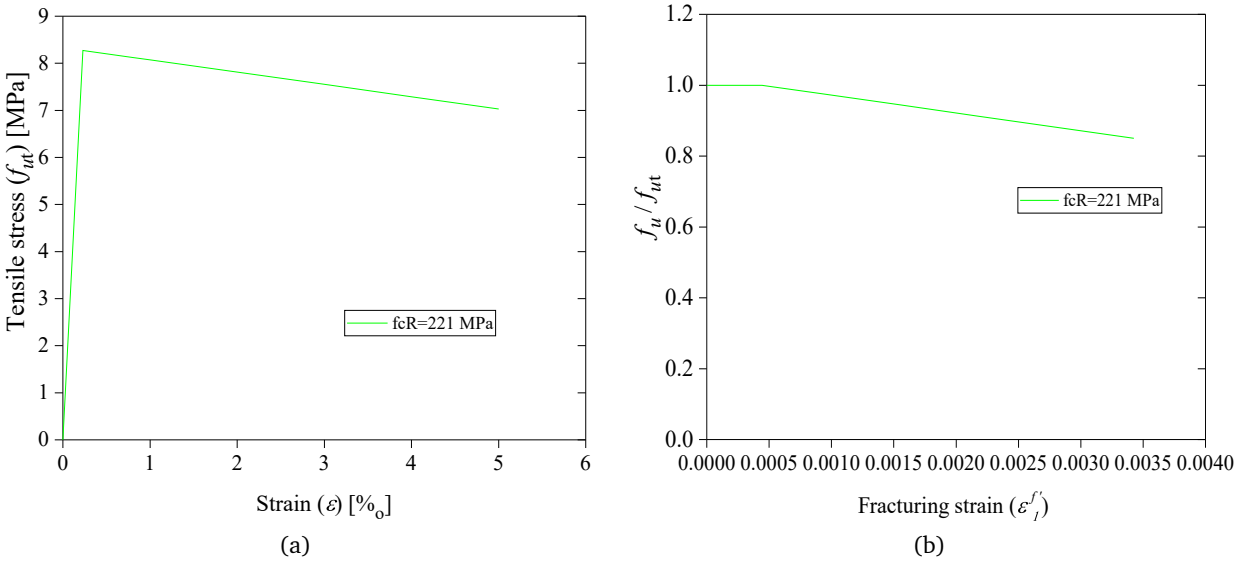

Figure 7.9 – Tensile stress-strain model of UHPFRC for C model represented by: a) Simplified diagram, b) Constitutive model in Atena.

Figure 7.10 shows the comparison between the tensile strain-stress curves obtained from the simplified formulation (Figure 7.6) and numerical dog-bone models, with good accuracy in the results for all the cases. Thus, the functions used in ATENA in these models were utilized in the simulations of all specimens.

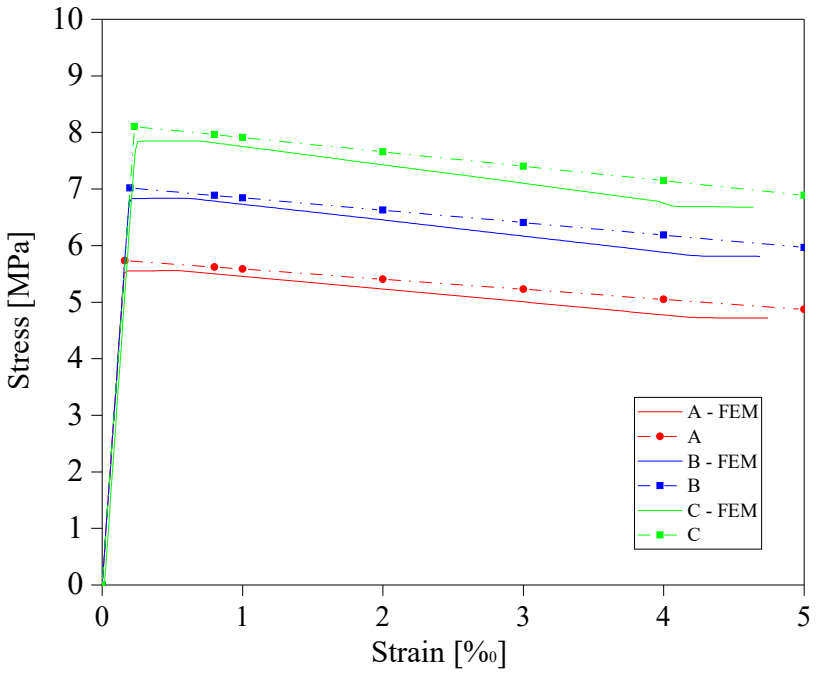

Figure 7.10 – Comparison between analytical and numerical functions of HPFRC tensile behavior for A, B, and C models.

7.2 Analytical models

The analytical method presented in Chapter 4 was used to determine the maximum shear forces in the column (V_c). This method can be considered a good tool for assessing the shear V_c with low computational cost. Table 7.3 summarizes the main geometrical and mechanical properties of the joints utilized in the flexural model validation. The tensile parameters of HPFRC material were taken from the diagrams shown in Figures 7.7, 7.8, and 7.9. It is emphasized that all models were assumed to exhibit flexural failure, as the application of flexural modeling techniques is valid only for specimens characterized by this specific failure mechanism.

Table 7.3 – Specimens properties used for the flexural model of parametric study

Specimen ID	R [mm]	B [mm]	H [mm]	f_{cR} [MPa]	f_{sy} [MPa]	A_{sc} [mm^2]	A_{sc} [mm^2]	f_{ut} [MPa]	f_{ut1} [MPa]	$_{ut,crack}$	$_{ut}$
A15 (A15-M)	15	330	515	110.50	365	427.3	628.3	5.8	4.9	0.000163	0.005
B15	15	330	515	165.75	365	427.3	628.3	7.1	6.0	0.000199	0.005
C15	15	330	515	221.00	365	427.3	628.3	8.2	7.0	0.000229	0.005
A30 (A30-M)	30	360	530	110.50	365	427.3	628.3	5.8	4.9	0.000163	0.005
B30	30	360	530	165.75	365	427.3	628.3	7.1	6.0	0.000199	0.005
C30	30	360	530	221.00	365	427.3	628.3	8.2	7.0	0.000229	0.011
A45 (A45-M)	45	390	545	110.50	365	427.3	628.3	5.8	4.9	0.000163	0.005
B45	45	390	545	165.75	365	427.3	628.3	7.1	6.0	0.000199	0.005
C45	45	390	545	110.50	365	427.3	628.3	8.2	7.0	0.000229	0.005
A15-L	15	330	515	110.50	365	270.1	383.3	5.8	4.9	0.000163	0.005
A15-H	15	330	515	110.50	445	716.3	1030.4	5.8	4.9	0.000163	0.005
A30-L	30	360	530	110.50	365	270.1	383.3	5.8	4.9	0.000163	0.005
A30-H	30	360	530	110.50	445	716.3	1030.4	5.8	4.9	0.000163	0.005
A45-L	45	390	545	110.50	365	270.1	383.3	5.8	4.9	0.000163	0.005
A45-H	45	390	545	110.50	445	716.3	1030.4	5.8	4.9	0.000163	0.005

7.3 Results of parametric study

7.3.1 Numerical results

The numerical shear forces V_c were achieved from the peak value of each load-displacement curve, corresponding to fifteen different joints. Furthermore, this work also presents the hysteresis curves and the cracking panorama of each retrofitted joint obtained from the numerical results.

Figure 7.11 illustrates the comparison of the hysteresis curves of non-retrofitted (named Control Specimen (CS)) and retrofitted (with different thicknesses of HPFRC jacket) joints. Here, all the joints had a compressive strength of HPFRC and concrete of 110.5 MPa (Model A) and 27 MPa, respectively. Is it important to highlight that the simulation of the CS model in the ATENA software was needed because, in the experimental test, the specimen without retrofit had a compressive strength of concrete of 38.7 MPa instead of 27 MPa (BESCHI et al., 2015).

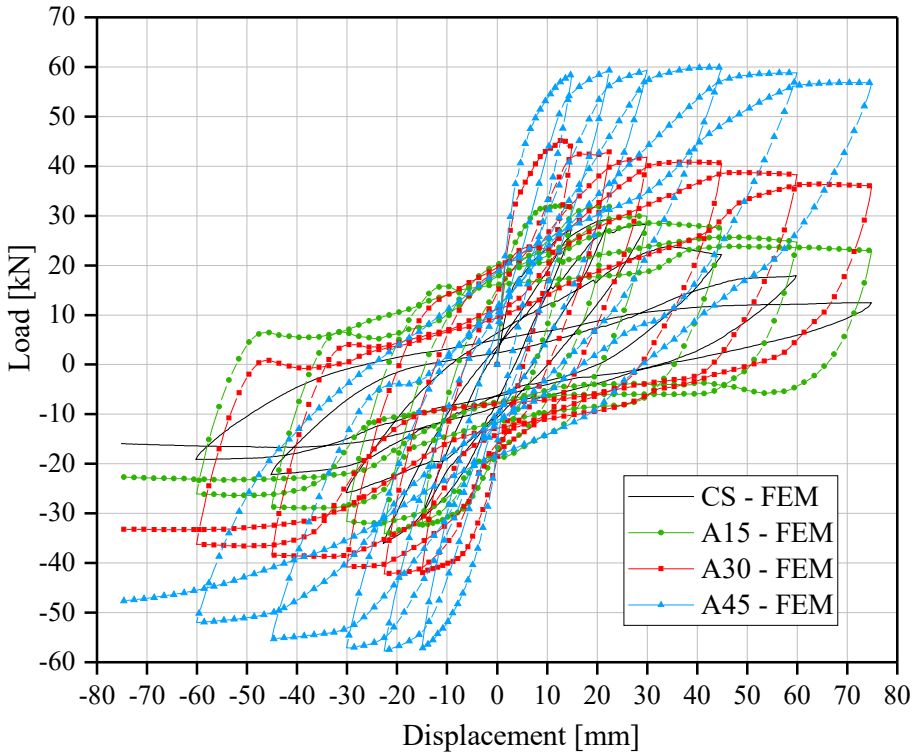

Figure 7.11 – Hysteresis curves of non-retrofitted joint and retrofitted joints with HPFRC jackets of different thicknesses

The results show that the retrofit layer's thickness influenced the column's shear force. When the thickness ($_R$) increased, the shear force in the column (V_c) also increased, as expected. The non-retrofitted joint (CS joint) had a maximum shear force of +29.3 kN at a displacement of +22.5 mm, while the joint retrofitted with HPFRC jackets 15 mm, 30 mm, and 45 mm thick presented a maximum shear force of +33.0 kN, +45.5 kN, and +59.9 kN, respectively, at displacements of -22.5 mm, +15 mm, and +22.5. In addition, the CS joint presented a higher stiffness degradation than retrofitted joints as the cyclic displacements increased, which can be caused by the absence of the retrofit jacket. However, the A45 joint showed the lowest reduction in stiffness compared with the A15 and A30 models, showing that as the jacket thickness increases,

its capacity to maintain close values of V_c in all its cycles also increases.

The beneficial effect of the HPFRC jacket thickness has been quantified through the factor of retrofit (F_R), which is determined as the ratio between the shear force of the retrofitted joint and CS joint ($F_R = V_{c,retrofitted joint}/V_{c,CS joint}$), as proposed by Lampropoulos et al. (2024). Figure 7.12 presents the F_R value for each HPFRC jacket thickness.

Figure 7.12 shows F_R values in the range from 1.1 to 2.0, with specific values of 1.1, 1.6, and 2.0 for the A15, A30, and A45 joints, respectively. A slight reduction in the slope of the F_R curve was evidenced when the joints were strengthened with jackets of thickness higher than 30 mm. A similar behavior was exhibited in columns with jackets of thickness of 50 mm (LAMPROPOULOS et al., 2024).

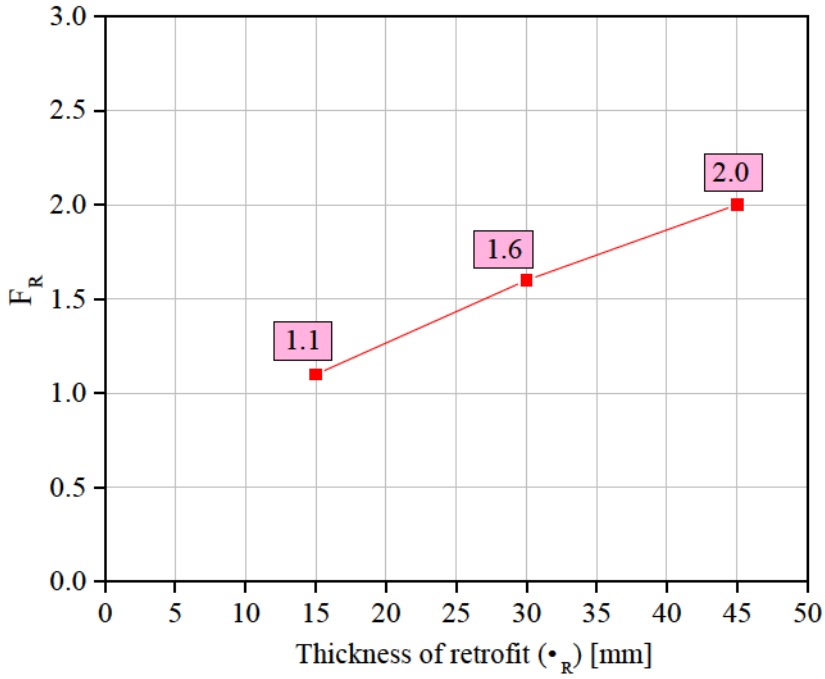

Figure 7.12 – F_R factor for joints retrofitted with different thicknesses

Figure 7.13 presents the hysteresis curves of joints retrofitted with UHPFRC jackets 15 mm, 30 mm, and 45 mm thick, respectively, with different compressive strengths of HPFRC, designed as models A, B, and C. The results showed that with the increase of strength f_{cR} and jacket thickness (δ_R), the V_c force also increased. The specimens C15, C30, and C45 presented the highest shear force values of 36.4 kN, 51.6 kN, and 71.2 kN, respectively, at horizontal displacements of +22.5 mm, +15 mm, and +45 mm, respectively.

A bigger pinching effect was observed in joints strengthened with jackets of 45 mm than in those with jackets with 15 mm and 30 mm. In addition, all specimens showed a greater stiffness degradation in the negative cycles than in the positive cycles, mainly those of low thickness ρ_R. The joints retrofitted with HPFRC jackets of 15 mm, 30 mm, and 45 mm presented a maximum reduction in the force V_c of 29.8%, 21.0%, and 16.6%, respectively, between the first and the ultimate negative displacement (-15 mm and -75 mm). Thus, the joints retrofitted with a 45 mm HPFRC layer exhibited the least reduction in shear force and tended to maintain stability during

positive displacements, thereby enhancing the ductility of the joints.

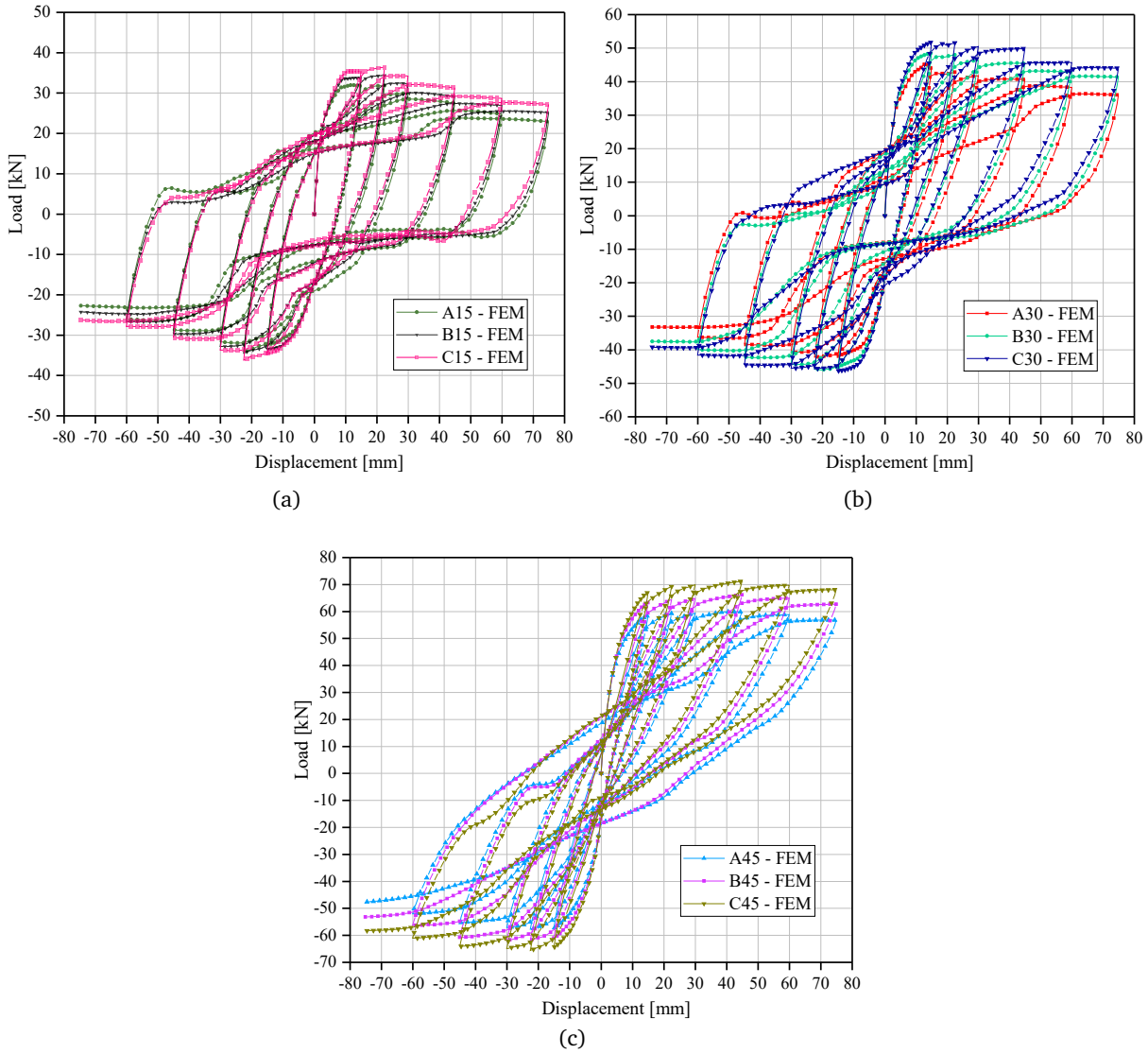

Figure 7.13 – Hysteresis curves of BCJS retrofitted with HPFRC jacket of thickness a) 15 mm, b) 30 mm, and c) 45 mm, varying the compressive strength of HPFRC (models A, B, and C)

The curves presented in Figure 7.14 show the hysteresis behavior of the retrofitted joints with UHPFRC jacket of 15 mm, 30 mm, and 45 mm thick, respectively, with different beam's reinforcement ratios of 0.4%, 0.7%, and 1.2%, named with the letters *L* (Low), *M* (Medium), and *H* (High), respectively. The joints with a ratio of 1.2% (High ratio) showed higher values of force V_c (63.4 kN, 56.4 kN, and -49.2 kN), compared with the joints of Low (29.1 kN, 41.2 kN, and 50 kN) and Medium ratio (32 kN, 45.5 kN, and 59.9 kN). A bigger stiffness degradation was evidenced in the joints with Low ratio, compared with joints with a High beam's reinforcement ratio. The capacity to absorb fracture energy was bigger in joints with High ratio, presenting hysteresis curves with a smaller pinching effect.

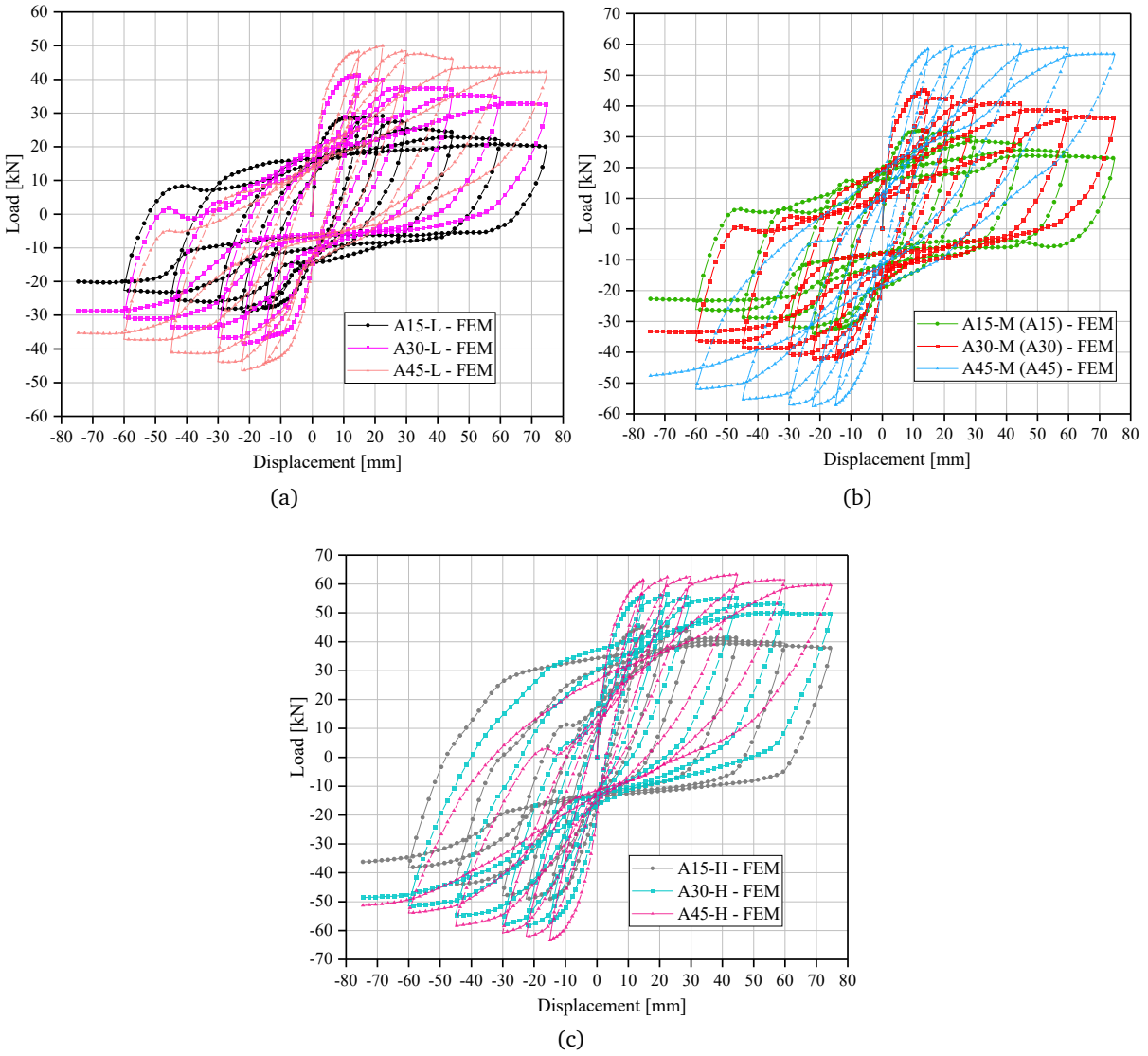

Figure 7.14 – Hysteresis curves of BCJs with beam's reinforcement ratios of a) 0.4% (L), b) 0.7% (M), and c) 1.2% (H), varying the thickness of the HPFRC layer

It is important to observe that the specimens A15-H and A30-H presented higher values of V_c (49.2 kN and 56.4 kN), compared with C15 and C30, with values of 36.4 kN and 51.6 kN, respectively, showing better results with the increasing of the ratio $_b$ instead of the compressive strength f_{cR}. However, when the specimen was retrofitted with a layer of 45 mm, this situation was more beneficial for f_{cR}, with values of 63.4 kN for A45-H and 71.20 kN for C45. Therefore, the ratio $_b$ has a bigger effect on the joint's shear capacity than the strength f_{cR} up to a retrofit layer of 30 mm, since 45 mm thick jackets did not exhibit the same.

The effect on the shear force, varying the compressive strength and the thickness of the HPFRC also was investigated. Figures 7.15 and 7.16 show the comparative of the shear force in the column with different values of $_R$ and fc_R, and beam's reinforcement ratio of 0.7%. These graphics showed a marked impact in the shear force, where the increasing percentage when the joint was retrofitted with a jacket from 15 mm to 30 mm and with a compressive strength of 221 MPa was 41.8%, and for compressive strength of 110.5 MPa was 42.2%. In addition, increasing

the compressive strength and maintaining the same thickness of the jacket, the shear force also increased (e.g., joints retrofitted with a jacket of 15 mm evidenced an increase of 7.8% when changing f_{cR} from 110.5 MPa to 165.8 MPa and of 5.5% when changing the f_{cR} of 165.8 MPa to 221.0 MPa). However, the increase of the force was smaller when the specimens changed f_{cR} from 165.8 MPa to 221.0 MPa (5.5%, 6.3%, and 7.6%), and from 30 mm to 45 mm (31.6%, 36.5%, and 37.9%), compared with the increase obtained from 110.5 MPa to 165.8 MPa (7.8%, 6.6%, and 10.5%), and from 15 mm to 30 mm (42.2%, 36.5%, and 37.9%).

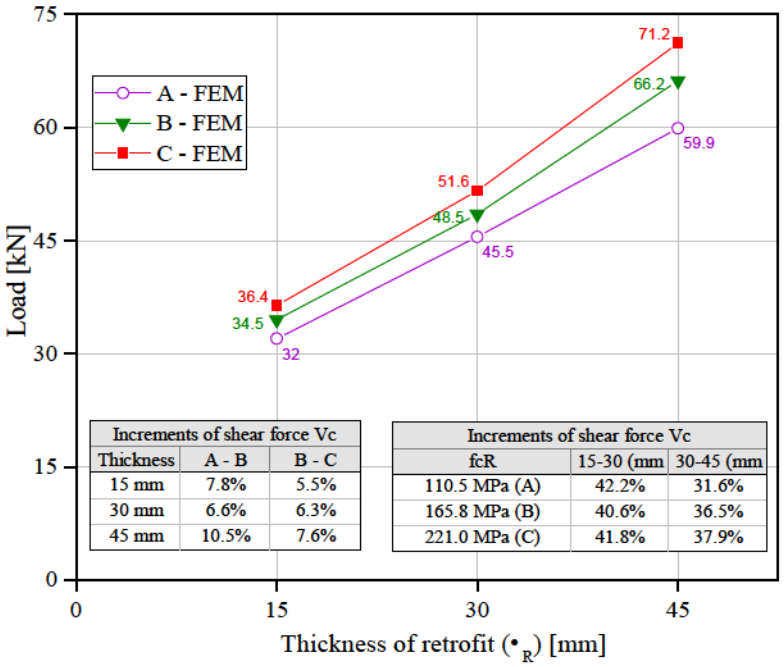

Increments of shear force Vc		
Thickness	A - B	B - C
15 mm	7.8%	5.5%
30 mm	6.6%	6.3%
45 mm	10.5%	7.6%

Increments of shear force Vc		
fcR	15-30 (mm	30-45 (mm
110.5 MPa (A)	42.2%	31.6%
165.8 MPa (B)	40.6%	36.5%
221.0 MPa (C)	41.8%	37.9%

Figure 7.15 – Shear values of the strengthened joints varying the thickness δ_R and compressive strength of the HPFRC jacket f_{cR}

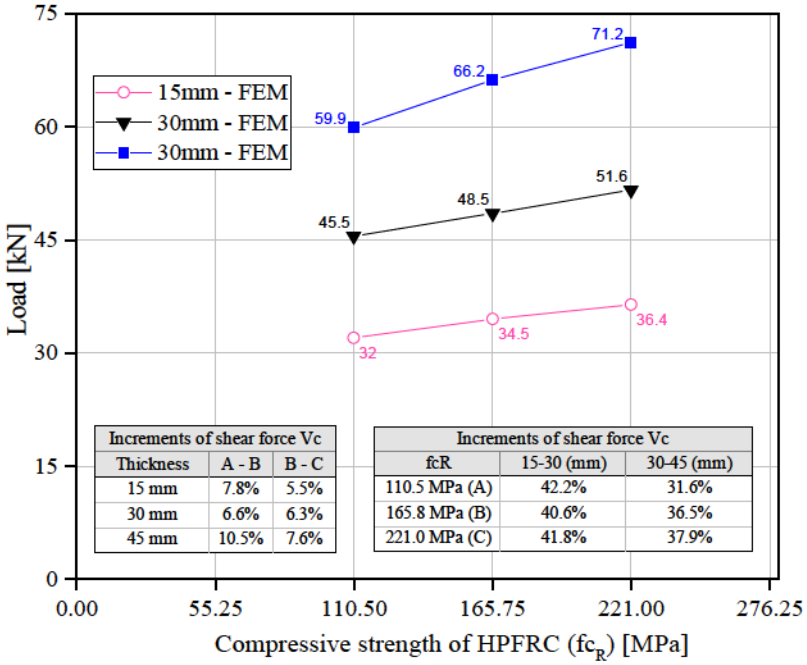

Increments of shear force Vc		
Thickness	A - B	B - C
15 mm	7.8%	5.5%
30 mm	6.6%	6.3%
45 mm	10.5%	7.6%

Increments of shear force Vc		
fcR	15-30 (mm)	30-45 (mm)
110.5 MPa (A)	42.2%	31.6%
165.8 MPa (B)	40.6%	36.5%
221.0 MPa (C)	41.8%	37.9%

Figure 7.16 – Shear values of the strengthened joints varying the compressive strength and thickness of the HPFRC jacket

On the other hand, Figure 7.17 shows the variation of the force V_c as a function of jacket thickness (δ_R) and beam's reinforcement ratio (ρ_b). The gain of V_c for all the ρ_b values was smaller when the joints thickness increased from 30 mm to 45 mm (21.4%, 31.6%, 8.5%), in comparison when it was modified from 15 mm to 30 mm (41.6%, 42.2%, 19.1%). Furthermore, significant improvements were observed in increasing the force V_c as the ratios ρ_b increased. For a layer of 15 mm thick, the increments of the shear V_c were 9.9% and 53.8% when ρ_b changed from low to medium ratio and from medium to high ratio, respectively, for a layer of 15 mm thick. For a layer of 30 mm thick, those increments were 10.4% and 28.8%. However, for a thickness of 45 mm, this effect was not observed, presenting increments from 19.8% (ρ_b=0.4% to ρ_b=0.7%) to 6.2% (ρ_b=0.7% to ρ_b=1.2%). In addition, the gains with a ratio of 1.2% (19.1% and 8.5%), were smaller compared with the ones obtained for 0.7% (42.2% and 31.6%) and 0.4% (41.6% and 21.4%).

As the beam's reinforcement ratio increased, the force V_c also increased. Nevertheless, for thicker layers (e.g., δ_R=45 mm), this enhancement was not observed. Furthermore, the improvements of V_c increasing its thickness were more significant for low and medium ratios (0.4% and 0.7%).

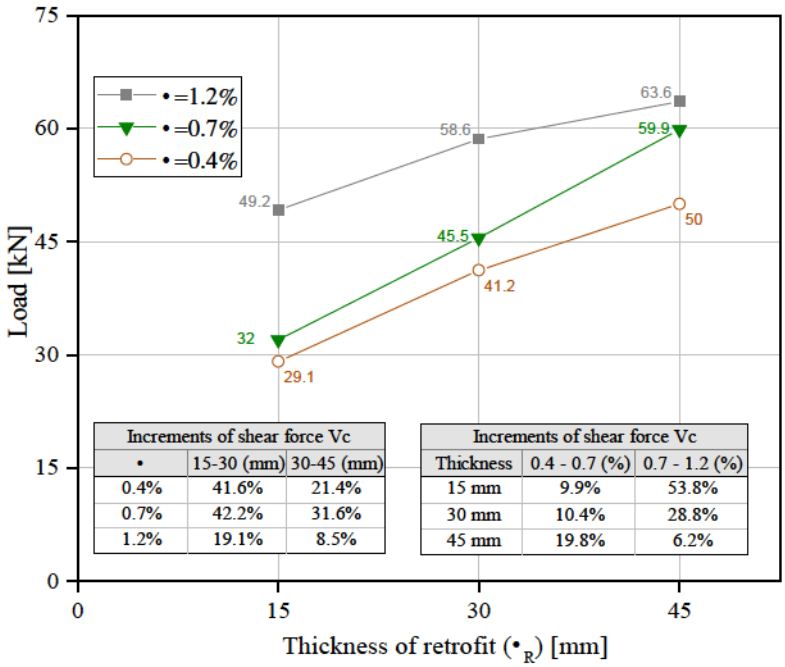

Increments of shear force Vc		
•	15-30 (mm)	30-45 (mm)
0.4%	41.6%	21.4%
0.7%	42.2%	31.6%
1.2%	19.1%	8.5%

Increments of shear force Vc		
Thickness	0.4 - 0.7 (%)	0.7 - 1.2 (%)
15 mm	9.9%	53.8%
30 mm	10.4%	28.8%
45 mm	19.8%	6.2%

Figure 7.17 – Shear values of the strengthened joints varying the thickness of the HPFRC jacket and beam's reinforcement ratio

The three parameters studied in this work (δ_R, f_{cR}, and ρ_b) influenced the shear capacity of the column (V_c). When the depth of the HPFRC layer was fixed, the increase of the ratio ρ_b increased the shear force V_c (53.8%) more than when the compressive strength of HPFRC f_{cR} (10.5%) was increased. This is a result of the increased reinforcement ratio in the tension zone of RC beam.

However, the V_c values were closer (Figures 7.15 and 7.17) except for the case when the beam had a reinforcement ratio of 1.2%, where the higher values of V_c were observed in joints

retrofitted with jackets of 15 mm and 30 mm thick, showing that for great thickness of retrofit, the increase of the ratio was not very significant. On the other hand, the increase in the thickness $_R$ from 30 mm to 45 mm had a greater impact with a fixed compressive strength f_{cR} (37.9%) than with a fixed ratio $_b$ (8.5%).

7.3.2 Cracking Pattern

The specimens' cracking pattern resulted from the parametric study is also presented in this thesis. Appendix B shows the evolution of the cracks in the HPFRC jacket and in the concrete (joint core) as the horizontal cyclic displacements increased.

Figures B.1, B.2, and B.3 in the Appendix B show vertical cracks at the beam-joint interface for joints retrofitted with 15 mm and 30 mm thick HPFRC layers at horizontal displacements of +15 mm and -15 mm. In contrast, joints with 45 mm thick jackets did not show significant cracks. However, cracks appeared in the core region of both the HPFRC and the concrete (joint core) at a displacement of +22.5 mm. Vertical cracks continued to propagate through the interface for joints strengthened with 30 mm and 45 mm layers. This behavior can be attributed to the higher lateral loads sustained by joints A45, B45, and C45, which caused greater degradation in the joint core (concrete), resulting in higher stresses in the HPFRC material. The most significant cracks were observed in the final loading cycles, as expected.

A similar behavior was observed in the joints with a high beam's steel ratio ($_b$=1.2%), corresponding to A15-H, A30-H, and A45-H models. For displacements higher than +22.5 mm, cracks in the core and interface beam-joint of both the concrete and HPFRC material were evidenced, (Figures B.4, B.5, and B.6 in the Appendix B). Thus, can be concluded that for large thicknesses of the HPFRC jacket and high beam's steel ratio, the presence of cracks in the core region is more evident after the early cycles, caused by its high capacity to lateral shear loads. It is essential to point out that no specimens studied in the parametric analysis reached their rupture load.

7.3.3 Analytical results

Table 7.3 presents the shear load values (V_c) obtained from the analytical and numerical models. The shear force V_c increased with the increase of the beam's reinforcement ratio, thickness jacket, and compressive strength of HPFRC, as demonstrated also by other research (AL-OSTA et al., 2017; ISA, 2017; BAHRAQ et al., 2021; LAMPROPOULOS et al., 2024).

Regarding the comparison between numerical and analytical values of V_c, the results were close, presenting good accuracy. The maximum differences were evidenced in the joints with a high beam's reinforcement ratio (H), with values of 1.18. 1.18 and 1.27 for A15-H, A30-H, and A45-H, respectively. This may be because the mechanical parameters of steel bars of 20 mm were adopted the same as those of 16 mm. Thus, it is recommended to simulate the joints with values obtained in the laboratory test and perform a new comparison. However, both the methodology used and the results obtained in this thesis could be considered satisfactory, and useful to be used by engineers.

Table 7.4 – Results of parametric study for the retrofitted joints - Flexural model

Specimen ID	x_c **[mm]**	**Case**	M_{ana} **[kN.m]**	$V_{c,ana}$ **[kN]**	$V_{c,FEM}$ **[kN]**	$V_{c,ana}/V_{c,FEM}$
A15 (A15-M)	33.24	Case 3	102.39	34.13	32.00	1.07
B15	32.78	Case 3	109.52	36.51	34.50	1.06
C15	32.00	Case 3	115.50	38.50	36.40	1.06
A30 (A30-M)	39.97	Case 3	135.58	45.19	44.10	1.02
B30	36.68	Case 3	150.52	50.17	48.50	1.03
C30	35.11	Case 3	163.06	54.35	51.80	1.05
A45 (A45-M)	41.77	Case 3	171.55	57.18	59.90	0.95
B45	39.65	Case 3	194.99	65.00	66.20	0.98
C45	37.31	Case 3	214.32	71.44	71.20	1.00
A15-L	26.79	Case 2	76.74	25.58	29.10	0.88
A30-L	32.88	Case 3	110.11	36.70	41.20	0.89
A45-L	37.58	Case 3	146.20	48.73	50.00	0.97
A15-H	49.10	Case 3	174.03	58.01	49.20	1.18
A30-H	51.14	Case 3	207.02	69.01	58.60	1.18
A45-H	53.03	Case 3	242.80	80.93	63.60	1.27

The internal forces in the concrete and HPFRC material obtained from the analytical model of all specimens are presented in Appendix C (Table C).

8 Conclusions

This thesis developed a numerical model of RC frame under monotonic load, and numerical and analytical models of exterior beam-column joints with and

- The state-of-the-art joint's shear analytical models was raised, showing the diversity of models available in the literature. The correlations between the analytical and experimental data ranged from 0.7468 to 0.97578. However, all the models were developed exclusively for unretrofitted RC joints.
- A bidimensional numerical simulation of RC frame to monotonic was developed in the ATENA software. The results showed good accuracy with experimental ones regarding peak load, load-displacement curve, and cracking pattern, showing the efficiency of the numerical methodology employed to simulate RC frames.
- The analytical flexural proposed achieved showed a good accuracy with the experimental ones regarding the ultimate flexural moment. A maximum difference of 15.2% was obtained, which corresponds to this one with tensile parameters unknown. Thus, knowing all the required properties can help to improve reliability in the prediction of the moment in the beam strengthened by UHPFRC jackets.
- The novel shear model proposed considered the confinement of the retrofit material on the concrete through the parameters $_2$ and f_{cc}. The model predicted shear strengths greater than the acting shear forces in the joints, with differences of up to 49.9%. Therefore, the proposed model could serve as a valuable tool for engineers and researchers, assisting in practical design and in predicting the shear behavior of BCJs retrofitted with UHPFRC/HPFRC jackets.
- The retrofitting with HPFRC jackets increased the shear strength of the joints, promoting the flexural failure of the beam. This confirms UHPFRC as a good retrofitting material that helps to avoid undesirable shear failure in non-seismic exterior BCJs subject to cyclic load.
- An interface model was used to simulate the connection between the concrete and the HPFRC jacket in the joints, helping to obtain good results in terms of peak load, hysteresis curve, and cracking pattern, which was concentrated in the beam-joint interface region, as expected.
- A parametric study with factors affecting the shear capacity in the column (V_c) of joints retrofitted with HPFRC was conducted after the verification of the numerical model (RCJ2). The increase of the thickness of HPFRC, reinforcement ratio in the beam, and compressive strength of the HPFRC increased the shear capacity of the joint.

- The HPFRC material increased 1.1-2.0 times the ultimate shear capacity (V_c) of the joints with jackets of thicknesses of 30-45 mm compared with the initial load of the non-retrofitted joint.

- For all compressive strengths of the HPFRC (Models A, B, and C), the increase in shear capacity (V_c) was more significant when the thickness changed from 15 mm to 30 mm, compared to the one from 30 mm to 45 mm, corresponding to an increment of 42.2%. In addition, for all HPFRC jacket thicknesses (15, 30, and 45 mm), the improvement in shear capacity (V_c) was greater when the compressive strength increased from 110.5 MPa to 165.8 MPa, with values of 10.5%, rather than from 165.8 MPa to 221.0 MPa.

- For a fixed HPFRC depth, the increase of the beam's reinforcement ratio $_b$ increased the shear force V_c (53.8%) more than when the compressive strength of HPFRC f_{cR} (10.5%) was increased, caused by the increased reinforcement ratio in the tension zone of RC beam. However, both cases presented close V_c values, except for the case when the beam had a reinforcement ratio of 1.2%, where higher values of V_c were observed in joints retrofitted with jackets of 15 mm and 30 mm thick.

- To increase the shear force V_c in joints retrofitted with a high thick of UHPFRC jacket (e.g., 45 mm), it is recommended to enhance either the compressive strength f_{cR} instead of the beam's steel ratio $_b$.

9 Suggestions for future work

Based on the findings of this research, several future investigation directions are proposed to further advance the understanding and application of UHPFRC in the retrofitting of beam column joints. These future efforts aim to refine the proposed analytical model, expand its applicability, and improve its practical implementation in structural engineering.

- Conduct additional experimental tests to confirm the predictions of the analytical shear strength model for beam-column joints retrofitted with UHPFRC.
- Extend the model to different loading conditions, such as dynamic impacts and higher intensity seismic effects.
- Develop guidelines to determine the optimal thickness of the UHPFRC layer, maximizing strength and minimizing costs.

Bibliography

ACI COMMITTEE 318. **Building Code Requirements for Structural Concrete and Commentary (ACI 318-19)**. American Concrete Institute, Farmington Hills, Michigan, 2019.

AFGC, A. F. d. G. C. S. d. t. d. r. e. a. S. **Bétons fibrés à ultra-hautes performances, Recommandations provisoires**. [S.l.: s.n.], 2002.

AIJ Structural Committee. **Design for Earthquake Resistant Reinforced Concrete Buildings Based on Ultimate Strength Concept**. [S.l.: s.n.], 1990.

AL-OSTA, M.; ISA, M.; BALUCH, M.; RAHMAN, M. Flexural behavior of reinforced concrete beams strengthened with ultra-high performance fiber reinforced concrete. **Construction and Building Materials**, Elsevier, v. 134, p. 279–296, 2017. Available at: <https://doi.org/10.1016/j.conbuildmat.2016.12.094>.

AL-OSTA, M. A.; KHAN, M. I.; BAHRAQ, A. A.; XU, S.-Y. Application of ultra-high performance fiber reinforced concrete for retrofitting the damaged exterior reinforced concrete beam-column joints. **Earthquakes and Structures**, Techno-Press, v. 19, n. 5, p. 361–377, 2020.

ALAMEDDINE, F. F. **Seismic design recommendations for high- strength concrete beam-to-column connections**. (PhD Thesis) — University of Arizona, 1990.

ALAVI-DEHKORDI, S.; MOSTOFINEJAD, D.; ALAEE, P. Effects of high-strength reinforcing bars and concrete on seismic behavior of RC beam-column joints. **Engineering Structures**, Elsevier, v. 183, n. July 2018, p. 702–719, 2019. ISSN 18737323. Available at: <https://doi.org/10.1016/j.engstruct.2019.01.019>.

ALFARAH, B. Doctoral Thesis: Advanced Computationally Efficient Modeling of RC Structures Nonlinear Cyclic Behavior. n. June, p. 1–198, 2017.

ALFARAH, B.; LÓPEZ-ALMANSA, F.; OLLER, S. New methodology for calculating damage variables evolution in Plastic Damage Model for RC structures. **Engineering Structures**, Elsevier Ltd, v. 132, p. 70–86, 2017. ISSN 18737323. Available at: <http://dx.doi.org/10.1016/j.engstruct.2016.11.022>.

ALVA, G. M. S.; de Cresce El Debs, A. L. H.; El Debs, M. K. An experimental study on cyclic behaviour of reinforced concrete connections. **Canadian Journal of Civil Engineering**, v. 34, n. 4, p. 565–575, 2007. ISSN 03151468.

American Concrete Institute. **Building code requirements for structural concrete (ACI 318-95) and commentary**. [S.l.], 1995.

American Concrete Institute. **Building code requirements for structural concrete (ACI 318-02) and commentary**. [S.l.], 2002.

American Concrete Institute. **Building code requirements for structural concrete (ACI 318-05) and commentary**. [S.l.], 2005.

American Concrete Institute. **Building code requirements for structural concrete (ACI 318-14) and commentary**. [S.l.], 2014.

American Concrete Institute. **Building Code Requirements for Structural Concrete and Commentary (ACI 318-19)** . [S.l.], 2019.

American Society of Civil Engineersn). **Seismic rehabilitation of existing buildings**. [S.l.], 2007.

ANDERSON, M.; LEHMAN, D.; STANTON, J. A cyclic shear stress–strain model for joints without transverse reinforcement. **Engineering Structures**, Elsevier, v. 30, n. 4, p. 941–954, 2008.

AROWOJOLU, O.; IBRAHIM, A. Plastic hinge relocation in exterior reinforced beam–column joint and compliance issues to seismic design guidelines—A review. **Structural Concrete**, v. 21, n. 5, p. 1938–1958, 2020. ISSN 17517648.

ASSOCIAÇÃO BRASILEIRA DE NORMAS TéCNICAS. **ABNT NBR 6118: Projeto de Estruturas de Concreto**. Rio de Janeiro, 2014. (in Portuguese).

Associação Brasileira de Normas Técnicas - ABNT. **NBR 6118: Projeto de estruturas de concreto**. Rio de Janeiro: [s.n.], 2023.

ATTARI, N.; AMZIANE, S.; CHEMROUK, M. Efficiency of beam–column joint strengthened by frp laminates. **Advanced Composite Materials**, Taylor & Francis, v. 19, n. 2, p. 171–183, 2010. Available at: <https://doi.org/10.1163/092430409X12605406698192>.

BAHRAQ, A. A.; AL-OSTA, M. A.; KHAN, M. I.; AHMAD, S. Numerical and analytical modeling of seismic behavior of beam-column joints retrofitted with ultra-high performance fiber reinforced concrete. **Structures**, Elsevier Ltd, v. 32, n. February, p. 1986–2003, 2021. ISSN 23520124. Available at: <https://doi.org/10.1016/j.istruc.2021.04.004>.

BAZANT, Z. P.; OH, B. H. Crack band theory for fracture of concrete. **Matériaux et construction**, v. 16, n. 3, p. 155–177, 1983. ISSN 05677572.

BAZANT, Z. P.; OH, B. H. Deformation of Progressively Cracking Reinforced Concrete Beams. **Journal of the American Concrete Institute**, v. 81, n. 3, p. 268–278, 1984. ISSN 00028061.

BECKINGSALE, C. **Post elastic behaviour of reinforced concrete beam-column joints**. 399 p. (PhD Thesis) — University of Canterbury, Christchurch, New Zealand, 1980. Available at: <http://ir.canterbury.ac.nz/handle/10092/7749>.

BEDIRHANOGLU, I.; LLKI, A.; PUJOL, S.; KUMBASAR, N. Behavior of deficient joints with plain bars and low-strength concrete. **ACI Structural Journal**, v. 107, n. 3, p. 300–310, 2010. ISSN 08893241.

BESCHI, C.; RIVA, P.; METELLI, G.; MEDA, A. Hpfrc jacketing of non seismically detailed rc corner joints. **Journal of Earthquake Engineering**, Taylor & Francis, v. 19, n. 1, p. 25–47, 2015. Available at: <https://doi.org/10.1080/13632469.2014.948646>.

BEYDOKHTY, E. Z.; SHARIATMADAR, H. Behavior of damaged exterior rc beam-column joints strengthened by cfrp composites. **Latin American journal of solids and structures**, SciELO Brasil, v. 13, p. 880–896, 2016. Available at: <https://doi.org/10.1590/1679-78252258>.

BIGAJ, A. J. Structural dependence of rotations capacity of plastic hinges in rc beams and slabs. 1999.

BINDHU, K. R.; SUKUMAR, P. M.; JAYA, K. P. Performance of exterior beam-column joints under seismic type loading. **ISET Journal of Earthquake Technology**, v. 46, n. 2, p. 47–64, 2009. ISSN 09720405.

BIRSS, G. R. **The elastic behaviour of earthquake resistant reinforced concrete interior beam-column joints**. (PhD Thesis) — University of Canterbury, 1978.

BRAGA, F.; GIGLIOTTI, R.; LATERZA, M. R/C Existing Structures with Smooth Reinforcing Bars: Experimental Behaviour of Beam-Column Joints Subject to Cyclic Lateral Loads. **The Open Construction and Building Technology Journal**, v. 3, n. 1, p. 52–67, 2009. ISSN 18748368.

CEN (European Committee for Standardization). **EN 1992-1-1:2004: Eurocode 2: Design of Concrete Structures. Part 1-1: General rules and rules for buildings**. Brussels, Belgium, 2004.

ČERVENKA, J.; PAPANIKOLAOU, V. K. Three dimensional combined fracture-plastic material model for concrete. **International Journal of Plasticity**, v. 24, n. 12, p. 2192–2220, 2008. ISSN 07496419.

CERVENKA, V. Constitutive Model for Cracked Reinforced Concrete. **Journal of the American Concrete Institute**, v. 82, n. 6, p. 877–882, 1985. ISSN 00028061.

ČERVENKA, V.; JENDELE, L.; ČERVENKA, J. **ATENA Program Documentation Part 1: Theory**. [S.l.: s.n.], 2021. 350 p.

CHOI, K.-k.; KIM, J.-c.; DINH, N.-h. Behaviour of non-seismic detailed reinforced-concrete beam – column connections. 2017.

CHOUDHURY, A.; DEB, S.; DUTTA, A. Study on size effect of fibre reinforced polymer retrofitted reinforced concrete beam–column connections under cyclic loading. **Canadian Journal of Civil Engineering**, NRC Research Press, v. 40, n. 4, p. 353–360, 2013. Available at: <https://doi.org/10.1139/cjce-2012-0041>.

CHUN, S. C.; KIM, D. Y. Evaluation of Mechanical Anchorage of Reinforcement by Exterior Beam-Column Joint Experiments. **13th World Conference on Earthquake Engineering**, n. 0326, p. 0326, 2004. Available at: <http://www.iitk.ac.in/nicee/wcee/article/13{_}326.pdf>.

CHUN, S. C.; SHIN, Y. S. Cyclic testing of exterior beam-column joints with varying joint aspect ratio. **ACI Structural Journal**, v. 111, n. 3, p. 693–704, 2014. ISSN 08893241.

CLYDE, C.; PANTELIDES, C. P.; REAVELEY, L. D. Performance-based evaluation of reinforced concrete building exterior joints for seismic excitation. **Earthquake Spectra**, v. 18, n. 3, p. 449–480, 2002. ISSN 87552930.

COMMITTEE, J. . C. et al. Standard specifications for concrete structures—2007. **Japan Society of Civil Engineers: Tokyo, Japan**, 2010.

Concrete Structures Standard. **Code of Practice for the Design of Concrete Structures, NZS 3101 Part 1:1982**. [S.l.], 1982.

Concrete Structures Standard. **Concrete structures standard, Part 1 and 2, Code and commentary on the design of concrete structures**. [S.l.], 1995.

COSGUN, C.; TURK, A. M.; MANGIR, A.; COSGUN, T.; KIYMAZ, G. Experimental behaviour and failure of beam-column joints with plain bars, low-strength concrete and different anchorage details. **Engineering Failure Analysis**, Elsevier, v. 109, n. February 2019, 2020. ISSN 13506307.

De Risi, M. T.; RICCI, P.; VERDERAME, G. M.; MANFREDI, G. Experimental assessment of unreinforced exterior beam-column joints with deformed bars. **Engineering Structures**, Elsevier Ltd, v. 112, p. 215–232, 2016. ISSN 18737323. Available at: <http://dx.doi.org/10.1016/j.engstruct.2016.01.016>.

DEATON, J. B. PhD Proposal - Nonlinear Finite Element Analysis of Reinforced Concrete Exterior Beam-Column Joints with Nonseismic Detailing. n. May, 2010.

DEBORST, R. Non-linear analysis of frictional materials. p. 138, 1986. Available at: <http://www.narcis.nl/publication/RecordID/oai:tudelft.nl:uuid:d52ac7f8-d56f-4e0c-ab14-455ed02fcffe>.

DHAKAL, R. P.; MAEKAWA, K. Path-dependent cyclic stress-strain relationship of reinforcing bar including buckling. **Engineering Structures**, v. 24, n. 11, p. 1383–1396, 2002. ISSN 01410296.

DURRANI, A. J. **Experimental and analytical study of internal beam to column connections subjected to reversed cyclic loading**. (PhD Thesis) — University of Michigan, 1982.

DURRANI, A. J.; WIGHT, J. K. Behavior of Interior Beam-to-Column Connections Under Earthquake-Type Loading I. **Journal proceedings**, v. 82, p. 343–349, 1985.

DYNGELAND, T. Behavior of reinforced concrete panels. **Doktor Ingenierafhandling (Ph. D. thesis, Institut for Betongkonstruksjoner, Trondheim**, 1989.

EBANESAR, A.; GLADSTON, H.; FARSANGI, E. N.; SHARMA, S. V. Strengthening of rc beam-column joints using steel plate with shear connectors: Experimental investigation. In: ELSEVIER. **Structures**. 2022. v. 35, p. 1138–1150. Available at: <https://doi.org/10.1016/j.istruc.2021.08.042>.

EHSANI, M.; MOUSSA, A.; VALLENILLA, C. Comparison of inelastic Behavior of Reinforced Ordinary and High-Strength Concrete Frames. **Structural Journal**, v. 84, n. 2, p. 161–169, 1987.

EHSANI, M. R.; ALAMEDDINE, F. Design recommendations for type 2 high strength reinforced concrete connections. **Structural Journal**, 1991.

EHSANI, M. R.; WIGHT, J. K. Effect of Transverse Beams and Slab on Behavior of Reinforced Concrete Beam-to-Column Connections. **Journal proceedings**, v. 82, p. 188–195, 1985.

European Committee For Standardization. **Eurocode 8: design of structures for earthquake resistance – part 1: general rules, seismic actions and rules for buildings**. Lausanne, Switzerland, 2004.

FADWA, I.; ALI, T. A.; NAZIH, E.; SARA, M. Reinforced concrete wide and conventional beam-column connections subjected to lateral load. **Engineering Structures**, Elsevier Ltd, v. 76, p. 34–48, 2014. ISSN 01410296. Available at: <http://dx.doi.org/10.1016/j.engstruct.2014.06.029>.

FAYAZ, Q.; KAUR, G.; BANSAL, P. P. Numerical modelling of seismic behaviour of an exterior rc beam column joint strengthened with uhpfrc and cfrp. **Arabian Journal for Science and Engineering**, Springer, p. 1–16, 2022.

Federal Emergency anAgency Managent. **FEMA 273: NEHRP Guidelines for the Seismic Rehabilitation of Buildings**. Washington, 1997.

FEHLING, E.; SCHMIDT, M. **Ultra-High Performance Concrete UHPC: Fundamentals, Design, Examples**. [S.l.]: Betonkalender, Wilhelm Ernst & Sohn, 2014. ISBN 9783433030004.

FIB (FÉDÉRATION INTERNATIONALE DU BÉTON). ***fib* Model Code for concrete structures 1990**. Lausanne, Switzerland, 1990.

FIB (FÉDÉRATION INTERNATIONALE DU BÉTON). ***fib* Model Code for concrete structures 2010**. Lausanne, Switzerland, 2013.

French Standard Institute. **National addition to Eurocode 2 – Design of concrete structures: specific rules for Ultra-High Performance Fibre-Reinforced Concrete (UPHFRC)**. France, 2016.

GAO, F.; TANG, Z.; MEI, S.; HU, B.; HUANG, S.; CHEN, J. Seismic behavior of exterior beam–column joints withhigh-performance steel rebar: Experimental and numerical investigations. **Advances in Structural Engineering**, v. 24, n. 1, p. 90–106, 2021. ISSN 20484011.

GENESIO, G. **Seismic Assessment of RC Exterior Beam- Column Joints and Retrofit with Haunches Using Post-Installed Anchors**. [S.l.: s.n.], 2012. ISBN 9783981168242.

GIUFFRÈ, A. Il comportamento del cemento armato per sollecitazioni cicliche di forte intensità. **Giornale del Genio Civile**, Istituto di Tecnica Delle Costruzioni, Facolta Di Architettura, Universita . . . , 1970.

GRAYBEAL, B. A. et al. **Material property characterization of ultra-high performance concrete**. [S.l.], 2006.

GUNER, S. **PERFORMANCE ASSESSMENT OF SHEAR-CRITICAL**. 429 p. (PhD Thesis) — University of Toronto, 2008.

GUO, W.; FAN, W.; SHAO, X.; SHEN, D.; CHEN, B. Constitutive model of ultra-high-performance fiber-reinforced concrete for low-velocity impact simulations. **Composite Structures**, Elsevier, v. 185, p. 307–326, 2018. Available at: <https://doi.org/10.1016/j.compstruct.2017.11.022>.

HAACH, V. G. Análise teórico-experimental da influência da força normal em nós de pórtico externos de concreto armado. p. 159, 2005.

HAACH, V. G.; Lúcia Homce De Cresce El Debs, A.; Khalil El Debs, M. Evaluation of the influence of the column axial load on the behavior of monotonically loaded R/C exterior beam-column joints through numerical simulations. **Engineering Structures**, v. 30, n. 4, p. 965–975, 2008. ISSN 01410296.

HABEL, K.; DENARIÉ, E.; BRÜHWILER, E. Structural response of elements combining ultrahigh-performance fiber-reinforced concretes and reinforced concrete. **Journal of structural engineering**, American Society of Civil Engineers, v. 132, n. 11, p. 1793–1800, 2006.

HAKUTO, S.; PARK, R.; TANAKA, H. Seismic load tests on interior and exterior beam-column joints with substandard reinforcing details. **ACI Structural Journal**, v. 97, n. 1, p. 11–25, 2000. ISSN 08893241.

HANSON, N. W.; CONNOR, H. W. Seismic Resistance of Reinforced Concrete Beam-Column joints. **Journal of the Structural Division**, v. 93, n. 5, p. 533–560, 1967.

HARIS, I.; ROSZEVÁK, Z. Finite element analysis of cast-in-situ RC frame corner joints under quasi-static and cyclic loading. **Revista de la construcción**, v. 18, n. 3, p. 579–594, 2019. ISSN 0718-915X.

HASSAN, W. M.; MOEHLE, J. P. Shear strength of exterior and corner beam-column joints without transverse reinforcement. **ACI Structural Journal**, v. 115, n. 6, p. 1719–1727, 2018. ISSN 08893241.

HORDIJK, D. **Local Approach to Fracture of Concrete**. (PhD Thesis) — Doctoral Thesis. Delft University of Technology, Delft, The Netherlands, 1991.

HUANG, Y.; GRÜNEWALD, S.; SCHLANGEN, E.; LUKOVIĆ, M. Strengthening of concrete structures with ultra high performance fiber reinforced concrete (uhpfrc): A critical review. **Construction and Building Materials**, Elsevier, v. 336, p. 127398, 2022. Available at: <https://doi.org/10.1016/j.conbuildmat.2022.127398>.

HUANG, Y.; GRÜNEWALD, S.; SCHLANGEN, E.; LUKOVIĆ, M. Strengthening of concrete structures with ultra high performance fiber reinforced concrete (uhpfrc): A critical review. **Construction and Building Materials**, Elsevier, v. 336, p. 127398, 2022.

HWANG, S.; LEE, H.; LIAO, T.; WANG, K.; Tsai H. Role of Hoops on Shear Strength of Reinforced Concrete Beam-Column Joints. **ACI structural journa**, v. 102, n. 10, p. 445, 2005. ISSN 17517702.

HWANG, S. J.; LEE, H. J. Analytical model for predicting shear strengths of interior reinforced concrete beam-column joints for seismic resistance. **ACI Structural Journal**, v. 97, n. 1, p. 35–44, 1999. ISSN 08893241.

HWANG, S.-J.; LEE, H.-J. Strength Prediction for Discontinuity Regions by Softened Strut-and-Tie Model. **Journal of Structural Engineering**, v. 128, n. 12, p. 1519–1526, 2002. ISSN 0733-9445.

HWANG, S.-J.; LEE, H.-J.; Wang Kuo-Chou. Seismic design and detailing of exterior reinforced concrete beam column joints. In: **13th World Conference on Earthquake Engineering**. [S.l.: s.n.], 2004.

ILIA, E.; MOSTOFINEJAD, D.; MOGHADDAS, A. Cyclic behavior of strong beam–weak column joints strengthened with different configurations of cfrp sheets. **Archives of Civil and Mechanical Engineering**, Springer, v. 20, p. 1–26, 2020. Available at: <https://doi.org/10.1007/s43452-020-0015-7>.

ILKI, A.; BEDIRHANOGLU, I.; KUMBASAR, N. Behavior of frp-retrofitted joints built with plain bars and low-strength concrete. **Journal of Composites for Construction**, American Society of Civil Engineers, v. 15, n. 3, p. 312–326, 2011. Available at: <https://doi.org/10.1061/(asce)cc.1943-5614.0000156>.

ISA, M. Flexural improvement of plain concrete beams strengthened with high performance fibre reinforced concrete. **Nigerian Journal of Technology**, v. 36, n. 3, p. 697–704, 2017. Available at: <https://doi.org/10.4314/njt.v36i3.6>.

JOH, O.; GOTO, Y. Beam-Column Joint Behavior After Beam Yielding in R / C Ductile. **12th World Conference on Earthquake Engineering**, p. 1–8, 2000.

JOH, O.; GOTO, Y.; SHIBATA, T. Behavior of Reinforced Concrete Beam-Column Joints With Eccentricity. **Special Publication**, v. 123, p. 317–358, 1991. Available at: <https://www.concrete.org/publications/internationalconcreteabstractsportal/m/details/id/2863>.

Joint ACI-ASCE Committee 352. **Recommendations for Design of Beam-Column Joints in Monolithic Reinforced Concrete Structures**. [S.l.], 2002.

KAIKEA, S.; KARIHALOO, B. Performance of high-performance fiber-reinforced concrete in structural applications. **Magazine of Concrete Research**, v. 66, n. 2, p. 101–110, 2014.

KAKU, T.; ASAKUSA, H. Ductility Estimation of Exterior Beam-Column Subassemhlages in Reinforced Concrete Frames. **Special Publication**, v. 123, p. 167–186, 1991.

KAM, W. Y.; Quintana Gallo, P.; AKGUZEL, U.; PAMPANIN, S. Influence of slab on the seismic response of sub-standard detailed exterior reinforced concrete beam column joints. 2010.

KAMIMURA, T.; TAKEDA, S.; TOCHIO, M. Influence of joint reinforcement on strength and deformation of interior beam-column subassemblages. In: **12 th World Conference on Earthquake Engineering**. [S.l.: s.n.], 2000.

KARAYANNIS, C.; CHALIORIS, C.; SIDERIS, K. Effectiveness of rc beam-column connection repair using epoxy resin injections. **Journal of Earthquake Engineering**, World Scientific, v. 2, n. 02, p. 217–240, 1998.

KARAYANNIS, C. G.; CHALIORIS, C. E.; SIRKELIS, G. M. Local retrofit of exterior rc beam–column joints using thin rc jackets—an experimental study. **Earthquake Engineering & Structural Dynamics**, Wiley Online Library, v. 37, n. 5, p. 727–746, 2008.

KASSEM, W. Strut-and-tie modelling for the analysis and design of RC beam-column joints. **Materials and Structures/Materiaux et Constructions**, Springer Netherlands, v. 49, n. 8, p. 3459–3476, 2016. ISSN 13595997.

KAUNG, J. S.; WONG, H. F. Effectiveness of horizontal stirrups in joint core for exterior beam-column joints with nonseismic design. **Procedia Engineering**, Elsevier B.V., v. 14, p. 3301–3307, 2011. ISSN 18777058. Available at: <http://dx.doi.org/10.1016/j.proeng.2011.07.417>.

KHAN, M. I.; AL-OSTA, M. A.; AHMAD, S.; RAHMAN, M. K. Seismic behavior of beam-column joints strengthened with ultra-high performance fiber reinforced concrete. **Composite Structures**, Elsevier, v. 200, n. July 2017, p. 103–119, 2018. ISSN 02638223. Available at: <https://doi.org/10.1016/j.compstruct.2018.05.080>.

KIM, C.-G.; PARK, H.-G.; EOM, T.-S. Shear Strength of Exterior Beam-Column Joints with Limited Ductility Details. **Journal of Structural Engineering**, v. 146, n. 2, p. 04019204, 2020. ISSN 0733-9445.

KIM, J.; LAFAVE, J. M. Key influence parameters for the joint shear behaviour of reinforced concrete (rc) beam–column connections. **Engineering Structures**, v. 29, n. 10, p. 2523–2539, 2007. ISSN 0141-0296. Available at: <https://www.sciencedirect.com/science/article/pii/S0141029606005074>.

KIM, J.; LAFAVE, J. M.; SONG, J. Joint shear behaviour of reinforced concrete beam-column connections. **Magazine of Concrete Research**, v. 61, n. 2, p. 119–132, 2009. ISSN 00249831.

KUANG, J. S.; WONG, H. F. Effects of beam bar anchorage on beam – column joint behaviour. **Proceedings of the Institution of Civil Engineers-Structures and Buildings**, v. 159, n. April, p. 115–124, 2006.

KUPFER, H.; HILSDORF, H. K.; RUSCH, H. Behavior of Concrete Masonry Under Biaxial Stresses. **Journal proceedings**, v. 66, n. 8, p. 656–666, 1969.

KUSUHARA, F.; SHIOHARA, H. New instrumentation for damage and stress in reinforced concrete beam-column joint. **8th US National Conference on Earthquake Engineering 2006**, v. 7, n. 1214, p. 4006–4015, 2006.

KUSUHARA, F.; SHIOHARA, H. Tests of R / C Beam-Column Joint with Variant Boundary Conditions and Irregular Details on Anchorage of Beam Bars. In: **The 14th World Conference on Earthquake Engineering**. [S.l.: s.n.], 2008. p. 1–8.

LAMPROPOULOS, A.; PASCHALIS, S.; TSIOULOU, O.; DRITSOS, S. Strengthening of existing reinforced concrete (rc) columns using ultra high performance fiber reinforced concrete (uhpfrc) jackets. Preprints, 2024.

LAMPROPOULOS, A.; PASCHALIS, S. A.; TSIOULOU, O.; DRITSOS, S. E. Strengthening of reinforced concrete beams using ultra high performance fibre reinforced concrete (uhpfrc). **Engineering Structures**, Elsevier, v. 106, p. 370–384, 2016. Available at: <https://doi.org/10.1016/j.engstruct.2015.10.042>.

LEE, W.-T.; CHIOU, Y.-J.; SHIH, M. Reinforced concrete beam–column joint strengthened with carbon fiber reinforced polymer. **Composite Structures**, Elsevier, v. 92, n. 1, p. 48–60, 2010. Available at: <https://doi.org/10.1016/j.compstruct.2009.06.011>.

LI, B.; KULKARNI, S. A. Seismic Behavior of Reinforced Concrete Exterior Wide Beam-Column Joints. **Journal of Structural Engineering**, v. 136, n. 1, p. 26–36, 2010. ISSN 0733-9445.

LI, S.; LI, Q.; JIANG, H.; ZHANG, H.; ZHANG, L. Experimental research on seismic performance of a new-type of r/c beam-column joints with end plates. **Shock and Vibration**, Hindawi Limited, v. 2017, p. 1–11, 2017. Available at: <https://doi.org/10.1155/2017/3823469>.

LIU, A. **Seismic Assessment and Retrofit of pre-1970s Reinforced Concrete Frame Structures**. 398 p. (PhD Thesis), 2001.

LIU, A.; PARK, R. Seismic load tests on two interior beam column joints reinforced by plain round bars designed to pre 1970s seismic codes. **Bulletin of the New Zealand Society for Earthquake Engineering**, v. 31, n. 3, p. 164–176, 1998.

MA, C.; WANG, D.; WANG, Z. Seismic retrofitting of full-scale rc interior beam-column-slab subassemblies with cfrp wraps. **Composite Structures**, Elsevier, v. 159, p. 397–409, 2017. Available at: <https://doi.org/10.1016/j.compstruct.2016.09.094>.

MA, C.; WANG, Z.; SMITH, S. T. Seismic Performance of Large-Scale RC Eccentric Corner Beam-Column-Slab Joints Strengthened with CFRP Systems. **Journal of Composites for Construction**, v. 24, n. 2, p. 04019066, 2020. ISSN 1090-0268.

MATSAGAR, V. Advances in structural engineering: Materials, volume three. **Advances in Structural Engineering: Materials, Volume Three**, n. December, p. 1619–2647, 2015.

MEAS, K.; LI, B.; PHAM, T. Experimental and numerical studies on the seismic performance of RC interior beam-column joints. **Advances in Structural Engineering**, v. 17, n. 2, p. 233–248, 2014. ISSN 13694332.

MEGGET, L. M. Cyclic behavior of exterior reinforced concrete beam column joints. **Bulletim of the New Zealand Society for Earthquake Engineering**, v. 7, n. 1, p. 27–47, 1974.

MEINHEIT, D.; JIRSA, J. O. **The Shear Strength of Reinforced Concrete Beam-Column Joints**. [S.l.], 1977. Available at: <https://elibrary.ru/item.asp?id=7207697>.

MELO, J.; VARUM, H.; COSTA, A. Cyclic response of RC beam-column joints reinforced with plain bars : An experimental testing campaign. In: **Proceedings of the 15th World Conference on Earthquake Engineering**. [S.l.: s.n.], 2012. p. 24–28.

MELO, J.; VARUM, H.; ROSSETTO, T. Cyclic behaviour of interior beam – column joints reinforced with plain bars. **Earthquake Engineering and Structural Dynamics**, v. 44, n. 9, p. 1351–1371, 2015.

MENEGOTTO, M. Method of analysis for cyclically loaded rc plane frames including changes in geometry and non-elastic behavior of elements under combined normal force and bending. In: **Proc. of IABSE Symposium on Resistance and Ultimate Deformability of Structures Acted on by Well Defined Repeated Loads**. [S.l.: s.n.], 1973. p. 15–22.

MENETREY, P.; WILLIAM, K. J. Triaxial failure criterion for concrete and its generalization. **ACI Structural Journal**, v. 92, n. 3, p. 311–318, 1995. ISSN 08893241. Available at: <http://dx.doi.org/10.14359/1132>.

MENNA, C.; MAZIA, C.; SGOBBA, S.; ASPRONE, D.; PROTA, A. Structural behavior of strengthened rc columns using high performance fiber reinforced concrete. In: **4th international conference symposium on ultra high performance concrete and high performance construction materials**. [S.l.: s.n.], 2016. p. 9–11.

MERTOL, H. C.; RIZKALLA, S.; ZIA, P.; MIRMIRAN, A. Characteristics of compressive stress distribution in high-strength concrete. **ACI Structural Journal**, American Concrete Institute, v. 105, n. 5, p. 626, 2008.

METELLI, G.; MESSALI, F.; BESCHI, C.; RIVA, P. A model for beam-column corner joints of existing RC frame subjected to cyclic loading. **Engineering Structures**, Elsevier Ltd, v. 89, p. 79–92, 2015. ISSN 1873-7323. Available at: <http://dx.doi.org/10.1016/j.engstruct.2015.01.038>.

MINAMI, K.; NISHIMURA, Y. Anchorage strength of bent bar in exterior joints. In: **Design of Reinforced Beam-Column-Joints: 2nd US–NZ–Japan Seminar, Tokyo. Tokyo: University, Dept. of Architecture**. [S.l.: s.n.], 1985.

Ministero delleInfrastrutture e dei Trasporti. **NTC18 Decreto ministeriale 20/2/2018: norme tecniche delle costruzioni. Ministero delleInfrastrutture e dei trasporti, S.O. No. 8 alla G.U. No. 42 del 20/2/2018**. Rome, Italy, 2018.

MOURLAS, C.; PAPADRAKAKIS, M.; MARKOU, G. A computationally efficient model for the cyclic behavior of reinforced concrete structural members. **Engineering Structures**, Elsevier Ltd, v. 141, n. June 2018, p. 97–125, 2017. ISSN 18737323. Available at: <http://dx.doi.org/10.1016/j.engstruct.2017.03.012>.

MUKHERJEE, A.; JOSHI, M. Frpc reinforced concrete beam-column joints under cyclic excitation. **Composite structures**, Elsevier, v. 70, n. 2, p. 185–199, 2005. Available at: <https://doi.org/10.1016/j.compstruct.2004.08.022>.

NAAMAN, A.; REINHARDT, H. Characterization of high performance fiber reinforced cement composites—hpfrcc. In: **High performance fiber reinforced cement composites**. [S.l.: s.n.], 1996. v. 2, p. 1–24.

NAAMAN, A. E.; REINHARDT, H.-W. Proposed classification of hpfrc composites based on their tensile response. **Materials and structures**, Springer, v. 39, p. 547–555, 2006.

NAGIB, M. T.; SAKR, M. A.; EL-KHORIBY, S. R.; KHALIFA, T. M. Interfacial shear behavior between uhpfrc layers and normal concrete substrate for shear-strengthened squat rc shear walls under cyclic loading. **Engineering Structures**, Elsevier, v. 254, p. 113850, 2022.

NAJAFGHOLIPOUR, M. A.; DEHGHAN, S. M.; DOOSHABI, A.; NIROOMANDI, A. Finite element analysis of reinforced concrete beam-column connections with governing joint shear failure mode. **Latin American Journal of Solids and Structures**, v. 14, n. 7, p. 1200–1225, 2017. ISSN 16797825.

NOYAN, M. M. A. Experimental study on the behavior of rc beam-column joint retrofitted with ferrocement jacket under cyclic loading. Department of Civil Engineering, 2014.

OBAIDAT, Y. T.; ABU-FARSAKH, G. A.; ASHTEYAT, A. M. Retrofitting of partially damaged reinforced concrete beam-column joints using various plate-configurations of cfrp under cyclic loading. **Construction and Building Materials**, Elsevier, v. 198, p. 313–322, 2019. Available at: <https://doi.org/10.1016/j.conbuildmat.2018.11.267>.

PALOMO, I. R. I.; FRAPPA, G.; ALMEIDA, L. C. de; TRAUTWEIN, L. M.; PAULETTA, M. Analytical and numerical models to determine the strength of rc exterior beam–column joints retrofitted with uhpfrc. **Engineering Structures**, Elsevier, v. 312, p. 118244, 2024.

PAMPANIN, S.; BOLOGNINI, D.; PAVESE, A. Performance-based seismic retrofit strategy for existing reinforced concrete frame systems using fiber-reinforced polymer composites. **Journal of composites for construction**, American Society of Civil Engineers, v. 11, n. 2, p. 211–226, 2007. Available at: <https://doi.org/10.1061/(asce)1090-0268(2007)11:2(211)>.

PAMPANIN, S.; CALVI, G. M.; MORATTI, M. Seismic behaviour of RC beam-column joints designed for gravity only. 2002.

PANTELIDES, C. P.; HANSEN, J.; NADAULD, J.; REAVELEY, L. D. Assessment of Reinforced Concrete Building Exterior Joints with Substandard Details. **Technical Rep. No., PEER 2002, 18**, n. May, p. 114, 2002.

PARATE, K. N.; KUMAR, R. Simplified empirical model for shear strength of RC beam–column joints. **Asian Journal of Civil Engineering**, Springer International Publishing, v. 20, n. 1, p. 87–111, 2018. ISSN 15630854. Available at: <https://doi.org/10.1007/s42107-018-0090-8>.

PARATE, K. N.; KUMAR, R. Shear strength model for reinforced concrete beam-column joints based on hybrid approach. **Computers and Concrete**, v. 23, n. 6, p. 377–398, 2019. ISSN 1598818X.

PARK, R. Ductility evaluation from laboratory and analytical testing. **Proceedings of the 9th world conference on earthquake engineering**, v. 8, p. 605–6016, 1988.

PARK, R.; MILBURN, J. R. Comparison of Recent New Zealand and United States Seismic Design Provisions for Reinforced Concrete Beam-Column Joints and Test Results From Four Units Designed According To the New Zealand Code. **Bulletin of the New Zealand National Society for Earthquake Engineering**, v. 16, n. 1, p. 3–24, 1983. ISSN 01100718.

PARK, S.; MOSALAM, K. M. Shear strength models of exterior beam-column joints without transverse reinforcement. **PEER report**, v. 106, 2009.

PARK, S.; MOSALAM, K. M. **Analytical model for predicting shear strength of unreinforced exterior beam-column joints**. 2012. 149–160 p.

PARK, S.; MOSALAM, K. M. Parameters for shear strength prediction of exterior beam–column joints without transverse reinforcement. **Engineering structures**, Elsevier, v. 36, p. 198–209, 2012.

PARK, S.; MOSALAM, K. M. Experimental Investigation of Nonductile RC Corner Beam-Column Joints with Floor Slabs. **Journal of Structural Engineering**, v. 139, n. 1, p. 1–14, 2013. ISSN 0733-9445.

PARK, S. H.; KIM, D. J.; RYU, G. S.; KOH, K. T. Tensile behavior of ultra high performance hybrid fiber reinforced concrete. **Cement and Concrete Composites**, Elsevier, v. 34, n. 2, p. 172–184, 2012.

PARVIN, A.; ALTAY, S.; YALCIN, C.; KAYA, O. Cfrp rehabilitation of concrete frame joints with inadequate shear and anchorage details. **Journal of Composites for Construction**, American Society of Civil Engineers, v. 14, n. 1, p. 72–82, 2010. Available at: <https://doi.org/10.1061/(asce)cc.1943-5614.0000055>.

PASCHALIS, S. A.; LAMPROPOULOS, A. P. Developments in the use of ultra high performance fiber reinforced concrete as strengthening material. **Engineering Structures**, Elsevier, v. 233, p. 111914, 2021.

PASCHALIS, S. A.; LAMPROPOULOS, A. P.; TSIOULOU, O. Experimental and numerical study of the performance of ultra high performance fiber reinforced concrete for the flexural strengthening of full scale reinforced concrete members. **Construction and building materials**, Elsevier, v. 186, p. 351–366, 2018. Available at: <https://doi.org/10.1016/j.conbuildmat.2018.07.123>.

PAULAY, T. Equilibrium Criteria for Reinforced Concrete Beam-Column Joints. **Structural Journal**, v. 86, n. 6, p. 635–643, 1989.

PAULAY, T.; PRIESTLEY, M. N. **Seismic design of reinforced concrete and masonry buildings**. [S.l.: s.n.], 1992.

PAULAY, T.; SCARPAS, A. The behaviour of exterior beam-column joints. **Bulletim of the New Zealand Society for Earthquake Engineering**, v. 4, p. 131–144, 1981.

PAULETTA, M.; Di Luca, D.; RUSSO, G. Exterior beam column joints - Shear strength model and design formula. **Engineering Structures**, Elsevier Ltd, v. 94, p. 70–81, 2015. ISSN 1873-7323. Available at: <https://doi.org/10.1016/j.engstruct.2015.03.040>.

POHORYLES, D. A.; MELO, J.; ROSSETTO, T.; D'AYALA, D.; VARUM, H. Experimental comparison of novel cfrp retrofit schemes for realistic full-scale rc beam–column joints. **Journal of Composites for Construction**, American Society of Civil Engineers, v. 22, n. 5, p. 04018027, 2018. Available at: <https://doi.org/10.1061/(asce)cc.1943-5614.0000865>.

PRIESTLEY, M. J. Displacement-based seismic assessment of reinforced concrete buildings. **Journal of Earthquake Engineering**, v. 1, n. 1, p. 157–192, 1997. ISSN 13632469.

REALFONZO, R.; NAPOLI, A.; PINILLA, J. G. R. Cyclic behavior of rc beam-column joints strengthened with frp systems. **Construction and Building Materials**, Elsevier, v. 54, p. 282–297, 2014. Available at: <https://doi.org/10.1016/j.conbuildmat.2013.12.043>.

RICCI, P.; , M. T.; VERDERAME, G. M.; MANFREDI, G. Experimental tests of unreinforced exterior beam-column joints with plain bars. **Engineering Structures**, Elsevier Ltd, v. 118, p. 178–194, 2016. ISSN 18737323. Available at: <http://dx.doi.org/10.1016/j.engstruct.2016.03.033>.

RISI, M. T. D.; VERDERAME, G. M. Experimental assessment and numerical modelling of exterior non-conforming beam-column joints with plain bars. **Engineering Structures**, Elsevier Ltd, v. 150, p. 115–134, 2017. ISSN 18737323. Available at: <http://dx.doi.org/10.1016/j.engstruct.2017.07.039>.

RUSSELL, H. G.; GRAYBEAL, B. A.; RUSSELL, H. G. et al. **Ultra-high performance concrete: A state-of-the-art report for the bridge community (No. FHWA-HRT-13-060).** [S.l.], 2013.

SABAH, H. A. H.; HARBA, I. S. I. A Review-Behavior of Reinforced Concrete Exterior Beam-Column Connections under Cyclic Loading. **E3S Web of Conferences**, v. 318, p. 03008, 2021.

SAFDAR, M.; MATSUMOTO, T.; KAKUMA, K. Flexural behavior of reinforced concrete beams repaired with ultra-high performance fiber reinforced concrete (uhpfrc). **Composite structures**, Elsevier, v. 157, p. 448–460, 2016. Available at: <https://doi.org/10.1016/j.compstruct.2016.09.010>.

SAHARAN, S.; KAUR, G.; BANSAL, P. P. Confined ultrahigh-performance fibre-reinforced concrete in retrofitted beam–column joint: experimental study. **Magazine of Concrete Research**, Thomas Telford Ltd, v. 75, n. 5, p. 217–233, 2023.

SAID, A.; NEHDI, M. Rehabilitation of rc frame joints using local steel bracing. **Structures and Infrastructure Engineering**, Taylor & Francis, v. 4, n. 6, p. 431–447, 2008. Available at: <https://doi.org/10.1016/j.istruc.2021.08.042>.

SAKR, M. A.; KORANY, T. M. E.; OSAMA, B. Analysis of rc columns strengthened with ultra-high performance fiber reinforced concrete jackets under eccentric loading. **Engineering Structures**, Elsevier, v. 220, p. 111016, 2020.

SAMANI, A. K.; ATTARD, M. M. Lateral strain model for concrete under compression. **ACI Structural Journal**, American Concrete Institute, v. 111, n. 2, p. 441–451, 2014.

SARSAM, K. F.; PHIPPS, M. E.; SARSAM, K. F.; PHIPPS, M. E. The shear design of in situ reinforced concrete beam-column joints subjected to monotonic loading. **Magazine of Concrete Research**, v. 37, n. 130, p. 16–28, 1985. ISSN 1751763X.

SASMAL, S.; NOVÁK, B.; RAMANJANEYULU, K. Numerical analysis of fiber composite-steel plate upgraded beam–column sub-assemblages under cyclic loading. **Composite Structures**, Elsevier, v. 93, n. 2, p. 599–610, 2011. Available at: <https://doi.10.1016/j.compstruct.2010.08.019>.

SCHMIDT, M.; FEHLING, E. Ultra-high-performance concrete: Research, development and application in Europe. **American Concrete Institute, ACI Special Publication**, SP-228, n. September 2015, p. 51–77, 2005. ISSN 01932527.

SCOTT, B. D.; PARK, R.; PRIESTLEY, M. J. N. Stress-Strain Behavior of Concrete Confined by Overlapping Hoops at Low and High Strain Rates. **aci journal**, n. 79, p. 13–27, 1982.

SEZEN, H. Repair and strengthening of reinforced concrete beam-column joints with fiber-reinforced polymer composites. **Journal of Composites for Construction**, American Society of Civil Engineers, v. 16, n. 5, p. 499–506, 2012. Available at: <https://doi.org/10.1061/(asce)cc.1943-5614.0000290>.

SHAFAEI, J.; HOSSEINI, A.; MAREFAT, M. S.; INGHAM, J. M.; ZARE, H. Experimental Evaluation of Seismically and Non-Seismically Detailed External RC Beam-Column Joints. **Journal of Earthquake Engineering**, v. 21, n. 5, p. 776–807, 2017. ISSN 13632469.

SHANNAG, M.; ALHASSAN, M. Seismic upgrade of interior beam-column subassemblages with high-performance fiber-reinforced concrete jackets. **ACI structural journal**, American Concrete Institute, v. 102, n. 1, p. 131, 2005. Available at: <https://doi.org/10.14359/13538>.

SHANNAG, M.; BARAKAT, S.; ABDUL-KAREEM, M. Cyclic behavior of hpfrc-repaired reinforced concrete interior beam-column joints. **Materials and Structures**, Springer, v. 35, p. 348–356, 2002.

SHARMA, A.; ELIGEHAUSEN, R.; REDDY, G.; VAZE, K.; GHOSH, A.; KUSHWAHA, H. Investigations on inelastic behavior of non-seismically detailed reinforced concrete beam-column joints under cyclic excitations. **BARC External Report No. BARC/2008/E/017 Bhabha Atomic Research Centre**, 2008.

SHARMA, R.; BANSAL, P. P. Behavior of rc exterior beam column joint retrofitted using uhp-hfrc. **Construction and Building Materials**, Elsevier, v. 195, p. 376–389, 2019. Available at: <https://doi.org/10.1016/j.conbuildmat.2018.11.052>.

SHIRAI, N. Evaluation of cyclic deterioration and post-peak behavior of rc beam-column joint assemblages by 3-d fe analysis. **American Concrete Institute, ACI Special Publication**, SP-237, p. 129–148, 2006. ISSN 01932527.

SOHAIL, M.; JUNAID, M.; ASLAM, M.; KHAN, K. A review on high performance fiber reinforced concrete: Properties and applications. **Journal of Building Engineering**, v. 44, p. 103299, 2021.

SOLEIMANI, D.; POPOV, E. P.; BERTERO, V. V. Hysteretic Behavior of Reinforced Concrete Beam-Column Subassemblages. **Journal of the American Concrete Institute**, v. 76, n. 11, p. 1179–1195, 1979. ISSN 00028061.

TAMBUSAY, A.; SURYANTO, B.; SUPROBO, P. Nonlinear finite element analysis of reinforced concrete beam-column joints under reversed cyclic loading. **IOP Conference Series: Materials Science and Engineering**, v. 930, n. 1, 2020. ISSN 1757899X.

TRAN, T. M.; HADI, M. N.; PHAM, T. M. A new empirical model for shear strength of reinforced concrete beam-column connections. **Magazine of Concrete Research**, v. 66, n. 10, p. 514–530, 2014. ISSN 1751763X.

TSONOS, A. G. Lateral load response of strengthened reinforced concrete beam-to-column joints. **ACI Structural Journal**, v. 96, n. 1, p. 46–56, 1999. ISSN 08893241.

TSONOS, A. G. Cyclic load behaviour of reinforced concrete beam-column subassemblages of modern structures. **WIT Transactions on the Built Environment**, v. 81, n. 104, p. 439–449, 2005. ISSN 17433509.

TSONOS, A. G. Effectiveness of CFRP-jackets and RC-jackets in post-earthquake and pre-earthquake retrofitting of beam-column subassemblages. **Engineering Structures**, v. 30, n. 3, p. 777–793, 2008. ISSN 01410296.

UZUMERI, B. S. M. Strength and Ductility of Cast-In-Place Beam-Column Joints. In: **From the American Concrete Institute Annual Convention, Symposium on Reinforced Concrete Structures in Seismic Zone**. [S.l.: s.n.], 1977.

VAGHANI, M.; VASANWALA, S. a.; DESAI, a. K. Performance of RC Beam Column Connections Subjected to Cyclic Loading. **IOSR Journal of Mechanical and Civil Engineering**, v. 12, n. 2, p. 2320–334, 2015. Available at: <www.iosrjournals.org>.

Van Mier, J. G. Multiaxial strain softening of concrete. **Materials and Structures/Materiaux et Constructions**, v. 19, n. 111, p. 190–200, 1986. ISSN 13595997. Available at: <https://doi.org/10.1007/BF02472035>.

Van Mier, J. G.; VONK, R. A. Fracture of concrete under multiaxial stress-recent developments. **Materials and Structures**, v. 24, n. 1, p. 61–65, 1991. ISSN 00255432.

VANDANA, R. K.; BINDHU, K. R. Influence of geometric and material characteristics on the behavior of reinforced concrete beam-column connections. **Canadian Journal of Civil Engineering**, v. 44, n. 5, p. 377–386, 2017. ISSN 12086029.

VECCHIO, C. D.; LUDOVICO, M. D.; BALSAMO, A.; PROTA, A.; MANFREDI, G.; DOLCE, M. Experimental investigation of exterior rc beam-column joints retrofitted with frp systems. **Journal of Composites for Construction**, American Society of Civil Engineers, v. 18, n. 4, p. 04014002, 2014. Available at: <https://doi.org/10.1061/(asce)cc.19435614.0000459>.

VECCHIO, F. J.; COLLINS, M. P. **Modified Compression-Field Theory for Reinforced Concrete Elements Subjected To Shear.** 1986. 219–231 p.

VECCHIO, F. J.; COLLINS, M. P. The Modified Compression-Field Theory for Reinforced Concrete Elements Subjected To Shear. **Journal of the American Concrete Institute**, v. 83, n. 2, p. 219–231, 1986. ISSN 00028061.

VECCHIO, F. J.; EMARA, M. B. **Shear deformations in reinforced concrete frames**. 1992. 46–56 p.

VERDERAME, G. M.; De Risi, M. T.; RICCI, P. Experimental Investigation of Exterior Unreinforced Beam-Column Joints with Plain and Deformed Bars. **Journal of Earthquake Engineering**, Taylor & Francis, v. 22, n. 3, p. 404–434, 2018. ISSN 13632469.

WALLACE, J. L. **Behaviour of beam lap splices under seismic loading**. (PhD Thesis) — University of Canterbury, 1996.

WALRAVEN, J. High performance fiber reinforced concrete: Progress in knowledge and design codes. **Materials and Structures**, v. 42, p. 1247–1260, 2009.

WANG, G.-l.; DAI, J.-g.; TENG, J. G. Shear strength model for RC beam – column joints under seismic loading. **Engineering Structures**, Elsevier Ltd, v. 40, p. 350–360, 2012.

WILLE, K.; EL-TAWIL, S.; NAAMAN, A. E. Properties of strain hardening ultra high performance fiber reinforced concrete (uhp-frc) under direct tensile loading. **Cement and Concrete Composites**, Elsevier, v. 48, p. 53–66, 2014. Available at: <https://doi.org/10.1016/j.cemconcomp.2013.12.015>.

WONG, H. **Shear strength and seismic performance of non-seismically designed RC beam-column joints**. (PhD Thesis) — PhD thesis, 2005.

XIN, T.; ZHI, F.; TENG, Z.; XIANG, Y. Behavior and constitutive model of ultra-high-performance concrete under monotonic and cyclic tensile loading. **Construction and Building Materials**, Elsevier, v. 389, p. 131634, 2023.

YANG, H.; ZHAO, W.; ZHU, Z.; FU, J. Seismic behavior comparison of reinforced concrete interior beam-column joints based on different loading methods. **Engineering Structures**, Elsevier, v. 166, n. October 2017, p. 31–45, 2018. ISSN 18737323.

ZERBE, H. E. **Effect of a slab on the behavior of exterior beam to column connections**. (PhD Thesis), 1985.

Appendix

APPENDIX A –

Table A.1 – Database of experimental tests of joints with and without seismic criteria

No. / Ref	*Name*	*Reinf.*	f_c $[MPa]$	f_{yb} $[MPa]$	f_{yjh} $[MPa]$	f_{yjv} $[MPa]$	b_b $[mm]$	b_c $[mm]$	h_b $[mm]$	h_c $[mm]$	A_{sb} $[mm^2]$	A_{sb} $[mm^2]$	A_{sc} $[mm^2]$	A_{sjh} $[mm^2]$	A_{sjv} $[mm^2]$	N_c $[kN]$	a_c $[mm]$	V_b $[kN]$	$V_{jh.exp}$ $[kN]$
1 Hanson and Connor (1967)	I	R	23.9	347	321	483	305	381	508	381	2579	1289	8059	1267	2015	644	155.4	126.3	819.7
2 Hanson and Connor (1967)	IA	R	22.1	347	364	483	305	381	508	381	2579	1289	8059	713	2015	647	160.6	101.9	662.4
3 Hanson and Connor (1967)	II	R	25.2	347	378	483	305	381	508	381	2579	1289	8059	1267	2015	284	120.4	117.4	761.1
4 Hanson and Connor (1967)	III	R	22.1	347	339	483	305	381	508	305	2579	1289	8059	1267	0	335	110.0	89.9	585.4
5 Hanson and Connor (1967)	IV	R	24.0	347	359	483	305	381	508	305	2579	1289	8059	1267	0	30	79.0	48.9	318.1
6 Hanson and Connor (1967)	V	UR	22.8	347	0	483	305	381	508	381	2579	1289	8059	0	2015	636	157.5	89.9	583.9
7 Megget (1974)	A	R	22.1	375	319	365	255	380	460	330	1642	1321	1062	1018	760	200	102.8	161.4	531.0
8 Megget (1974)	B	R	22.1	375	319	365	255	380	460	330	1642	1321	1062	1018	760	200	102.8	161.4	531.0
9 Uzumeri (1977)	1	R	30.8	347	0	332	305	381	508	381	1934	190	-	0	1013.4	520	132.9	–	626.7
10 Uzumeri (1977)	2	R	31.1	349	0	335	305	381	508	381	1934	190	-	0	1013.4	520	132.5	–	608.9
11 Uzumeri (1977)	3	R	27.0	351	428	337	305	381	508	381	1934	1290	-	5705	1013.4	520	138.1	–	648.1
12 Uzumeri (1977)	4	R	31.0	349	380	333	305	381	508	381	1934	1290	-	1013	1013.4	520	132.7	–	734.4
13 Uzumeri (1977)	5	R	31.9	348	0	336	305	381	508	381	1934	1290	-	0	1013.4	520	131.6	–	608.0
14 Uzumeri (1977)	6	UR	36.2	353	357	340	305	381	508	381	1934	1290	-	1013	1013.4	520	127.3	–	728.1
15 Uzumeri (1977)	7	R	30.8	353	366	340	305	381	508	381	1934	1290	-	1013	1013.4	520	132.9	–	698.8
16 Uzumeri (1977)	8	R	26.4	353	366	390	305	381	508	381	2579	1934	-	1013	1013.4	520	139.3	–	838.0
17 Paulay and Scarpas (1981)	1	UR	22.6	296	326	300	356	457	610	457	1885	1885	-	1357	1256.6	250.2	134.8	160	623.1
18 Paulay and Scarpas (1981)	2	UR	22.5	297	326	300	356	457	610	457	2790	2790	-	943	1256.6	704.9	172.5	222.0	878.8
19 Paulay and Scarpas (1981)	3	R	26.9	296	326	300	356	457	610	457	1885	1885	-	1357	1256.6	297.8	134.8	170	659.8
20 Ehsani and Wight (1985)	1B	R	33.6	338	437	490	259	300	480	300	2019	2019	2850	887	570	178	89.9	142.3	498.4
21 Ehsani and Wight (1985)	2B	R	35.0	338	437	490	259	300	439	300	2019	2019	3420	887	570	178	89.4	133.4	531.9
22 Ehsani and Wight (1985)	3B	R	40.9	338	437	490	259	300	480	300	2019	2019	2850	887	570	178	87.3	177.9	620.2
23 Ehsani and Wight (1985)	4B	R	44.6	338	437	490	259	300	439	300	2019	2019	3420	887	570	178	86.2	169.0	670.0
24 Ehsani and Wight (1985)	5B	R	24.4	331	437	414	300	340	480	340	2328	2328	6080	887	1013	229	108.6	164.6	583.3
25 Ehsani and Wight (1985)	6B	R	39.8	338	437	490	300	340	480	340	1734	1734	2850	887	570	229	99.5	155.7	538.1
26 Ehsani et al. (1987)	1	R	64.7	455	455	455	300	340	480	340	1164	1164	2692	887	570	133	90.2	144.6	543.3
27 Ehsani et al. (1987)	2	R	67.3	455	455	455	300	340	480	340	1425	1425	2692	887	570	338	97.6	184.6	735.0
28 Ehsani et al. (1987)	3	R	64.7	455	455	455	259	300	439	300	1251	1251	2692	887	570	383	91.7	135.7	581.1
29 Ehsani et al. (1987)	4	R	67.3	455	455	455	259	300	439	300	1560	1560	3579	887	776	325	88.6	157.9	682.2
30 Ehsani et al. (1987)	5	R	44.6	455	455	455	259	300	439	300	2019	2019	2850	887	570	222	89.1	169.0	692.7
31 Ehsani and Alameddine (1991)	LL8	R	55.1	457	447	463	318	356	508	356	2228	2228	3579	1161	776	294	101.6	249.2	894.3
32 Ehsani and Alameddine (1991)	LH8	R	55.1	457	447	463	318	356	508	356	2228	2228	3579	1935	776				
33 Ehsani and Alameddine (1991)	HL8	R	55.1	443	447	457	318	356	508	356	2780	2780	3040	1161	1013	507	110.9	267.0	974.6
34 Ehsani and Alameddine (1991)	HH8	R	55.1	443	447	457	318	356	508	356	2780	2780	4054	1935	1013	507	110.9	267.0	974.6
35 Ehsani and Alameddine (1991)	LL11	R	75.8	457	447	463	318	356	508	356	2228	2228	3579	1161	776	285	97.9	235.9	819.1
36 Ehsani and Alameddine (1991)	LH11	R	75.8	457	447	463	318	356	508	356	2228	2228	3579	1935	776	276	97.6	284.8	1007.4
37 Ehsani and Alameddine (1991)	HL11	R	75.8	443	447	457	318	356	508	356	2780	2780	4054	1161	1013	587	107.4	271.5	958.4
38 Ehsani and Alameddine (1991)	HH11	R	75.8	443	447	457	318	356	508	356	2780	2780	4054	1935	1013	605	108.0	293.7	1046.6
39 Ehsani and Alameddine (1991)	LL14	R	96.5	457	447	463	318	356	508	356	2228	2228	3579	1161	776	236	94.7	267.0	950.1
40 Ehsani and Alameddine (1991)	LH14	R	96.5	457	447	463	318	356	508	356	2228	2228	3579	1935	776	223	94.4	271.5	965.9
41 Ehsani and Alameddine (1991)	HH14	R	96.5	443	447	457	318	356	508	356	2780	2780	4054	1935	1013	476	100.7	293.7	1072.9
42 Kaku and Asakusa (1991)	1	R	31.1	391	250	360	160	220	220	220	531	531	804	226	0	258	87.1	43.0	207.0
43 Kaku and Asakusa (1991)	2	R	41.7	391	250	360	160	220	220	220	531	531	804	226	0	199	73.4	55.0	263.2
44 Kaku and Asakusa (1991)	3	R	41.7	391	250	360	160	220	220	220	531	531	804	226	0	0	55.0	43.5	208.2
45 Kaku and Asakusa (1991)	4	R	44.7	391	281	360	160	220	220	220	531	531	804	57	0	360	86.1	50.0	239.0

Name: Name of specimen; *R*: Reinforced joint; *UR*: Unreinforced joint

No. / Ref	Name	Reinf.	f_c [MPa]	f_{yb} [MPa]	f_{yjh} [MPa]	f_{yjv} [MPa]	b_b [mm]	b_c [mm]	h_b [mm]	h_c [mm]	A_{sb} [mm^2]	A_{sb} [mm^2]	A_{sc} [mm^2]	A_{sjh} [mm^2]	A_{sjv} [mm^2]	N_c [kN]	a_c [mm]	V_b [kN]	$V_{jh.exp}$ [kN]
46 Kaku and Asakusa (1991)	5	R	36.7	391	281	360	160	220	220	220	531	531	804	57	0	160	71.8	45.0	215.9
47 Kaku and Asakusa (1991)	6	R	40.4	391	281	360	160	220	220	220	531	531	804	57	0	0	55.0	41.0	196.3
48 Kaku and Asakusa (1991)	7	R	32.2	391	250	395	160	220	220	220	531	531	942	226	314	194	78.3	55.0	264.6
49 Kaku and Asakusa (1991)	8	R	41.2	391	250	395	160	220	220	220	531	531	942	226	314	160	70.0	54.0	258.5
50 Kaku and Asakusa (1991)	9	R	40.6	391	250	395	160	220	220	220	531	531	942	226	314	0	55.0	54.0	258.6
51 Kaku and Asakusa (1991)	10	R	44.4	391	281	395	160	220	220	220	531	531	942	57	314	360	86.3	55.0	262.9
52 Kaku and Asakusa (1991)	11	R	41.9	391	281	395	160	220	220	220	531	531	942	57	314	160	69.8	48.0	229.7
53 Kaku and Asakusa (1991)	12	R	35.1	391	281	395	160	220	220	220	531	531	942	57	314	0	55.0	47.0	225.7
54 Kaku and Asakusa (1991)	14	R	41.0	391	250	315	160	220	220	220	531	531	757	57	113	160	70.1	46.0	220.2
55 Kaku and Asakusa (1991)	15	R	39.7	391	250	390	160	220	220	220	531	531	757	57	157	160	70.6	46.0	220.4
56 Tsonos (1999)	M1	R	34.0	497	495	465	200	200	300	200	383	383	314	402	0	300	87.5	67.0	214.3
57 Tsonos (1999)	M2	R	33.5	485	495	465	200	200	300	200	616	616	314	402	0	300	88.0	90.0	294.0
58 Hakuto et al. (2000)	O6	R	31.0	333	0	333	300	450	500	460	804	804	-	0	0	0	115.0	62.0	434
+ 59 Clyde et al. (2002)	2	UR	46.2	454	0	470	305	305	406	457	2579	2579	3104	0	776	645	153.2	269.0	1036.4
60 Clyde et al. (2002)	4	UR	41.0	454	0	470	305	305	406	457	2579	2579	3104	0	776	1429	211.5	275.0	1062.2
61 Clyde et al. (2002)	5	UR	37.1	454	0	470	305	305	406	457	2579	2579	3104	0	776	1292	211.5	266.9	1033.0
62 Clyde et al. (2002)	6	UR	40.2	454	0	470	305	305	406	457	2579	2579	3104	0	776	560	153.2	262.4	1014.1
63 Pantelides et al. (2002)	1	UR	33.1	459	0	470	406	406	406	406	2579	2579	4054	0	0	547	136.1	194.8	884.4
64 Pantelides et al. (2002)	2	UR	30.2	459	0	470	406	406	406	406	2579	2579	4054	0	0	1247	188.0	189.9	863.8
65 Pantelides et al. (2002)	3	UR	34.0	459	0	470	406	406	406	406	2579	2579	4054	0	0	562	136.1	187.7	851.6
66 Pantelides et al. (2002)	4	UR	31.6	459	0	470	406	406	406	406	2579	2579	4054	0	0	1305	188.0	211.3	960.0
67 Pantelides et al. (2002)	5	UR	31.7	459	0	470	406	406	406	406	2579	2579	4054	0	0	524	136.1	193.9	881.1
68 Pantelides et al. (2002)	6	UR	31.0	459	0	470	406	406	406	406	2579	2579	4054	0	0	1280	188.0	197.5	897.7
69 Hwang et al. (2004)	70-3T44	UR	76.8	430	498	421	320	420	450	420	2027	2027	-	1140	1635	196	110.2	–	1065.0
70 Hwang et al. (2004)	70-3T4	UR	75.2	491	436	458	320	450	450	450	2027	2027	-	1520	1635	196	117.4	–	1110
71 Hwang et al. (2004)	70-2T5	UR	76.6	491	469	458	320	450	450	450	2027	2027	-	792	1635	196	117.3	–	1162.0
72 Hwang et al. (2004)	70-1T55	UR	69.7	491	469	458	320	450	450	450	2027	2027	-	792	1635	196	117.8	–	1126.0
73 Hwang et al. (2004)	28-3T4	UR	35.0	491	436	458	380	550	500	550	2027	2027	-	760	3269	196	146.2	–	1290
74 Hwang et al. (2004)	28-0T0	UR	33.0	491	0	458	380	550	500	550	2027	2027	-	0	3269	196	146.7	–	1138.0
75 Chun and Kim (2004)	JC-1	UR	40.8	392	392	392	350	500	500	500	1521	1140	-	314	2281	490	145.4	175.0	825.2
76 Chun and Kim (2004)	JM-1	UR	40.8	392	392	392	350	500	500	500	1521	1140	-	314	2281	490	145.4	137.0	646.0
77 Chun and Kim (2004)	JC-2	R	40.8	392	392	392	350	500	500	500	3041	2281	-	314	2281	490	145.4	250	1216.7
78 Chun and Kim (2004)	JM-2	R	40.8	392	392	392	350	500	500	500	3041	228	-	314	2281	490	145.4	260	1265.4
79 Tsonos (2005)	A1	R	35.0	500	540	500	200	200	300	200	314	314	-	283	157	200	74.3	57.0	165.4
80 Tsonos (2005)	E1	R	22.0	495	540	495	200	200	300	200	462	462	-	283	308	200	88.6	70	208.3
81 Tsonos (2005)	E2	R	35.0	495	540	495	200	200	300	200	308	308	-	283	308	200	74.3	53.0	153.7
82 Tsonos (2005)	G1	UR	22.0	495	540	495	200	200	300	200	462	462	-	113	308	200	88.6	62.0	184.5
83 Kuang and Wong (2006)	BS-L	R	38.6	520	0	520	260	300	450	300	942	942	1963	0	0	504	112.0	90.2	316.0
84 Kuang and Wong (2006)	BS-OL	R	38.6	520	0	520	260	300	450	300	942	942	1963	0	0	504	112.0	68.9	232.6
85 Kuang and Wong (2006)	BS-LL	R	52.6	520	0	520	260	300	450	300	942	942	1963	0	0	686	112.0	83.5	280.3
86 Kuang and Wong (2006)	BS-U	R	38.8	520	0	520	260	300	450	300	942	942	1963	0	0	506	112.0	96.2	324.7
87 Kuang and Wong (2006)	BS-L-LS	R	39.5	520	0	520	260	300	450	300	942	942	1963	0	0	515	112.0	86.8	292.9
88 Kusuhara and Shiohara (2008)	A2	R	28.3	456	326	357	300	300	300	300	1062	1061	-	170	796	216	96.6	150.3	769.2
89 Kusuhara and Shiohara (2008)	B1	R	28.3	456	326	357	300	300	300	300	1327	1327	-	170	266	216	96.6	98.4	509.0
90 Kusuhara and Shiohara (2008)	B2	R	28.3	456	326	357	300	300	300	300	1327	1327	-	170	266	216	96.6	92.2	477.0

Name: Name of BCJ joint; *R*: Reinforced joint *UR*: Unreinforced joint

No. / Ref	Name	Reinf.	f_c [MPa]	f_{yb} [MPa]	f_{yjh} [MPa]	f_{yjv} [MPa]	b_b [mm]	b_c [mm]	h_b [mm]	h_c [mm]	A_{sb} [mm^2]	A_{sb} [mm^2]	A_{sc} [mm^2]	A_{sjh} [mm^2]	A_{sjv} [mm^2]	N_c [kN]	a_c [mm]	V_b [kN]	$V_{jh.exp}$ [kN]
91 Kusuhara and Shiohara (2008)	E1	UR	30.4	379	366	375	300	300	300	300	1206	1206	-	170	266	216	95.1	73.2	375.5
92 Kusuhara and Shiohara (2008)	E2	UR	30.4	379	366	375	300	300	300	300	1206	1206	-	170	266	216	95.1	65.0	333.4
93 Bindhu et al. (2009)	A1-456	UR	44.2	432	432	432	100	100	150	150	157	157	-	28	101	16	40.6	15.7	68.0
94 Bindhu et al. (2009)	A1-13920	UR	44.2	432	432	432	100	100	150	150	157	157	-	28	101	16	40.6	16.2	70.1
95 Bindhu et al. (2009)	A2-456	UR	44.2	432	432	432	100	100	150	150	157	157	-	57	101	53	47.7	18.6	80.7
96 Bindhu et al. (2009)	A2-13920	R	44.2	432	432	432	100	100	150	150	157	157	-	57	101	53	47.7	19.6	85.0
97 Bedirhanoglu et al. (2010)	JO1	R	8.3	333	0	333	250	250	500	500	804	804	-	0	0	130	178.1	70	163.9
98 Bedirhanoglu et al. (2010)	JO4	R	8.3	333	0	333	250	250	500	500	804	804	-	0	0	519	337.5	70	163.9
99 Bedirhanoglu et al. (2010)	JO5	R	8.3	333	0	333	250	250	500	500	804	804	-	0	0	130	178.1	55.0	128.8
100 Bedirhanoglu et al. (2010)	JO6	R	8.3	333	0	333	250	250	500	500	804	804	-	0	0	0	125.0	55.0	128.8
101 Bedirhanoglu et al. (2010)	JO7	R	8.3	333	0	333	250	250	500	500	804	804	-	0	0	519	337.5	70	163.9
102 Kaung and Wong (2011)	BS450	UR	38.6	520	0	520	260	300	450	300	942	942	1963	0	0	0	75.0	100.9	315.5
103 Kaung and Wong (2011)	BS-450-H1T10	R	41.6	520	500	520	260	300	450	300	942	942	1963	157	0	0	75.0	124.5	389.3
104 Kaung and Wong (2011)	BS-450-H2T10	R	52.6	520	500	520	260	300	450	300	942	942	1963	314	0	0	75.0	153.2	479.3
105 Kaung and Wong (2011)	BS600	R	45.5	520	500	520	260	300	600	300	942	942	1963	0	0	0	75.0	132.7	283.9
106 Kaung and Wong (2011)	BS-600-H2T8	R	52.7	520	500	520	260	300	600	300	942	942	1963	201	0	0	75.0	170.8	360.1
107 Kaung and Wong (2011)	BS-600-H4T8	UR	37.1	520	0	520	260	300	600	300	942	942	1963	402	0	0	75.0	162.4	342.4
108 Genesio (2012)	2D Pre 1970s	UR	17.7	430	0	430	230	230	330	230	314	314	471	0	0	195	98.1	24.8	112.5
109 Genesio (2012)	JT2-1	UR	24.4	310	0	310	300	350	400	300	829	829	471	0	0	195	94.4	41.5	266.2
110 Melo et al. (2012)	TPA-1	UR	24.2	333	0	333	250	250	400	250	804	804	-	0	0	200	90.6	18.8	93.1
111 Melo et al. (2012)	TPA-2	R	25.8	333	0	333	250	250	400	250	804	804	-	0	0	200	88.9	19.6	97.0
112 Melo et al. (2012)	TPB1	R	15.8	333	0	333	250	250	400	250	804	804	-	0	0	200	105.5	18.5	91.6
113 Melo et al. (2012)	TPB2	R	27.3	333	0	333	250	250	400	250	804	804	-	0	0	200	87.4	19.7	97.5
114 Melo et al. (2012)	TPC	R	23.8	333	0	333	250	250	400	250	804	804	-	0	0	200	91.1	18.2	90.1
115 Chun and Shin (2014)	H0.7S	UR	30.2	488	445	363	250	300	200	300	1140	855	-	649	1013	0	75.0	–	646.0
116 Chun and Shin (2014)	H1.0S	UR	30.2	488	445	363	250	300	300	300	1140	855	-	649	1013	0	75.0	–	563.0
117 Chun and Shin (2014)	H1.5S	UR	30.2	488	445	363	250	300	450	300	1140	855	-	649	1013	0	75.0	–	498.0
118 Chun and Shin (2014)	H2.0S	UR	37.3	488	445	363	250	300	600	300	1140	855	-	649	1013	0	75.0	–	526.0
119 Chun and Shin (2014)	H2.5S	UR	37.3	488	445	363	250	300	750	300	1140	855	-	649	1013	0	75.0	–	454.0
120 Chun and Shin (2014)	H0.7U	UR	30.2	488	430	363	250	300	200	300	1140	855	-	428	1013	0	75.0	–	611.0
121 Chun and Shin (2014)	H1.0U	UR	30.2	488	430	363	250	300	300	300	1140	855	-	428	1013	0	75.0	–	529.0
122 Chun and Shin (2014)	M0.7S	UR	30.2	488	445	363	250	300	200	300	1140	855	-	649	1013	0	75.0	–	596.0
123 Chun and Shin (2014)	M1.0S	R	30.2	488	445	363	250	300	300	300	1140	855	-	649	1013	0	75.0	–	557.0
124 Chun and Shin (2014)	M1.5S	R	30.2	488	445	363	250	300	450	300	1140	855	-	649	1013	0	75.0	–	530
125 Chun and Shin (2014)	M2.0S	R	37.3	488	445	363	250	300	600	300	1140	855	-	649	1013	0	75.0	–	493.0
126 Chun and Shin (2014)	M2.5S	R	37.3	488	445	363	250	300	750	300	1140	855	-	649	1013	0	75.0	–	455.0
127 Chun and Shin (2014)	M0.7U	R	30.2	488	430	363	250	300	200	300	1140	855	-	428	1013	0	75.0	–	683.0
128 Chun and Shin (2014)	M1.0U	R	30.2	488	430	363	250	300	300	300	1140	855	-	428	1013	0	75.0	–	592.0
129 Fadwa et al. (2014)	ECBCC	R	34.0	498	347	345	300	400	550	450	804	616	3054	1005	616	230	126.9	189.2	539.9
130 Ricci et al. (2016)	Test 1#P	UR	28.8	344	0	344	300	300	500	300	1257	1257	2513	0	0	260	100.6	79.2	273.7
131 Ricci et al. (2016)	Test 2#P	UR	28.8	316	0	316	300	300	500	300	616	616	1232	0	0	260	100.6	52.8	181.0
132 Shafaei et al. (2017)	C1	R	23.0	460	350	460	220	250	250	250	616	462	1232	302	308	220	95.0	41.9	270.5
133 Shafaei et al. (2017)	C2	UR	23.3	460	0	460	220	250	250	250	616	462	1232	0	0	220	94.6	37.1	239.4
134 Shafaei et al. (2017)	C3	UR	24.7	460	0	460	220	250	250	250	616	462	1232	0	0	220	92.8	36.3	233.9
135 Risi and Verderame (2017)	1bP	R	17.7	333	0	333	300	300	400	300	804	804	-	0	0	159	100	51.7	214.7

Name: Name of BCJ test; *R*: Reinforced joint; *UR*: UnReinforced joint

No. / Ref	*Name*	*Reinf.*	f_c $[MPa]$	f_{yb} $[MPa]$	f_{yjh} $[MPa]$	f_{yjv} $[MPa]$	b_b $[mm]$	b_c $[mm]$	h_b $[mm]$	h_c $[mm]$	A_{sb} $[mm^2]$	A_{sb} $[mm^2]$	A_{sc} $[mm^2]$	A_{sjh} $[mm^2]$	A_{sjv} $[mm^2]$	N_c $[kN]$	a_c $[mm]$	V_b $[kN]$	$V_{jh.exp}$ $[kN]$
136 Risi and Verderame (2017)	2bP	R	17.7	333	0	333	300	300	400	300	804	804	-	0	0	159	100	50.3	207.6
137 Risi and Verderame (2017)	1cP	R	17.7	333	0	333	300	300	600	300	804	804	-	0	0	159	100	68.4	172.1
138 Risi and Verderame (2017)	2cP	UR	17.7	333	0	333	300	300	600	300	804	804	-	0	0	159	100	46.9	117.6
139 Verderame et al. (2018)	#1D	UR	28.8	487	0	487	300	300	500	300	1257	1257	2513	0	0	260	100.6	72.4	241.5
140 Verderame et al. (2018)	#2D	UR	28.8	459	0	459	300	300	500	300	452	452	905	0	0	260	100.6	58.3	241.5
141 Alavi-Dehkordi et al. (2019)	NS30	R	30.0	420	420	420	250	250	300	250	565	565	1232	402	308	160	80.6	47.8	227.0
142 Alavi-Dehkordi et al. (2019)	RHS30	R	30.0	600	420	600	250	250	300	250	393	393	905	402	226	160	80.6	42.7	208.0
143 Alavi-Dehkordi et al. (2019)	NS70	R	70.0	420	420	420	250	250	300	250	565	565	1232	402	308	160	70.3	46.6	220.0
144 Alavi-Dehkordi et al. (2019)	RHS70	R	70.0	600	420	600	250	250	300	250	393	393	905	402	226	160	70.3	43.7	222.0
145 Alavi-Dehkordi et al. (2019)	CNS70	R	70.0	600	420	420	250	250	300	250	688	688	905	402	226	160	70.3	70.8	343.0
146 Alavi-Dehkordi et al. (2019)	RCHS70	R	70.0	600	420	600	250	250	300	250	688	688	628	402	157	160	70.3	69.2	328.0
147 Cosgun et al. (2020)	J1-REF	UR	9.0	276	445	276	150	150	200	150	308	804	-	302	0	20	50.3	13.0	62.0
148 Cosgun et al. (2020)	J2	UR	9.0	276	0	276	150	150	200	150	308	804	-	0	0	20	50.3	8.8	36.2
149 Cosgun et al. (2020)	J3	R	9.0	276	0	276	150	150	200	150	308	804	-	0	0	20	50.3	7.8	31.8
150 Cosgun et al. (2020)	J4	R	9	276	0	276	150	150	200	150	308	804	-	0	0	20	50.3	6.7	27.3

Name: Name of BCJ joint; *R*: Reinforced joint; *UR*: Unreinforced joint

Table A.2 – Experimental tests validated in the analytical models

Model	*Specimens*
Paulay and Priestley (1992)	[1-8]; [17-57]; [59-98]; [83-87]; [102-109]; [129-134]; [139-146]
NZS 3101 (1995)	[1-5]; [7-8]; [17-57]; [103-106]; [129]; [132]; [141-146]
Priestley (1997)	[6]; [59-68]; [83-87]; [102]; [107-109]; [130-131]; [133-134]; [139-140]
Tsonos (1999)	[1-8]; [17-57]; [59-68]; [83-87]; [102-109]; [129-134]; [139-146]
Pampanin et al. (2002)	[6]; [59-68]; [83-87]; [102]; [107-109]; [130-131]; [133-134]; [139-140]
Hwang and Lee (2002)	[1-5]; [7-8]; [17-57]; [103-104]; [106-107]; [129]; [132]; [141-146]
ASCE SEI/41 (2007)	[1-8]; [17-57]; [59-68]; [102-109]; [129-134]; [139-146]
Kim et al. (2009)	[1-8]; [17-57]; [59-68]; [83-87]; [102-109]; [129-134]; [139-146]
Wang et al. (2012)	[1-8]; [17-57]; [59-68]; [83-87]; [102-109]; [129-134]; [139-146]
Park and Mosalam (2012a)	[6]; [59-68]; [83-87]; [102]; [107-109]; [130-132]; [134]; [139-140]
ACI 318 (2014)	[1-8]; [17-57]; [59-68]; [83-87]; [102-109]; [129-134]; [139-146]
Tran et al. (2014)	[1-8]; [17-57]; [59-68]; [83-87]; [102-109]; [129-134]; [139-146]
Metelli et al. (2015) - PSLM	[58]; [97-101]; [110-114]; [130-131]; [135-138]; [148-150]
Pauletta et al. (2015)	[1-150]
Kassem (2016)	[1-8]; [17-57]; [59-68]; [83-87]; [102-109]; [129-134]; [139-146]
Parate and Kumar (2018)	[1-8]; [17-57]; [59-68]; [83-87]; [102-109]; [129-134]; [139-146]
Hassan and Moehle (2018) - STM	[6]; [59-68]; [83-87]; [102]; [107-109]; [130-131]; [133-134]; [139-140]
Hassan and Moehle (2018) - EMPIR	[6]; [59-68]; [83-87]; [102]; [107-109]; [130-131]; [133-134]; [139-140]
Parate and Kumar (2019)	[1-8]; [17-57]; [59-68]; [83-87]; [102-109]; [129-134]; [139-146]

APPENDIX B –

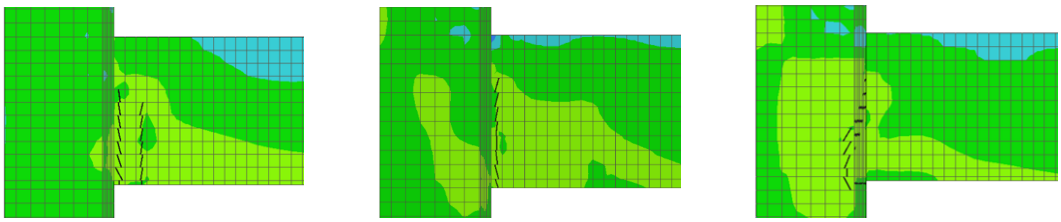

(a) Retrofit: A15 +15mm (b) Retrofit: A30 +15mm (c) Retrofit: A45 +15mm

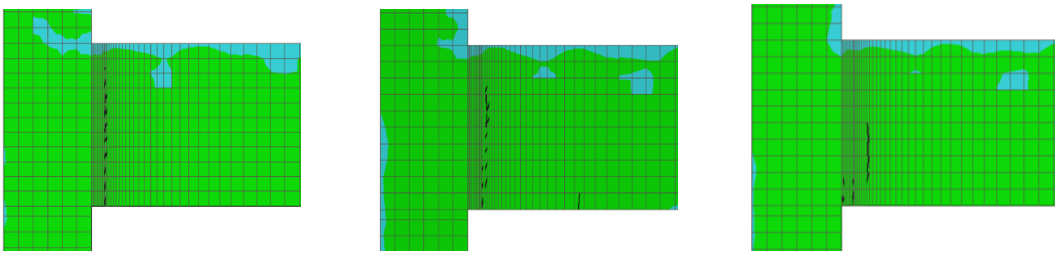

(d) Joint core: A15 +15mm (e) Joint core: A30 +15mm (f) Joint core: A45 +15mm

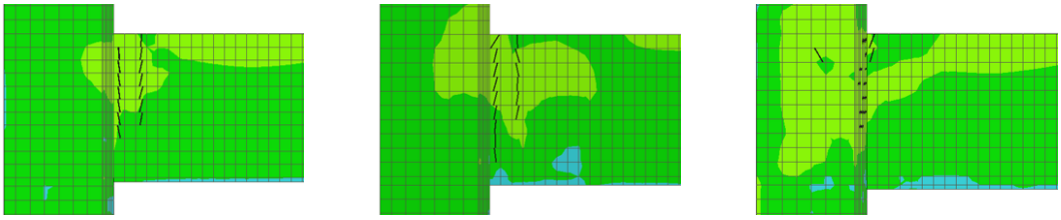

(g) Retrofit: A15 -15mm (h) Retrofit: A30 -15mm (i) Retrofit: A45 -15mm

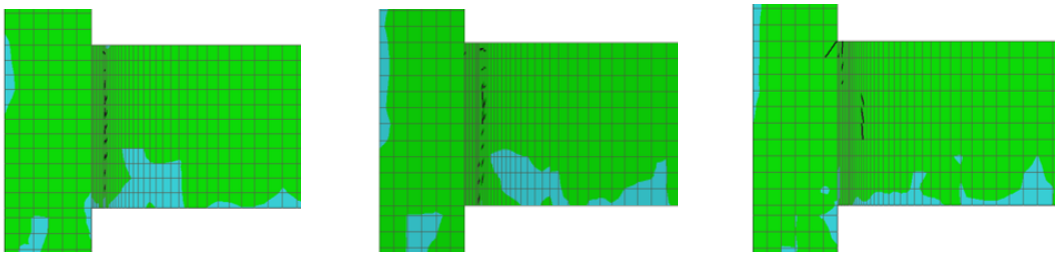

(j) Joint core: A15 -15mm (k) Joint core: A30 -15mm (l) Joint core: A45 -15mm

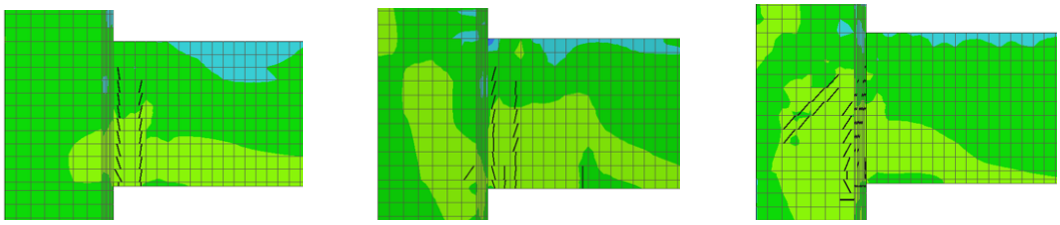

(m) Retrofit: A15 +22.5mm (n) Retrofit: A30 +22.5mm (o) Retrofit: A45 +22.5mm

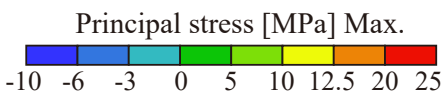

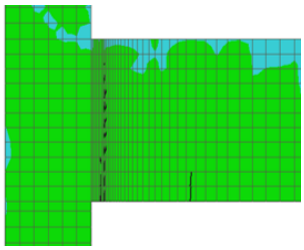

(p) Joint core: A15 +22.5mm

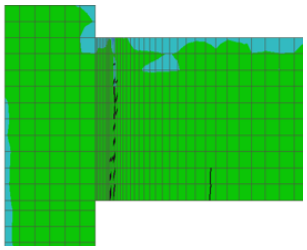

(q) Joint core: A30 +22.5mm

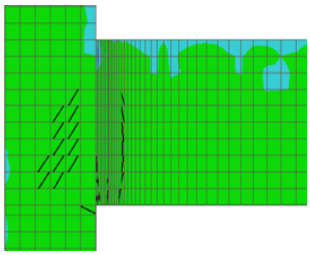

(r) Joint core: A45 +22.5mm

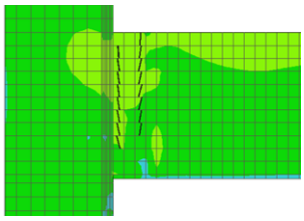

(s) Retrofit: A15 -22.5mm

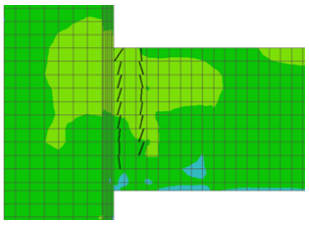

(t) Retrofit: A30 -22.5mm

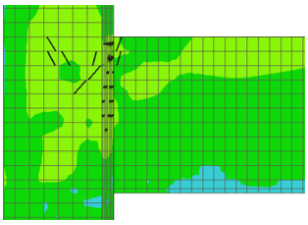

(u) Retrofit: A45 -22.5mm

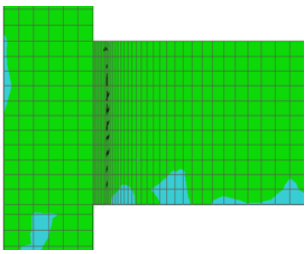

(v) Joint core: A15 -22.5mm

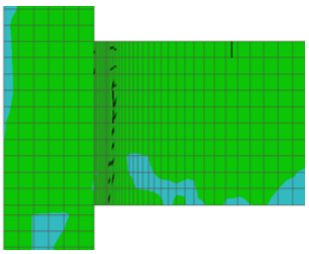

(w) Joint core: A30 -22.5mm

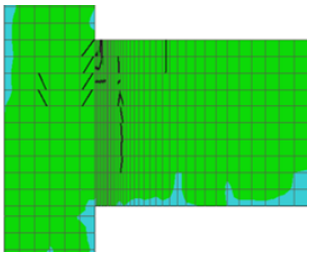

(x) Joint core: A45 -22.5mm

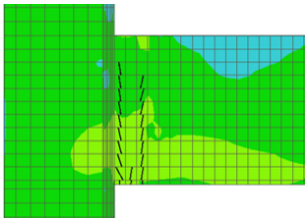

(y) Retrofit: A15 +30mm

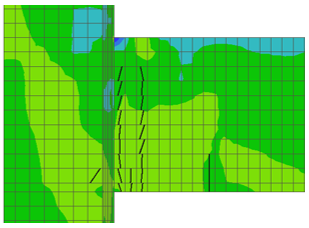

(z) Retrofit: A30 +30mm

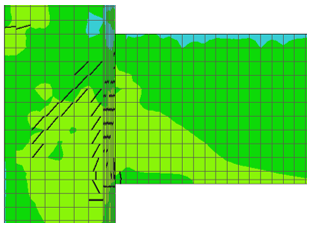

(aa) Retrofit: A45 +30mm

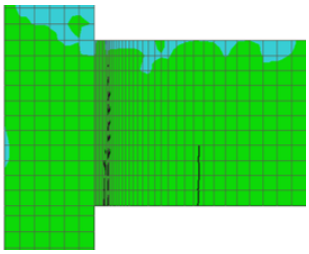

(ab) Joint core: A15 +30mm

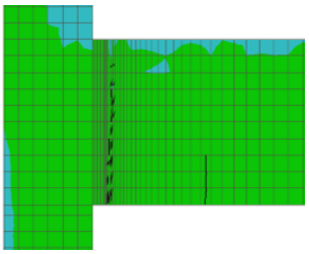

(ac) Joint core: A30 +30mm

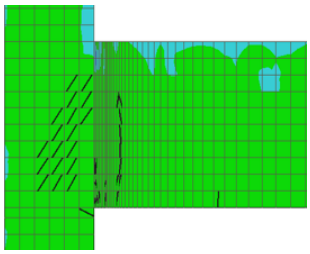

(ad) Joint core: A45 +30mm

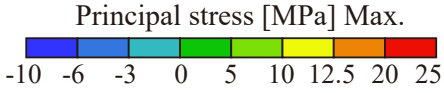

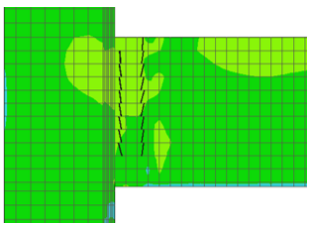

(ae) Retrofit: A15 -30mm

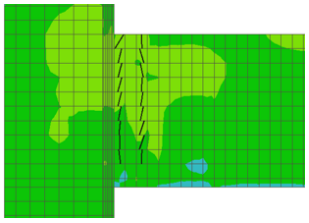

(af) Retrofit: A30 -30mm

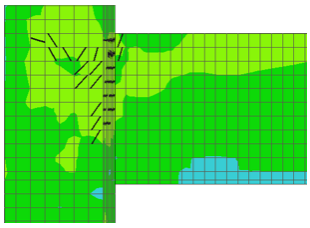

(ag) Retrofit: A45 -30mm

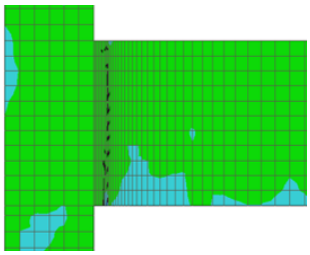

(ah) Joint core: A15 -30mm

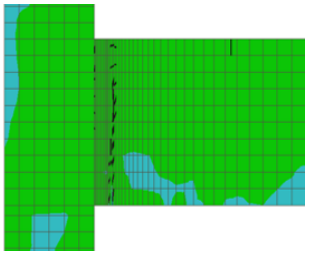

(ai) Joint core: A30 -30mm

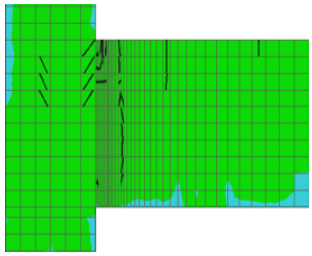

(aj) Joint core: A45 -30mm

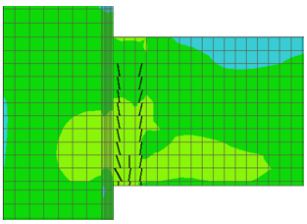

(ak) Retrofit: A15 +45mm

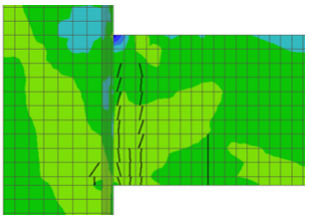

(al) Retrofit: A30 +45mm

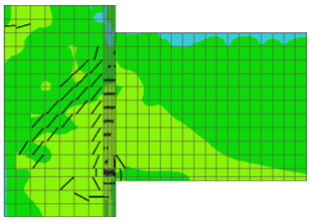

(am) Retrofit: A45 +45mm

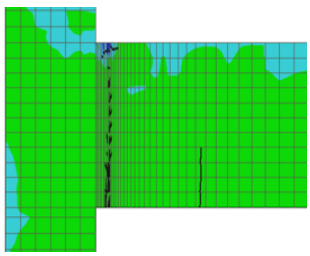

(an) Joint core: A15 +45mm

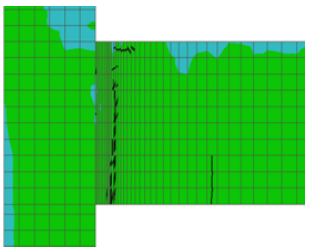

(ao) Joint core: A30 +45mm

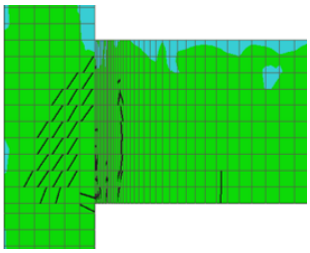

(ap) Joint core: A45 +45mm

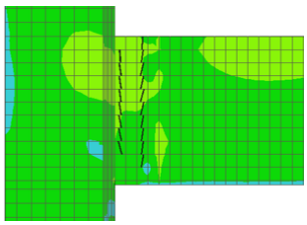

(aq) Retrofit: A15 -45mm

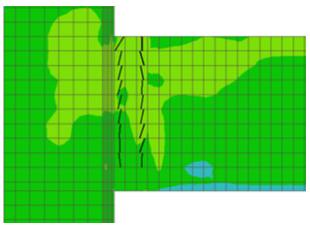

(ar) Retrofit: A30 -45mm

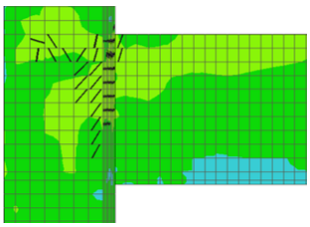

(as) Retrofit: A45 -45mm

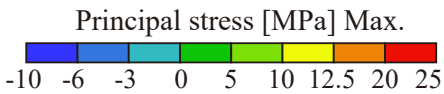

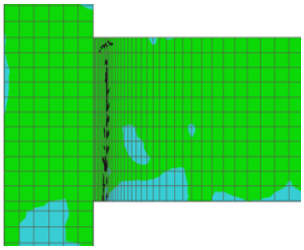

(at) Joint core: A15 - 45mm

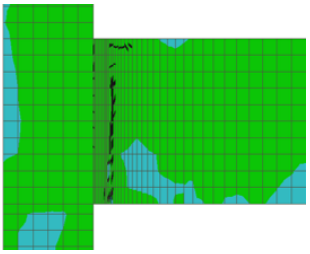

(au) Joint core: A30 - 45mm

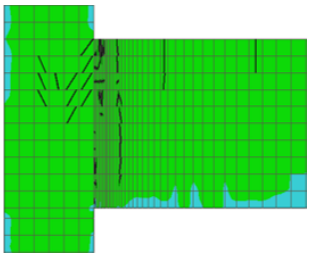

(av) Joint core: A45 - 45mm

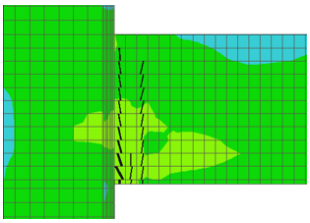

(aw) Retrofit: A15 +60mm

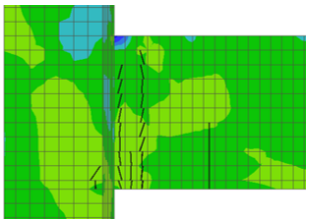

(ax) Retrofit: A30 +60mm

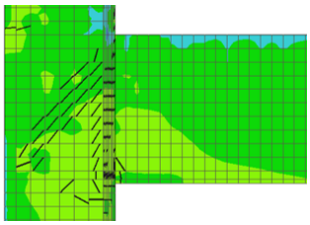

(ay) Retrofit: A45 +60mm

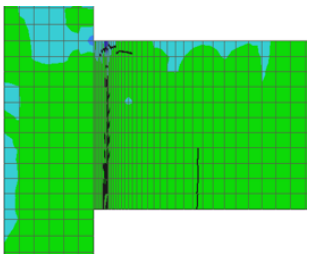

(az) Joint core: A15 +60mm

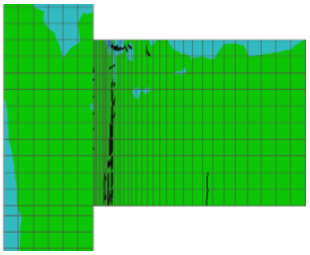

(ba) Joint core: A30 +60mm

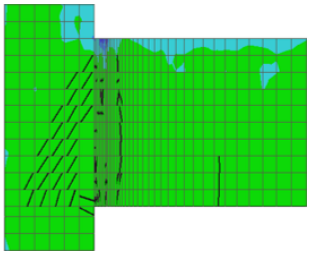

(bb) Joint core: A45 +60mm

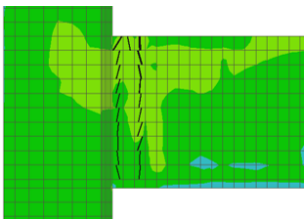

(bc) Retrofit: A15 -60mm

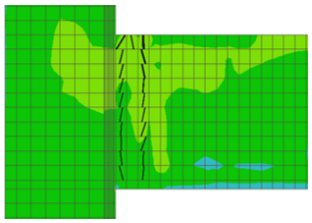

(bd) Retrofit: A30 -60mm

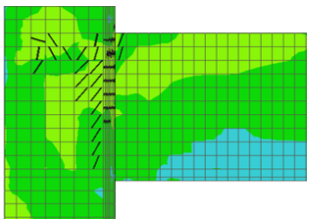

(be) Retrofit: A45 -60mm

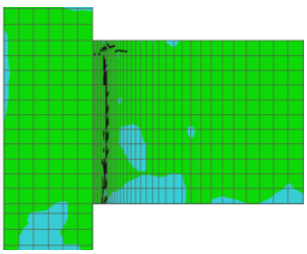

(bf) Joint core: A15 - 60mm

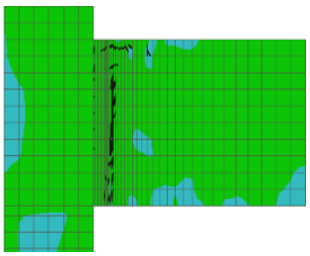

(bg) Joint core: A30 - 60mm

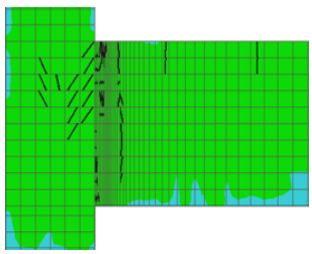

(bh) Joint core: A45 - 60mm

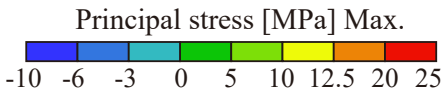

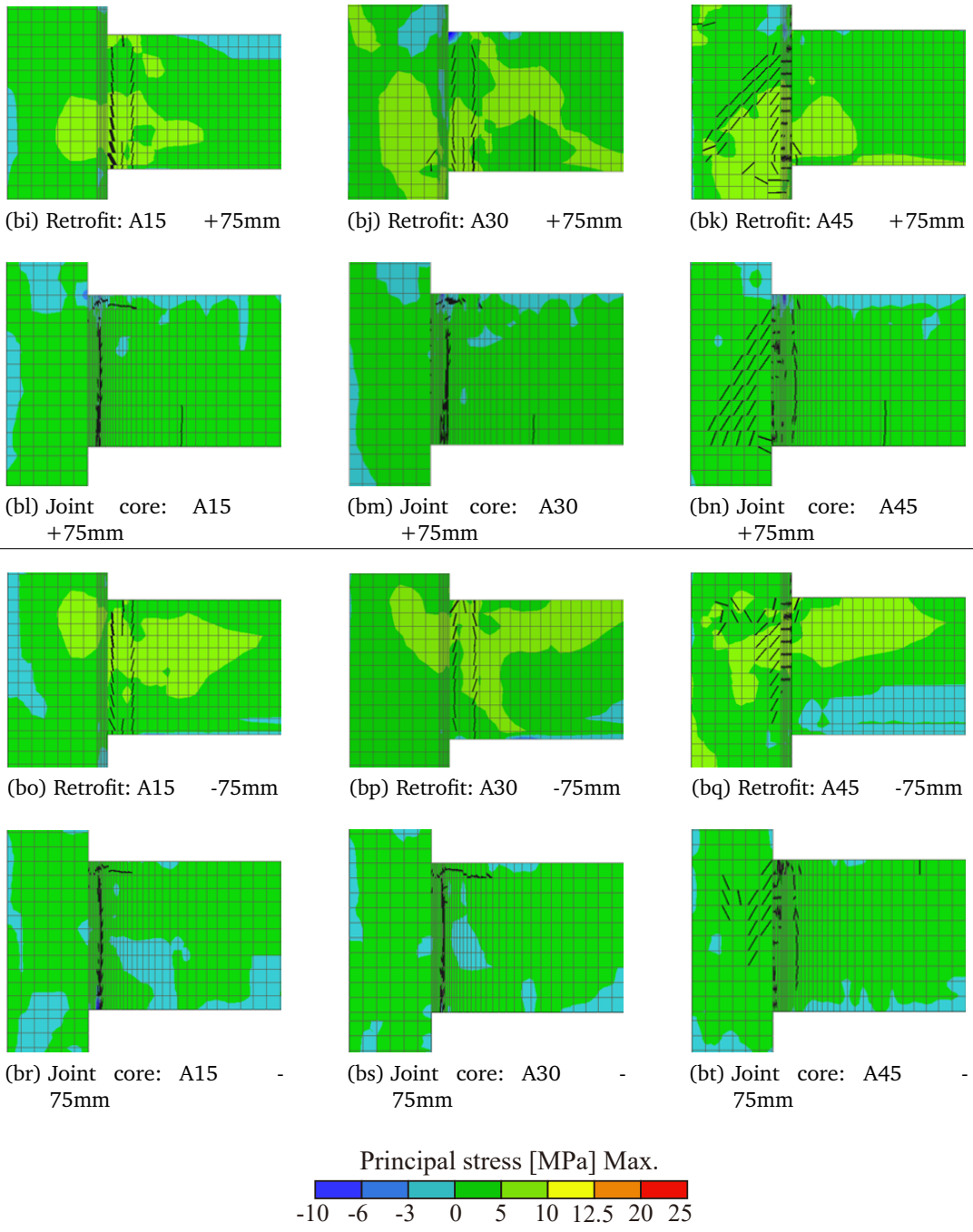

(bi) Retrofit: A15 +75mm (bj) Retrofit: A30 +75mm (bk) Retrofit: A45 +75mm

(bl) Joint core: A15 +75mm (bm) Joint core: A30 +75mm (bn) Joint core: A45 +75mm

(bo) Retrofit: A15 -75mm (bp) Retrofit: A30 -75mm (bq) Retrofit: A45 -75mm

(br) Joint core: A15 -75mm (bs) Joint core: A30 -75mm (bt) Joint core: A45 -75mm

Figure B.1 – Cracking pattern of BCJs of model A, with and no with retrofit, varying the thickness of retrofit

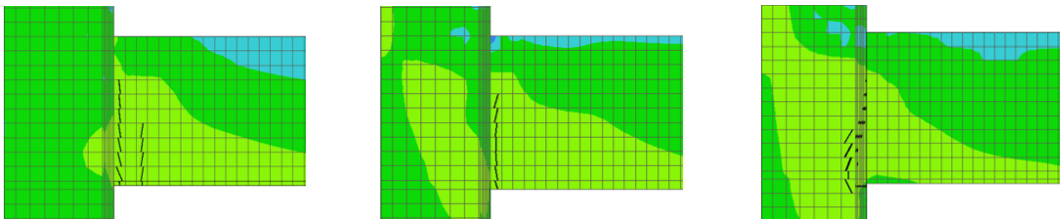

(a) Retrofit: B15 +15mm (b) Retrofit: B30 +15mm (c) Retrofit: B45 +15mm

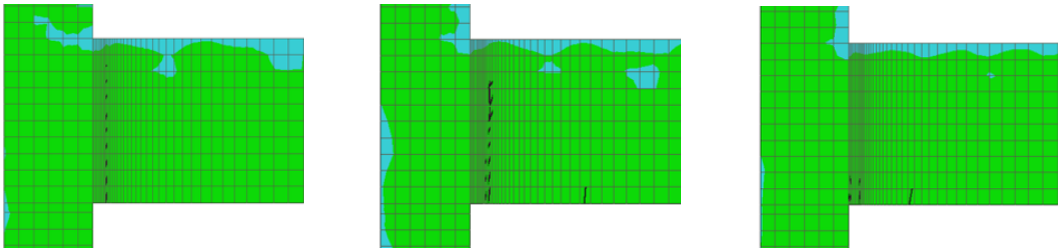

(d) Joint core: B15 +15mm (e) Joint core: B30 +15mm (f) Joint core: A45 +15mm

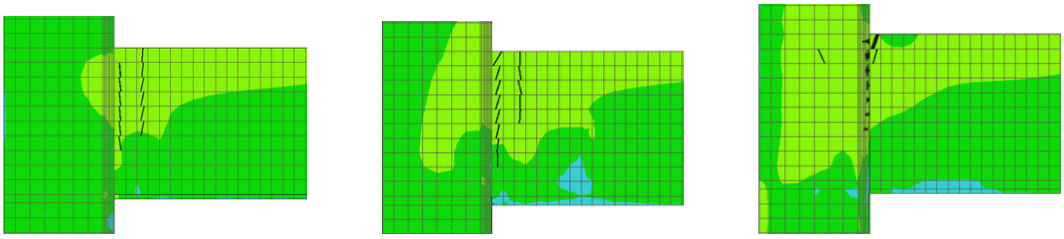

(g) Retrofit: B15 -15mm (h) Retrofit: B30 -15mm (i) Retrofit: B45 -15mm

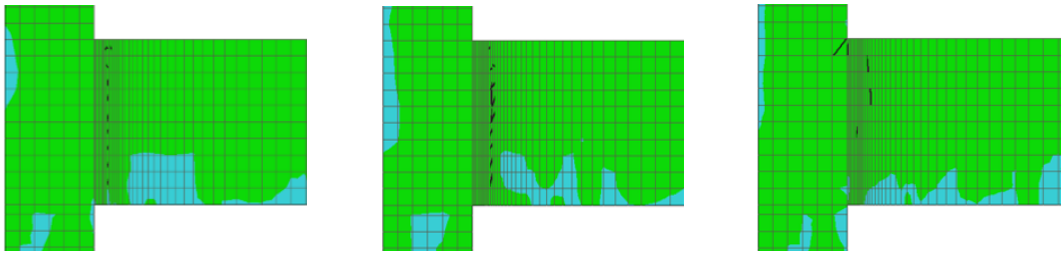

(j) Joint core: B15 -15mm (k) Joint core: B30 -15mm (l) Joint core: B45 -15mm

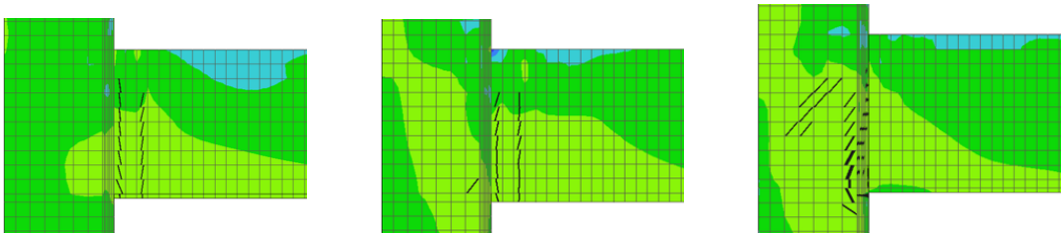

(m) Retrofit: B15 +22.5mm (n) Retrofit: B30 +22.5mm (o) Retrofit: B45 +22.5mm

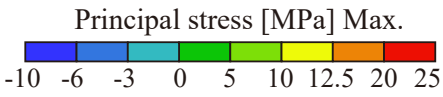

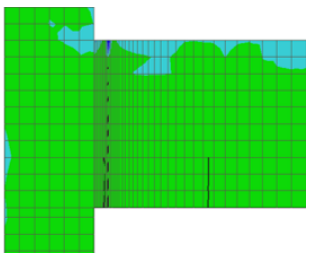

(p) Joint core: B15 +22.5mm

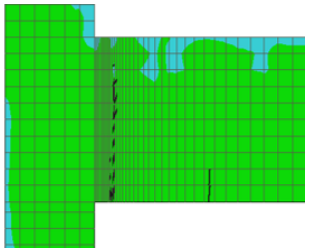

(q) Joint core: B30 +22.5mm

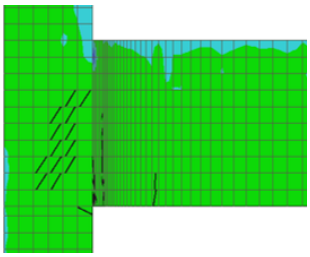

(r) Joint core: B45 +22.5mm

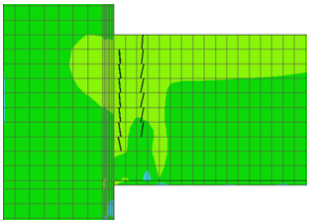

(s) Retrofit: B15 -22.5mm

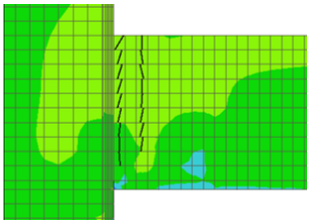

(t) Retrofit: B30 -22.5mm

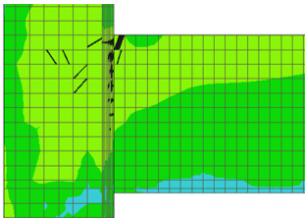

(u) Retrofit: B45 -22.5mm

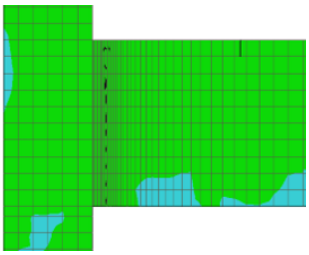

(v) Joint core: B15 -22.5mm

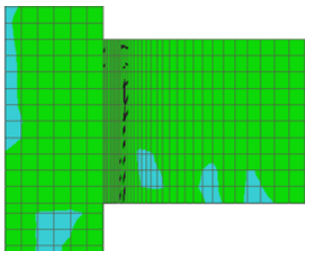

(w) Joint core: B30 -22.5mm

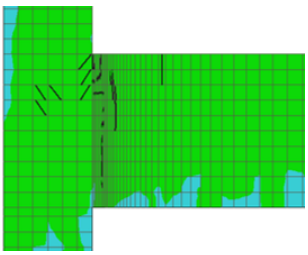

(x) Joint core: B45 -22.5mm

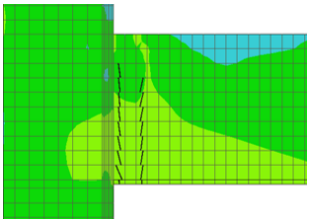

(y) Retrofit: B15 +30mm

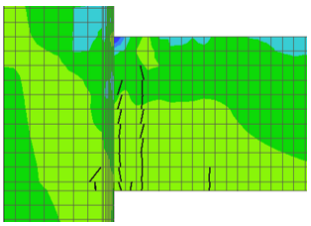

(z) Retrofit: B30 +30mm

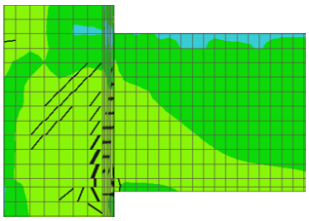

(aa) Retrofit: B45 +30mm

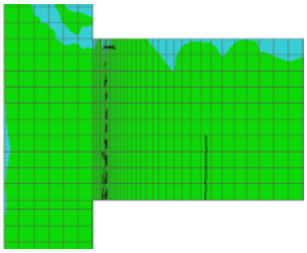

(ab) Joint core: B15 +30mm

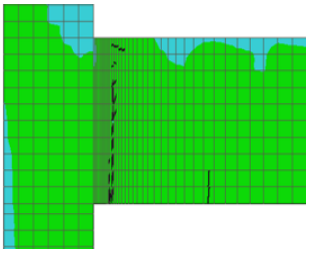

(ac) Joint core: B30 +30mm

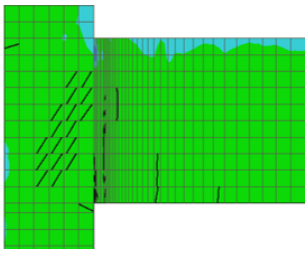

(ad) Joint core: B45 +30mm

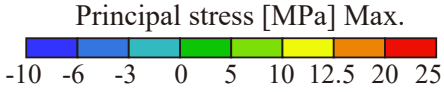

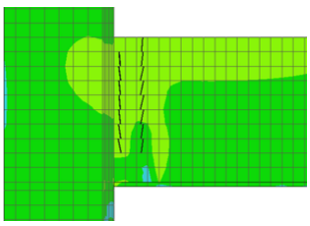

(ae) Retrofit: B15 -30mm

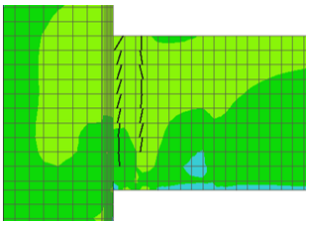

(af) Retrofit: B30 -30mm

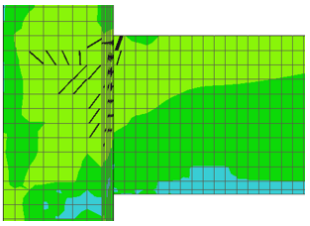

(ag) Retrofit: B45 -30mm

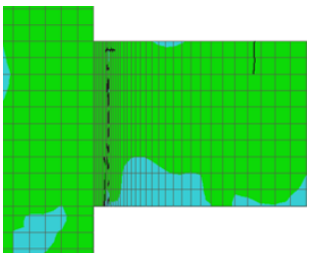

(ah) Joint core: B15 -30mm

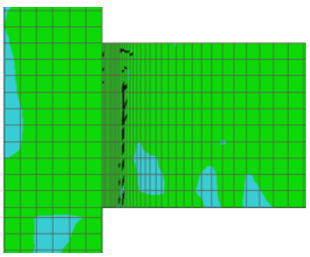

(ai) Joint core: B30 -30mm

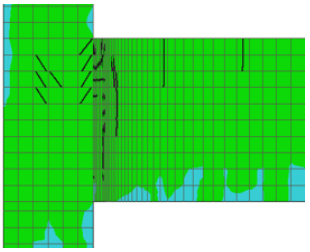

(aj) Joint core: B45 -30mm

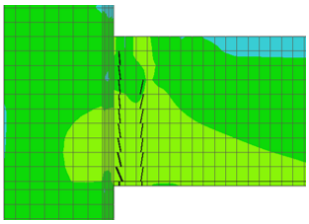

(ak) Retrofit: B15 +45mm

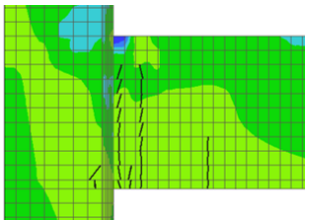

(al) Retrofit: B30 +45mm

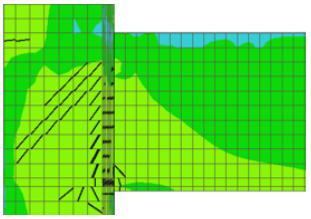

(am) Retrofit: B45 +45mm

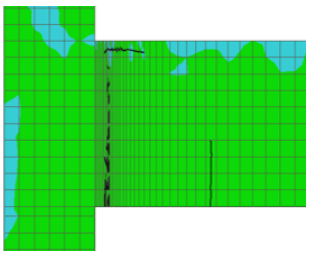

(an) Joint core: B15 +45mm

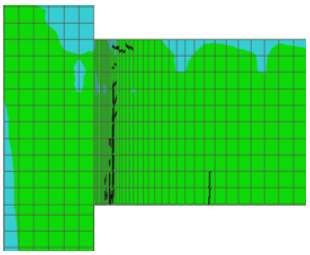

(ao) Joint core: B30 +45mm

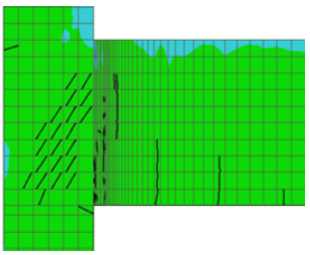

(ap) Joint core: B45 +45mm

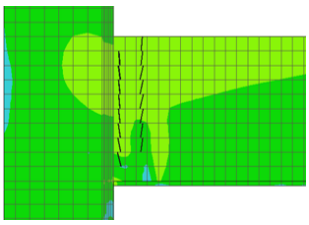

(aq) Retrofit: B15 -45mm

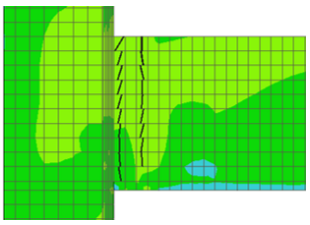

(ar) Retrofit: B30 -45mm

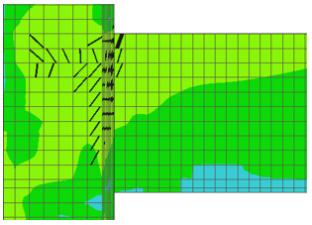

(as) Retrofit: B45 -45mm

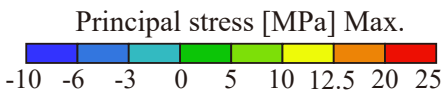

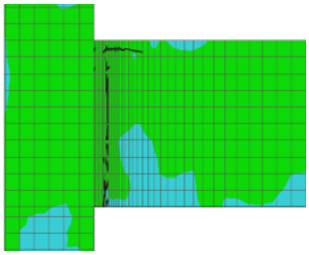

(at) Joint core: B15 - 45mm

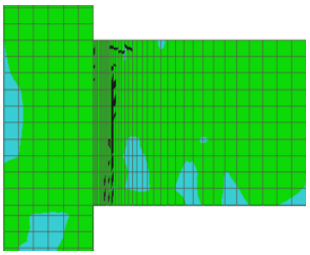

(au) Joint core: B30 - 45mm

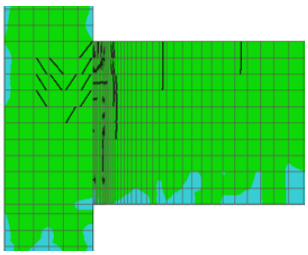

(av) Joint core: B45 - 45mm

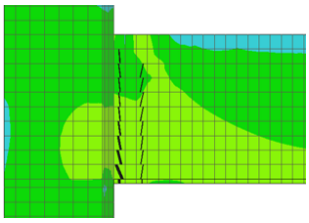

(aw) Retrofit: B15 +60mm

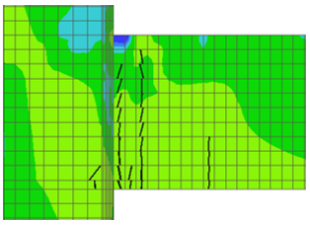

(ax) Retrofit: B30 +60mm

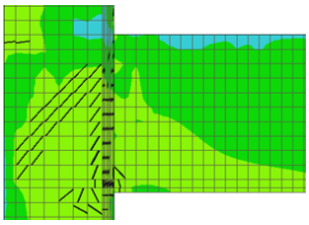

(ay) Retrofit: B45 +60mm

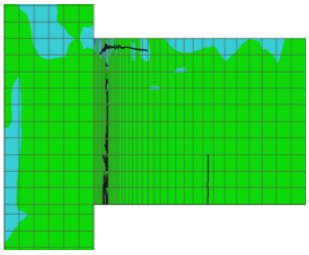

(az) Joint core: B15 +60mm

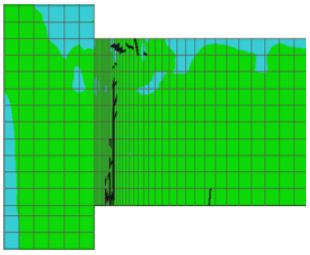

(ba) Joint core: B30 +60mm

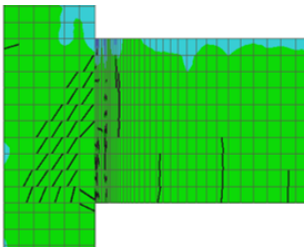

(bb) Joint core: B45 +60mm

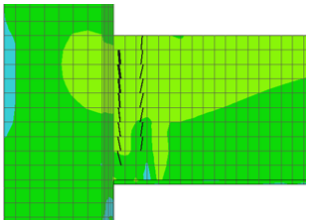

(bc) Retrofit: B15 -60mm

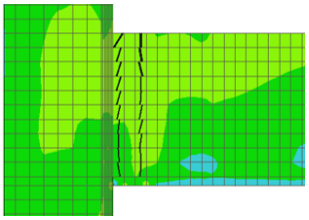

(bd) Retrofit: B30 -60mm

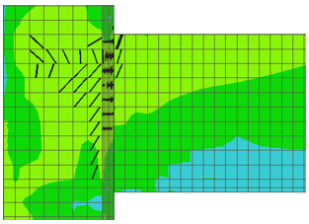

(be) Retrofit: B45 -60mm

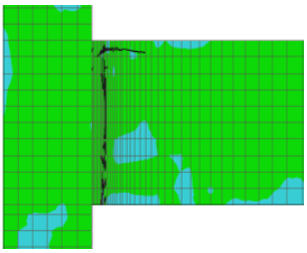

(bf) Joint core: B15 - 60mm

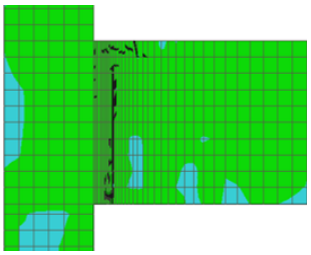

(bg) Joint core: B30 - 60mm

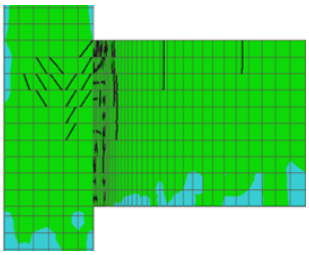

(bh) Joint core: B45 - 60mm

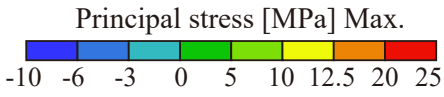

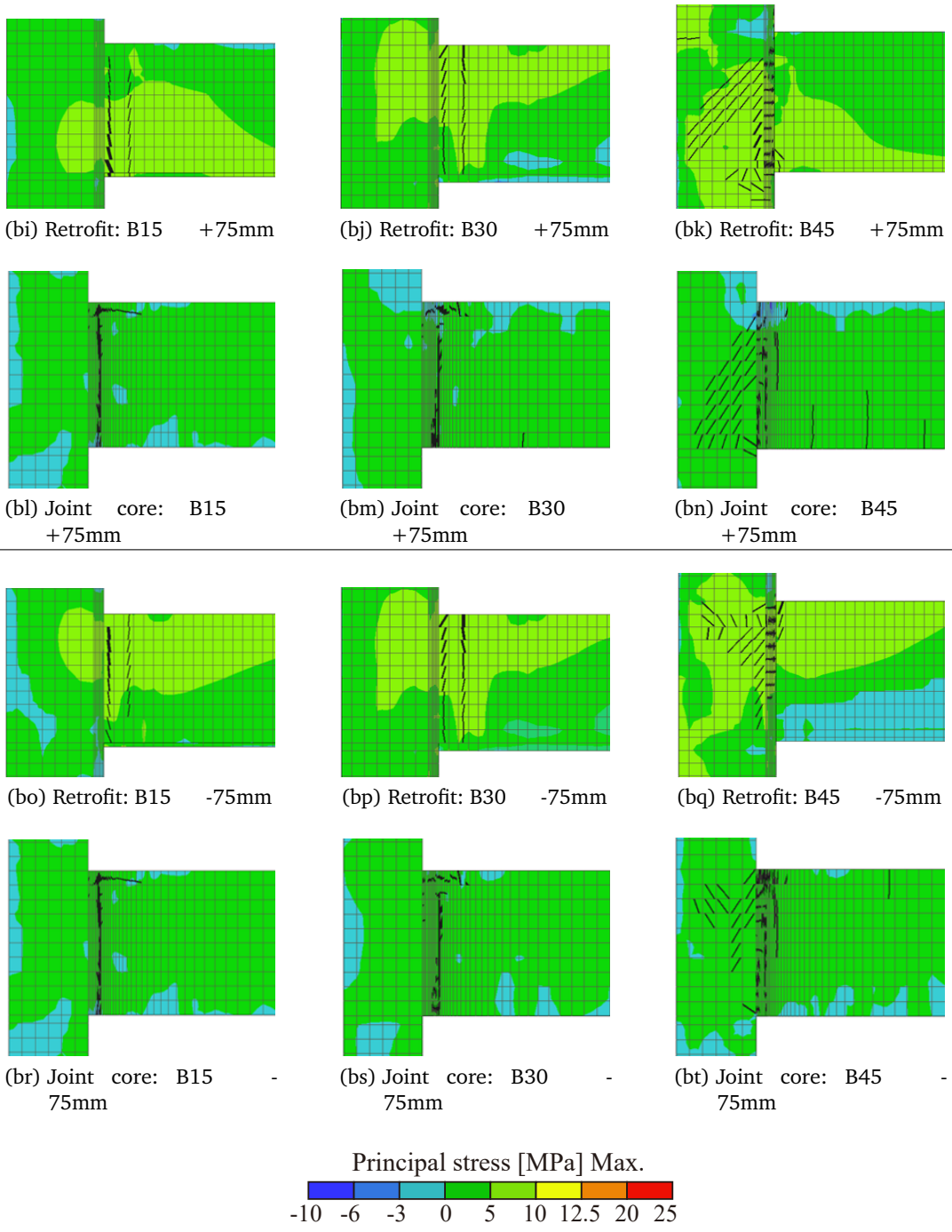

Figure B.2 – Cracking pattern of BCJs of model B, with and no with retrofit, varying the thickness of retrofit

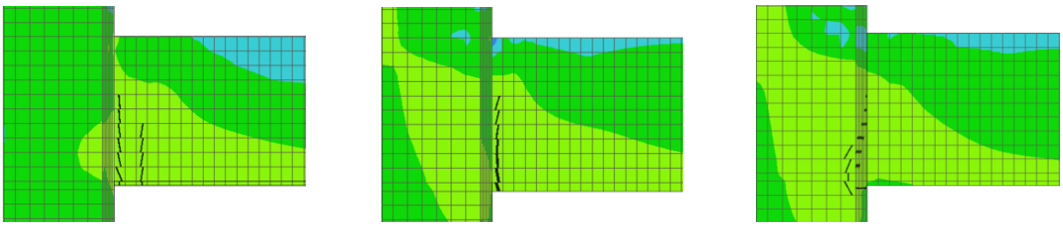

(a) Retrofit: C15 +15mm (b) Retrofit: C30 +15mm (c) Retrofit: C45 +15mm

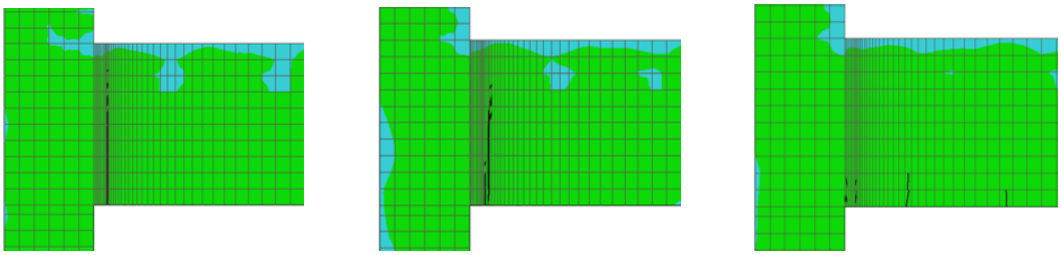

(d) Joint core: C15 +15mm (e) Joint core: C30 +15mm (f) Joint core: C45 +15mm

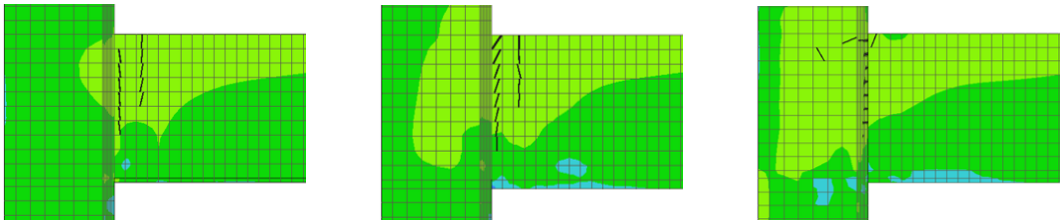

(g) Retrofit: C15 -15mm (h) Retrofit: C30 -15mm (i) Retrofit: C45 -15mm

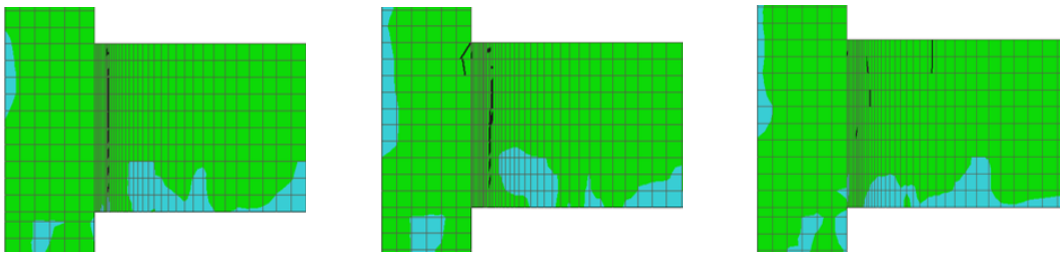

(j) Joint core: C15 -15mm (k) Joint core: C30 -15mm (l) Joint core: C45 -15mm

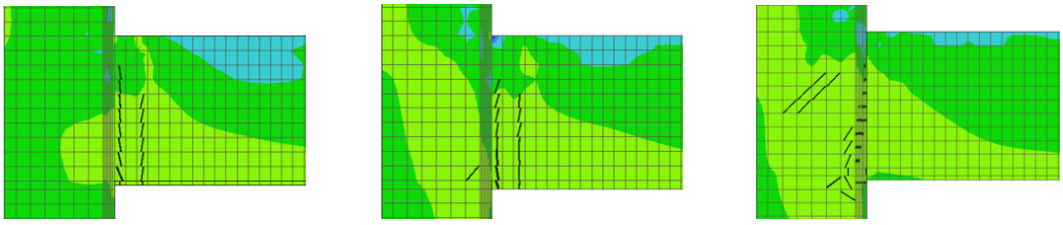

(m) Retrofit: C15 +22.5mm (n) Retrofit: C30 +22.5mm (o) Retrofit: C45 +22.5mm

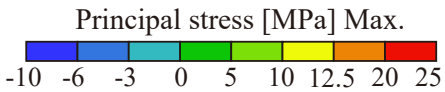

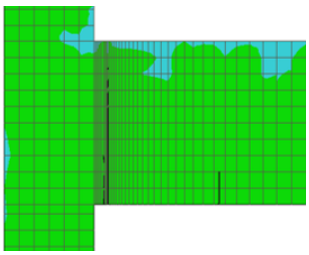

(p) Joint core: C15 +22.5mm

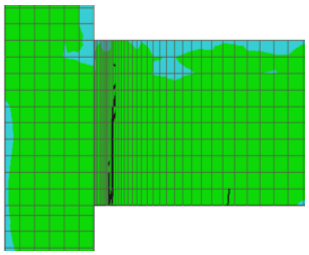

(q) Joint core: C30 +22.5mm

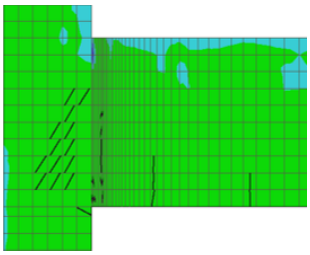

(r) Joint core: C45 +22.5mm

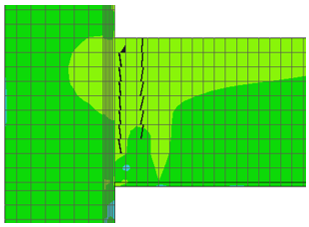

(s) Retrofit: C15 -22.5mm

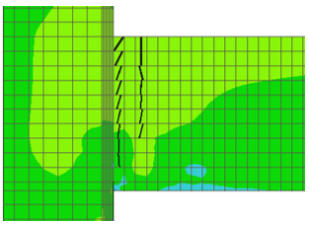

(t) Retrofit: C30 -22.5mm

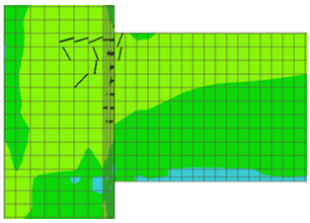

(u) Retrofit: C45 -22.5mm

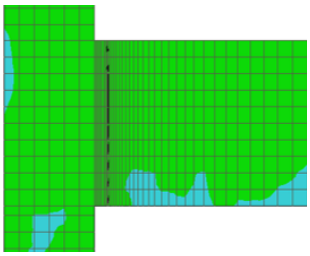

(v) Joint core: C15 -22.5mm

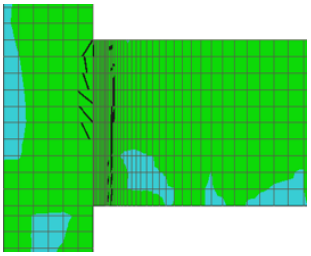

(w) Joint core: C30 -22.5mm

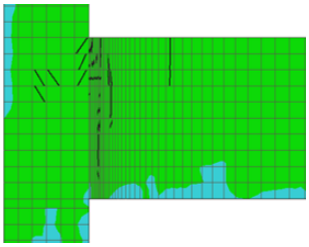

(x) Joint core: C45 -22.5mm

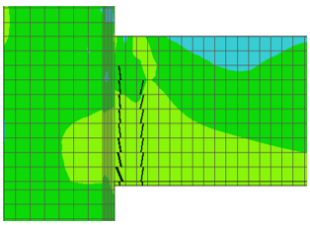

(y) Retrofit: C15 +30mm

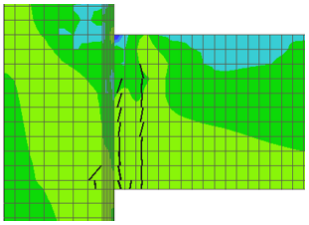

(z) Retrofit: C30 +30mm

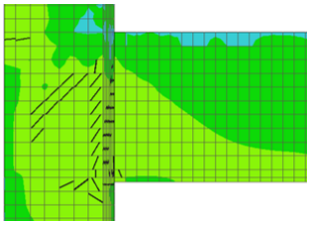

(aa) Retrofit: C45 +30mm

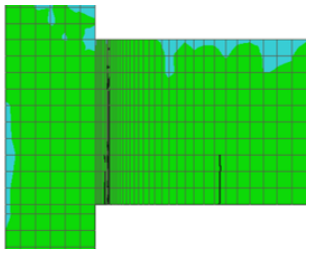

(ab) Joint core: C15 +30mm

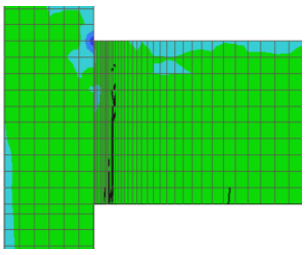

(ac) Joint core: C30 +30mm

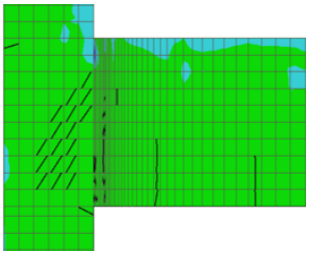

(ad) Joint core: C45 +30mm

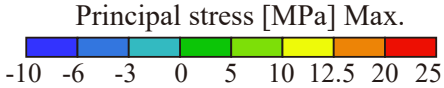

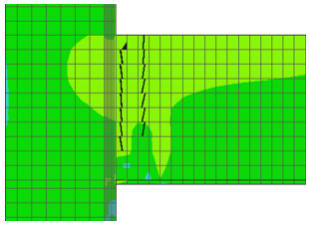

(ae) Retrofit: C15 -30mm

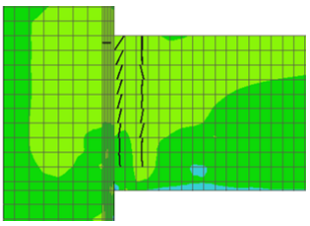

(af) Retrofit: C30 -30mm

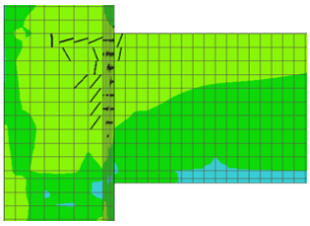

(ag) Retrofit: C45 -30mm

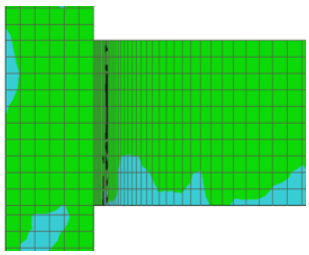

(ah) Joint core: C15 -30mm

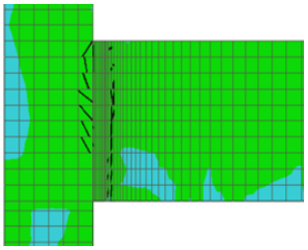

(ai) Joint core: C30 -30mm

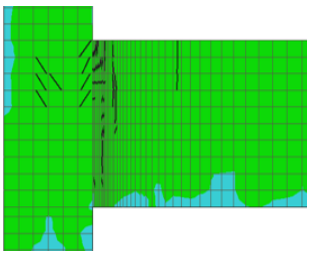

(aj) Joint core: C45 -30mm

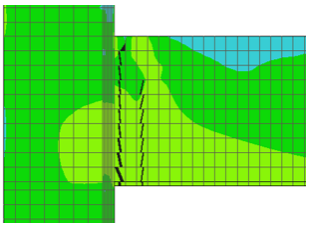

(ak) Retrofit: C15 +45mm

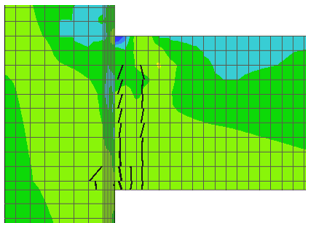

(al) Retrofit: C30 +45mm

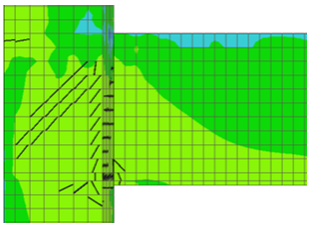

(am) Retrofit: C45 +45mm

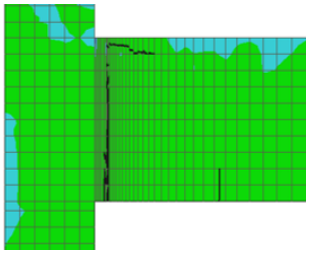

(an) Joint core: C15 +45mm

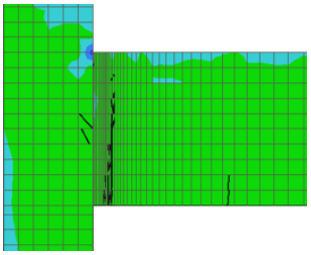

(ao) Joint core: C30 +45mm

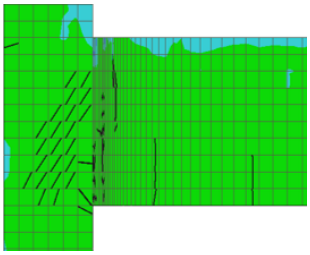

(ap) Joint core: C45 +45mm

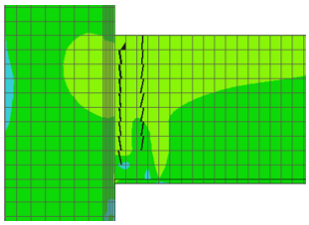

(aq) Retrofit: C15 -45mm

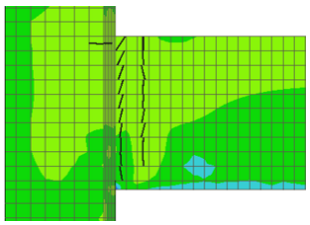

(ar) Retrofit: C30 -45mm

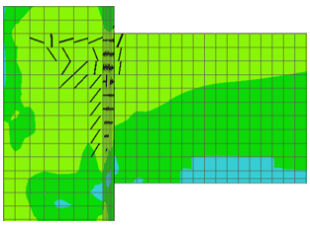

(as) Retrofit: C45 -45mm

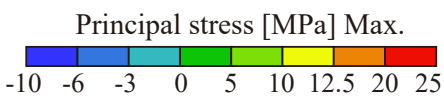

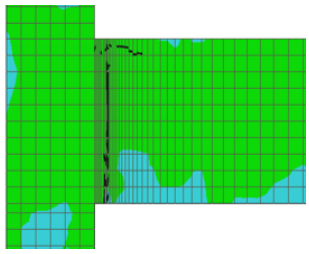

(at) Joint core: C15 - 45mm

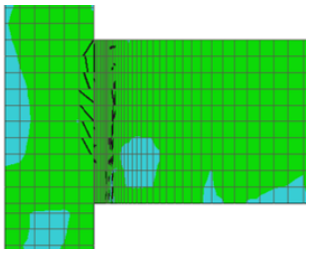

(au) Joint core: C30 - 45mm

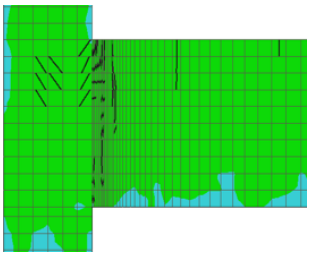

(av) Joint core: C45 - 45mm

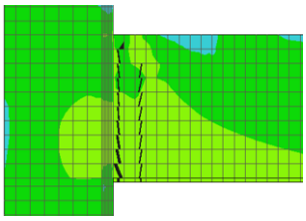

(aw) Retrofit: C15 +60mm

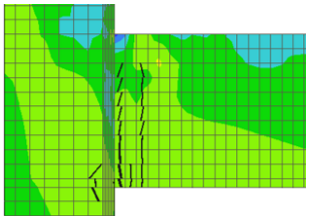

(ax) Retrofit: C30 +60mm

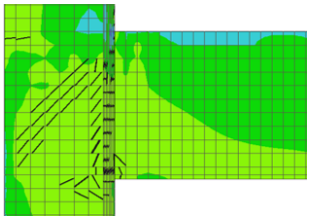

(ay) Retrofit: C45 +60mm

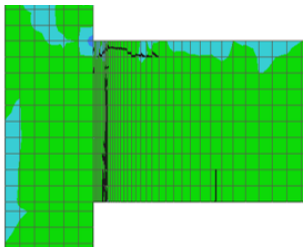

(az) Joint core: C15 +60mm

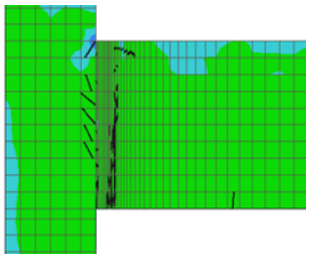

(ba) Joint core: C30 +60mm

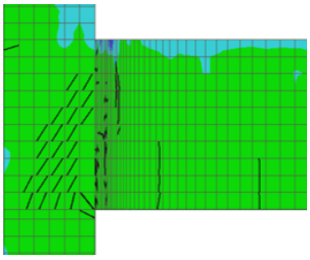

(bb) Joint core: C45 +60mm

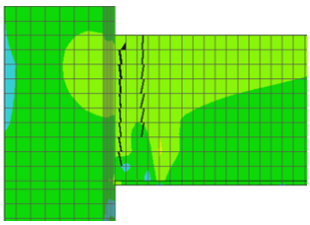

(bc) Retrofit: C15 -60mm

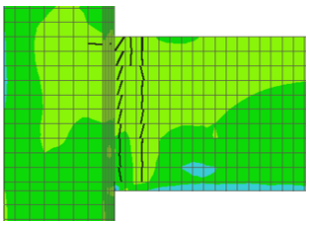

(bd) Retrofit: C30 -60mm

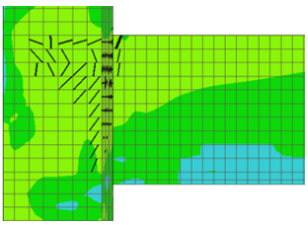

(be) Retrofit: C45 -60mm

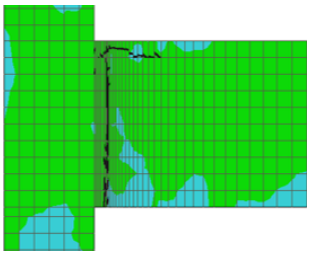

(bf) Joint core: C15 - 60mm

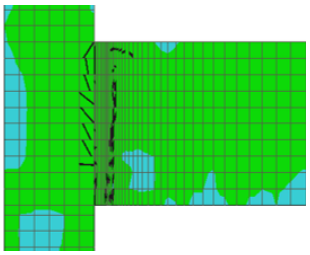

(bg) Joint core: C30 - 60mm

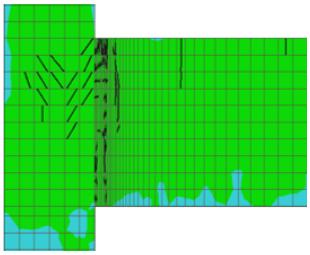

(bh) Joint core: C45 - 60mm

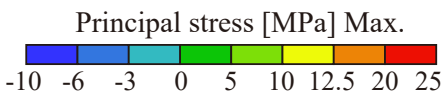

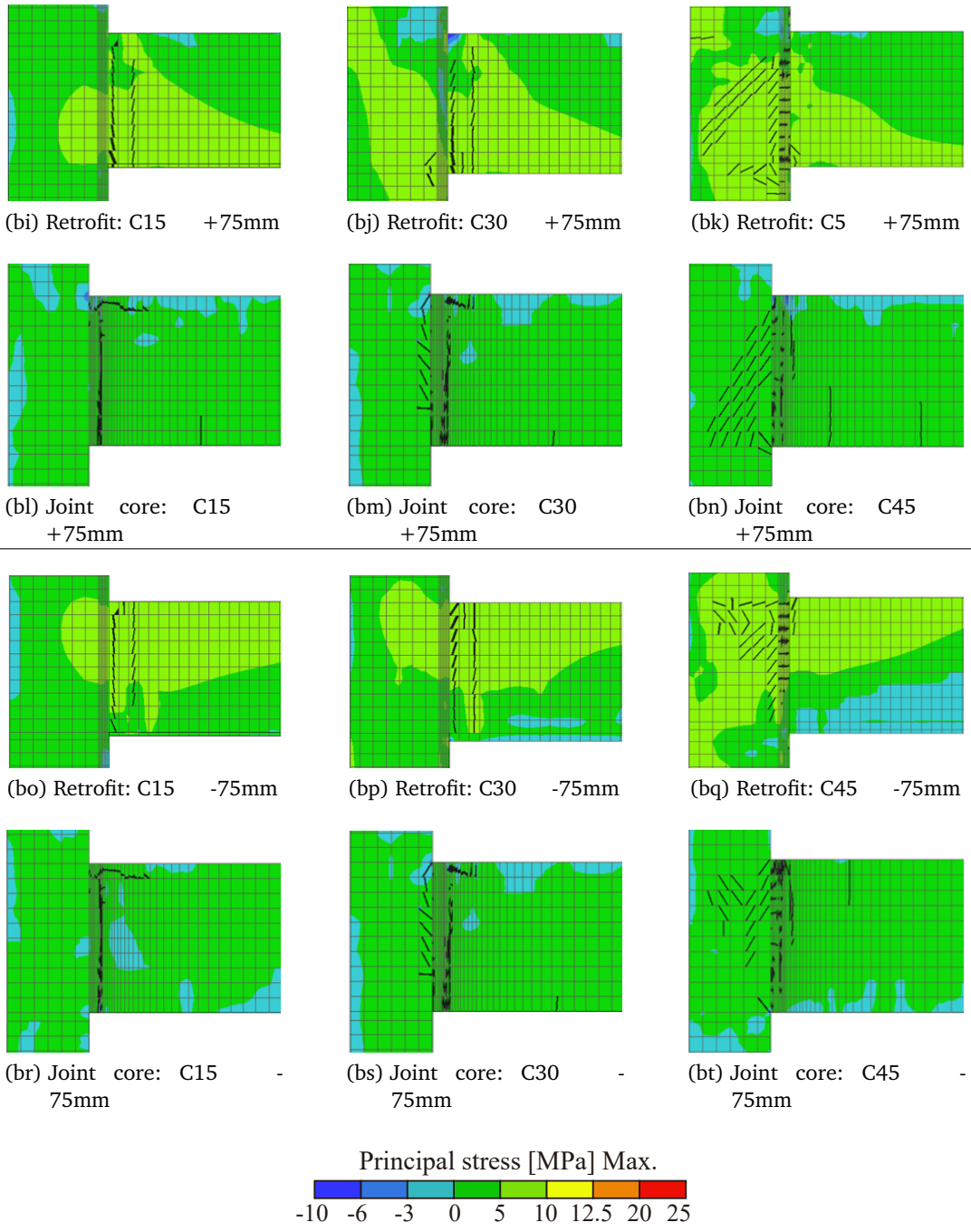

Figure B.3 – Cracking pattern of BCJs of model C, with and no with retrofit, varying the thickness of retrofit

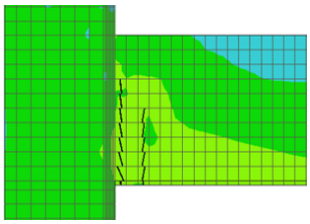

(a) Retrofit: A15-L +15mm

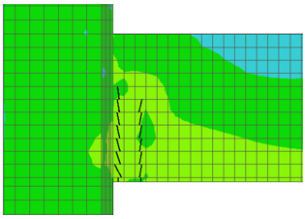

(b) Retrofit: A15-M +15mm

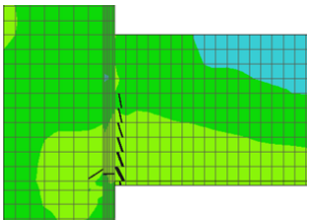

(c) Retrofit: A15-H +15mm

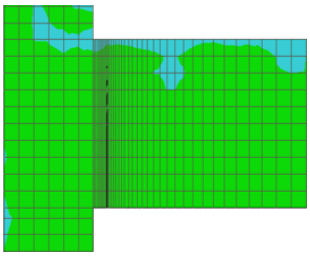

(d) Joint core: A15-L +15mm

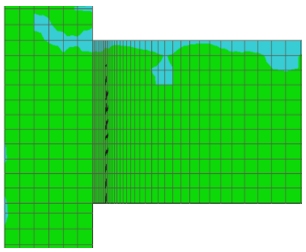

(e) Joint core: A15-M +15mm

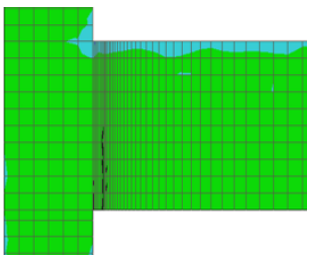

(f) Joint core: A15-H +15mm

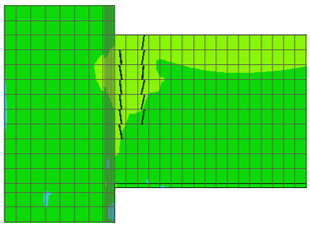

(g) Retrofit: A15-L -15mm

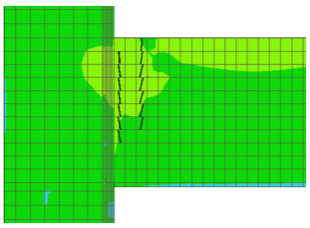

(h) Retrofit: A15-M -15mm

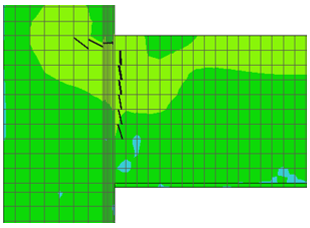

(i) Retrofit: A15-H -15mm

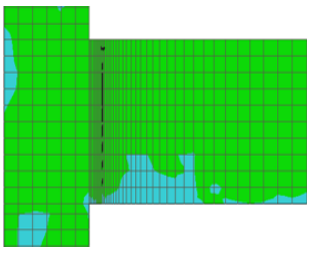

(j) Joint core: A15-L -15mm

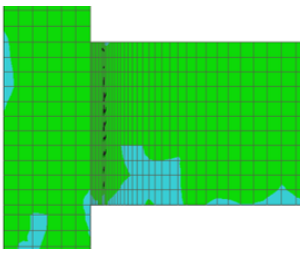

(k) Joint core: A15-M -15mm

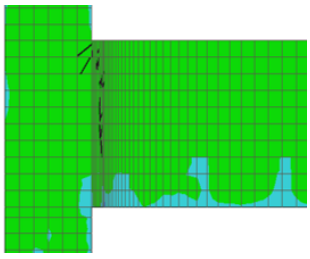

(l) Joint core: A15-H -15mm

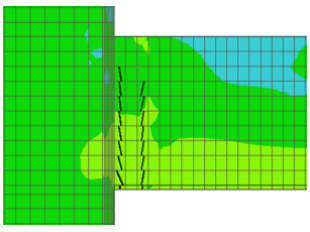

(m) Retrofit: A15-L +22.5mm

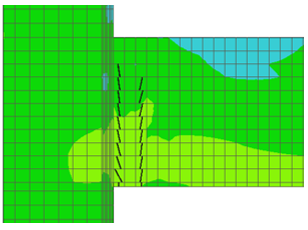

(n) Retrofit: A15-M +22.5mm

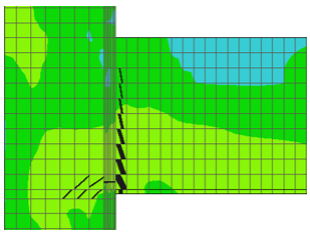

(o) Retrofit: A15-H +22.5mm

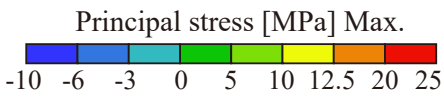

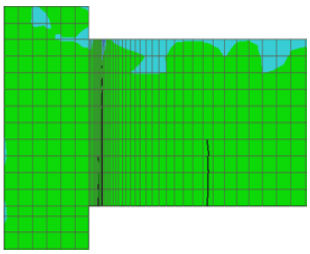

(p) Joint core: A15-L +22.5mm

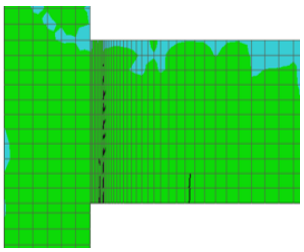

(q) Joint core: A15-M +22.5mm

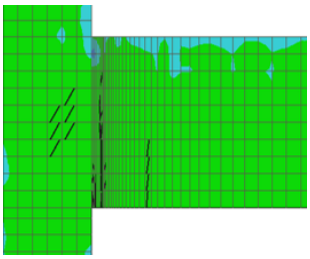

(r) Joint core: A15-H +22.5mm

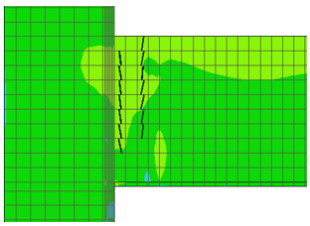

(s) Retrofit: A15-H -22.5mm

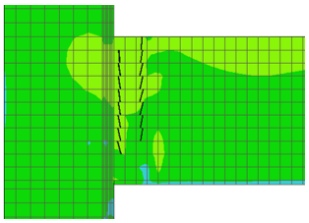

(t) Retrofit: A15-M -22.5mm

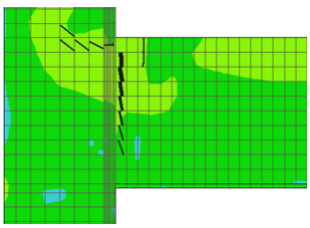

(u) Retrofit: A15-H -22.5mm

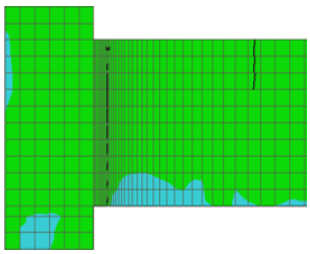

(v) Joint core: A15-L -22.5mm

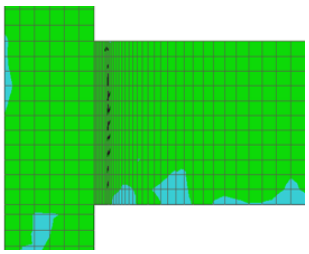

(w) Joint core: A15-M -22.5mm

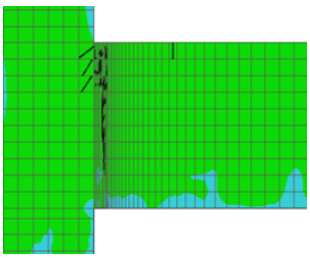

(x) Joint core: A15-H -22.5mm

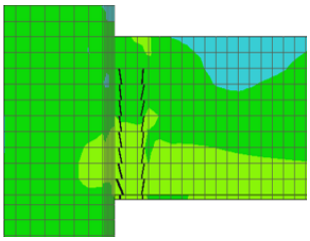

(y) Retrofit: A15-L +30mm

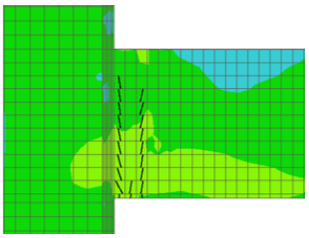

(z) Retrofit: A15-M +30mm

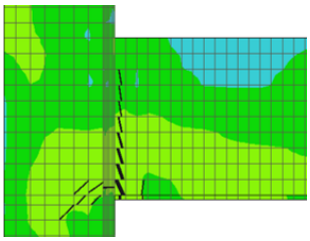

(aa) Retrofit: A15-H +30mm

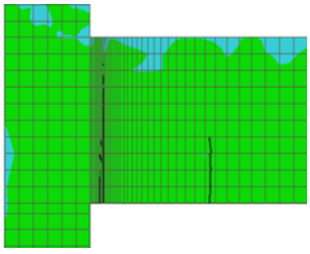

(ab) Joint core: A15-L +30mm

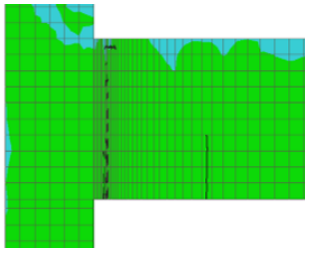

(ac) Joint core: A15-M +30mm

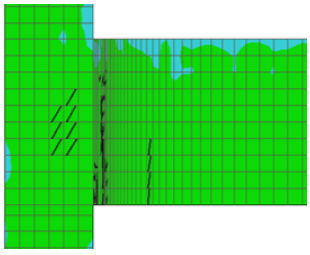

(ad) Joint core: A15-H +30mm

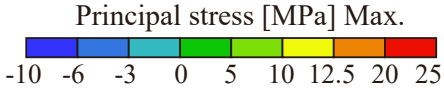

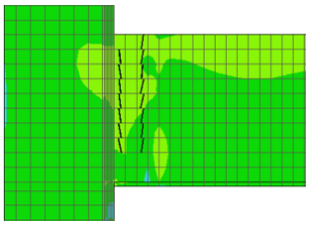

(ae) Retrofit: A15-L -30mm

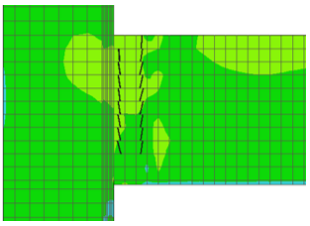

(af) Retrofit: A15-M -30mm

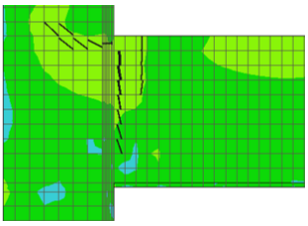

(ag) Retrofit: A15-H -30mm

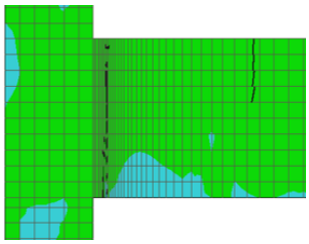

(ah) Joint core: A15-L -30mm

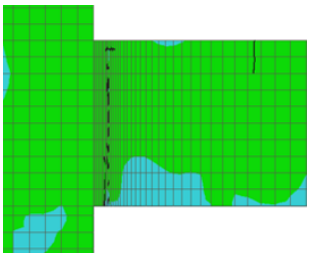

(ai) Joint core: A15-M -30mm

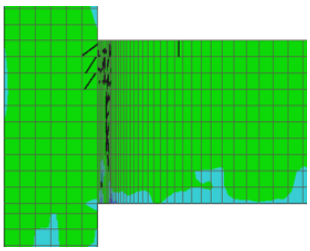

(aj) Joint core: A15-H -30mm

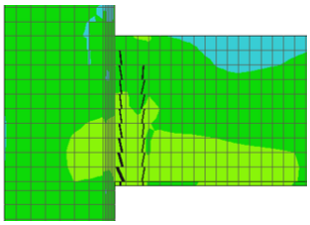

(ak) Retrofit: A15-L +45mm

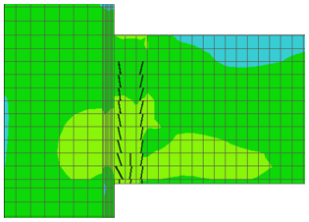

(al) Retrofit: A15-M +45mm

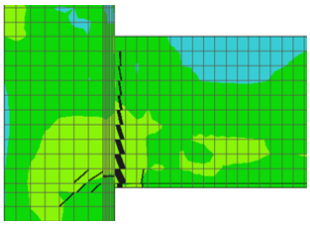

(am) Retrofit: A15-H +45mm

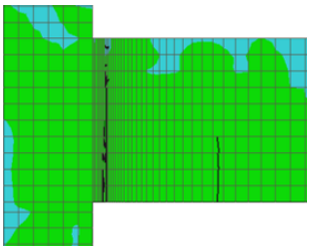

(an) Joint core: A15-L +45mm

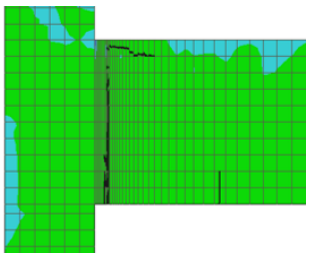

(ao) Joint core: A15-M +45mm

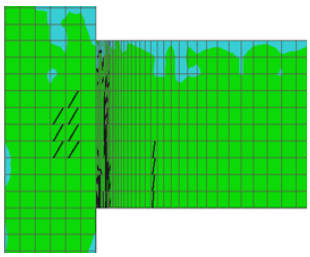

(ap) Joint core: A15-H +45mm

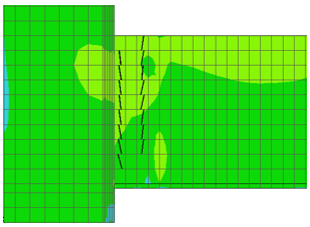

(aq) Retrofit: A15-L -45mm

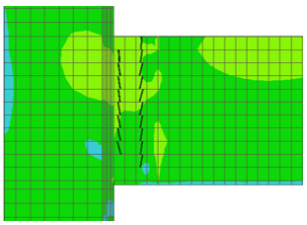

(ar) Retrofit: A15-M -45mm

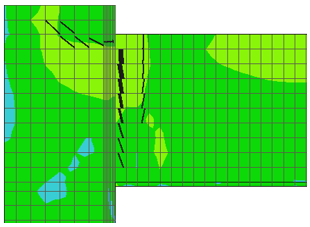

(as) Retrofit: A15-H -45mm

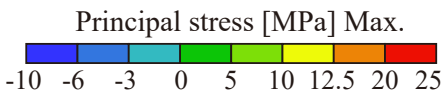

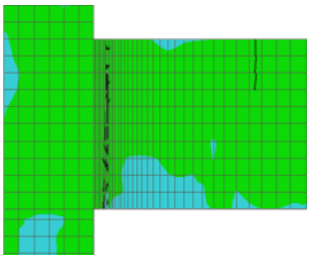

(at) Joint core: A15-L - 45mm

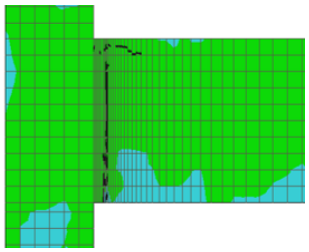

(au) Joint core: A15-M - 45mm

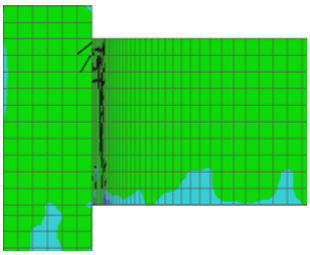

(av) Joint core: A15-H - 45mm

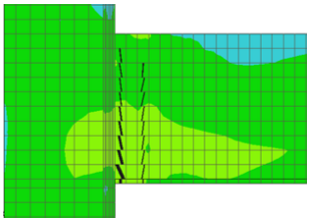

(aw) Retrofit: A15-L +60mm

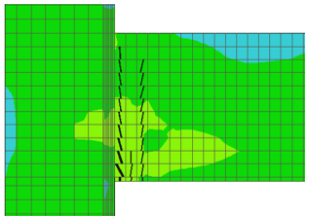

(ax) Retrofit: A15-M +60mm

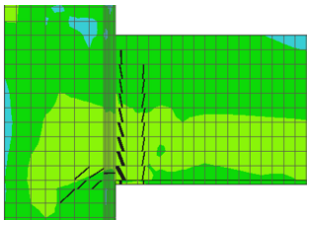

(ay) Retrofit: A15-H +60mm

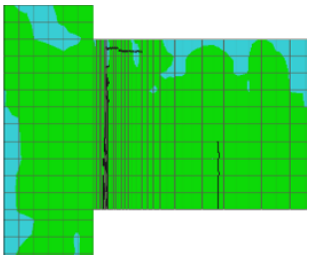

(az) Joint core: A15-L +60mm

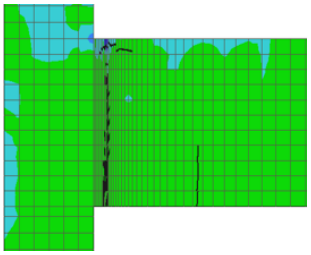

(ba) Joint core: A15-M +60mm

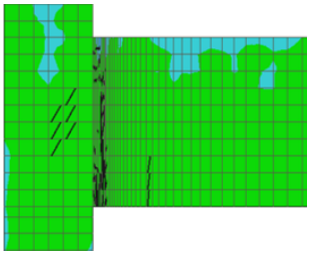

(bb) Joint core: A15-H +60mm

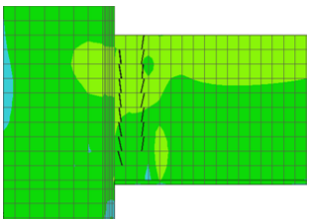

(bc) Retrofit: A15-L -60mm

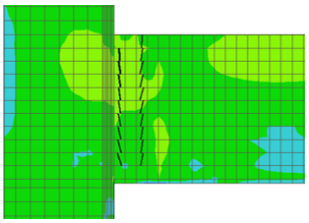

(bd) Retrofit: A15-M - 60mm

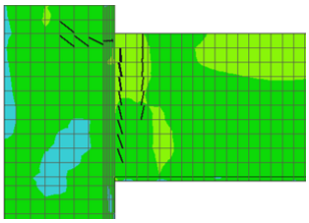

(be) Retrofit: A15-H - 60mm

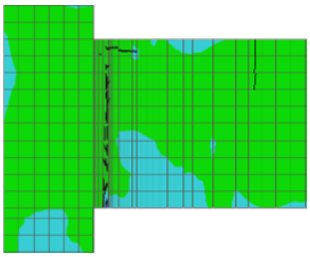

(bf) Joint core: A15-L - 60mm

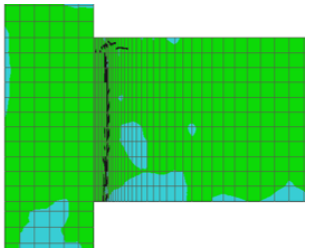

(bg) Joint core: A15-M - 60mm

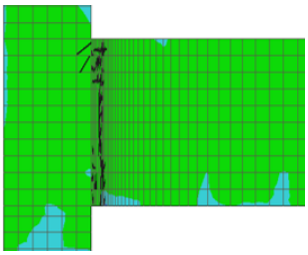

(bh) Joint core: A15-H - 60mm

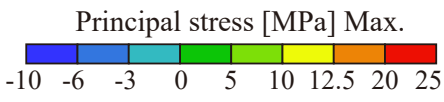

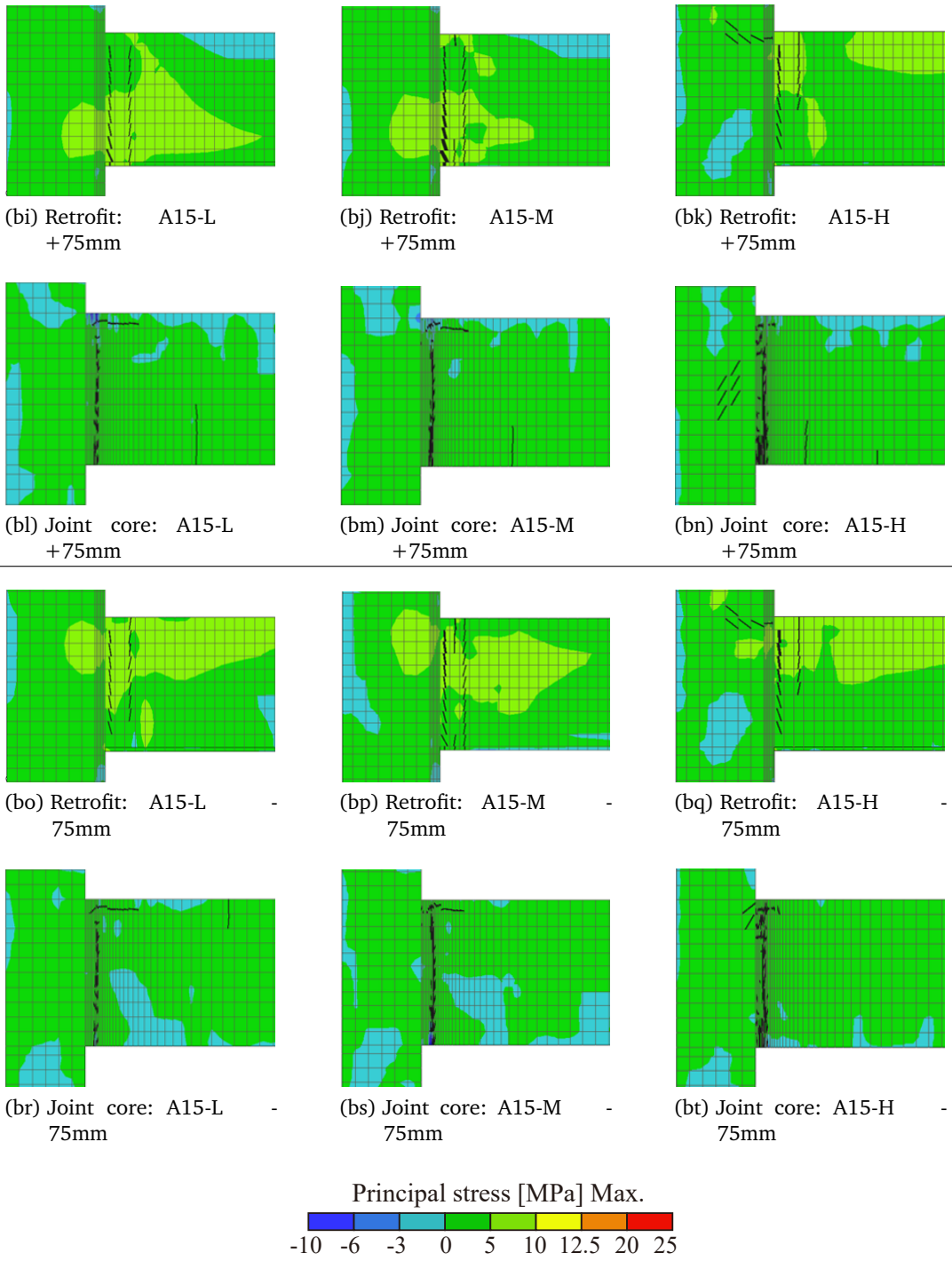

Figure B.4 – Cracking pattern of BCJs with a HPFRC jacket of 15 mm, with and no with retrofit, varying the beam's reinforcement ratio

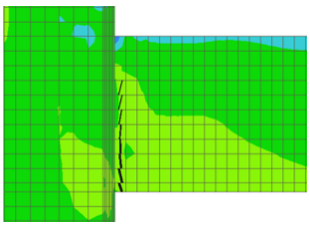

(a) Retrofit: A30-L +15mm

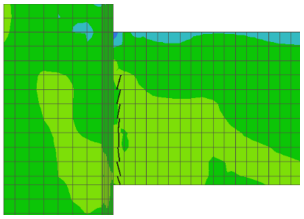

(b) Retrofit: A30-M +15mm

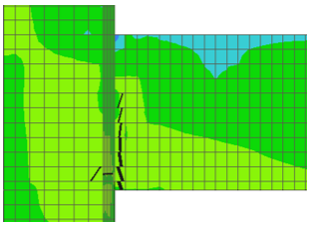

(c) Retrofit: A30-H +15mm

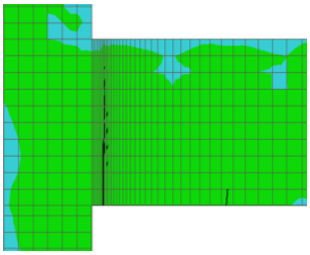

(d) Joint core: A30-L +15mm

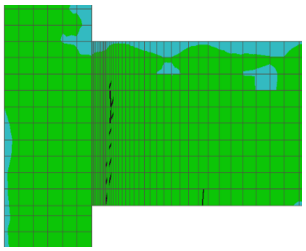

(e) Joint core: A30-M +15mm

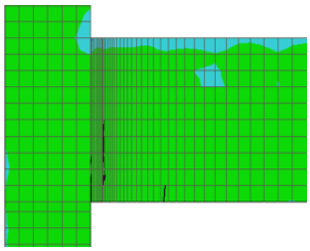

(f) Joint core: A30-H +15mm

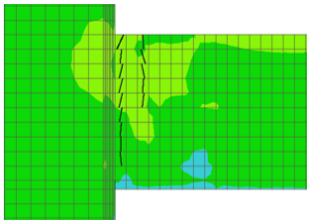

(g) Retrofit: A30-L -15mm

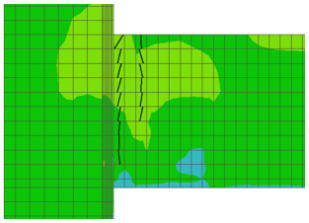

(h) Retrofit: A30-M -15mm

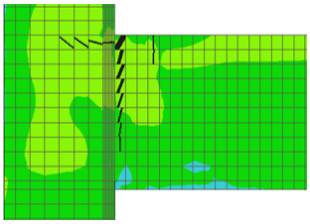

(i) Retrofit: A30-H -15mm

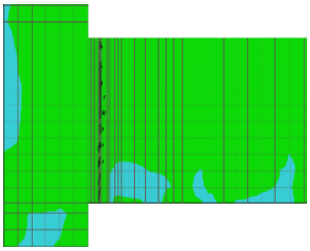

(j) Joint core: A30-L -15mm

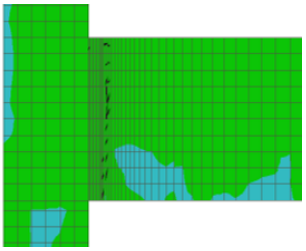

(k) Joint core: A30-M -15mm

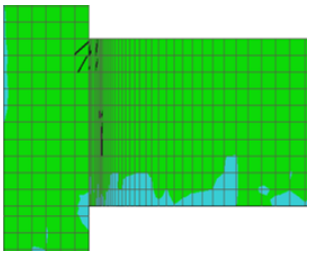

(l) Joint core: A30-H -15mm

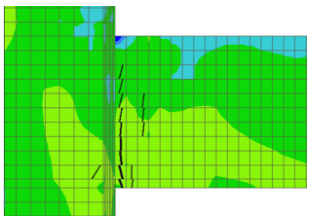

(m) Retrofit: A30-L +22.5mm

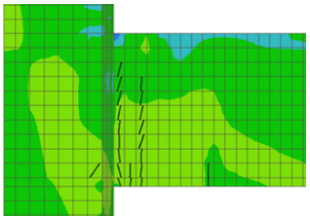

(n) Retrofit: A30-M +22.5mm

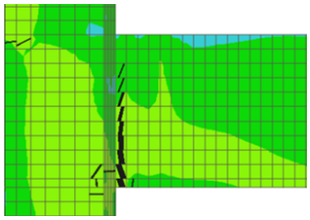

(o) Retrofit: A30-H +22.5mm

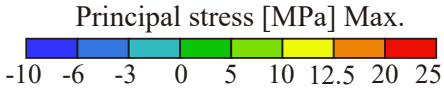

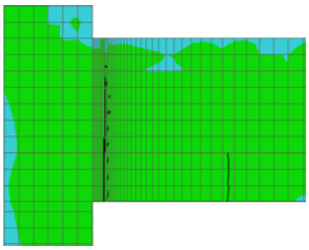

(p) Joint core: A30-L +22.5mm

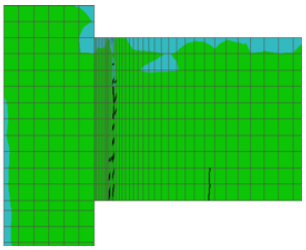

(q) Joint core: A30-M +22.5mm

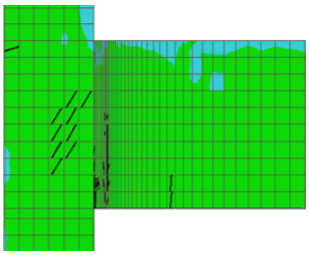

(r) Joint core: A30-H +22.5mm

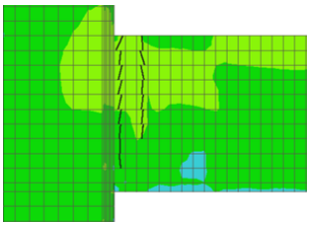

(s) Retrofit: A30-H -22.5mm

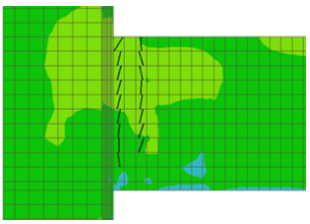

(t) Retrofit: A30-M -22.5mm

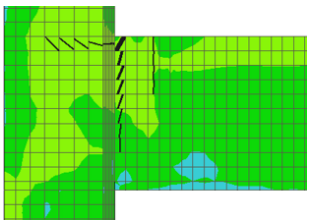

(u) Retrofit: A30-H -22.5mm

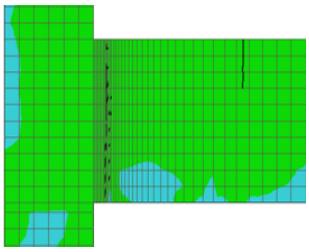

(v) Joint core: A30-L -22.5mm

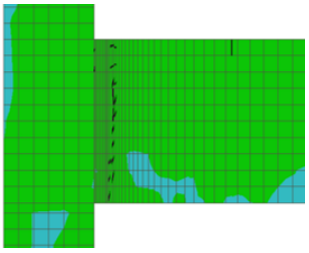

(w) Joint core: A30-M -22.5mm

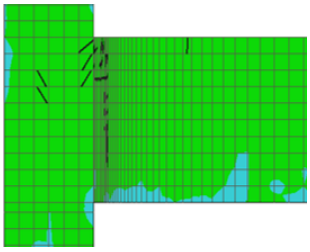

(x) Joint core: A30-H -22.5mm

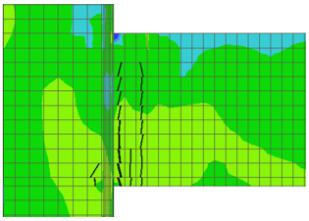

(y) Retrofit: A30-L +30mm

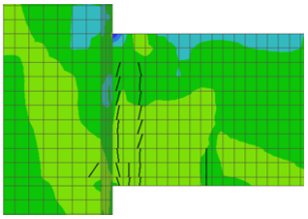

(z) Retrofit: A30-M +30mm

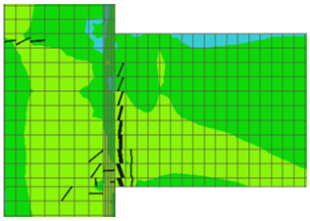

(aa) Retrofit: A30-H +30mm

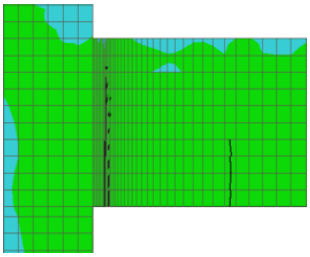

(ab) Joint core: A30-L +30mm

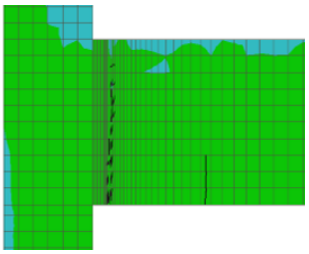

(ac) Joint core: A30-M +30mm

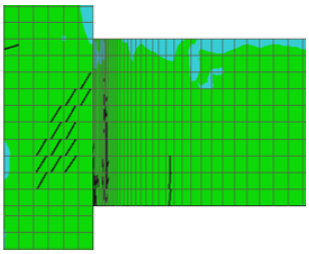

(ad) Joint core: A30-H +30mm

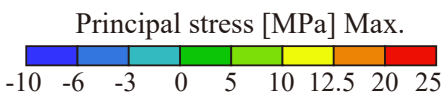

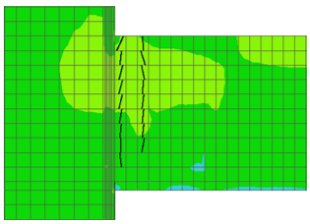

(ae) Retrofit: A30-L -30mm

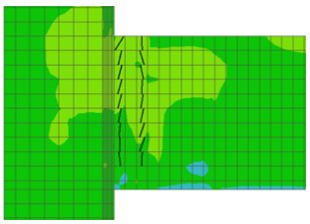

(af) Retrofit: A30-M -30mm

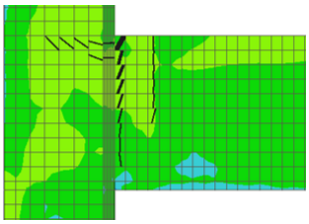

(ag) Retrofit: A30-H -30mm

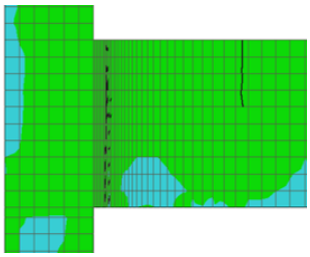

(ah) Joint core: A30-L -30mm

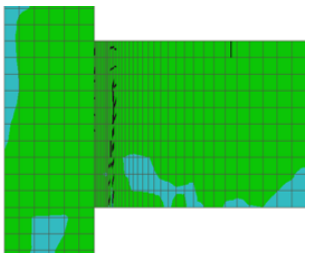

(ai) Joint core: A30-M -30mm

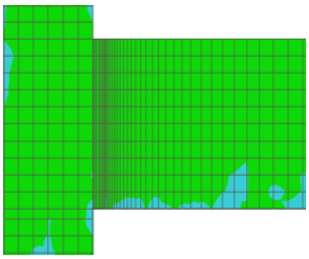

(aj) Joint core: A30-H -30mm

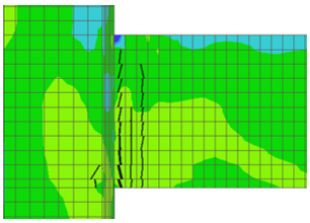

(ak) Retrofit: A30-L +45mm

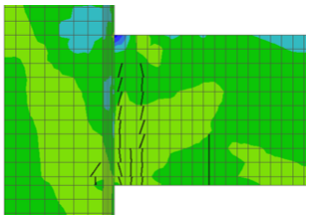

(al) Retrofit: A30-M +45mm

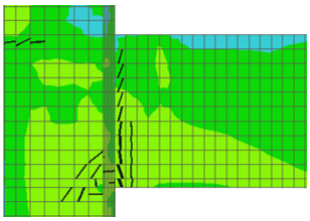

(am) Retrofit: A30-H +45mm

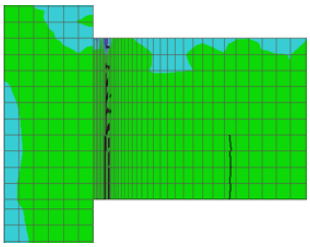

(an) Joint core: A30-L +45mm

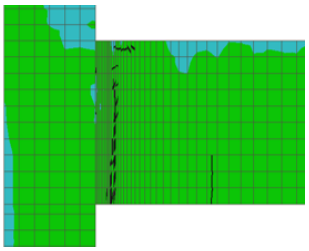

(ao) Joint core: A30-M +45mm

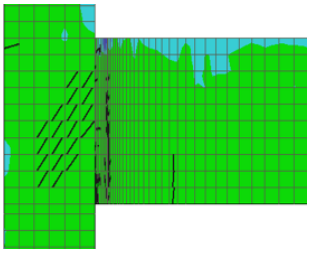

(ap) Joint core: A30-H +45mm

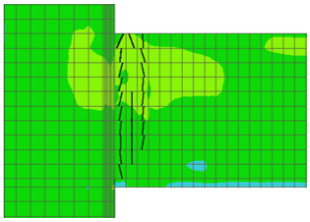

(aq) Retrofit: A30-L -45mm

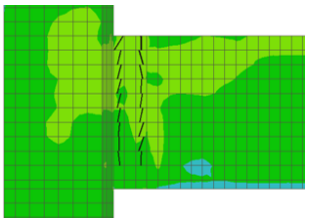

(ar) Retrofit: A30-M -45mm

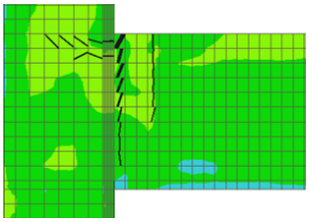

(as) Retrofit: A30-H -45mm

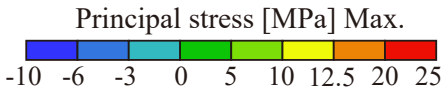

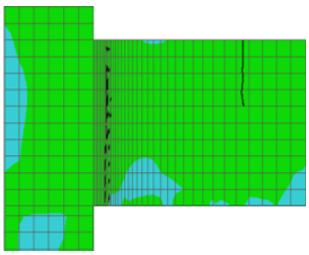

(at) Joint core: A30-L - 45mm

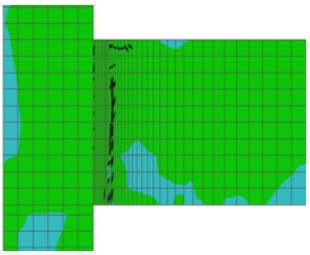

(au) Joint core: A30-M - 45mm

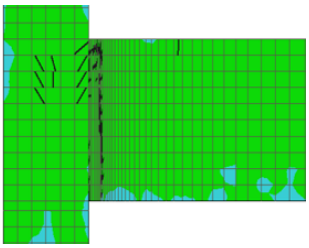

(av) Joint core: A30-H - 45mm

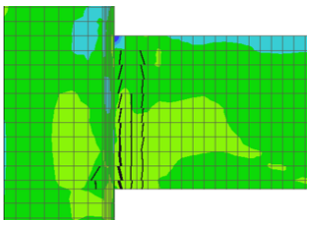

(aw) Retrofit: A30-L +60mm

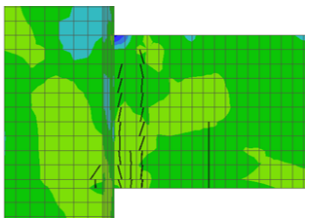

(ax) Retrofit: A30-M +60mm

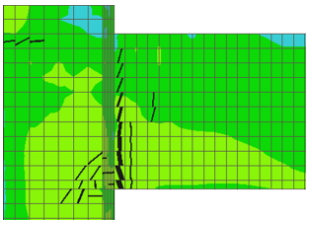

(ay) Retrofit: A30-H +60mm

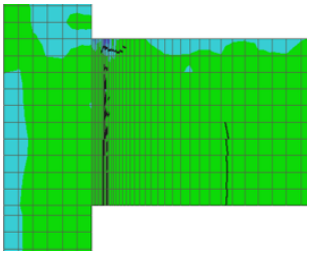

(az) Joint core: A30-L +60mm

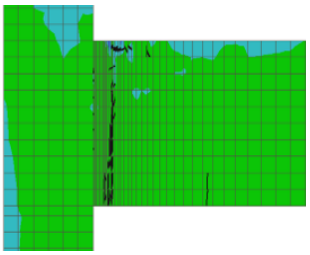

(ba) Joint core: A30-M +60mm

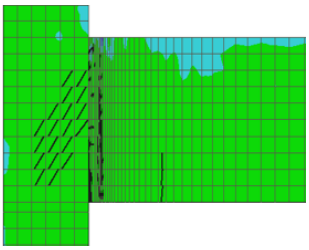

(bb) Joint core: A30-H +60mm

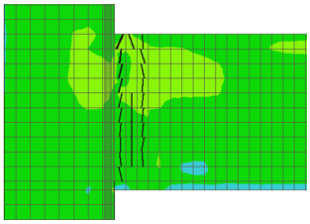

(bc) Retrofit: A30-L -60mm

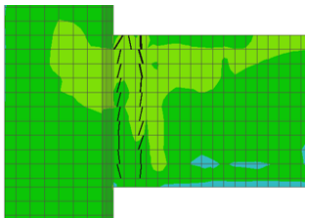

(bd) Retrofit: A30-M - 60mm

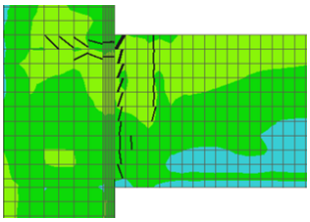

(be) Retrofit: A30-H - 60mm

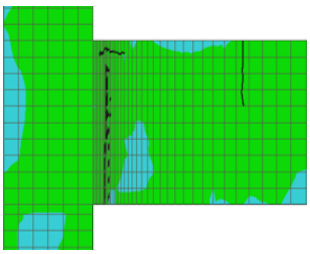

(bf) Joint core: A30-L - 60mm

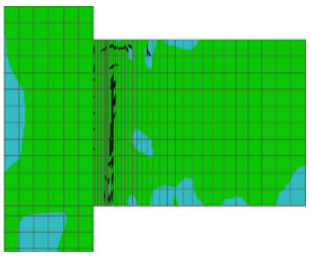

(bg) Joint core: A30-M - 60mm

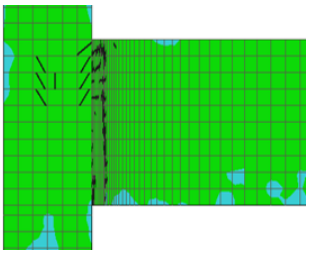

(bh) Joint core: A30-H - 60mm

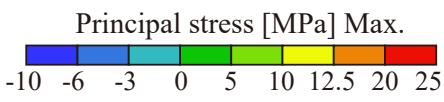

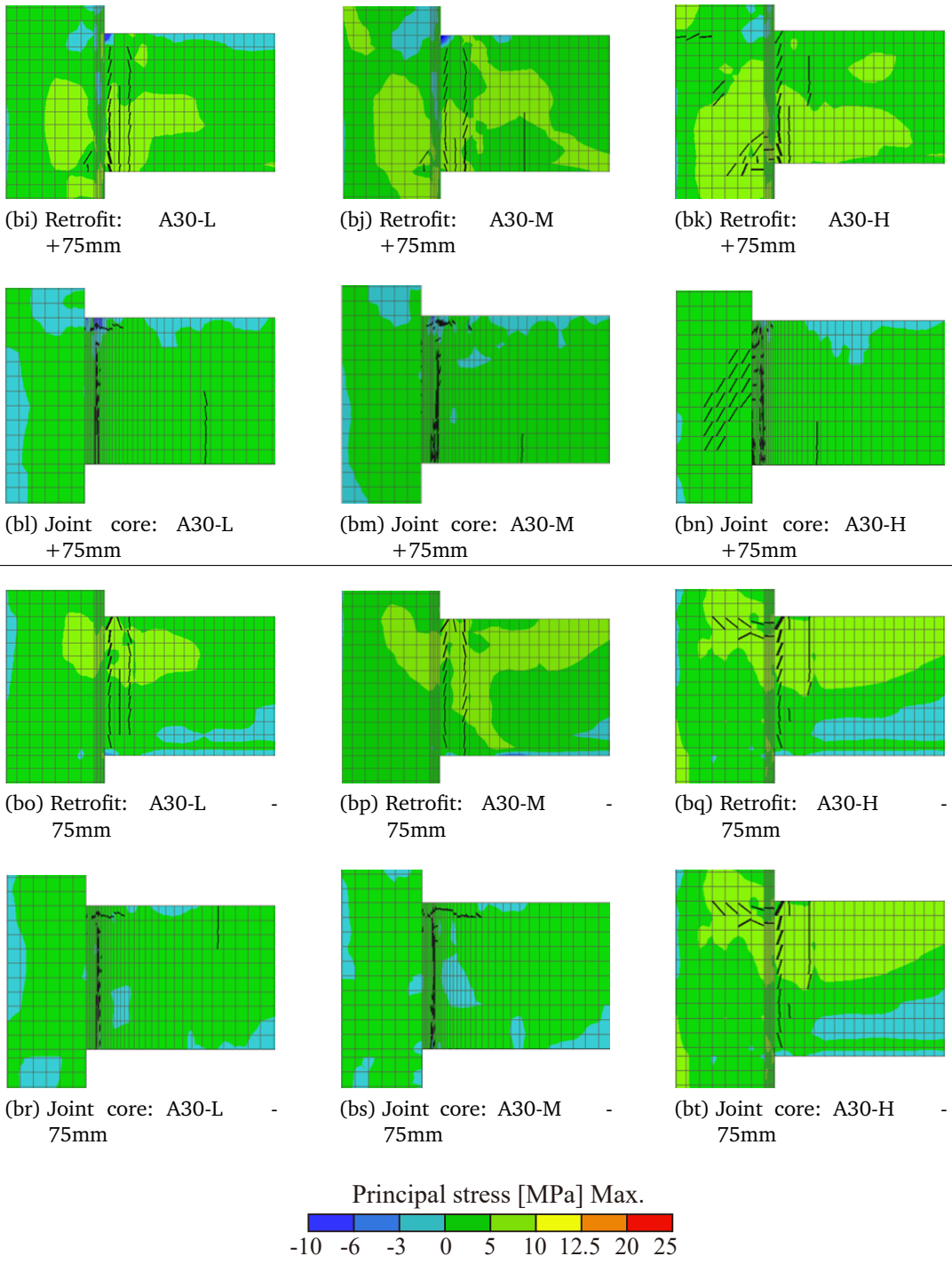

(bi) Retrofit: A30-L +75mm

(bj) Retrofit: A30-M +75mm

(bk) Retrofit: A30-H +75mm

(bl) Joint core: A30-L +75mm

(bm) Joint core: A30-M +75mm

(bn) Joint core: A30-H +75mm

(bo) Retrofit: A30-L - 75mm

(bp) Retrofit: A30-M - 75mm

(bq) Retrofit: A30-H - 75mm

(br) Joint core: A30-L - 75mm

(bs) Joint core: A30-M - 75mm

(bt) Joint core: A30-H - 75mm

Figure B.5 – Cracking pattern of BCJs with a HPFRC jacket of 30 mm, with and no with retrofit, varying the beam's reinforcement ratio

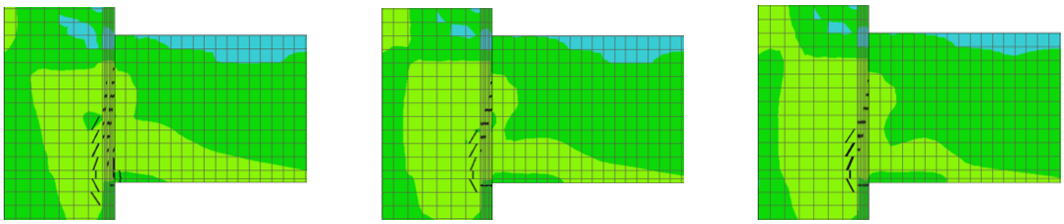

(a) Retrofit: A45-L +15mm

(b) Retrofit: A45-M +15mm

(c) Retrofit: A45-H +15mm

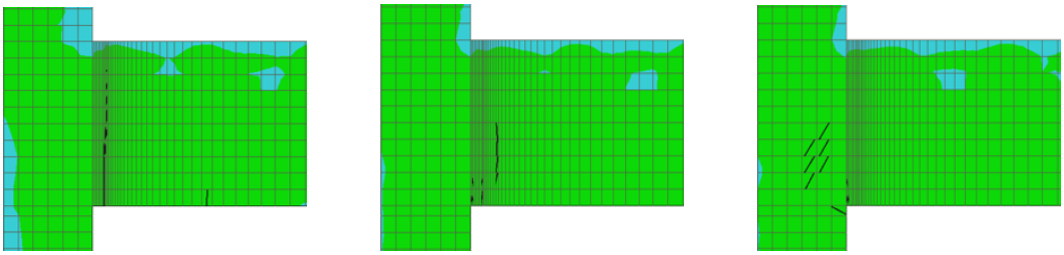

(d) Joint core: A45-L +15mm

(e) Joint core: A45-M +15mm

(f) Joint core: A45-H +15mm

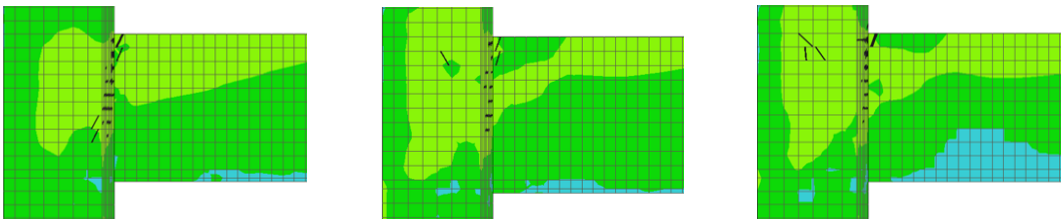

(g) Retrofit: A45-L -15mm

(h) Retrofit: A45-M -15mm

(i) Retrofit: A45-H -15mm

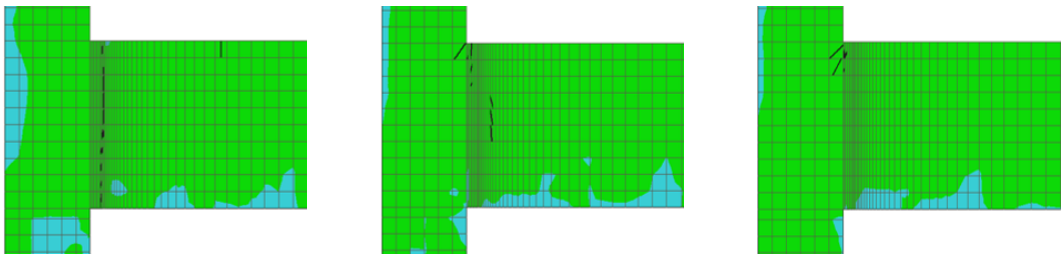

(j) Joint core: A45-L -15mm

(k) Joint core: A45-M -15mm

(l) Joint core: A45-H -15mm

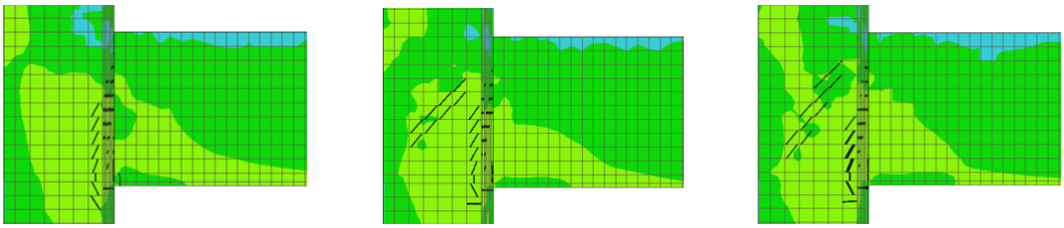

(m) Retrofit: A45-L +22.5mm

(n) Retrofit: A45-M +22.5mm

(o) Retrofit: A45-H +22.5mm

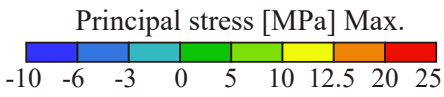

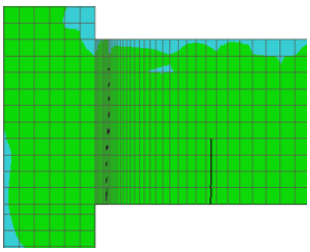

(p) Joint core: A45-L +22.5mm

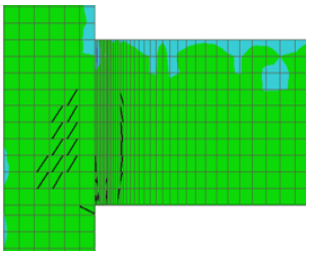

(q) Joint core: A45-M +22.5mm

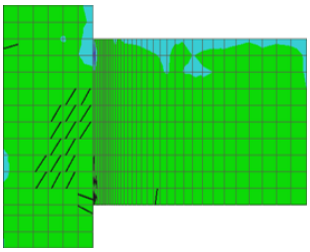

(r) Joint core: A45-H +22.5mm

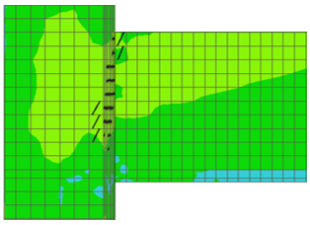

(s) Retrofit: A45-H -22.5mm

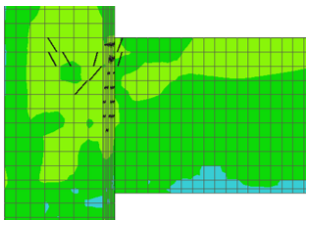

(t) Retrofit: A45-M -22.5mm

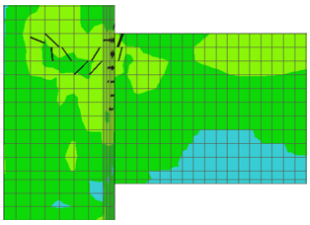

(u) Retrofit: A45-H -22.5mm

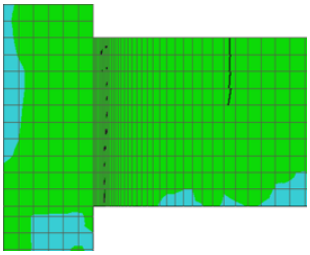

(v) Joint core: A45-L -22.5mm

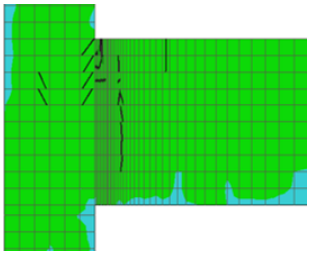

(w) Joint core: A45-M -22.5mm

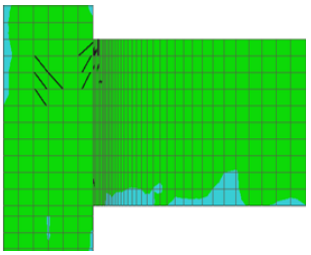

(x) Joint core: A45-H -22.5mm

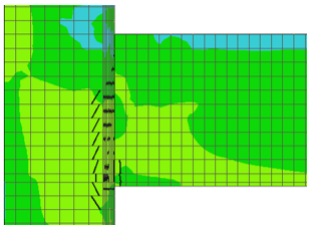

(y) Retrofit: A45-L +30mm

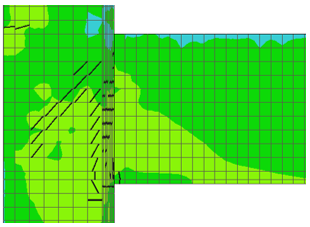

(z) Retrofit: A45-M +30mm

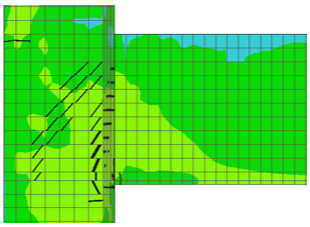

(aa) Retrofit: A45-H +30mm

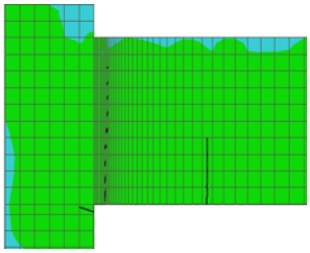

(ab) Joint core: A45-L +30mm

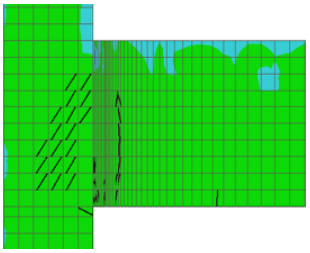

(ac) Joint core: A45-M +30mm

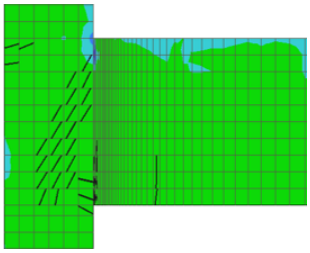

(ad) Joint core: A45-H +30mm

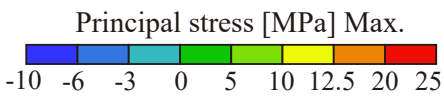

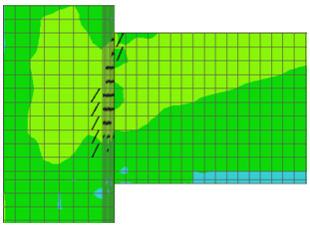

(ae) Retrofit: A45-L -30mm

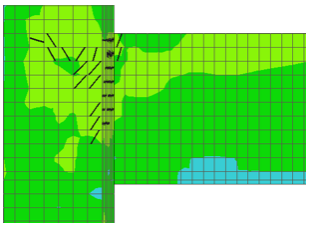

(af) Retrofit: A45-M -30mm

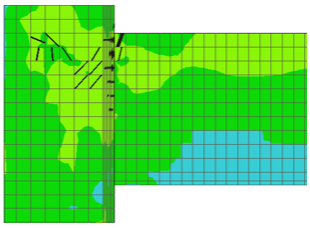

(ag) Retrofit: A45-H -30mm

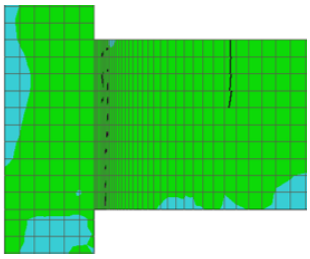

(ah) Joint core: A45-L -30mm

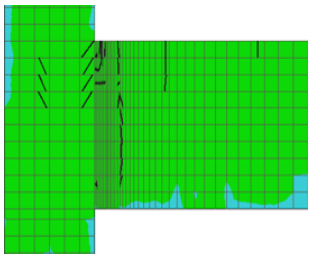

(ai) Joint core: A45-M -30mm

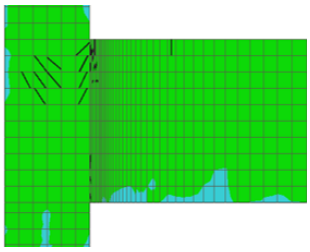

(aj) Joint core: A45-H -30mm

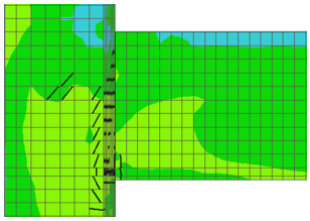

(ak) Retrofit: A45-L +45mm

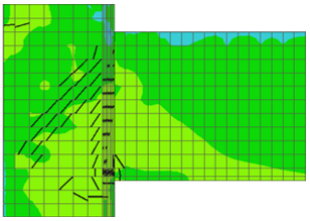

(al) Retrofit: A45-M +45mm

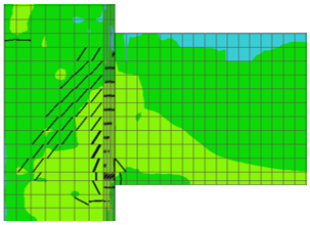

(am) Retrofit: A45-H +45mm

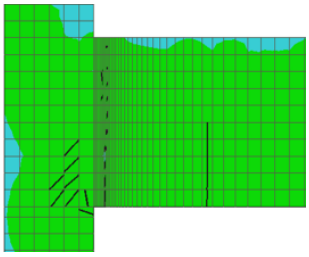

(an) Joint core: A45-L +45mm

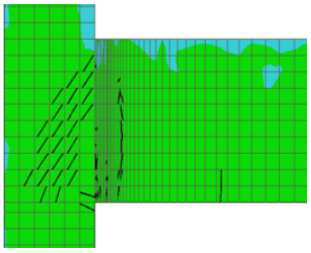

(ao) Joint core: A45-M +45mm

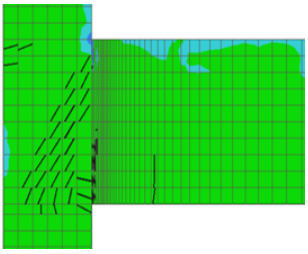

(ap) Joint core: A45-H +45mm

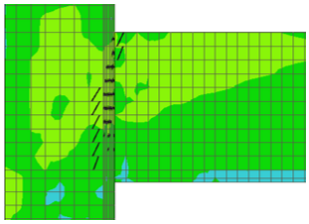

(aq) Retrofit: A45-L -45mm

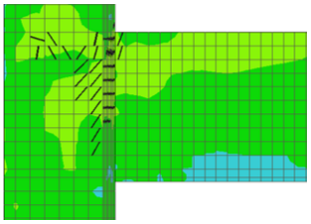

(ar) Retrofit: A45-M -45mm

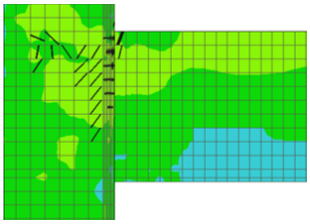

(as) Retrofit: A45-H -45mm

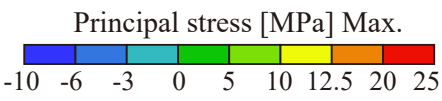

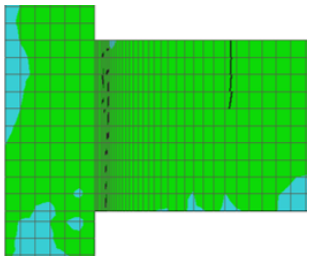

(at) Joint core: A45-L - 45mm

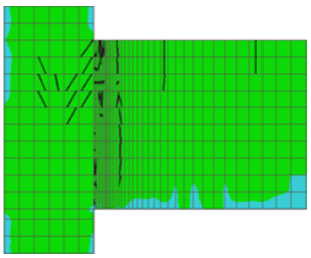

(au) Joint core: A45-M - 45mm

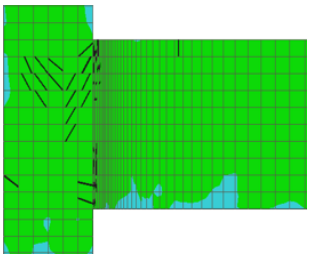

(av) Joint core: A45-H - 45mm

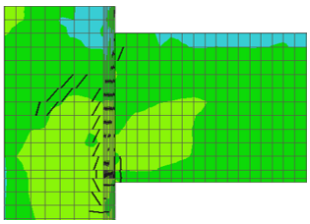

(aw) Retrofit: A45-L +60mm

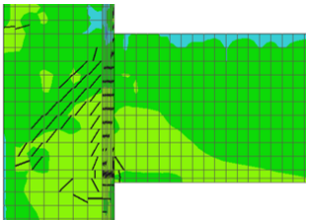

(ax) Retrofit: A45-M +60mm

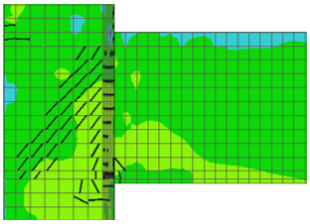

(ay) Retrofit: A45-H +60mm

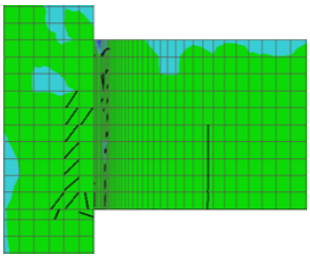

(az) Joint core: A45-L +60mm

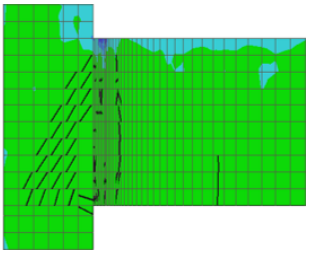

(ba) Joint core: A45-M +60mm

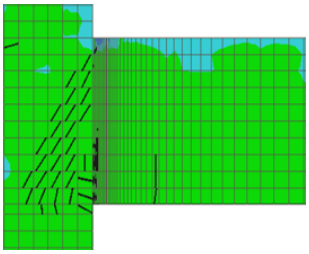

(bb) Joint core: A45-H +60mm

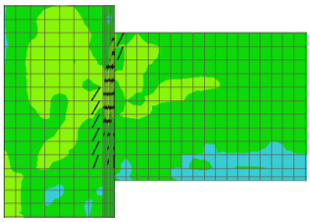

(bc) Retrofit: A45-L -60mm

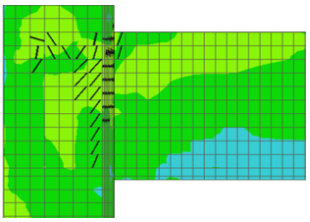

(bd) Retrofit: A45-M - 60mm

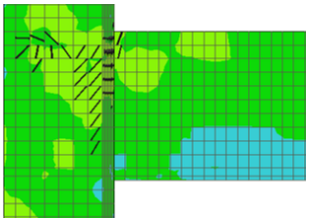

(be) Retrofit: A45-H - 60mm

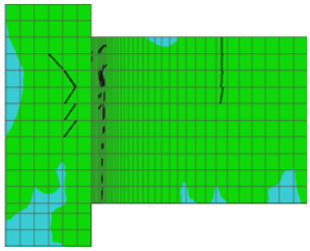

(bf) Joint core: A45-L - 60mm

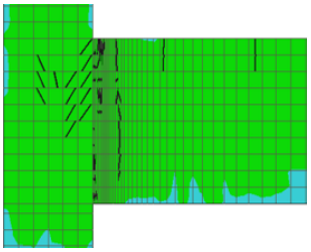

(bg) Joint core: A45-M - 60mm

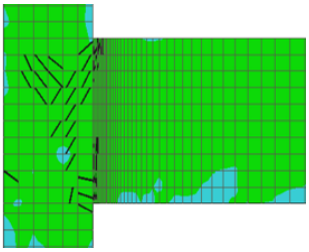

(bh) Joint core: A45-H - 60mm

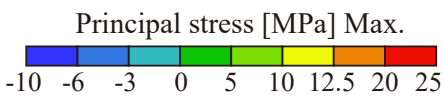

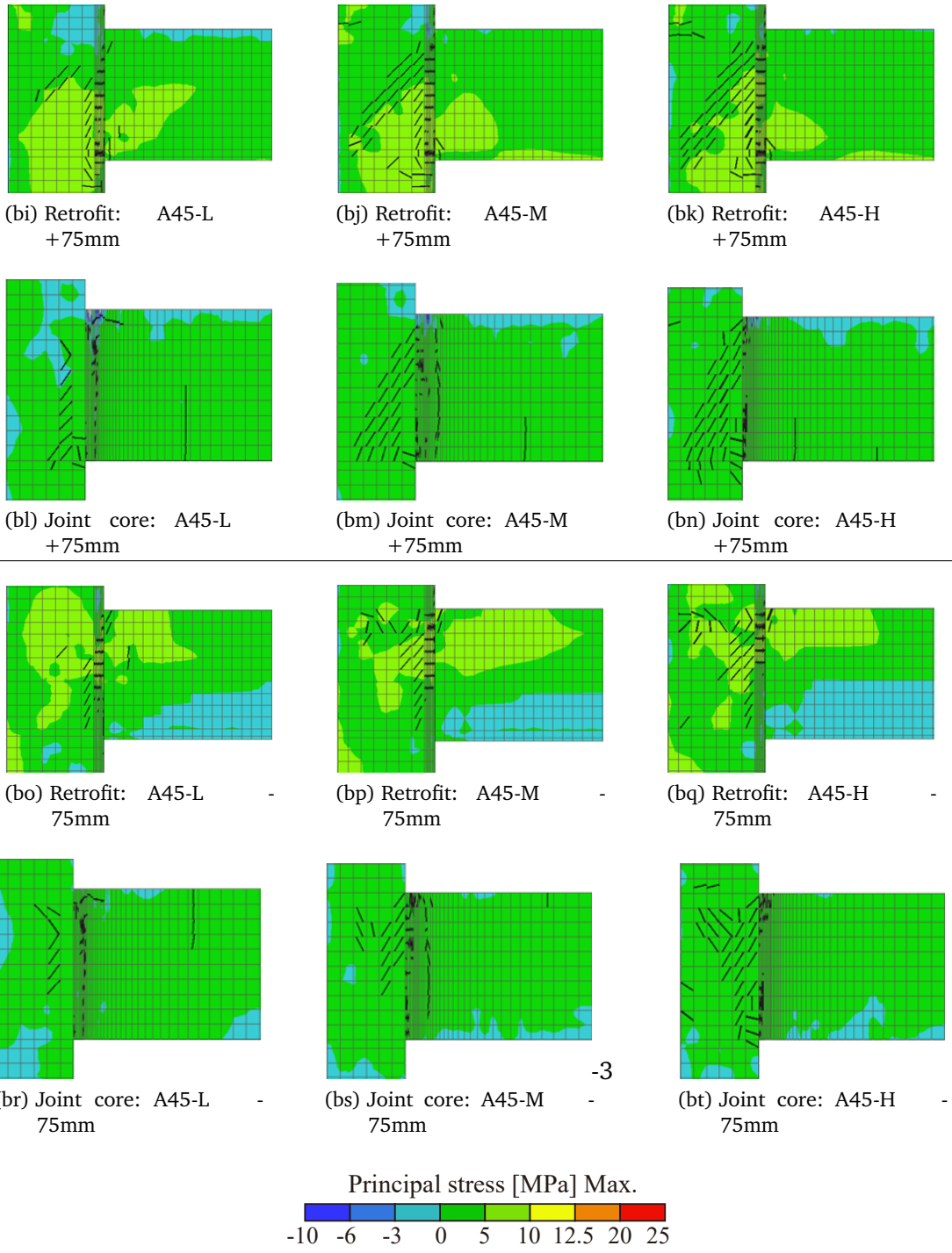

Figure B.6 – Cracking pattern of BCJs with a HPFRC jacket of 45 mm, with and no with retrofit, varying the beam's reinforcement ratio

APPENDIX C –

Table C.1 – Results of parametric study for the retrofitted joints - Flexural model.

Specimen	C_c [N]	C_{R2} [N]	T_{R1} [N]	T_{R2} [N]	T_{R3} [N]	T_{R4} [N]	T_{R5} [N]	C_{sc} [N]	C_{sc} [N]	V_c [kN]
A15 (A15-M)	194,533.9	53,719.3	1,378.1	5,742.6	67,674.7	69.9	24,616.4	155,948.7	7,177.0	34.13
B15	191,814.4	79,452.5	2,072.8	7,224.6	82,325.6	89.1	30,140.6	155,948.7	6,534.3	36.51
C15	187,292.8	103,439.5	2,744.1	8,016.9	94,587.9	99.8	34,803.5	155,948.7	5,468.5	38.50
A30 (A30-M)	222,218.9	122,728.8	2,815.0	10,994.4	134,553.1	298.5	53,708.4	155,948.7	13,370.3	45.19
B30	214,684.7	177,851.6	4,240.9	13,851.3	163,967.9	380.0	65,761.2	155,948.7	11,613.7	50.17
C30	205,497.3	226,987.1	5,623.4	15,393.1	188,643.4	425.1	75,934.8	155,978.7	9,484.0	54.35
A45 (A45-M)	244,472.9	202,529.0	4,305.4	15,826.7	200,991.8	711.3	87,276.2	155,948.7	18,058.1	57.18
B45	232,018.2	288,316.8	6,516.6	19,968.7	245,338.7	904.1	106,862.0	155,948.7	15,203.7	65.00
C45	218,345.5	361,768.5	8,580.1	20,969.3	282,366.7	952.9	123,394.1	155,948.7	12,097.7	71.44
A15-L	156,800.1	43,299.4	1,422.3	5,820.8	68,561.7	69.0	24,616.4	98,614.6	994.8	25.58
A30-L	192,401.9	106,261.2	2,844.2	11,123.6	136,024.8	295.4	53708.4	98,614.6	3,947.8	36.70
A45-L	219,928.4	182,195.6	4,354.7	15,983.5	202,787.8	705.5	87,276.2	98,614.6	7,598.1	48.73
A15-H	287,344.8	79,348.5	1,332.8	5,541.0	65,385.4	72.2	24,616.4	318,746.0	49,000.5	58.01
A30-H	299,309.8	165,305.1	2,739.7	10,660.5	130,748	306.7	53,708.4	318,746.0	52,294.3	69.01
A45-H	310,330.6	257,087.6	4,222.1	15,398.8	196,089.2	727.6	87,276.2	318,746.0	55,041.6	80.93